



UNIVERSITÉ LIBRE DE BRUXELLES

Analysis and interpretation of Aerosol Optical Depth values retrieved from a Brewer spectrophotometer at Uccle, Belgium

Thesis presented to obtain the academic degree of Doctor of Sciences

Veerle De Bock

Promotor: Prof. Dr. Pierre-François Coheur (ULB)
Research Unit: Quantum Chemistry and Photophysics
Co-promotor : Dr. Hugo De Backer (KMI-IRM)
Academic year: 2018-2019

Analysis and interpretation of Aerosol Optical Depth values retrieved from a Brewer spectrophotometer at Uccle, Belgium

Thesis presented to obtain the academic degree of Doctor of Sciences

Veerle De Bock

Promotor: Prof. Dr. Pierre-François Coheur (ULB)
Research Unit: Quantum Chemistry and Photophysics
Co-promotor : Dr. Hugo De Backer (KMI-IRM)
Academic year: 2018-2019

Dankwoord

Een aantal mensen verdienen een woord van dank voor hun bijdrage tot het tot stand komen van dit doctoraat.

Vooreerst wil ik mijn promotor, Dr. Pierre-François Coheur, bedanken om me de kans te geven te doctoreren aan de ULB. Ik heb zijn begeleiding en goede raad enorm geapprecieerd. Dit doctoraat zou ook nooit tot stand zijn gekomen zonder de aanmoediging van Dr. Hugo De Backer, mijn co-promotor en afdelingshoofd op het KMI. Hij is diegene die me als eerste in de richting van een doctoraat stuurde en die altijd tijd heeft om me met goede raad en wetenschappelijke kennis bij te staan. Ik mag van geluk spreken dat ik deel uitmaak van zijn team. Daarnaast wil ik de andere leden van de ozon-, UV- en aerosolgroep op het KMI (Roeland, Alexander, Andy, Quentin, Willem en Pieter) vermelden voor hun individuele bijdragen aan mijn onderzoek. Ik wil ook graag Kevin bedanken voor de gezellige lunches in de tuin van het KMI. Als het even wat minder vlot ging met mijn doctoraat, kon ik steeds bij hem mijn hart luchten. Verder wil ik nog de overige leden van mijn doctoraatscomité (Dr. Lieven Clarisse en Dr. Jean Vander Auwera) en de externe juryleden (Dr. Michel Van Roozendael en Dr. Alkis Bais) bedanken voor het doornemen en evalueren van dit werk.

Tijdens mijn studie geografie aan de universiteit in Gent heb ik het geluk gehad een aantal personen te leren kennen die vrienden voor het leven zullen blijven. Frauke, Carlo, Jeroen, Stefanie, Valerie en Wim: ook al zien we elkaar niet altijd even vaak, ik zou de gezelschapsspelletjes-namiddagen, leuke uitstapjes/reizen en gezellige babbelavonden niet kunnen missen! Ze zorgden vaak voor de nodige ontspanning tijdens dit doctoraat. Het is al een beetje langer geleden, maar ook tijdens mijn zomers op het speelplein, maakte ik vriendinnen die nu nog steeds een belangrijke plaats in mijn hart innemen. Marte, Eline, Elke, Karen en Sofie: ik hoop dat we nog lang ons hart bij elkaar kunnen uitstorten!

Tot slot wil ik ook graag mijn familie bedanken, in het bijzonder mijn ouders en zus, om me altijd te steunen, bij te staan en in mij te geloven! Zonder dat geloof had er nooit sprake geweest van dit doctoraat!

Abstract

The first part of this PhD describes an adapted and improved method for the retrieval of AOD values using sun scan measurements from a Brewer spectrophotometer at 340 nm at Uccle. The retrieved AOD values are subjected to a cloud screening technique and are compared to quasi simultaneous, collocated CIMEL AOD values. The good agreement between both instruments highlights that the Brewer is largely sensitive to AOD at 340 nm and it justifies its use in sun scan mode to expand the AOD retrieval network of instruments. The monthly and seasonal behavior of the retrieved AOD values is also studied in this work and our results agree with results found in literature.

The second part of this work focuses on the relation between the erythemal UV dose, global solar radiation, total ozone column and AOD (at 320 nm) at Uccle. Simultaneous measurements of these variables are available at Uccle for a time period of 25 years (1991–2015) and this time series is long enough to allow for reliable determination of significant changes. Different analysis techniques are combined to allow for an extensive study of the relations between the variables. First, a change point analysis is performed to determine whether there are sudden changes in our time series (of either natural or instrumental origin). Linear trends are calculated for the monthly anomalies time series of the variables and changes in the minimum and maximum values and in the frequency distribution are also investigated. Finally, a multiple linear regression technique is applied to investigate the relation between the erythemal UV dose, global solar radiation, total ozone and AOD (at 320 nm) at Uccle in order to increase our understanding of observed changes in UV radiation at Uccle.

List of acronyms

AATSR	Advanced Along Track Scanning Radiometer
ACE-FTS	Atmospheric Chemistry Experiment – Fourier Transform Spectrometer
ACE-MAESTRO	Atmospheric Chemistry Experiment - Measurement of Aerosol Extinction in the Stratosphere and Troposphere Retrieved by Occultation
ACSAF	Atmospheric Composition Satellite Application Facility
AEROCAN	AEROSol CANada
AERONET	AEROSol RObotic NETwork
AIRS	Atmospheric Infrared Sounder
AOD	Aerosol Optical Depth (without wavelength specification)
ATSR-2	Along Track Scanning Radiometer
AVHRR	Advanced Very High Resolution Radiometer
BC	Black Carbon
BISA	Belgian Institute of Space Aeronomy
BM	Brewer Mast
BSRN	Baseline Surface Radiation Network
BUV	Backscatter UltraViolet
CALIOP	Cloud-Aerosol Lidar with Orthogonal Polarization
CALIPSO	Cloud-Aerosol Lidar and Infrared Pathfinder Satellite Observation
CARIBIC	Civil Aircraft for the Regular Investigation of the atmosphere Based on an Instrument Container
CARSNET	China Aerosol Remote Sensing NETwork
CCD	Calibration quality Clear Day
CCI	Climate Change Initiative
CCN	Cloud Condensation Nuclei
CDNC	Cloud Droplet Number Concentration
CDR	Climate Data Record
CERES	Clouds and the Earth's Radiant Energy System
CF	Calibration Factor
CFC	ChloroFluoroCarbons
CIE	Commission Internationale de l'Eclairage
CLAES	Cryogenic Limb Array Etalon Spectrometer
CNES	Centre National d'Études Spatiales
CNRS-INSU	Centre National de la Recherche Scientifique – Institut National des Sciences de l'Univers
COST	European Cooperation on Science and Technology
CRDP	Climate Research Data Package
DIAL	Differential Absorption Lidar
DMS	DiMethyl Sulphide
DOAS	Differential Optical Absorption Spectroscopy
DS	Direct Sun

DU	Dobson Unit
EBAF	Energy Balanced And Filled
ECC	Electrochemical Concentration Cell
ECV	Essential Climate Variable
EDUCE	European Database for UV Climatology and Evaluation
EESC	Equivalent Effective Stratospheric Chlorine
ERBS	Earth Radiation Budget Satellite
ERF	Effective Radiative Forcing
ERS	European Research Satellites
ESA	European Space Agency
ETC	ExtraTerrestrial Constant
EUBREWNET	EUropean BREWer NETwork
EUMETSAT	EUropean organization for the exploitation of METeorological SATellites
FIR	Far InfraRed
FOV	Field Of View
FTIR	Fourier Transform InfraRed
FWHM	Full Width at Half Maximum
GACP	Global Aerosol Climatology Project
GAW	Global Atmospheric Watch
GCOS	Global Climate Observing System
GEBA	Global Energy Balance Archive
GOME	Global Ozone Monitoring Experiment
GOMOS	Global Ozone Monitoring by Occultation of Stars
HALOE	Halogen Occultation Experiment
HIRDLS	The High Resolution Dynamics Limb Sounder
HIRS	High-resolution Infrared Radiation Sounder
IASI	Infrared Atmospheric Sounding Interferometer
ICNIRP	International Commission on Non-Ionizing Radiation Protection
IGACO	Integrated Global Atmospheric Chemistry Observations
ILAS	Improved Limb Atmospheric Spectrometer
IMG	Interferometric Monitor for Greenhouse gases
IN	Ice Nuclei
IPCC	Intergovernmental Panel on Climate Change
IR	InfraRed
ISAMS	Improved Stratospheric and Mesospheric Sounder
KC	Kobayashi cell
LIDAR	Light Detection And Ranging
LIMS	Limb Infrared Monitor of the Stratosphere
LPM	Langley Plot Method
LRIR	Limb Radiance Inversion Radiometer
LWC	Liquid Water Content
MABE	Mean Absolute Bias Error
MAN	Maritime Aerosol Network

MBE	Mean Bias Error
MCFR	Multi-Channel Filter Radiometers
MERIS	Medium Resolution Imaging Spectrometer for passive atmospheric sounding
MetOp	Meteorological Operational satellite program
MFRSR	MultiFilter Rotating Shadowband Radiometer
MIPAS	Michelson Interferometer for Passive Atmospheric Sounding
MISR	Multi-angle Imaging SpectroRadiometer
MLH	Mixing Layer Height
MLR	Multiple Linear Regression
MLS	Microwave Limb Sounder
MODIS	Moderate Resolution Imaging Spectrometer
MOZAIC	Measurement of Ozone and Water Vapour on Airbus in-service Aircraft
NASA	National Aeronautics and Space Administration
NDACC	Network for the Detection of Atmospheric Composition Change
NIR	Near InfraRed
NMSC	Non-Melanoma Skin Cancers
NOAA	National Oceanic and Atmospheric Administration
O3MSAF	Ozone Monitoring Satellite Application Facility
OA	Organic Aerosol
ODS	Ozone Depleting Substances
OMI	Ozone Monitoring Instrument
OMPS	Ozone Mapping and Profiler Suite
OSIRIS	Optical Spectrograph and InfraRed Imaging System
PARASOL	Polarization and Anisotropy of Reflectances for Atmospheric Sciences coupled with Observations from a Lidar
PBAPs	Primary Biological Aerosol Particles
PFR	Precision Filter Radiometer
PHOTONS	PHOTométrie pour le Traitement Opérationnel de Normalisation Satellitaire
PM	Particulate Matter
POA	Primary Organic Aerosol
POAM	Polar Ozone and Aerosol Measurement
POES	Polar Orbiting Environmental Satellites
POLDER	POlarization and Directionality of the Earth's Reflectances
PSC	Polar Stratospheric Cloud
QUASUME	Quality Assurance of Spectral UV Measurements in Europe
RF	Radiative Forcing
RMIB	Royal Meteorological Institute of Belgium
RMSE	Root Mean Square Error
RTM	Radiative Transfer Model
SAG	Scientific Advisory Group
SAGE	Stratospheric Aerosol and Gas Experiment
SAOZ	Système d'Analyse par Observations Zénithales

SBUV	Solar Backscatter UltraViolet radiometer
SCIAMACHY	Scanning Imaging Absorption spectroMeter for Atmospheric CartographY
SeaWiFS	Sea-Viewing Wide Field-of-View Sensor
SHADOZ	Southern Hemisphere ADditional OZonesondes network
SMILES	Superconducting Submillimeter-Wave Limb-Emission Sounder
SMR	Solar Mesospheric Experiment
SOA	Secondary Organic Aerosol
SORCE	Solar Radiation and Climate Experiment
SS	Sun Scans
SSA	Single Scattering Albedo
SSR	Surface Solar Radiation
SZA	Solar Zenith Angle
TES	Tropospheric Emission Spectrometer
TIR	Thermal InfraRed
TOA	Top Of Atmosphere
TOMS	Total Ozone Mapping Spectrometer
TROPOMI	TROPOspheric Monitoring Instrument
TUV	Tropospheric Ultraviolet and Visible
UNEP	United Nations Environmental Program
UV	UltraViolet
UVI	UV Index
VIS	VISible
VOC	Volatile Organic Compound
WHO	World Health Organization
WMO	World Meteorological Organization
WOUDC	World Ozone and Ultraviolet radiation Data Center

Table of Contents

1. Introduction	1
1.1 The Earth's atmosphere	3
1.1.1 Composition	3
1.1.2 Vertical structure	3
1.2 Radiation	5
1.2.1 What is radiation?	5
1.2.2 Main quantitative characteristics of a radiation field	7
1.2.3 Solar radiation	11
1.2.4 The electromagnetic spectrum	12
1.2.5 The Earth's energy budget	14
1.3 Ultraviolet radiation	16
1.3.1 Definition of the UV-index	17
1.3.2 Factors that influence surface UV radiation	17
1.3.3 Effects of UV-B radiation	19
1.3.4 Measurements of UV	20
1.4 Aerosols	20
1.4.1 Basic information	20
1.4.2 Effects of aerosols	23
1.4.3 Definition of Aerosol Optical Depth	27
1.4.4 Measurement of Aerosol Optical Depth	27
1.5 Ozone	27
1.5.1 What is ozone?	27
1.5.2 Sources of ozone	28
1.5.3 Effects of ozone: 'good' versus 'bad' ozone	33
1.5.4 Measurements of ozone	34
1.6 Measurements	34
1.6.1 In situ measurements	34
1.6.2 Remote sensing	36
1.7 Aim of this work	54
2. Instruments and location	57
2.1 The Brewer spectrophotometer	57
2.1.1 The spectrophotometer	59
2.1.2 Direct Sun (DS) ozone measurements	62

2.1.3 UV measurements	66
2.1.4 AOD retrievals	67
2.1.5 Calibration history.....	69
2.2 The CIMEL sun photometer	69
2.3 Pyranometer.....	70
2.4 Pyrhelimeter.....	71
3. AOD retrieval method using sun scan Brewer measurements	73
3.1 The Beer-Lambert law	73
3.2 The Langley Plot Method	75
3.2.1 Selection of cloudless days	76
3.2.2 Stability of the Calibration Factors	78
3.2.3 Basic requirements for the Langley Plot Method	80
3.3 Sources of uncertainty	81
3.3.1 Earth-Sun distance	81
3.3.2 Uncertainties in the ozone term	82
3.3.3 Uncertainties in the Rayleigh term.....	84
3.3.4 Uncertainties by not including NO ₂ in the calculations.....	87
3.3.5 Uncertainties by not including SO ₂ in the calculations.....	87
3.3.6 Instrumental issues	88
3.3.7 Summary	89
4. Cloud screening of AOD values.....	91
4.1 Initial cloud screening.....	91
4.2 Improved cloud screening technique	92
5. AOD data analysis.....	95
5.1 Comparison with CIMEL data.....	95
5.2 Comparison with Direct Sun $\tau_{\text{aer},320}$ measurements	97
5.3 Monthly and seasonal analysis	98
5.4 Weekly periodicity.....	103
6. Relationship between erythemal UV dose, global solar radiation, total ozone and AOD at Uccle.....	105
6.1 Monthly anomalies	105
6.2 Change point analysis.....	106
6.3 Linear trend analysis.....	107
6.3.1 Method	107

6.3.2 Results	108
6.3.3 Discussion of trends	112
6.4 Multiple linear regression (MLR) analysis	120
6.4.1 Method	120
6.4.2 Results	123
6.4.3 Discussion of the results	130
7. Conclusion and outlook	133
References	137
Appendices	167
Appendix A: Seasonal MLR 2 results	169
Appendix B: Table of quantities and constants mentioned in this work	171
Appendix C: list of publications	175
Articles:	179

1. Introduction

Aerosols are particles in the solid or liquid phase that are suspended in the atmosphere. They have an important influence on the atmospheric chemistry and physics (Cheymol and De Backer, 2003; Raghavendra Kumar et al., 2010). They affect the tropospheric chemical composition, they can reduce visibility and they have important impacts on human health (Unger et al., 2009; Lyamani et al., 2010; Raghavendra Kumar et al., 2010). Aerosols also influence the Earth's radiation budget (Ramanathan et al., 2001). Because of a lack of information concerning the temporal and spatial distribution of aerosols, they are key contributors to the uncertainties in current climate studies (Andreae et al., 2005; IPCC, 2007). The influence of aerosols on ultraviolet (UV) radiation has received a lot of attention in research. The increase of anthropogenic aerosols in non-urban areas of the industrialized countries since the industrial revolution is supposed to have decreased the biologically active UV radiation by 5 to 18% (Liu et al., 1991). Accuracy in UV prediction can be improved if the influence of aerosols on surface UV radiation is clarified (Kim et al., 2008). However, little information is available on the optical properties of atmospheric aerosols in the UV spectral region, compared to the visible (VIS) spectral range (Sellitto et al., 2006). To gain a better understanding of the effect of aerosols in the UV, knowledge of the parameters that determine the optical and physical properties of aerosols is essential (Cazorla et al., 2009; Kazadzis et al., 2009). One of these parameters is the Aerosol Optical Depth (AOD), an integral measurement of the combined aerosol scattering and absorption in the atmospheric column (Mulcahy et al., 2009). When assessing changes in surface UV radiation over time, knowledge of the AOD is of high importance. Without such knowledge, it is very likely that a change in surface UV irradiance is attributed to a change in ozone amount, whereas it could actually be the result of an increase or decrease in aerosol load.

There are more than 200 Brewer instruments operational around the world and previous research has proved that these instruments are capable of retrieving AOD in the UV range, which shows their capacity to substantially expand the global network of AOD observations. Some authors based their retrieval on the absolute calibration of the solar spectral intensity measured by the Brewer (Bais, 1997; Marenco et al., 1997; Kazadzis et al., 2005) whereas others use the Langley extrapolation method to determine the absolute calibration of the intensity (Kirchhoff et al., 2001; Marenco et al., 2002; Cheymol and De Backer, 2003). Arola and Koskela (2004) discussed the systematic errors in the AOD retrieval from Brewer direct sun (DS) measurements, which led to improvements of the conventional Langley Plot Method (LPM) (e.g. Cheymol et al., 2009). Retrieval of AOD at the DS ozone wavelengths (306.3, 310.1, 313.5, 316.8 and 320.1 nm) is possible for all Brewer instruments and since some instruments have already been measuring since the 1980s, long AOD time series can be built in this way.

The aim of this PhD is to improve the observation capacity of the instrument, by using a different type of measurements to retrieve the AOD. Instead of using the standard DS measurements from the Brewer instrument dedicated to ozone retrieval (which are performed at 5 specific wavelengths) (as in Cheymol and De Backer, 2003), sun scan (SS) measurements between 335 and 345 nm, convoluted with the band pass function of the CIMEL sun

photometer filter at 340 nm, are used to obtain AOD values at 340 nm (represented by $\tau_{\text{aer},340}$ in this work). This method was first presented in De Bock et al. (2010). The use of SS measurements at 340 nm allows for a direct comparison between the retrieved Brewer AOD values and the AODs from the CIMEL sun photometer at the same wavelength. To make wider usage of these data possible, an estimate of the uncertainty budget for these measurements is presented in this work. A cloud screening method is developed simultaneously to filter out the measurements that are perturbed by clouds. This cloud screening method was introduced in De Bock et al. (2014).

An important point of concern in scientific communities is the known adverse effect of UV radiation on human health, the biosphere and atmospheric chemistry. Therefore it is important to assess the changes in UV irradiance over prolonged periods of time. Not only do adverse health and environmental effects often relate to long-term exposure (from years to a lifetime); also the timescales of the atmospheric processes that are involved, such as ozone depletion and recovery, are beyond decades (Chubarova, 2008; den Outer et al., 2010). Apart from its obvious relation with global solar radiation and ozone, the amount of UV radiation that reaches the surface of the Earth also depends on the characteristics and quantity of aerosols in the atmosphere and accuracy in UV prediction can be improved if the influence of aerosols on surface UV radiation is clarified. For this reason, the second part of this work focuses on the relation between the erythemal UV dose, global solar radiation, total ozone column and AOD (at 320 nm) at Uccle. Simultaneous measurements of these variables are available at Uccle for a time period of 25 years (1991–2015) and this time series is long enough to allow for reliable determination of significant changes (a minimum of 15 years is required as shown in Weatherhead et al., 1998 and Glandorf et al., 2005). The availability of the simultaneous time series allows an extensive study in which different analysis techniques (e.g. linear trend analysis and multiple linear regression analysis) are combined in order to increase our insights on the relations between the variables.

This PhD is structured as follows: The introduction presents basic information concerning the Earth's atmosphere (Section 1.1), (UV) radiation (Section 1.2 and 1.3), aerosols (Section 1.4), ozone (Section 1.5) and the different measurement techniques (Section 1.6). The instruments and the measurements that are used in this study are presented in Section 2. Section 3 explains how $\tau_{\text{aer},340}$ values are retrieved using sun scan measurements. Here, the uncertainty of the method is also addressed. The developed cloud screening method is discussed in Section 4 after which the resulting $\tau_{\text{aer},340}$ values are analyzed through comparison with CIMEL values and by looking at their weekly, monthly and seasonal behavior (Section 5). In the next section (Section 6), different statistical tools are implemented to gain more understanding in the long-term behavior of and the relations between erythemal UV dose, total global radiation, total ozone column and $\tau_{\text{aer},320}$ at Uccle. The results of this analysis are also discussed in this section. Finally, the conclusions of this work are presented together with future plans in Section 7.

1.1 The Earth's atmosphere

The atmosphere is a thin, gaseous envelope surrounding the Earth, comprised mostly of nitrogen (N₂) and oxygen (O₂), with small amounts of other gases such as water vapor (H₂O) and carbon dioxide (CO₂) (Ahrens, 2007). It extends upward for many hundreds of kilometers, but due to the force of gravity almost 99% of the atmosphere lies within 30 km from the surface of the Earth. There is no clear upper limit to the atmosphere. The density of the atmosphere decreases with altitude and the atmosphere then gradually merges with empty space, which surrounds all the planets.

1.1.1 Composition

More than 99% of the atmosphere consists out of N₂ or O₂ (Ahrens, 2007). The other constituents are present in much lower quantities. Table 1 shows the major constituents of Earth's atmosphere. As aerosols and ozone are of particular interest in this work, they are discussed in more detail in sections 1.4 and 1.5 respectively.

Table 1 : Main constituents of the atmosphere (from Ahrens, 2007). The constituents are divided into permanent and variable gases.

Permanent gases			Variable gases		
		Percent (by volume) dry air			Percent (by volume)
Nitrogen	N ₂	78.08	Water vapor	H ₂ O	0 to 4
Oxygen	O ₂	20.95	Carbon Dioxide	CO ₂	0.038
Argon	Ar	0.93	Methane	CH ₄	$1.4 \cdot 10^{-4}$
Neon	Ne	$1.8 \cdot 10^{-3}$	Nitrous Oxide	N ₂ O	$3 \cdot 10^{-5}$
Helium	He	$5 \cdot 10^{-4}$	Ozone	O ₃	$4 \cdot 10^{-6}$
Hydrogen	H ₂	$6 \cdot 10^{-5}$	Particles (dust, soot, ...)		$1 \cdot 10^{-6}$
Xenon	Xe	$9 \cdot 10^{-6}$	Chlorofluorocarbons (CFCs)		$2 \cdot 10^{-8}$

1.1.2 Vertical structure

The atmosphere can be divided into several layers based on the variation of temperature (Figure 1).

1.1.2.1 Troposphere (0- 16 km)

The troposphere is the layer from the surface of the Earth up to about 9 km (at the poles) to 16 km (at the equator), depending on season and latitude (Saha, 2008). It is characterized by a decrease in temperature with height at a rate of about 6.5°C per km and minimum values of about -55°C to -60°C are reached. The distribution of the temperature within the troposphere is maintained by convective and turbulent transfer of heat due to absorption of solar radiation at the surface to the atmosphere. The troposphere contains all of the weather we are familiar

with on Earth and is relatively well-mixed as a result of rising and descending air currents (Ahrens, 2007).

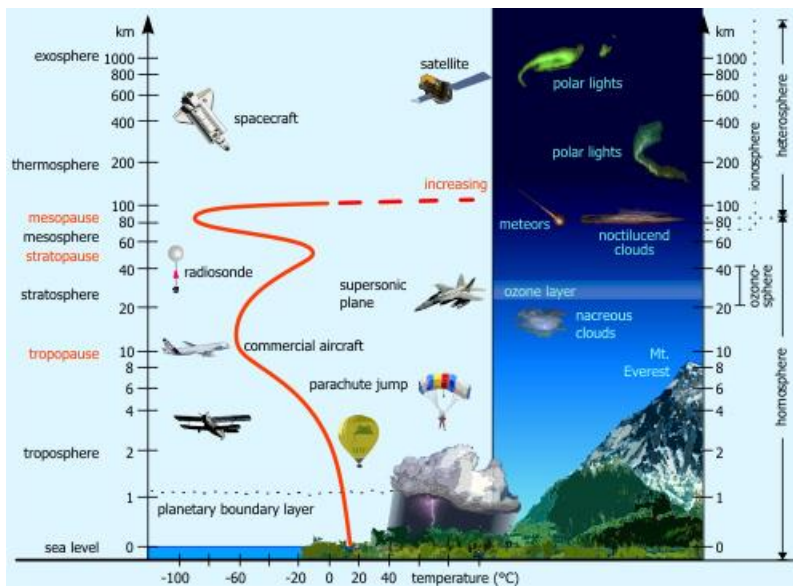


Figure 1 : Layers of the atmosphere based on the variation in temperature, which is represented by the red line¹.

The boundary between the troposphere and stratosphere is known as the tropopause. It can be defined in various ways (Reichler et al., 2003). The traditional definition is based on the rate of decrease of temperature with height (i.e. the lapse rate) (= thermal tropopause). The World Meteorological Organization (WMO) defines the tropopause as the lowest level at which the lapse rate decreases to 2°C/km or less, provided that the average lapse rate between this level and all higher levels within 2 km does not exceed 2°C/km (WMO, 1957). The advantage of the thermal definition is that it can be applied globally, as it only needs the local vertical profile of atmospheric temperature as input parameter. A disadvantage is that it leads to ambiguities in the presence of multiple stable layers. Another way to define the tropopause is based on critical values of isentropic potential vorticity² and variations thereof (= dynamical tropopause). Finally, the tropopause can also be defined based on the chemical composition where the tropopause is associated with sharp gradients in trace gases such as ozone (i.e. ozonopause).

1.1.2.2 Stratosphere (16-50 km)

In the stratosphere, the temperature gradually increases with height to reach a maximum of about 0°C at about 50 km altitude (Saha, 2008). The reason for the temperature inversion in this layer is the presence of ozone which absorbs energetic solar UV energy and warms the stratosphere in this way (Ahrens, 2007). The maximum amount of ozone is located around 25 km altitude. However, the maximum temperature in the stratosphere is not reached at 25 km

¹ <http://www.theozonehole.com/atmosphere.htm>, visited on 17/02/2017

² The potential vorticity (PV) is the absolute circulation of an air parcel that is enclosed between two isentropic surfaces. If PV is displayed on a surface of constant potential temperature, then it is officially called IPV (isentropic potential vorticity)

but around 50 km. Here the air is less dense so the absorption of solar energy raises the temperature of fewer molecules to a much greater degree. Also, much of the solar energy responsible for the heating is absorbed in the upper part of the stratosphere and therefore does not reach down to the level of the ozone maximum. And due to the low air density, the transfer of energy downward from the upper stratosphere is quite slow. The boundary between the stratosphere and mesosphere is called the stratopause.

1.1.2.3 Mesosphere (50-85 km)

The density of the air and the atmospheric pressure in the mesosphere are quite low (Ahrens, 2007). Only 0.1% of all the atmosphere's molecules are found above this level. The temperature decreases with height because there is little ozone in this layer to absorb solar radiation. The lowest temperatures (of about -100 °C) are reached around 85 km. The mesopause is the boundary between the mesosphere and thermosphere.

1.1.2.4 Thermosphere (85-500 km)

This layer is called the 'hot' layer above the mesosphere where temperature starts to increase again with altitude (Ahrens, 2007). The thermosphere intercepts the highly charged particles from space and the high energy UV radiation from the Sun (Saha, 2008). The relatively few atoms that are present in this layer absorb the high energy shortwave radiation from the Sun and get ionized. This ionized layer helps global telecommunication by reflecting radio waves and is also known as the ionosphere. The temperature in this layer varies greatly with solar activity.

1.1.2.5 Exosphere (500-... km)

This layer is the upper limit of the atmosphere and starts around 500 km altitude (Ahrens, 2007). Atoms and molecules shoot off into space as lighter and fast moving molecules can escape the gravitational pull of the Earth.

1.2 Radiation

1.2.1 What is radiation?

Energy can be transferred in the atmosphere by convection, advection, conduction, phase changes and radiation. Radiation refers to the emission or propagation of energy in the form of waves or particles through vacuum or through a material medium. Only electromagnetic radiation can transport energy without a medium. In quantum physics, radiation is considered as a stream of particles (photons), whereas in electromagnetics, radiation is a wave of electric and magnetic fields. In meteorology, it is mostly described as electromagnetic waves but for interaction with matter, the quantum effects become important.

All objects with a temperature higher than absolute zero emit radiation (Ahrens, 2007). The amount of energy radiated from a body depends largely on the temperature of that body and at a given temperature there is a maximum amount of radiant energy that can be emitted per unit time per unit area of a body (Seinfeld & Pandis, 1998). This maximum amount of radiation for a certain temperature is called blackbody radiation. A body that radiates, for every wavelength, the maximum possible amount of radiant energy, is called a blackbody. The spectral irradiance (see also section 1.2.2) of a blackbody $E_{B,\lambda}$ (in $W \cdot m^{-3}$) is described by Planck's law (Eq. 1):

$$E_{B,\lambda} = \frac{2\pi hc^2}{\lambda^5} \frac{1}{e^{\frac{hc}{\lambda k_B T}} - 1} \quad (1)$$

with

- c: speed of light in vacuum ($= 2.9979 \cdot 10^8 \cdot m \cdot s^{-1}$)
- h: Planck's constant ($= 6.626 \cdot 10^{-34} \cdot J \cdot s$)
- λ : wavelength (in m)
- k_B : Boltzmann constant ($= 1.38064852 \cdot 10^{-23} \cdot J \cdot K^{-1}$)
- T: temperature (in K)

The wavelength (in nm) at which the maximum radiation is emitted by a blackbody is represented by Wien's law (Eq. 2):

$$\lambda_{\max} = \frac{2.897 \cdot 10^6 \cdot nm \cdot K}{T} \quad (2)$$

For solar and terrestrial radiation, the maximum amount is emitted at respectively 480 nm and 10000 nm (Figure 2).

The total emissive power E_B or irradiance (in $W \cdot m^{-2}$) is calculated by integrating $E_{B,\lambda}$ over all wavelengths (Eq. 3):

$$E_B = \int_0^{\infty} E_{B,\lambda} d\lambda = k_{SB} \cdot T^4 \quad (3)$$

with k_{SB} being the Stefan-Boltzmann constant (equal to $5.671 \cdot 10^{-8} \cdot W \cdot m^{-2} \cdot K^{-4}$).

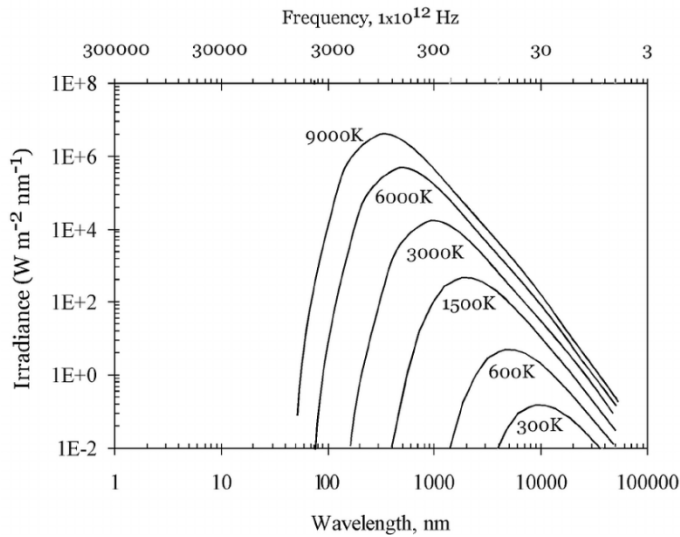


Figure 2 : Log-log plot of the relation between the blackbody irradiance (in $\text{W m}^{-2} \text{nm}^{-1}$) (y-axis) and the wavelength (lower x-axis; in nm) and frequency (upper x-axis; in Hz) as given by Planck’s law for objects with different temperatures (here represented by different curves). Higher temperature blackbodies generate more irradiance in total and at shorter wavelengths (higher frequency) (from Tilley, 2003).

1.2.2 Main quantitative characteristics of a radiation field

1.2.2.1 Solid angle

A solid angle is a three-dimensional angular volume that is defined analogously to the definition of a plane angle in two dimensions.

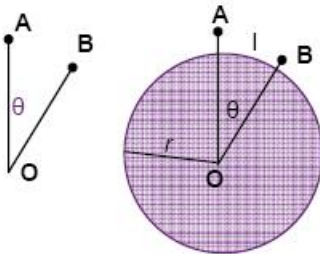


Figure 3 : Plane angle θ (adjusted from Arecchi et al. 2007).

A plane angle, θ , made up of the lines from two points meeting at a vertex, is defined by the arc length of a circle subtended by the lines (l) and by the radius of that circle (r) (Figure 3). It is given by Eq. 4 and its dimensionless unit is the radian, with 2π radians in a full circle.

$$\theta = \frac{l}{r} \tag{4}$$

A solid angle, ω , made up of all the lines from a closed curve meeting at a vertex, is defined by the surface area (A) of a sphere subtended by the lines and by the radius of that sphere (r) (Figure 4).

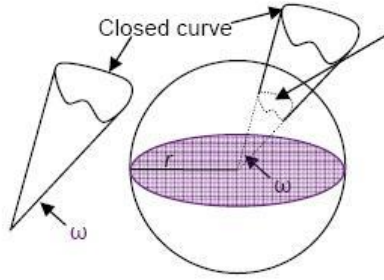


Figure 4 : Solid angle ω (adjusted from Arecchi et al. 2007).

It is given by Eq. 5 and its dimensionless unit is the steradian, with 4π steradians in a full sphere. The solid angle is a measure of how much of the visual field of view (FOV) of an observer, located at a certain point, is occupied by the object (Ryer, 1997). A steradian (sr) is defined as the solid angle which, having its vertex at the center of a sphere, cuts off a spherical surface area equal to the square of the radius of the sphere.

$$\omega = \frac{A}{r^2} \quad (5)$$

1.2.2.2 Quantities from the perspective of the radiation source

The way radiative quantities are defined depends on whether we study them at the source of the radiation (section 1.2.2.2) or as an observer of the radiation (section 1.2.2.3).

Table 2 : The radiometric terms and units discussed in section 1.2.2.2 are presented here. On the left side, the spectral quantities are presented and on the right side the corresponding monochromatic (i.e. at one specific wavelength) quantities are shown. The subscript s is used to emphasize that the quantities are defined from a source's perspective.

Spectral			Monochromatic		
Term	Symbol	Unit	Term	Symbol	Unit
Radiant flux	Φ	W	Spectral flux	Φ_λ	W m^{-1}
Intensity	I_s	W sr^{-1}	Spectral Intensity	$I_{s,\lambda}$	$\text{W sr}^{-1} \text{m}^{-1}$
Irradiance	E_s	W m^{-2}	Spectral Irradiance	$E_{s,\lambda}$	W m^{-3}
Radiance	L_s	$\text{W m}^{-2} \text{sr}^{-1}$	Spectral Radiance	$L_{s,\lambda}$	$\text{W m}^{-3} \text{sr}^{-1}$

1.2.2.2.1 Radiant flux Φ

The radiant flux Φ (in W or J/s) is the rate at which energy is radiated from a source. The spectral flux is denoted as Φ_λ and is expressed in W m^{-1} .

1.2.2.2.2 Radiant intensity I_s

Not all bodies radiate equally in every direction. To describe how much energy is radiated by a source in a certain direction, the radiant intensity I_s is used. It is the radiant flux radiated per unit solid angle in a particular direction (θ, φ) (Eq. 6) and is expressed in W sr^{-1} .

$$I_s = \frac{d\Phi}{d\omega} \quad (6)$$

The spectral intensity $I_{s,\lambda}$ is expressed in $\text{W sr}^{-1} \text{m}^{-1}$.

1.2.2.2.3 Irradiance E_s

The irradiance E_s is the rate at which radiant energy is falling upon a unit area of a surface (Eq. 7). It is a flux density and is expressed in W m^{-2} . It does not contain any information about the direction of the radiation.

$$E_s = \frac{d\Phi}{dA} \quad (7)$$

with A the surface area. The spectral irradiance $E_{s,\lambda}$ is expressed in W m^{-3} .

1.2.2.2.4 Radiance L_s

The radiance L_s is the radiant flux per unit solid angle and per unit area (Eq. 8). It is expressed in $\text{W m}^{-2} \text{sr}^{-1}$. The spectral radiance $L_{s,\lambda}$ is expressed in $\text{W sr}^{-1} \text{m}^{-3}$.

$$L_s = \frac{d^2\Phi}{d\omega \cdot dA} \quad (8)$$

1.2.2.3 Quantities from the perspective of the observer

When looking at this from the perspective of an observer/instrument (e.g. at the surface of the Earth), the concept changes slightly. The corresponding radiometric quantities are presented in Table 3.

Table 3 : The radiometric terms and units discussed in section 1.2.2.3 are presented here. On the left side, the spectral quantities are presented and on the right side the corresponding monochromatic (i.e. at one specific wavelength) quantities are shown.

Spectral			Monochromatic		
Term	Symbol	Unit	Term	Symbol	Unit
Intensity	I	$\text{W sr}^{-1} \text{m}^{-2}$	Spectral Intensity	I_λ	$\text{W sr}^{-1} \text{m}^{-3}$
Irradiance	E	W m^{-2}	Spectral Irradiance	E_λ	W m^{-3}

1.2.2.3.1 Spectral intensity I_λ

The spectral intensity I_λ is the amount of radiation energy, coming from a certain direction, that is received by the observer on a unit of area at a certain wavelength and is defined in $\text{W sr}^{-1} \text{m}^{-3}$. The intensity I is the integral over all wavelengths and is defined in $\text{W sr}^{-1} \text{m}^{-2}$.

1.2.2.3.2 Spectral irradiance or flux E_λ

The spectral irradiance E_λ can be defined as the amount of radiation energy from all directions that is received by the observer on a unit of area at a certain wavelength and is defined in W m^{-3} . The irradiance E is the integral over all wavelengths and is defined in W m^{-2} .

1.2.2.4 The Beer-Lambert law

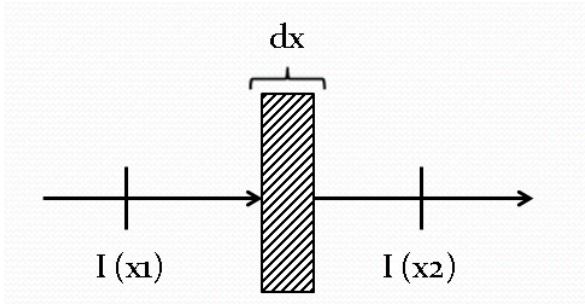


Figure 5: Propagation of radiation through a layer of thickness dx , perpendicular to a beam of intensity I .

Consider the propagation of radiation through a layer of thickness dx perpendicular to a beam of intensity I (Figure 5). The extinction of radiation on traversing an infinitesimal path length dx is linearly proportional to the amount of matter along the path (Eq. 9)

$$dI = -\alpha_e \cdot I \cdot dx \quad (9)$$

where α_e (units of inverse length) is called the extinction coefficient which is proportional to the density of the material in the medium. Extinction includes both absorption and scattering. Absorption is a process that removes the radiant energy from an electromagnetic field and transfers it to other forms of energy. In contrast to absorption, the radiant energy scattered remains in the form of radiation, but changes its direction from that of the incident radiation. For a finite path between x_1 and x_2 , integration of Eq. 9 gives Eq. 10:

$$I(x_2) = I(x_1) \exp(-\tau) \quad (10)$$

where

$$\tau = \int_{x_1}^{x_2} \alpha_e(x) dx \quad (11)$$

is the total optical thickness between x_1 and x_2 . When x is measured vertically in the atmosphere, the total optical thickness is called total optical depth. If the medium is homogeneous, $\alpha_e(x) = \alpha_e$, independent of x and

$$I(x_2) = I(x_1) \exp[-\alpha_e(x_2 - x_1)] \quad (12)$$

which is known as the Beer-Lambert law of extinction. Absorption and scattering occur simultaneously because all molecules and particles both absorb and scatter. The extinction coefficient is the sum of absorption and scattering:

$$\alpha_e = \alpha_a + \alpha_s \quad (13)$$

with α_a and α_s being the absorption and scattering coefficient respectively. Consequently, the total optical thickness can then be expressed as the sum of the optical thickness due to absorption (τ_a) and that due to scattering (τ_s):

$$\tau = \tau_a + \tau_s \quad (14)$$

1.2.2.5 Cross sections and solar zenith angle

The extinction cross section of a given particle (or molecule) is a parameter that measures the attenuation of electromagnetic radiation by this particle (or molecule). In the same fashion, scattering and absorption cross sections can be defined. If N is the particle (or molecule) number concentration of a given type of particles (or molecules) of the same size (in molecules cm^{-3}), then

$$\sigma_e(\lambda) = \frac{\alpha_e(\lambda)}{N} \text{ is the extinction cross section (in cm}^2 \text{ molecule}^{-1}\text{)} \quad (15)$$

$$\sigma_a(\lambda) = \frac{\alpha_a(\lambda)}{N} \text{ is the absorption cross section (in cm}^2 \text{ molecule}^{-1}\text{)} \quad (16)$$

$$\sigma_s(\lambda) = \frac{\alpha_s(\lambda)}{N} \text{ is the scattering cross section (in cm}^2 \text{ molecule}^{-1}\text{)} \quad (17)$$

The angle measured at the Earth's surface between the Sun and the zenith is called the solar zenith angle (SZA) and it is denoted by θ_0 . When the Sun is exactly overhead, $\theta_0=0^\circ$ and when it is at the horizon, $\theta_0=90^\circ$. As θ_0 increases, the path length of the solar beam through the atmosphere increases. If the relative path length of the solar beam from the top of the atmosphere (TOA) to the surface when the Sun is directly overhead is taken as 1.0, then the path length m at θ_0 , neglecting the sphericity of the Earth is

$$m = \frac{1}{\cos \theta_0} = \sec \theta_0 \quad (18)$$

The optical depth of the atmosphere increases as the path length increases since the solar beam transects a longer section of the atmosphere, and there is proportionally more opportunity for extinction to occur.

1.2.3 Solar radiation

The radiant energy of the Sun can be considered as practically the only source of energy that influences atmospheric motions and many processes in the atmosphere (Kondratyev, 1969). The maximum radiant energy from the moon is less than 0.002% compared to solar radiation. The Sun is a sphere with a radius of about $6.95 \cdot 10^5$ km and a mass of about $1.99 \cdot 10^{30}$ kg. About three quarters of the Sun's mass consists of hydrogen (H) and the remaining quarter is

mainly helium (He) (Sørensen 2010). In its core, energy is produced by nuclear reactions (fusion of 4 H atoms into 1 He atom) and it is believed that energy is transferred to the outer layers mainly by electromagnetic radiation. The photosphere (i.e. the outer 500 km of the Sun) emits most of the radiation received on Earth and the radiation emitted by the photosphere approximates that of a blackbody of 6000 K.

Annual fluctuations of the incoming solar radiation at the surface of the Earth are a result of the changing Earth-Sun distance over the course of a year. The average distance is $149.6 \cdot 10^6$ km and it varies with $5 \cdot 10^6$ km within one year (about 3.3%). Further fluctuations in the amount of solar radiation received at the top of the atmosphere are caused by slight irregularities in the photosphere (number of sunspots), in combination with the Sun's rotation (about one revolution per month) and by possible time variations in the surface luminosity of the Sun (Sørensen, 2010).

When the radiant energy of the Sun passes through the atmosphere, it can be absorbed or scattered. As a result, we don't only observe the direct solar radiation (i.e. the parallel beams of the Sun's rays) at the surface, but also diffuse solar radiation (i.e. coming from different points/directions in the sky). The direct and diffuse irradiance received at a given SZA θ_0 form the global radiation and the relation is described by Eq. 19:

$$E_{global} = E_{direct} \cdot \cos(\theta_0) + E_{diffuse} \quad (19)$$

1.2.4 The electromagnetic spectrum

The spectrum of radiation is the distribution of spectral radiant energy, arranged in order of its wavelengths. Three interrelated measures are used to specify the location in the electromagnetic spectrum:

1. wavelength λ (in m)
2. frequency ν (in $s^{-1} = \text{Hz}$)
3. wavenumber $\tilde{\nu} = \lambda^{-1}$ (in m^{-1})

Wavelength and frequency are related as follows:

$$\nu = \frac{c}{\lambda} \quad (20)$$

with c being the speed of light.

The electromagnetic spectrum³ is made up, in order of increasing wavelength (and decreasing energy), of gamma rays (< 10 nm), X-rays (10-100 nm), UV light (100-400 nm), visible light (400-750 nm), infrared light (750- 10^5 nm), micro waves (1 mm to 10^3 mm) and radio waves (1 mm to 10^8 mm) (Figure 6).

³ <https://science.nasa.gov/ems/>; visited 10/02/2017

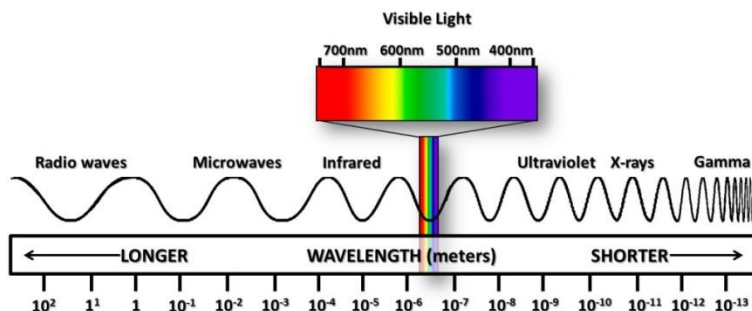


Figure 6 : The electromagnetic spectrum divided by wavelength (in m)⁴.

Gamma rays are produced in nuclear reactions and are often referred to as ionizing radiation⁵. X-rays are also ionizing radiation, but are somewhat less potent than gamma rays. They can be produced in nuclear reactions or by the bombardment of metal surfaces with very fast moving electrons. X-rays are deflected by electrons and atomic nuclei, which makes them useful both for medical imaging and for investigating the precise structure of molecules. The UV region is the one at wavelengths between 100 and 400 nm. A familiar division of the UV is the separation between UV-A, UV-B and UV-C that we will describe in more detail in chapter 1.3. Our eyes are sensitive to radiation in the VIS region and observe it as colors (Table 4). It coincides with the wavelengths at which the Sun emits the greatest amount of radiant energy (see Figure 2).

Table 4 : Wavelengths of the different colors in the visible part of the spectrum (source: Kondratyev, 1969).

COLOR	WAVELENGTH
Violet	390-455 nm
Dark blue	455-485 nm
Light blue	485-505 nm
Green	505-550 nm
Yellow-green	550-575 nm
Yellow	575-585 nm
Orange	585-620 nm
Red	620-760 nm

The infrared (IR) region covers wavelengths higher than 750 nm and can be divided into the Near Infrared (NIR: 750-3000 nm) and the Far Infrared (FIR: 3000 – $1 \cdot 10^5$ nm). Infrared radiation tends to change the vibrational states of molecules, i.e. how fast the atoms in a molecule are shaking back and forth. When the molecules absorb infrared radiation, they vibrate faster, and so the temperature of the molecules increases. Radio waves (1 mm to 10^8 mm) are used for transmission of data, via modulation. In astronomy, radio waves are used to gain information from distant stars using radio telescopes. Micro waves are the highest frequency of radio waves (1 mm to 1 m).

⁴ <http://www.ces.fau.edu/nasa/module-2/radiation-sun.php>; visited on 10/02/2017

⁵ When they pass through matter, they tend to knock electrons completely of their atoms and molecules, leaving the atoms or molecules as ions afterwards.

Radiation is usually called shortwave radiation when the wavelengths are between 300 and 3000 nm. Above this threshold, radiation is called long wave radiation.

1.2.5 The Earth's energy budget

The climate of the Earth is controlled by the amount of solar radiation intercepted by the planet and the fraction that is absorbed. The flux density of solar energy, integrated over all wavelengths, on a surface perpendicular to the solar beam at the Earth's orbit is about 1360 W m^{-2} (Hartmann et al., 2013). This is called the solar constant S_0 . The cross-sectional area of the Earth that intercepts the solar beam is πR^2 , with R the radius of the Earth. Thus the fraction of the solar constant received on average per unit area of the Earth is $(\pi R^2/4\pi R^2) = 1/4$ of the solar constant, about 340 W m^{-2} . Figure 7 shows the most recent global mean energy budget (from the latest Intergovernmental Panel on Climate Change (IPCC) report, Hartmann et al., 2013, adapted from Wild et al., 2013). In Figure 7, the following values are used (Wild et al., 2013):

- For the global mean TOA components representative for the beginning of the 21st century: 340 W m^{-2} (based on the Solar Radiation and Climate Experiment (SORCE) estimate of the solar irradiance)
- For the reflected solar radiation: 100 W m^{-2} (based on the estimates from the Clouds and the Earth's Radiant Energy System (CERES) Energy Balance And Filled (EBAF))
- For the outgoing thermal radiation: 239 W m^{-2} (based on the estimates from CERES EBAF).

The difference between the net absorbed solar radiation (240 W m^{-2}) and the outgoing thermal radiation (239 W m^{-2}) takes into account (in a rounded way) the effect of the approximately 0.6 W m^{-2} global energy imbalance inferred from ocean heat content measurements. For the downward solar radiation, a value of 185 W m^{-2} is used (which fits best to the direct surface observations). The estimate of the reflected solar radiation at Earth's surface is 24 W m^{-2} (assuming a global mean surface albedo of 0.13). With this 24 W m^{-2} reflected out of the total 185 W m^{-2} of downward solar radiation, 161 W m^{-2} is left for absorption at the surface of the Earth. If the estimates of TOA and surface absorbed solar radiation (respectively 240 W m^{-2} and 161 W m^{-2}) are combined, an amount of 79 W m^{-2} is left as a residual for the absorption of solar radiation in the atmosphere. For the global mean downward thermal radiation, an estimate of 342 W m^{-2} is used and for the upward thermal flux from the surface the value of 398 W m^{-2} is adopted. From these estimates of the thermal exchanges, a net surface thermal cooling of -56 W m^{-2} can be inferred. Together with the best estimate of 161 W m^{-2} for the surface absorbed solar radiation, this results in an estimate of 105 W m^{-2} for the global mean surface net radiation. This is the radiative energy available at the surface to be redistributed amongst the non-radiative surface energy balance components. It is predominantly used up by the turbulent fluxes of sensible and latent heat, while a small amount (0.6 W m^{-2}) is going into the subsurface, predominantly into the oceans, as the planet is not in equilibrium. This residual subsurface heat flux is shown by the green arrow in Figure 7. 104 W m^{-2} is then left for the sensible and latent heat fluxes. A value of 20 W m^{-2} is used for the global mean

sensible heat flux, whereas 84 W m^{-2} is adopted for the global mean latent heat flux (the energy equivalent of surface evaporation). All the above values are considered to represent present day climate. It should be noted that the components of the global energy balance are not necessarily stable over time, which means that an update might become necessary as time progresses (Wild et al., 2013).

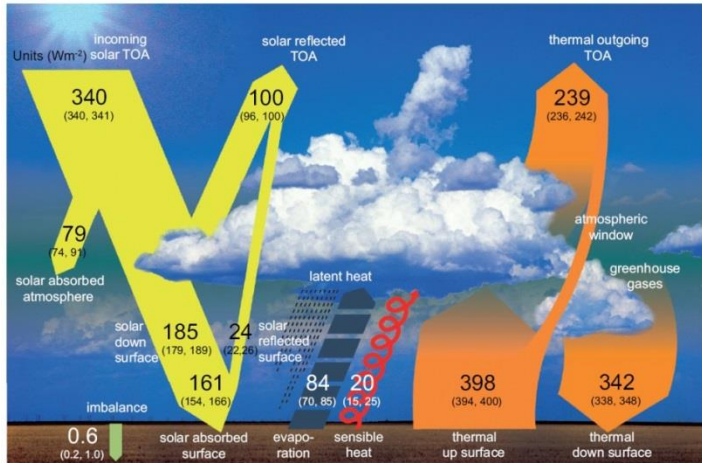


Figure 7 : Global mean energy budget under present-day climate conditions. Numbers state magnitudes of the individual energy fluxes in W m^{-2} , adjusted within their uncertainty ranges to close the energy budgets. Numbers in parentheses attached to the energy fluxes cover the range of values in line with observational constraints (from Hartmann et al., 2013).

1.2.5.1 Radiative forcing

Radiative forcing (RF) is one of the most widely used metrics to provide an estimate of the climate impact of individual factors (Myrhe et al., 2013). It is the net change in the energy balance of the Earth system due to some imposed perturbation and is usually expressed in W m^{-2} averaged over a period of time and quantifies the energy imbalance that occurs when the imposed change takes place. Both human activity and natural changes are drivers of climate change. A large number of greenhouse gases have substantially increased since the Industrial Era and some of them are entirely of anthropogenic origin. Human activity has also modified aerosol concentrations and land cover and changed the surface albedo. The two dominant natural contributors of climate change are solar and volcanic forcings.

1.2.5.2 Greenhouse effect

As explained in section 1.2.5, the Earth emits thermal infrared long wave radiation at its surface, which balances the incoming solar radiation. Part of this terrestrial infrared radiation leaves our atmosphere, however another part is absorbed by gases that are present in the atmosphere. The energy that escapes to space is significantly smaller than that emitted at the surface and this leads to a warming of the atmosphere, known as the greenhouse effect (Raval & Ramanathan, 1989). Without this natural greenhouse effect, the temperature of the Earth would be much lower, around -18°C , which is a temperature much too cold to support the diversity of life that exists today on the planet (Casper, 2010).

Anthropogenic activities increase since several decades the concentration of greenhouse gases in the atmosphere, which enhances the greenhouse effect (Figure 8) leading to an increased warming of the Earth. Some of the most important greenhouse gases include carbon dioxide (CO₂), methane (CH₄), nitrous oxide (N₂O) and several other fluorine-containing halogenated substances. Atmospheric water vapor is known to be the most abundant and effective greenhouse gas (Held and Soden, 2000). An increase of anthropogenic greenhouse gases (such as CO₂) will continue warming the Earth, which will lead to more evaporation of water from the surface, increasing the amount of water vapor in the atmosphere, and thereby the surface temperature. This effect is called the ‘positive water vapor feedback’ (Philipona et al., 2005).

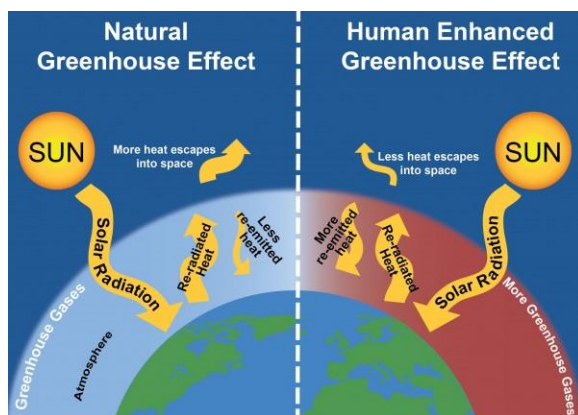


Figure 8 : The natural and human enhanced greenhouse effect⁶.

1.3 Ultraviolet radiation

Ultraviolet radiation (100-400 nm) is a part of the electromagnetic spectrum emitted by the Sun. As we detailed before, UV radiation can be further subdivided into three spectral bands: UV-A, UV-B and UV-C (World Health Organization (WHO), 2002). UV-C radiation (100-280 nm) is the most dangerous as it is the most energetic. This part of the UV spectrum is completely absorbed by stratospheric O₃ and O₂ and does not reach the Earth’s surface (Jégou et al., 2011). UV-B ranges in wavelengths between 280 and 315 nm. Approximately 90% of UV-B radiation is absorbed by O₃, H₂O, O₂ and CO₂ (WHO, 2002). O₃ absorbs much of the shorter wavelength radiation, but this absorption weakens as 315 nm is approached. The effects of UV-B exposure on humans and plants are significant and described in greater detail in Section 1.3.3. The wavelengths of UV-A radiation range between 315 and 400 nm. O₃ absorbs very little of this part of the UV spectrum. UV-A radiation is needed by humans for the synthesis of vitamin-D; however, too much UV-A causes photo-aging (toughening of the skin), suppression of the immune system and, to a lesser degree, reddening of the skin, and cataract formation⁷. Of the global UV irradiance at the surface, 94% is UV-A and 6% is UV-B (Jégou et al., 2011).

UV radiation can be measured as an irradiance (in W m⁻²) or as a radiant exposure or dose (in J m⁻²), which is the energy incident upon a surface unit area during a specified period of time.

⁶ <http://css.umich.edu/factsheets/climate-change-science-and-impacts-factsheet>; visited on 9/8/17

⁷ http://www.cpc.ncep.noaa.gov/products/stratosphere/uv_index/uv_nature.shtml; visited on 23/11/2016

The biological effects of UV energy are described by different action spectrum functions, which are used as a weighting function for the UV spectrum in an integration of the monochromatic UV irradiance (Jégou et al., 2011). These action spectra describe the sensitivity of a particular life form to UV radiation (Kerr, 2005).

1.3.1 Definition of the UV-index

Originally, the UV index (UVI) was formulated independently in several countries and used in programs for public information about UV radiation (Vanicek et al., 2000). Its definition has later been standardized and published as a joint recommendation by the WHO, the WMO, the United Nations Environmental Program (UNEP) and the International Commission on Non-Ionizing Radiation Protection (ICNIRP), in order to raise public awareness about the potential detrimental effects on health from solar UV exposure and to alert people of the need to adopt protective measures. The UV index is a measure of the UV radiation that is related to and defined for a horizontal surface. It is defined as the effective irradiance on a horizontal surface obtained by integrating the spectral irradiance weighted by the Commission Internationale de l'Eclairage (CIE) reference action spectrum for UV-induced erythema on the human skin (ISO, 1999; McKinlay and Diffey, 1987) up to and including 400 nm and normalized to 1.0 below 298 nm (Table 5). It is expressed numerically as the equivalent of multiplying the time weighted average effective irradiance (in $W m^{-2}$) by 40.

$$UVI = k_{er} \cdot \int_{250nm}^{400nm} E_{\lambda} \cdot S_{er}(\lambda) \cdot d\lambda \quad (21)$$

where E_{λ} is the spectral solar irradiance expressed in $W m^{-2} nm^{-1}$ at wavelength λ and $d\lambda$ is the wavelength interval used in the integral. $S_{er}(\lambda)$ is the erythema reference action spectrum (Table 5), and k_{er} is a constant equal to $40 m^2 W^{-1}$ (WHO, 2002). Expressed in this way, the UV index is a dimensionless quantity, where one unit is equal to an erythemal dose rate of $25 mW m^{-2}$. Of the erythemal UV irradiance at the surface, 17% is UV-A and 83% is UV-B (Jégou et al., 2011).

Table 5 : CIE action spectrum for erythema (Jégou et al., 2011).

$\lambda(nm)$	$S_{er}(\lambda)$
≤ 298	1
$298 < \lambda \leq 328$	$10^{0.094(298-\lambda)}$
$328 < \lambda \leq 400$	$10^{0.015(140-\lambda)}$

1.3.2 Factors that influence surface UV radiation

The amount of UV radiation that reaches the surface of the Earth is influenced by several factors (Vanicek et al., 2000; Kerr et al., 2003):

- Solar elevation: this is the angle between the horizon and the direction to the Sun, equal to $90^\circ - \theta_0$. For high solar elevations, the UV radiation is more intense because the rays from the Sun have a shorter path through the atmosphere and therefore pass through a smaller amount of absorbers. As the UV irradiance depends strongly on the solar elevation, it changes with latitude, season and time, being highest in the tropics, in summer and at noon.
- Clouds and haze: the UV irradiance is higher when the sky is cloudless. Clouds generally reduce the UV irradiance at the surface but the attenuation by clouds depends on both the thickness and the type of clouds. Thin or scattered clouds have only a little effect on UV at the ground. Under certain conditions and for short times, a small amount of clouds may even enhance the UV irradiance compared to fully clear skies. In hazy conditions, UV radiation is absorbed and scattered by water droplets and aerosols and this leads to a decrease of the UV irradiance.
- Atmospheric ozone: as explained at the start of this subsection, the solar UV radiation at the surface of the Earth is composed of a large amount of UV-A radiation and only a small amount of UV-B radiation. UV-B is known to be biologically damaging, whereas UV-A is less damaging but still known for its ability to tan the human skin. As ozone is the main absorber of UV-B radiation, the UV-B irradiance at the surface of the Earth depends strongly on the total amount of ozone in the atmosphere, thus on the thickness of the ozone layer.
- Altitude: the UV irradiance increases with altitude because the amount of absorbers in the overlying atmosphere decreases with altitude. Measurements show that the UV irradiance increases by 6-8% per 1000 m increase in altitude.
- Aerosols: depending on the circumstances and the physical and optical properties of aerosols, they are able to absorb or scatter UV radiation and hence decrease or increase the UV irradiance at the surface of the Earth. If there are predominantly particles of size much smaller than the UV wavelengths (i.e., freshly formed particles, Aitken mode particles (see also section 1.4.1)) and of high single scattering albedo (SSA)⁸, the UV radiation can be enhanced by the multiple scattering in the aerosol layer. However, if the amount of all particles exceeds a certain threshold value, absorption takes over, and this will lead to a decrease in UV irradiance. The aerosol composition, which determines whether a mixture is rather scattering or absorbing, the aerosol amount and the aerosol size distribution determine whether aerosols will scatter or absorb UV irradiance.
- Surface reflection (surface albedo): part of the UV radiation that reaches the ground is absorbed by the Earth's surface and part of it is reflected back to space. The reflectivity of the surface of the Earth, usually referred to as surface albedo, is defined as the ratio of the surface-reflected to the incident amount of radiation (Bais et al., 2015). The amount of reflected radiation depends on the properties of the surface. Most materials have a low reflectivity in the UV region (less than 10%) (Diffey, 2002). Snow and ice however, can reflect up to 90% of the UV radiation while sand

⁸ The single scattering albedo is the fraction of light scattering over the extinction and is calculated as follows:

$$SSA = \frac{\alpha_s}{\alpha_e} = \frac{\alpha_a}{\alpha_a + \alpha_s}$$

may reflect about 25%. In regions characterized by a large reflectivity, the UV exposure increases.

1.3.3 Effects of UV-B radiation

An overexposure to UV-B radiation can lead to serious health damage for humans such as skin cancer, accelerated aging of skin, cataract, photokeratitis and changes in the immune system (Rieder et al., 2008; Cordero et al., 2009; Lucas et al., 2015). UV-B radiation also has adverse effects on terrestrial plants (Tevini and Teramura, 1989; Zuk-Golaszewska et al., 2003; Cordero et al., 2009; Bornman et al., 2015) and on other elements of the biosphere (Diffey, 1991; Bornman et al., 2015).

1.3.3.1 Effects on humans

Small amounts of UV-B radiation are beneficial for people and essential in the production of vitamin D. UV radiation is also used to treat several diseases, including rickets, psoriasis and eczema. This takes place under medical supervision and the benefits of treatment versus the risks of UV radiation exposure are a matter of clinical judgment (WHO, 2002; Lucas et al., 2015). Prolonged human exposure to solar UV-B radiation may result in acute and chronic health effects on the skin, eye and immune system.

1.3.3.1.1 Effects on skin

The best known acute effect of excessive UV-B radiation exposure is erythema, the familiar skin reddening termed sunburn (WHO, 2002; Lucas et al., 2015). In addition, most people will tan from the UV-B radiation stimulation of melanin production, which occurs within a few days of exposure. A further, less obvious adaptive effect is the thickening of the outermost layers of the skin that attenuates UV radiation penetration to the deeper layers of the skin. Chronic exposure to UV-B radiation also causes a number of degenerative changes in the cells, fibrous tissue and blood vessels of the skin. UV-B radiation accelerates skin ageing, and the gradual loss of the skin's elasticity results in wrinkles and dry, coarse skin. UV-B exposure can also cause skin cancer (either non-melanoma skin cancers (NMSC) or malignant melanoma). People's behavior in the Sun is considered to be a major cause for the rise in skin cancer rates in recent decades. An increase in popular outdoor activities and changed sunbathing habits often result in excessive exposure to UV radiation.

1.3.3.1.2 Effects on the immune system

The immune system is the body's defense mechanism against infections and cancers, and is normally very effective at recognizing and responding to an invading microorganism or the onset of a tumor (WHO, 2002; Lucas et al., 2015). Although the data remain preliminary, there is increasing evidence for a systematic immunosuppressive effect of both acute and low-dose UV-B radiation exposure. Beyond its role in the initiation of skin cancer, Sun exposure

may reduce the body's defenses that normally limit the progressive development of skin tumors. Several studies have demonstrated that exposure to environmental levels of UV-B radiation alters the activity and distribution of some of the cells responsible for triggering immune responses in humans. Consequently, Sun exposure may enhance the risk of infection with viral, bacterial, parasitic or fungal infections. Furthermore, especially in countries of the developing world, high UV radiation levels may reduce the effectiveness of vaccines.

1.3.3.1.3 Effects on eyes

Acute effects of UV-B radiation exposure include photokeratitis⁹ and photoconjunctivitis¹⁰ (WHO, 2002; Lucas et al., 2015). These inflammatory reactions are comparable to sunburn of the very sensitive skin-like tissues of the eyeball and eyelids, and usually appear within a few hours of exposure. Both can be very painful, but are reversible and do not result in any long-term damage to the eye or vision. Even though cataracts appear to different degrees in most individuals as they age, Sun exposure, in particular exposure to UV-B, appears to be a major risk factor for cataract development. Some 12 to 15 million people are blind from cataracts. According to WHO estimates, up to 20% of these cases of blindness may be caused or enhanced by Sun exposure.

1.3.3.2 Effects on plants

Excessive UV-B exposure can also damage terrestrial plant life (Bornman et al., 2015). It is known to cause a decrease in plant height, leaf area, plant dry weight, relative growth rate and the plant's nitrogen productivity (Zuk-Golaszewska et al., 2003). The negative effects of UV-B radiation can also lead to deformed morphological parameters.

1.3.4 Measurements of UV

There are two ways to determine UV-B exposure at the surface of the Earth. It can be done either directly by measuring it with instruments at the ground (section 1.6.2.1) or more indirectly by using satellite measurements to estimate surface UV levels (section 1.6.3.1).

1.4 Aerosols

1.4.1 Basic information

Aerosols are defined as fine solid or liquid particles suspended in a gas (Seinfeld & Pandis, 1998). Aerosols can be divided into two main categories depending on their source: primary and secondary aerosols. Primary aerosols are emitted directly as particles, whereas secondary aerosols are formed in the atmosphere by gas-to-particle conversion processes (Seinfeld & Pandis, 1998). Primary aerosols include, for example, fly ash from industrial activities, sea-

⁹ Inflammation of the cornea

¹⁰ Inflammation of the conjunctiva (i.e. the membrane that lines the inside of the eyelids and eye socket)

salt particles emitted at the ocean surface, or mineral dust that is emitted by the effects of wind erosion on arid land (Haywood & Boucher, 2000). An example of secondary aerosol is sulphate aerosol that is formed from dimethyl sulfide (DMS) emissions by marine phytoplankton and from sulphur emissions from fossil fuel burning (Haywood & Boucher, 2000).

Another distinction which can be made is the one between natural and anthropogenic aerosols, where the latter are emitted or formed as a result of human activities (Seinfeld & Pandis, 1998). Significant natural sources of particles include soil and rock debris (terrestrial dust), volcanic action, sea spray, biomass burning and reactions between natural gaseous emissions. Anthropogenic aerosols arise primarily from four categories: fuel combustion, industrial processes, nonindustrial fugitive sources and transportation sources (see Table 6).

The size of aerosols varies from a few nanometers ($1 \text{ nm} = 10^{-9} \text{ m}$) to tens of micrometers ($1 \text{ }\mu\text{m} = 10^{-6} \text{ m}$) in diameter (Seinfeld & Pandis, 1998). Based on their size, particles are categorized as fine aerosols (particles $<1 \text{ }\mu\text{m}$) or coarse aerosols (particles $>1 \text{ }\mu\text{m}$). Within the fine aerosols mode, there is an additional subdivision into nucleation mode particles ($<10 \text{ nm}$), Aitken mode particles ($10 \text{ nm} - 0.1 \text{ }\mu\text{m}$) and accumulation mode particles ($0.1 - 1 \text{ }\mu\text{m}$) (Figure 9).

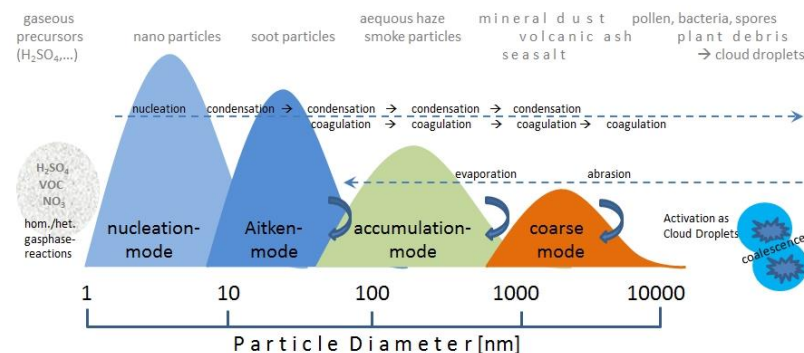


Figure 9: Schematic multi-modal particle size distribution with typical transformations and example particle types within each mode¹¹.

The aerosols from the nucleation mode are formed from condensation of hot vapors during combustion processes and from the nucleation of atmospheric species to form fresh particles. They are lost by coagulation with larger particles (Seinfeld & Pandis, 1998). Aitken mode particles form from the nucleation mode through coagulation or from incomplete combustion¹². The source of accumulation mode particles is the coagulation of particles in the Aitken mode and they are also formed from condensation of vapors onto existing particles. The coarse mode is formed by mechanical processes and usually consists of man-made and natural dust particles (Seinfeld & Pandis, 1998).

Aerosols are removed from the atmosphere through two processes: dry and wet deposition (Seinfeld & Pandis, 1998). Dry deposition is the transport of gaseous and particulate species

¹¹

http://www.dwd.de/EN/research/observing_atmosphere/composition_atmosphere/aerosol/cont_nav/particle_size_distribution_node.html ; visited on 28/9/2016

¹²

http://www.dwd.de/EN/research/observing_atmosphere/composition_atmosphere/aerosol/cont_nav/particle_size_distribution_node.html; visited on 28/9/2016

from the atmosphere onto surfaces in the absence of precipitation. The factors that determine dry deposition are the level of atmospheric turbulence, the chemical properties of the depositing species and the nature of the surface itself. Wet deposition is defined as the natural processes by which material is scavenged by hydrometeors (cloud and fog drops, rain, snow) and is consequently delivered to the Earth's surface. Two processes are especially important for aerosols: in-cloud and below-cloud scavenging. In-cloud scavenging describes the process where aerosols are incorporated into cloud and rain drops inside the raining cloud and is the result of nucleation scavenging (i.e. the growth of Cloud Condensation Nuclei (CCN) to cloud drops) and the collection of a fraction of the remaining aerosols by cloud or rain droplets. When a raindrop falls through the air, it can collide with aerosol particles and collect them. This is known as below-cloud scavenging. Whether a collision will occur or not depends on the size of the droplet and the particle and their relative locations.

Table 6: Aerosols sources and their size categories (Seinfeld & Pandis, 1998). The table makes the distinction between natural and anthropogenic aerosols and between primary and secondary aerosols.

Source	Particle Size Category
NATURAL	
Primary	
Soil dust	Mainly coarse
Sea salt	Coarse
Volcanic dust	Coarse
Biological debris	Coarse
Secondary	
Sulfates from biogenic gases	Fine
Sulfates from volcanic SO ₂	Fine
Organic matter from biogenic VOC	Fine
Nitrates from NO _x	Fine and coarse
ANTHROPOGENIC	
Primary	
Industrial dust etc. (except soot)	Fine and coarse
Soot	Mainly fine
Secondary	
Sulfates from SO ₂	Fine
Biomass burning	Fine
Nitrates from NO _x	Mainly coarse
Organics from anthropogenic VOC ¹³	Fine

The main constituents of the atmospheric aerosol are inorganic species (such as sulphate, nitrate, ammonium, sea salt), organic species (also termed organic aerosol or OA), black carbon (BC, a distinct type of carbonaceous material formed from the incomplete combustion of fossil and biomass based fuels under certain conditions), mineral species (mostly desert dust) and primary biological aerosol particles (PBAPs). Mineral dust, sea salt, BC and PBAPs are introduced into the atmosphere as primary particles, whereas non-sea-salt sulphate, nitrate

¹³ Volatile Organic Compounds

and ammonium are predominantly from secondary aerosol formation processes. The OA has both significant primary and secondary sources. In the present-day atmosphere, the majority of BC, sulphate, nitrate and ammonium comes from anthropogenic sources, whereas sea salt, most mineral dust and PBAPs are predominantly of natural origin. Primary and secondary organic aerosols (POA and SOA) are influenced by both natural and anthropogenic sources (Boucher et al., 2013).

1.4.2 Effects of aerosols

Anthropogenic emissions leading to atmospheric aerosol have increased dramatically over the past century and have been implicated in

- Perturbing the Earth's radiation balance
- Human health effects
- Visibility reduction in urban and regional areas
- Acid deposition

The first two are of major concern in the context of global environmental change and are detailed in section 1.4.2.1 and 1.4.2.2 below. Acid deposition also remains an important environmental issue and is addressed in section 1.4.2.3.

1.4.2.1 Effects of aerosols on the radiative budget of the Earth

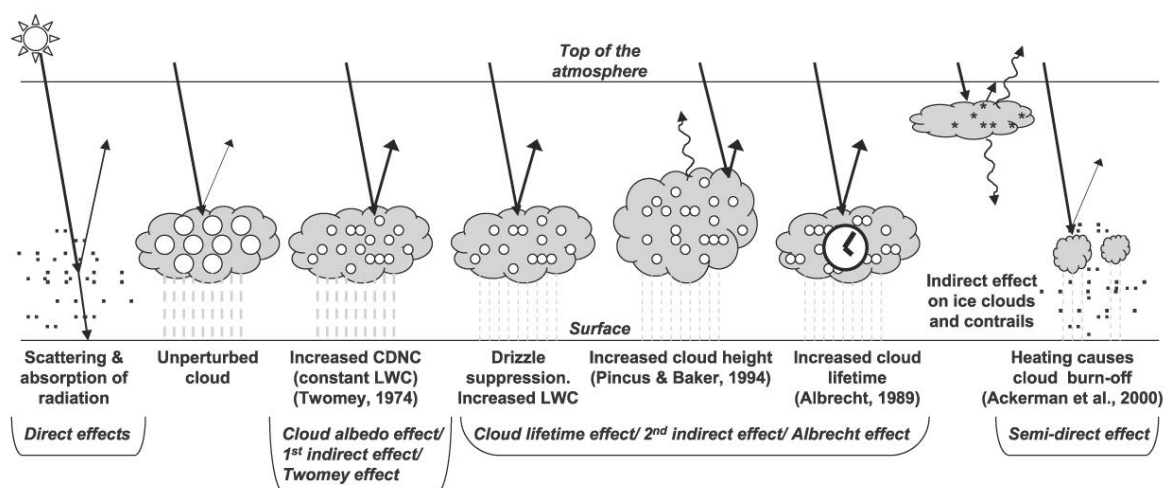


Figure 10: Schematic of the aerosol direct, indirect and semi-direct effects. CDNC stands for cloud droplet number concentrations and LWC stands for liquid water content (source: Forster et al., 2007).

Aerosols influence the Earth's radiation budget in a direct, semi-direct and indirect manner. This is schematized and explained in Figure 10 and further detailed in

Table 7.

Table 7: Overview and description of the indirect and semi-direct aerosol effects (IPCC, 2013). The table describes which types of clouds are affected and gives the sign of the change in TOA radiation and the potential magnitude of the effect.

Effect	Cloud types affected	Process	Sign of change in TOA radiation	Potential magnitude
Cloud albedo effect (1 st indirect effect)	All clouds	For the same cloud water or ice content, more but smaller cloud particles reflect more solar radiation	Negative	Medium
Cloud lifetime effect (2 nd indirect effect)	All clouds	Smaller cloud particles decrease the precipitation efficiency thereby presumably prolonging cloud lifetime	Negative	Medium
Semi-direct effect	All clouds	Absorption of solar radiation by absorbing aerosols affect static stability and the surface energy budget and may lead to an evaporation of cloud particles	Positive or negative	Small
Glaciation indirect effect	Mixed-phase clouds	An increase in ice nuclei increases the precipitation efficiency	Positive	Medium
Thermodynamic effect	Mixed-phase clouds	Smaller cloud droplets delay freezing causing super-cooled clouds to extend to colder temperatures	Positive or negative	Medium

The scattering and absorption of short and long wave radiation is called the direct effect (Ramanathan et al., 2001; Kaufman et al., 2002; Andreae et al., 2005; Myrhe, 2009). Aerosol scattering generally makes the planet more reflective and tends to cool the climate, while aerosol absorption has the opposite effect and tends to warm the climate system (Boucher et al., 2013). This direct effect results from well-understood physics and is close to being an observable quantity, yet our knowledge of aerosol and environmental characteristics needed to quantify it at the global scale remains incomplete (Boucher et al., 2013).

The semi-direct effect describes the warming of the boundary layer, through the absorption of radiation by aerosols, which can lead to evaporation of clouds. This will allow more solar radiation to reach the surface (Ramanathan et al., 2001; Cazorla et al., 2009).

The indirect effect describes the ability of aerosols to influence the microphysical and optical properties of clouds, thus changing the radiative and precipitation properties and the lifetime of clouds (Ramanathan et al., 2001; Kaufman et al., 2002; Lohmann, 2002a; Lohmann and Feichter, 2005; Unger et al., 2009). The aerosol indirect effect is usually split into two effects (Haywood & Boucher, 2000). The first indirect effect (or the cloud albedo effect) describes how an increase in aerosols concentrations causes an increase in droplet concentration, a decrease in droplet size and an increase in total droplet surface area for fixed liquid water content. This will lead to an increase in the reflectance of incoming solar radiation, hence of

the cloud albedo (Boucher et al., 2013). The second indirect effect (or the cloud lifetime effect) explains how the reduction in cloud droplet size affects the precipitation efficiency, tending to increase the liquid water content, the cloud lifetime and the cloud thickness. Other less known indirect effects are the glaciation and thermodynamic effects.

The glaciation effect refers to an increase in Ice Nuclei (IN) resulting in a rapid glaciation of a super-cooled liquid water cloud due to the difference in vapor pressure over ice and water. Unlike cloud droplets, these ice crystals grow in an environment of high super-saturation with respect to ice, quickly reaching precipitation size, with the potential to turn a non-precipitating cloud into a precipitating cloud (IPCC, 2007). Increases in IN, which lead to the formation of more ice particles, can thus result in more frequent glaciation of super-cooled stratiform clouds and increase the amount of precipitation via the ice phase. This in turn could decrease the cloud fraction allowing more shortwave radiation to be absorbed in the Earth-atmosphere system (Lohmann, 2002a/b).

The thermodynamic effect refers to a delay in freezing by the smaller droplets causing super-cooled clouds to exist at colder temperatures (IPCC, 2007, Lohmann 2002a). The semi-direct effect describes the warming of the boundary layer, through the absorption of radiation by aerosols, which can lead to evaporation of clouds. This will allow more solar radiation to reach the surface (Ramanathan et al., 2001; Cazorla et al., 2009).

Within the 5th IPCC assessment report (Boucher et al., 2013), a new terminology has been used to describe the interactions between aerosols and radiation and between aerosols and clouds (Figure 11).

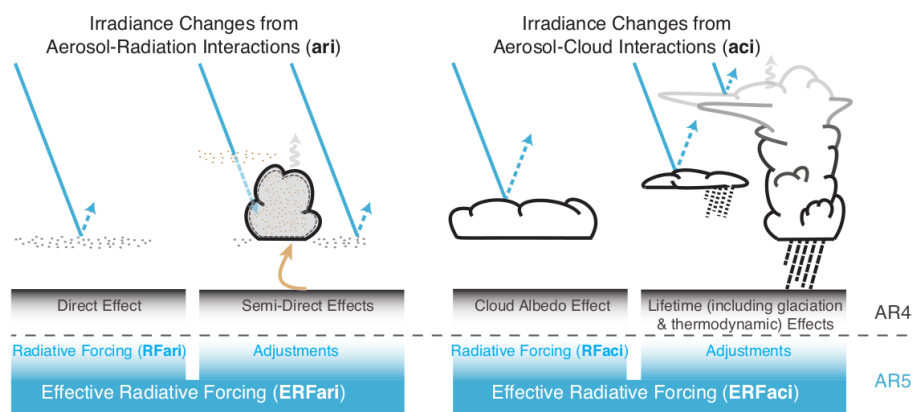


Figure 11 : Schematic overview of the new terminology used in the new assessment report (AR5) for aerosol-radiation and aerosol-cloud interactions and how they relate to the terminology used in the previous assessment report (AR4).

RFari is a radiative forcing that encompasses radiative effects from anthropogenic aerosols before any adjustment takes place and corresponds to what is usually referred to as the aerosol direct effect. Rapid adjustments induced by aerosol radiative effects on the surface energy budget, the atmospheric profile and cloudiness contribute to the Effective Radiative Forcing (ERF) from aerosol–radiation interactions (abbreviated ERFari). This radiative forcing term includes what has earlier been referred to as the semi-direct effect. The radiative forcing from aerosol–cloud interactions (abbreviated RFaci) refers to the instantaneous effect on cloud albedo due to changing concentrations of cloud condensation and ice nuclei, also known as

the Twomey effect. All subsequent changes to the cloud lifetime and thermodynamics are rapid adjustments, which contribute to the effective radiative forcing from aerosol–cloud interactions (abbreviated ERFaci).

1.4.2.2 Effects of aerosols on human health

Aerosol particles can contribute to a variety of human health problems. Particulate matter (PM) affects the health of more people than any other pollutant worldwide. According to estimates from the WHO, particle pollution contributes to approximately 7 million premature deaths each year, making it one of the leading causes of worldwide mortality¹⁴. The health effects of the particles are directly related to their size (Wilson & Spengler, 1996). Particles greater than 100 μm are generally too large to be inhaled. Particles between 10-100 μm can be inhaled, but are usually stopped by our body's filters (i.e. the mucus membranes in our respiratory system). The term “inhalable particles”, typically refers to particles less than 10 μm in size that can make it past the body's defenses and deep into the lungs. Inhalable coarse particles are particles between 2.5 and 10 μm in diameter (PM_{10}) and are typically found near highways and factories. Fine particles have a diameter less than 2.5 μm ($\text{PM}_{2.5}$) and are typically found in smoke and smog. These particles make it deeper into the lungs.

Apart from the health effects on the respiratory system (such as aggravated asthma, decreased lung function, irritation of airways, coughing, and difficulty breathing), particulate matter can also have adverse effects on the cardiovascular system (Nawrot et al., 2006). These effects can happen through three main mechanisms: (1) direct translocation of the particles to the circulation, (2) effects on the autonomic nervous system (which can lead to a decrease in heart rate variability and can affect the blood pressure) and (3) indirect effects due to particle-induced inflammation and oxidative stress which can lead to systematic inflammation (Jacobs et al., 2011).

1.4.2.3 Acid deposition

Acid deposition, or acid rain, includes any form of precipitation with acidic components that falls to the ground from the atmosphere in wet or dry forms (Seinfeld & Pandis, 1998).

Sulphuric (H_2SO_4) and nitric (HNO_3) acids are primarily responsible for the phenomenon of acid rain (Reid & Sayer, 2002). These acids can be produced by oxidation of the oxides of sulphur and nitrogen. In an unpolluted atmosphere the natural sources of sulphur dioxide (SO_2) and nitrogen dioxide (NO_2) provide a mechanism by which the pH of aerosol and rain are expected to be slightly acidic. However, large amounts of nitrogen monoxide (NO) and NO_2 (together denoted as NO_x) and SO_2 are produced during fossil fuel combustion, which makes the precipitation still more acidic and results in so-called acid rain. Acid deposition leads to acidification of surface waters and subsequent damage to aquatic systems and causes damage to forests, vegetation, materials and structures (Seinfeld & Pandis, 1998).

¹⁴ <http://www.who.int/mediacentre/news/releases/2014/air-pollution/en/>; visited on 28/11/2016

1.4.3 Definition of Aerosol Optical Depth

The extinction of radiation on traversing an infinitesimal path length dx is linearly proportional to the amount of matter along the path as was earlier described by Eq. 9. For a finite path between x_1 and x_2 , the total optical thickness was described by Eq. 11. When x is measured vertically in the atmosphere, the total optical thickness is called total optical depth. The total optical depth represents the total attenuation of the intensity of a beam on its (vertical) path through the atmosphere to which several mechanisms can contribute:

- Rayleigh scattering by air molecules with an optical depth represented by τ_r
- Gaseous absorption: (by gases such as O_3 , SO_2 and NO_2) with an optical depth represented by τ_g (with $\tau_g = \tau_{O_3} + \tau_{NO_2} + \tau_{SO_2}$)
- Aerosol extinction: with a contribution τ_{aer} most frequently referred to as Aerosol Optical Depth or AOD.

Thus, the total optical depth can be written as:

$$\tau_{tot} = \tau_r + \tau_{aer} + \tau_g \quad (22)$$

The Aerosol Optical Depth is an integral measurement of the combined aerosol scattering and absorption in the atmospheric column. It is a dimensionless number that is related to the amount of aerosol in the vertical column of the atmosphere over the observation location.

1.4.4 Measurement of Aerosol Optical Depth

The AOD is routinely measured by instruments coordinated in ground-based networks (section 1.6.2.2) and a number of satellite-based sensors (section 1.6.3.2).

1.5 Ozone

1.5.1 What is ozone?

Ozone is a gas that is naturally present in our atmosphere. An ozone molecule (O_3) consists of three oxygen molecules. It was discovered in laboratory experiments in the mid-1800s by Christian F. Schönbein (Cooper et al., 2014) and its presence in the atmosphere was later discovered using chemical and optical measurement methods. The word ozone is derived from the Greek word “ὄζειν” (ozein), meaning “to smell.” Ozone has indeed a pungent odor that allows it to be detected even at very low amounts. Ozone reacts rapidly with many chemical compounds and is explosive in concentrated amounts.

Most ozone (about 90%) is found in the stratosphere (Hegglin et al., 2015, Figure 12). The stratospheric region with the highest ozone concentration is commonly known as the ozone layer, which extends over the entire globe with some variation in altitude and thickness. Most

of the remaining ozone (about 10%) is found in the troposphere. The total column integrated ozone, i.e. the total amount of ozone integrated from the surface of the Earth to the top of the atmosphere, is often expressed in terms of Dobson Units (DU) (Seinfeld & Pandis, 1998). One DU is the thickness, measured in units of hundreds of a millimeter, that the ozone column would occupy at standard temperature and pressure (273 K and 1 atmosphere):

$$1 \text{ DU} = 10^{-3} \text{ atm}\cdot\text{cm} \approx 2.69 \cdot 10^{16} \text{ molecules}\cdot\text{cm}^{-2}.$$

The low amount present in the atmosphere can be appreciated by the fact that if all the atmosphere's ozone were brought down to the surface of the Earth at standard temperature and pressure, it would produce a layer only about 3 mm thick (Seinfeld & Pandis, 1998). Although ozone molecules have a low relative abundance in the atmosphere, they play a vital role in protecting life on Earth.

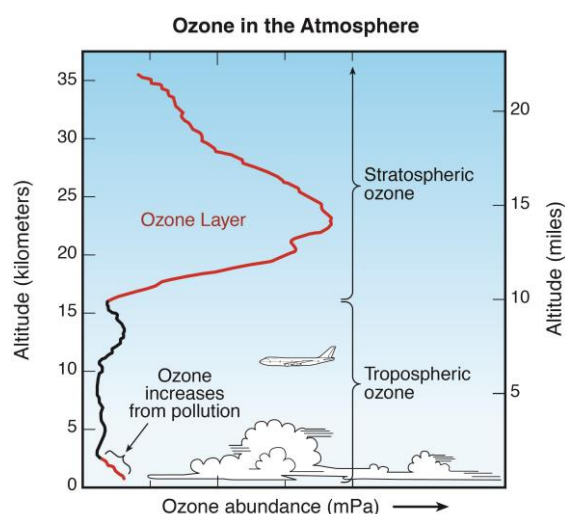


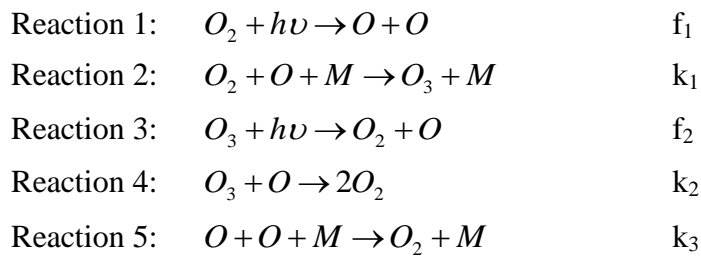
Figure 12: Abundance of ozone in the atmosphere, expressed as change in mPa over altitude in km and miles (from Hegglin et al., 2015).

1.5.2 Sources of ozone

Ozone is a secondary species of the atmosphere. It is formed in multistep chemical processes that require sunlight (Chapman, 1930; Solomon, 1999). In the stratosphere (section 1.5.2.1), the process begins with an oxygen molecule (O_2) being broken apart by UV radiation from the Sun. In the troposphere (section 1.5.2.2), ozone is formed by a different set of chemical reactions that involve naturally occurring gases and those from pollution sources.

1.5.2.1 Stratospheric ozone

The foundation of our current knowledge on stratospheric ozone formation was laid by Sydney Chapman, who proposed in 1930 that ozone is continually produced in the atmosphere by a cycle initiated by photolysis of O_2 in the upper stratosphere (Seinfeld & Pandis, 1998). The photochemical mechanism for ozone production in the stratosphere is called the Chapman cycle. The theory of Chapman describes a pure oxygen atmosphere (without hydrogen or nitrogen). Chapman considered the following five reactions as important to the ozone content of the atmosphere: (Chapman, 1930; Dütsch, 1968).

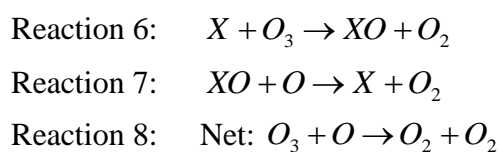


where M denotes a molecule (mostly oxygen or nitrogen), k_i and f_i denote the thermal reaction and photo-dissociation rates and h represents Planck's constant. The frequency ν of the required radiation in reaction 1 corresponds to wavelengths in the Schumann-Runge band of O_2 (130-205 nm) or in the Hertzberg continuum (200-250 nm). Reaction 3 requires radiation in the Hartley-Huggins band of ozone (230-400 nm).

In the first reaction, UV radiation (with a wavelength lower than 242 nm) breaks apart one oxygen molecule to produce two oxygen atoms. Each of these highly reactive oxygen atoms combines with an oxygen molecule in the presence of a third molecule M to form an ozone molecule (O_3) in the second reaction. The ozone produced in reaction 2 strongly absorbs radiation in the 240-320 nm range to decompose back to O_2 and O (reaction 3). Ozone can also react with atomic oxygen to regenerate two molecules of O_2 (reaction 4). The recombination reaction 5 is of importance in the mesosphere but can be neglected in the stratosphere. Reactions 2 and 3 proceed much faster than reactions 1 and 4 and represent fast conversion between O and O_3 . These reactions occur continuously whenever solar UV radiation is present in the stratosphere. As a result, the largest ozone production occurs in the tropical stratosphere (Brasseur & Solomon, 1986; Hegglin et al., 2015).

Until 1964, the Chapman mechanism was thought to represent the principal set of reactions governing the formation and destruction of ozone in the stratosphere (Seinfeld & Pandis, 1998). After that, improved measurements of the rate constant of reaction 4 (k_2), indicated that the reaction is considerably slower than previously thought, leading to larger abundances of ozone. Also, measurements indicated that the actual amount of ozone in the stratosphere is about a factor of 2 less than what is predicted by the Chapman mechanism. It was concluded that significant additional ozone destruction pathways are present beyond reaction 4.

In 1950, Bates & Nicolet introduced the idea of a catalytic loss process involving hydrogen radicals to explain the additional sink. In the beginning of the 1970s, Crutzen and Johnston revealed the role of nitrogen oxides in stratospheric ozone chemistry. After that, Stolarski & Cicerone (1974), Molina & Rowland (1974) and Rowland & Molina (1975) elucidated the effect of chlorine containing compounds on stratospheric ozone chemistry. It is now known that ozone destruction processes (under the form of catalytic cycles) must be added to the Chapman cycle. In a general way, this can be represented by reactions 6-8:



where X is a free radical catalyst which can be H, OH, NO, Cl or Br.

Note that part of the ozone formed in the stratosphere will be transported down across the tropopause by so-called tropopause folding events in which tongues of stratospheric air intrude into the troposphere (Seinfeld & Pandis, 1998). This constitutes an additional (dynamical) sink for stratospheric ozone and by way of consequence a source of tropospheric ozone.

1.5.2.2 Tropospheric ozone

Tropospheric ozone is a short-lived trace gas that is either transported down from the stratosphere or produced near the surface of the Earth by photochemical reactions involving ozone precursor gases (e.g. NO_x, non-methane volatile organic compounds, CH₄, CO) from natural and pollution sources and sunlight (Cooper et al., 2014). Natural sources include wildfires, biogenic hydrocarbon emissions, lightning NO_x and biogenic NO_x emitted from soils while anthropogenic sources are fossil and biofuel combustion and crop burning. It is important to note that the production of ozone near the surface does not significantly contribute to the abundance of stratospheric ozone. The amount of surface ozone is indeed too small in comparison and the transport of surface air to the stratosphere is not effective enough (it takes on average a decade for a tropospheric air mass to mix with the stratosphere). Ozone in the troposphere is, as in the stratosphere, destroyed chemically. Another significant input for tropospheric ozone is dry deposition at the surface. Observations indicate that tropospheric ozone increased globally during the 20th century (Cooper et al., 2014). The longest quantitative ozone records are in Europe and indicate that tropospheric ozone doubled there between the 1950s and 2000. From 1950–1979 until 2000–2010 all available monitoring sites in the Northern Hemisphere indicate increasing tropospheric ozone, with 11 of 13 sites having statistically significant trends corresponding to >100% tropospheric ozone increases since the 1950s, and 9–55% tropospheric ozone increases since the 1970s. This increase of tropospheric ozone is a major source of concern because of its adverse effects on humans, plants and other living systems (section 1.5.3.2).

1.5.2.3 Ozone depletion

1.5.2.3.1 History of ozone depletion

The total ozone column has been observed since the beginning of the twentieth century and systematic measurements have revealed that the total ozone abundances have decreased noticeably over many regions of the world since about 1980 (Solomon, 1999). Ozone depletion was first documented in the Antarctic spring at the British Antarctic Survey station at Halley by Farman et al. (1985). They showed that the ozone depletion is confined to particular seasons and to south polar latitudes. Space-based measurements and observations at other Antarctic sites quickly confirmed the original findings (Solomon, 1999). As the satellite measurements showed that the depletion extended roughly over the entire continent, the phenomenon became known as the Antarctic ozone hole. The discovery of this Antarctic ozone hole raised the question whether other latitudes also experienced this ozone depletion

and within a few years, statistically significant trends in ozone were found at northern midlatitudes (Ozone Trends Panel, 1988 and references therein). By the 1990s, significant trends had been established for both northern and southern mid-latitudes, not only in winter and spring but also in summer (WMO/UNEP, 1991, 1994; Stolarski et al., 1991; McPeters et al., 1996a,b; Harris et al., 1997; Staehelin et al., 1998a,b). The depletion of the global ozone layer is considered as one of the major global scientific and environmental issues of the twentieth century.

In 1974, Molina and Rowland were the first to propose that ozone could be depleted by the release of Chlorofluorocarbons¹⁵ (CFCs) to the atmosphere (Newman et al., 2009). The chemical breakdown of these CFCs and other Ozone Depleting Substances¹⁶ (ODSs) in the stratosphere releases Cl and Br atoms that destroy ozone in catalytic cycles. Early predictions by Hudson & Reed (1979) stated that an ozone loss of 15 to 18% is expected if CFCs added 5.5 to 7.0 ppbv¹⁷ of Cl to the stratosphere. Monitoring stations showed that the abundances of ODSs were steadily increasing in the atmosphere and observations confirmed that the resulting ozone depletion was taking place globally (Hegglin et al., 2015). Over the years, continuous scientific research led to a series of reports that culminated in the first WMO/UNEP scientific assessment of ozone depletion in 1985 (WMO, 1985). The assessment report concluded that CFCs and halons pose a serious threat to the ozone layer (Newman et al., 2009). As a response, the Montreal Protocol, an agreement to regulate the production of CFCs and other ODSs, was crafted in 1987 leading to a decrease in the production of ODSs around the world. The cumulative levels of both Br and Cl from the ODSs are now decreasing in the troposphere and stratosphere. Global ozone depletion now is no longer increasing and the ozone layer is expected to recover in response, albeit very slowly, mainly due to the long atmospheric residence time of the halocarbons responsible for the ozone depletion (Solomon et al., 2016). According to Solomon et al. (2016), this ozone recovery involves multiple stages, starting with a reduced rate of decline, followed by a leveling off of the depletion, and finally an identifiable ozone increase that can be linked to halocarbon reductions. The third stage is referred to as healing. All three stages of recovery have been documented in the upper stratosphere at mid- and low-latitudes, but are associated with uncertainties (Solomon et al., 2016 and references therein). Some studies provide evidence for all three recovery stages in ozone columns at mid-latitudes, despite dynamical variability.

1.5.2.3.2 Cause of ozone depletion

The general ozone destruction cycles are already given in section 1.5.2.1 (reactions 6-8). Here we present in more detail the reactions which have lead to the process of ozone depletion and the ozone hole. In a first step, gases containing Cl and Br are emitted at the surface of the Earth (Brasseur & Solomon, 1986; Hegglin et al., 2015). The most important Cl-containing halogen source gases emitted by human activities are CFCs, carbon tetrachloride (CCl₄) and

¹⁵ Anthropogenic compounds, containing only carbon, chlorine and fluorine, used for refrigeration, air conditioning, foam blowing and industrial cleaning and released into the atmosphere. They have a low toxicity, reactivity and flammability.

¹⁶ Ozone Depleting Substances refer to halogen source gases emitted by human activities and controlled by the Montreal Protocol. Halogen source gases that have only natural sources are not classified as ODSs.

¹⁷ parts per billion by volume

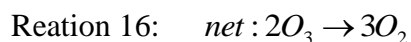
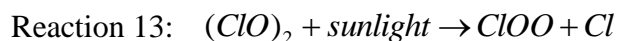
methyl chloroform (CH_3CCl_3). The most important sources for Br are halons (i.e. halocarbon gases originally developed to extinguish fires) and methyl bromide (CH_3Br). These source gases accumulate in the troposphere because they are unreactive and do not dissociate readily in rain or snow. Over time the source gases are transported to the stratosphere by natural air motions. Once they are in the stratosphere, these unreactive halogen source gases are chemically converted, under the influence of UV radiation from the Sun, to reactive halogen gases, some of which then participate in reactions that destroy ozone. The most reactive products, (i.e. chlorine monoxide (ClO), bromine monoxide (BrO), Cl and Br atoms) participate in reaction cycles that destroy ozone. Cycle 1 is made up of two basic reactions (reactions 9 and 10). The net result of cycle 1 (reaction 11) is to convert one ozone molecule and one oxygen atom into two oxygen molecules. In each cycle, chlorine acts as a catalyst because ClO and Cl react and are re-formed. In this way, one Cl atom participates in many cycles, destroying many ozone molecules.

Cycle 1:

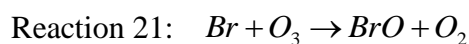
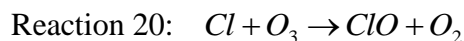
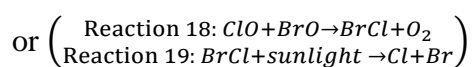
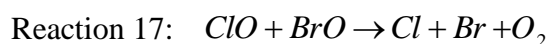


In polar regions, the abundance of ClO is greatly increased during winter as a result of surface reactions that occur at low temperatures on polar stratospheric clouds (PSCs). Cycles 2 and 3 are the dominant reaction mechanisms for polar ozone loss because of this high abundances of ClO and the relatively low abundance of atomic oxygen (which limits the rate of ozone loss by Cycle 1). Cycle 2 begins with the self-reaction of ClO (reaction 12). Cycle 3, which begins with the reaction of ClO with BrO (reaction 17), has two reaction pathways to produce either Cl and Br or BrCl . The net result of both cycles is to destroy two ozone molecules and create three oxygen molecules (reactions 16 and 22). Cycles 2 and 3 account for most of the ozone loss observed in the Arctic and Antarctic stratospheres in the late winter/early spring season.

Polar cycle 2:



Polar cycle 3:



Reaction 22: *net* : $2O_3 \rightarrow 3O_2$

Cycles 1 to 3 all require sunlight. For cycle 1, this is UV radiation, which is strong enough to break apart molecular oxygen into atomic oxygen. Cycle 1 is most important in the stratosphere at tropical and middle latitudes, where solar UV radiation is most intense. Cycles 2 and 3 require visible sunlight to complete the reaction cycles and to maintain ClO abundances. In the continuous darkness of winter in the polar stratosphere, cycles 2 and 3 cannot occur. It is only in late winter/early spring when sunlight returns to the polar regions that these cycles are active. Therefore, the greatest destruction of ozone occurs in the partially to fully sunlit periods after mid-winter in the polar stratosphere. The visible sunlight needed in cycles 2 and 3 is not sufficient to form ozone because this process requires solar UV radiation. In the late winter/early spring stratosphere, solar UV radiation is weak at low Sun angles. As a result, ozone destruction by cycles 2 and 3 in the sunlit winter stratosphere greatly exceeds ozone production. When air returns to the lower atmosphere, the reactive Cl and Br gases are removed from the atmosphere by rain and snow.

1.5.3 Effects of ozone: ‘good’ versus ‘bad’ ozone

Depending on its location in the atmosphere, ozone is involved in different chemical cycles and therefore has a different impact on life on Earth and the environment (Van Malderen et al., 2016).

1.5.3.1 Good ozone

Stratospheric ozone is considered good for humans and other life forms because it absorbs UV-B radiation from the Sun (Brasseur & Solomon, 1986; Hegglin et al., 2015). If not absorbed, UV-B radiation would reach the surface of the Earth in amounts that are harmful to a variety of life forms (see section 1.3.3). In addition, the absorption of UV-B radiation by ozone is a natural source of heat in the stratosphere, causing temperatures to increase with altitude. Stratospheric temperatures affect the balance of ozone production and destruction processes and air motions that redistribute ozone throughout the stratosphere (Brasseur & Solomon, 1986; Hegglin et al., 2015).

1.5.3.2 Bad ozone

Ozone near the surface in excess of natural amounts is considered bad ozone (Cooper et al., 2014; Hegglin et al., 2015). Increased surface ozone above natural levels is harmful to humans, plants and other living systems because ozone reacts strongly to destroy or alter many biological molecules. High ozone exposure caused by air pollution can lead to the following effects:

- Reduction of crop yield and forest growth
- Reduction of lung capacity for humans (chest pains, throat irritation, coughing, worsening of pre-existing health conditions related to heart and lungs)

- Warming of the surface of the Earth: Ozone acts as a greenhouse gas by absorbing IR and UV radiation. The globally averaged radiative forcing is estimated to be $0.40 \pm 0.20 \text{ W m}^{-2}$ (Myrhe et al., 2013)

1.5.4 Measurements of ozone

Ozone can be monitored in different ways. It can be measured in situ (section 1.6.1.1), by ground-based instruments (section 1.6.2.3) or by satellites (section 1.6.3.3).

1.6 Measurements

1.6.1 In situ measurements

In situ measurements determine trace gas concentrations at a particular location (Burrows et al., 2011). A typical way to analyze the trace gas composition of the atmosphere is to take a sample of air either in a suitable container for later analysis or inside an instrument. The biggest advantage of in situ measurements is their conceptual simplicity. They however require a certain effort and cost, especially when spatial distributions of relatively short lived species (e.g. air pollutants) are to be measured over large areas and over long periods. It is often difficult to perform in situ measurements at remote locations or over the oceans. For UV and AOD, in situ measurements are not possible. Ozone concentrations however can be measured in situ.

1.6.1.1 Ground-based in situ ozone measurements

The most common instrument for determining the ambient surface concentration of O_3 is the ultraviolet absorption ozone monitor (UV O_3 monitor) (Dunlea et al., 2006). Advantages of the UV absorption technique include its relatively low cost and overall reliability. UV O_3 monitors employ mercury (Hg) lamps as reliable sources of line UV radiation at 253.65 nm, corresponding closely to the peak in the O_3 cross section. A typical UV O_3 monitor utilizes an ozone-specific scrubber, often manganese dioxide (MnO_2) on a substrate or heated silver wool, to create an ozone-free air flow for reference. The UV radiation intensity passing through this reference flow is compared to that through a flow of ambient air and the number density of O_3 is determined by the Beer-Lambert absorption equation, which depends on the absorption cross section of the O_3 molecule at 253.65 nm. Scattering or absorption of UV radiation by ambient aerosols is typically prevented by a 5.0 μm Teflon particle filter placed in the inlet to the UV O_3 monitor.

1.6.1.2 Balloon-based in situ ozone measurements

Ozone sondes provide the vertical distribution of ozone at very high vertical resolution (typically a few 100 m), up to altitudes in the range of 30–35 km. They have been launched worldwide for already more than half a century and therefore constitute the most important

data source to derive long-term ozone trends with sufficient vertical resolution up to about 20 km (Van Malderen et al., 2016). They are the reference and are used for validation of other ozone profile measurements. Since the 1960s, three main types of electrochemical ozone sondes are in use: the Brewer–Mast (BM, Brewer and Milford, 1960), the electrochemical concentration cell (ECC; Komhyr, 1969), and the Japanese carbon iodine cell (KC; Kobayashi and Toyama, 1966). At present, most sites use ECC sondes. For the BM and the ECC sondes, the principle of operation is based on the chemical titration of O₃ in a potassium iodide (KI) sensing solution. For each molecule of O₃ entering the solution in the cell with the help of a very stable miniature piston pump, two iodide ions (I⁻) are oxidized to form iodine (I₂), which is subsequently reduced back to I⁻ at the electrodes, generating an electric current of two electrons. This current can directly be related to the number of moles of ozone, sampled per second and cubic centimeters (Van Malderen et al., 2016). Ozone profile measurements are archived by the World Ozone and Ultraviolet Radiation Data Center (WOUDC), the Network for the Detection of Atmospheric Composition Change (NDACC) and the Southern Hemisphere Additional Ozone sondes network (SHADOZ) (Hassler et al., 2014).

1.6.1.3 Airborne in situ ozone measurements

Within the Measurement of Ozone and water vapor on Airbus In-service Aircraft (MOZAIC; Marenco et al., 1998) and Civil Aircraft for the Regular Investigation of the atmosphere Based on an Instrument Container (CARIBIC¹⁸) programs, trace constituents, such as ozone, are routinely measured in situ onboard aircrafts (WMO, 2001).

MOZAIC data provide, in particular, detailed O₃ and H₂O climatologies at 9–12 km where subsonic aircrafts fly and which is a very critical altitude range (e.g., radiatively and for the stratosphere/troposphere exchanges) still imperfectly described in existing models (Marenco et al., 1998). The ozone analyzer is a dual beam UV absorption instrument.

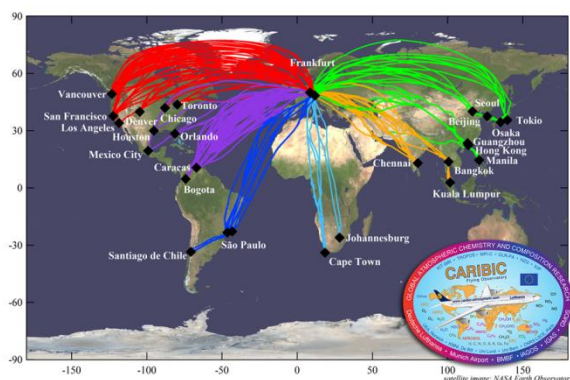


Figure 13 : CARIBIC flight routes between 2004 and 2016¹⁹.

CARIBIC is somewhere between a research aircraft and MOZAIC. Several automated analyzers and an air sampler are deployed in an air freight container. The container has equipment for measuring O₃, but also CO and dust particles. The container has a system for

¹⁸ <http://www.caribic-atmospheric.com/>; visited on 30/11/2016

¹⁹ <http://www.caribic-atmospheric.com/>; visited on 30/11/2016

collecting air samples, which are analyzed in the laboratory. For each sample more than 40 gases are measured, including CFC's and all greenhouse gases. Figure 13 shows the CARIBIC flight routes between 2004 and 2016.

1.6.2 Remote sensing

Remote sensing measurements allow the detection of properties of an object from a distance (remote from the probing instrument) (Burrows et al., 2011). In this way, larger spatial resolutions are possible and, in principle, measurements are possible at any point on Earth (also remote continental and marine areas). Remote sensing uses the interaction of electromagnetic radiation with trace constituents, i.e. the absorption, emission and scattering of radiation by molecules or particles results in changes in the spectral or temporal characteristics of the radiation. These changes can then be interpreted to reveal information about the object. Remote sensing is possible from the ground (section 1.6.2.1) or from space (section 1.6.2.2).

Passive remote sensing (Figure 14) exploits the measurement and analysis of the electromagnetic radiation coming from the Sun and the Earth itself, after it has passed through the atmosphere. In active remote sensing, artificial sources of radiation are used to detect the backscattered radiation and the temporal evolution of changes in intensity (Burrows et al., 2011).

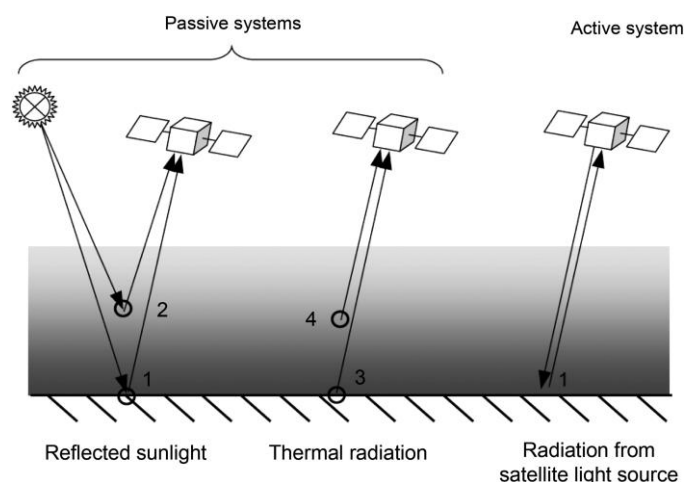


Figure 14 : Active and passive remote sensing systems. Possible pathways of the radiation from source to object and sensor are shown. Direct solar radiance can be reflected from the Earth's surface (1), or scattered in the atmosphere (2). Long-wave radiation is emitted from the Earth's surface (3) or from atmospheric gases (4) (Burrows et al., 2011).

1.6.2.1 Remote sensing from the ground

1.6.2.1.1 UV measurements

Generally, the coordinated measurements of UV radiation from the ground started in the late 1980s after the discovery of the ozone hole (Bais et al., 2015). Several ground-based networks now provide data records in excess of 20 years with instruments deployed in the United States, Canada, South America, Europe, New Zealand, Australia, the Arctic and Antarctic.

Relatively few measurements have been performed historically in Africa, the Middle East and Asia. Ground-based instruments generally measure the intensity of radiation falling on a diffuse horizontal surface (Kerr, 2005). The number of ground-based remote sensing UV instruments is limited by cost and by the inaccessibility of many locations around the globe. Ground-based remote sensing instruments that measure UV from the ground are spectrophotometers, array spectroradiometers, narrowband radiometers, multi-channel filter radiometers and broadband radiometers.

Spectrophotometers and array spectroradiometers are both spectral instruments that measure the intensity of the radiation over a spectral range at a large number of discrete wavelengths (with a Full Width at Half Maximum (FWHM) less than 1 nm) (Kerr, 2005). Spectrophotometers measure the spectra with a single detector that samples the individual components of the spectra using a wavelength scanning mechanism. These scanning measurements generally take a few minutes to complete, so there is a possibility that measured spectra are subject to changing conditions (e.g., cloud or haze) during the course of the scan. The Brewer spectrophotometer, which is the instrument used for UV monitoring at Uccle, is discussed in more detail in section 2.1. Array spectroradiometers are spectroradiometers for measuring UV radiation based on a different measurement principle: instead of rotating the grating to scan the spectrum across an exit slit onto a photomultiplier detector, the spectrum of UV irradiance is imaged onto a detector consisting of many elements e.g., a diode array (WMO/GAW, 2010b). Thus the entire spectral region of interest is measured at essentially the same time. The major advantage of array spectroradiometers is their relatively fast detection of the spectrum so rapid changes during the sample period have a much smaller impact on the shape of the spectrum. Other advantages include: (1) portability that arises from their compact design, (2) stability and reliability that arises from having no moving parts, and (3) good stability of the photodiodes compared with photomultipliers. The main disadvantage of array spectroradiometers is their inability to reduce stray light²⁰, which limits the lowest wavelength achievable to longer than 300 nm for solar measurements. Correction methods can however be applied. Other disadvantages include: (1) the higher detection threshold of diode array spectroradiometers compared with scanning spectroradiometers using photomultipliers, and (2) the uncertainties associated with the correction of the dark current, which may vary from diode to diode and is strongly temperature dependent.

Narrowband radiometers filter out only a certain very narrow part of the spectrum at one UV-A or UV-B wavelength. Narrowband radiometers generally combine a detector with a wavelength-selective device (such as a color glass filter or interference filter) and suitable input optics (Diffey, 2002). Narrowband radiometers have been replaced by broadband radiometers because their measurements are not very representative of UV-A and UV-B under a range of sky and atmospheric conditions²¹.

²⁰ Stray or scattered light caused by unwanted imaging and scattering on the optical elements of the instrument (surfaces, mounts, internal baffles, higher-order diffraction, fluorescence, etc.). Stray light can originate from the elements of an extended source inside and outside the instrument's overall field of view and from the spectral components of the particular source element inside and outside the instrument's spectral range (Zong et al. 2006).

²¹ <http://kippzonen-brewer.com/uv/measure-uv-radiation/>; visited on 28/9/2017

Multi-channel filter radiometers (MCFRs) make measurements in several discrete wavelength bands with bandwidths of typically 1 to 10 nm FWHM (WMO/GAW, 2010a). These instruments can be used to reconstruct spectra of global solar irradiance, to derive specific products such as erythemally weighted irradiance, or to determine total column ozone. Compared to single-channel broadband instruments or broadband instruments measuring erythemally weighted solar radiation, they allow separation of the influence of different atmospheric parameters affecting UV irradiance (e.g., total column ozone, cloud attenuation, aerosol effects, etc.). Furthermore, they are not restricted to only one action spectrum. If equipped with a solar tracker or a shadowband they have the capability to determine direct solar spectral irradiance, both at the center wavelength of the individual channels or at all wavelengths in the UV by means of spectral reconstruction.

Broadband radiometers are designed for measuring the incoming irradiance weighted with a specific spectral responsivity, e.g. the action spectrum for ultraviolet induced erythema (Hülse et al., 2008). The output signal of these instruments depends therefore on the intensity of the receiving radiation and on its spectral shape. The knowledge about the spectral responsivity of the detector is an important step in the calibration procedure. As this function differs from the nominal action spectrum, a suitable conversion is required to convert from the detector weighted radiation to the one representative for the desired weighting. A second requirement for such instruments is the application of a correction for the cosine error²².

Several factors make the routine measurement of UV radiation on an absolute scale and over a long time period a challenging task (Kerr, 2005). The first reason for this is the reliability of the absolute reference against which the spectral instruments are calibrated. Not only is the output of the calibration lamps very sensitive to the power supplied to the lamp, but the lamps also degrade with time, so periodic replacements with newly calibrated lamps are necessary. The second difficulty for obtaining good quality long-term spectral data is the question of instrument stability.

1.6.2.1.2 AOD measurements

There are several passive ground-based remote sensing networks that measure AOD, using different types of instruments (CIMEL sunphotometers, Prede-POM sun-sky radiometers, MultiFilter Rotating Shadowband Radiometers, Precision Filter Radiometers, Brewer spectrophotometers) (Table 8).

The Aerosol Robotic Network (AERONET²³; Holben et al., 1998) program is a federation of ground-based remote sensing aerosol networks established by National Aeronautics and Space Administration (NASA) and PHOtométrie pour le Traitement Opérationnel de Normalisation Satellitaire (PHOTONS; University of Lille, Centre National d'Études Spatiales (CNES) and Centre National de la Recherche Scientifique – Institut National des Sciences de l'Univers (CNRS-INSU)) and is greatly expanded by networks and collaborators from national agencies, institutes, universities, individual scientists and partners. It relies on the use of sun

²² A radiation beam received by an instrument at the incident angle θ should produce a signal proportional to the cosine of θ (Feister et al., 1997). Fore-optics (such as diffusers) of radiation instruments however very often lack an ideal cosine response, i.e. radiation measured by a horizontal receiver surface can be distorted mainly in dependence of θ .

²³ <http://aeronet.gsfc.nasa.gov/>

photometer CIMEL CE_318 instruments to retrieve AOD within the spectral range 340-1020 nm by means of a filtered detector that measures the spectral extinction of direct beam radiation according to Beer-Lambert's law (see also Section 1.2.2.5) (Dayou et al., 2014). AERONET provides globally distributed (Figure 15) observations of spectral AOD, inversion products²⁴ and precipitable water in diverse aerosol regimes. AOD data are retrieved from the radiance for three data quality levels: Level 1.0 (unscreened), Level 1.5 (cloud screened), and Level 2.0 (cloud screened and quality-assured).



Figure 15 : Map of AERONET stations (as of 24/5/2018)²⁵.

The AEROSol CANada (AEROCAN) sun photometer network²⁶ (Bokoye et al., 2001) is run as a joint collaboration between the Université de Sherbrooke and the Meteorological Service of Canada. It is a federated member of the much larger AERONET system of CIMEL sun photometers run out of NASA's Goddard Space Flight Center.

China Aerosol Remote Sensing NETwork (CARSNET; Che et al., 2009, Dayou et al., 2014) was established in 2002 and is a routine operation network, purposely launched for the study of aerosol properties and for validation of satellite aerosol retrievals. Similar to AERONET, it deploys CIMEL sun photometers for the measurement of direct spectral solar intensity.

To extend the aerosol monitoring over the ocean, the Maritime Aerosol Network (MAN) has been established as a component of AERONET since November 2006 (Dayou et al., 2014). It employs Microtops handheld sun photometers and utilizes calibration and data processing procedures traceable to AERONET.

The SKYNET network consists of Prede POM sun sky radiometers (Campanelli et al., 2016). These scanning spectral radiometers are able to perform automated measurements of direct and scattered solar radiation at seven wavelengths from 315 to 1020 nm (model POM-01) or from 315 to 2200 nm (model POM-2). SKYNET provides AOD and SSA at 340, 380, 400,

²⁴ Sun photometer radiance measurements can be inverted to produce aerosol optical properties such as size distribution, single scattering albedo, phase functions, and the complex index of refraction. Sun photometers measure the radiance at four or more wavelengths using almucantar and principle plane scenarios. The almucantar scenario measures radiance at azimuthal angles relative to the sun. For at least single-scattering approximation, sky radiances in the almucantar are not sensitive to aerosol vertical variations. The principle plane scenario measures radiance at scattering angles away from the sun. These radiance data in combination with aerosol optical depth measurements and estimations of land and water surface reflectance are inverted to estimate aerosol optical properties.

²⁵ https://aeronet.gsfc.nasa.gov/cgi-bin/type_piece_of_map_opera_v2_new; visited on 24/5/2018

²⁶ <http://www.aerocanonline.com/>; visited on 28/11/2016

500, 675, 870 and 1020 nm, volume size distribution of aerosols, the refractive index, phase function and asymmetry factors.

MultiFilter Rotating Shadowband Radiometer (MFRSR) networks measure total and diffuse solar irradiances at multiple wavelengths using the shadowband technique (Dayou et al., 2014). Direct solar irradiance is obtained by subtracting the diffuse radiation from the total radiation. These networks use an automated cloud screening algorithm (Alexandrov et al., 2004) and retrieve aerosol optical depth and particle size over a large geographical area of the United States (Alexandrov et al., 2002).

The Global Atmospheric Watch Precision Filter Radiometers (GAW-PFR) network started in 1999 as a pilot project. The GAW Scientific Advisory Group (SAG) for aerosols selected a number of existing GAW stations as candidates for the deployment of 12 PFRs. The pilot network is based on mutual collaboration between GAW stations. AOD measurements using PFR instruments are now made at 24 additional locations in Europe, Japan and Antarctica²⁷. The PFR accurately measures direct solar radiation transmitted in 4 narrow spectral bands (368, 412, 500 and 862 nm) (PFR manual²⁸). It is designed for continuous, automated operation under a broad range of weather conditions and to make reliable measurements of traceable quality. From these measurements, the atmospheric AOD can be derived by a collection of algorithms. The instrument is especially suited for very low AOD values (Laj et al., 2009).

A number of studies have already shown that AOD can be retrieved using direct sun measurements of Brewer spectrophotometers (e.g. Bais, 1997, Marengo et al., 1997, Kirchhoff et al., 2001; Marengo et al., 2002; Cheymol & De Backer, 2003; Kazadzis et al., 2005). The retrieval of AOD within the Brewer network could be very interesting as the network is a global one (with more than 200 instruments distributed over the world; see Figure 16) and many stations have long datasets available at their measurement sites. Within the European Brewer Network (Eubrewnet²⁹, COST ES 1207), AOD will become a product in the near future.



Figure 16 : Global map of Brewer stations³⁰.

²⁷ <http://www.wmo.int/pages/prog/arep/gaw/aerosol.html>; visited on 28/11/2016

²⁸ ftp://ftp.pmodwrc.ch/pub/projects/worcc/PFR_Manual_2011_V4.1.pdf; visited on 24/5/2018

²⁹ www.eubrewnet.org; visited on 24/5/2018

³⁰ adapted from <http://kippzonen-brewer.com/community/brewer-map/>; visited on 30/11/2016

Table 8 : Overview of different AOD measurement networks. This table shows the instruments used in each network, the type of measurement used to retrieve AOD, the retrieval (calibration) method, the wavelengths at which the AOD is retrieved and the number of stations worldwide.

Network	THIS WORK	EUBREWNET	AERONET
Instrument	Brewer spectrophotometer	Brewer spectrophotometer	CIMEL sun sky radiometer
Type of measurements	Sun Scan measurement (see section 2.1.4 for more details)	Direct Sun measurement with FOV of 2.6° (see section 2.1.2 for more details)	Direct Sun measurement with FOV of 1.2° (see section 2.2 for more details)
Retrieval method	On-site Langley calibration	On-site Langley calibration	Comparison with standard instrument (transfer of calibration)
AOD wavelengths	340 nm	306.3, 310.3, 313.5, 316.8, 320.1 nm	340, 380, 440, 500, 675, 870, 1020 nm
Number of stations	> 200	> 200	~ 480
References	De Bock et al., 2010	Cheyamol & De Backer, 2003, 2009	Holben et al., 1998
Network	SKYNET ³¹	GAW-PFR ³²	SURFRAD (MFRSR) ³³
Instrument	PREDE POM sun sky radiometer	Precision Filter Radiometer	MultiFilter Rotating Shadowband Radiometer
Type of measurements	Direct Sun measurement with FOV of 1°	Direct Sun measurement with FOV of 2.5°	Direct irradiance as residual calculation from global and diffuse irradiance measurements
Retrieval method	On-site Langley calibration	Comparison with absolute spectral radiometer; refined Langley and ratio-Langley calibration	On-site Langley calibration
AOD wavelengths	340, 380, 400, 500, 675, 870, 1020 nm	368, 412, 500, 862 nm	415, 500, 614, 670, 868 nm
Number of stations	~ 60	36	7 (in the US)
References	Campanelli et al., 2007	McArthur et al., 2003; Nyeki et al., 2012	Augustine et al., 2008

1.6.2.1.3 Column ozone measurements

Several instruments (e.g. Dobson spectrophotometer, Brewer spectrophotometer, UV-VIS absorption spectrometer) rely on the Differential Optical Absorption Spectroscopy (DOAS) principle for the measurement of the total ozone column. The DOAS technique determines the concentrations and total amounts of atmospheric trace gases from remote sensing

³¹ <https://www.skynet-isdc.org/aboutSKYNET.php>; visited on 27/9/2018

³² <https://www.pmodwrc.ch/weltstrahlungszentrum/worcc/>; visited on 27/9/2018

³³ <https://www.esrl.noaa.gov/gmd/grad/surfrad/aod/>; visited on 27/9/2018

measurements of light in the UV, visible, and NIR spectral range and uses absorption spectroscopy as the basic principle. It relies on the application of the Beer-Lambert law (section 1.2.2.6) to the whole atmosphere in a limited range of wavelengths. This law describes the attenuation of radiation travelling through a medium over a certain distance. In the atmosphere, multiple effects contribute to this overall attenuation. Also, there is rarely only one absorber relevant at a given wavelength, which needs to be taken into account. As each molecule has a characteristic absorption spectrum, simultaneous measurements at different wavelengths should allow separating the contributions of different absorbers.

The Dobson and Brewer spectrophotometers provide total ozone content and the measurement principle of both instruments is based on the wavelength dependence of the absorption coefficients of ozone (Dobson, 1957, Brewer, 1973). Total ozone is determined by comparing the UV light intensity at wavelengths that are strongly absorbed and weakly absorbed by ozone. The Dobson spectrophotometer (Dobson, 1957) was developed in the 1920s. Currently around 90 instruments are in operation worldwide³⁴. The Brewer spectrophotometer was developed in the 1980s (Kerr, 1988) and at the moment, more than 200 instruments are operated worldwide³⁵. This work mostly uses measurements from the Brewer spectrophotometer, which is described in detail in Section 2.1.

For more than two decades, stratospheric ozone (and related trace gases such as NO₂, BrO, and OCIO) has been monitored at a number of stations belonging to NDACC using ground-based zenith-sky UV-visible absorption spectrometers (Hendrick et al., 2011), which measure in the Chappuis bands (between 375 and 650 nm). It allows twice daily ozone measurements at twilight throughout the year at all latitudes up to the polar circle, with however limited sensitivity to the cloud cover. In the UV-VIS spectrometry technique, trace gas species amounts are retrieved from zenith-sky radiance spectra at large solar zenith angle using the DOAS method consisting of fitting the narrow absorption features of the species with laboratory absorption cross sections without further calibration procedure. The Système d'Analyse par Observations Zénithales (SAOZ) network³⁶, which is part of NDACC, consists of about 20 zenith sky UV-VIS spectrometers, located around the world, which are used to retrieve mean values of total ozone and NO₂ at sunrise and sunset on a daily basis.

Fourier Transform InfraRed (FTIR) spectroscopy allows measuring a large suite of trace gases, among which ozone, using direct sun absorption measurements spectra (Barret et al., 2002; Viatte et al., 2011). A low resolution vertical profile is usually retrieved from the measured radiances using a constrained method (Optical Estimation Method) from which the total column can then be recalculated.

1.6.2.1.4 Profile ozone measurements

Dobson and Brewer spectrophotometers can use the Umkehr technique to get information on vertical profiles of ozone at an altitude resolution from 5 km (WMO, 2001; Petropavlovskikh et al., 2011). The Umkehr measurement is a sequence of morning or afternoon zenith-sky measurements recorded as a relative change of transmission at two spectral channels (Dobson)

³⁴ <http://www.o3soft.eu/dobsonweb/instruments.html>; visited on 30/11/2016

³⁵ <http://kippzonen-brewer.com/community/brewer-map/>; visited on 30/11/2016

³⁶ <http://www.cas.manchester.ac.uk/restools/instruments/remotesensing/saozinstrument/>; visited on 14/6/2018

or photon counts at individual spectral channels (Brewer), all selected in the UV part of the zenith-sky spectrum (Hassler et al., 2014). Measurements are taken when the sun elevation changes between 60° and 90° solar zenith angle, and under the assumption of static atmospheric conditions and no clouds in the zenith viewing area. The vertical resolution of an Umkehr ozone profile is ≈ 10 km.

The Light Detection And Ranging (LIDAR) technique is an active remote sensing measurement technique using the scattering properties of light by gases, liquids, and solids in order to infer their physical or chemical properties. The Differential Absorption Lidar (DIAL) technique is used to measure ozone (typically 10-45 km in the stratosphere, 1-10 km in the troposphere) (Duflot et al., 2017). Concretely, laser beams at two different wavelengths are sent into the atmosphere and the wavelengths are chosen so that one of them is significantly more absorbed than the other. The difference in the absorption along the beam path causes the returned lidar signals to yield a different altitude dependence. Knowing from laboratory work the absorption cross-sections of the constituent at both wavelengths, the atmospheric number density can be deduced from the ratio of the slope of the logarithm of the signals at the two wavelengths. This technique does not require any calibration. There are fourteen DIAL systems included in NDACC³⁷. Three systems are dedicated to the measurement of tropospheric ozone (0-10 to 20 km), and the others are dedicated to the measurements of stratospheric ozone (10-45 to 50 km). For the measurements in the stratosphere where ozone is very abundant, the wavelengths used are typically 308 nm and 355 nm, while for the measurements in the troposphere where ozone is less abundant, they are typically at 289 nm and 299 nm.

Microwave radiometry is a passive technique based on the detection and analysis of radiation emitted by molecules undergoing rotational transitions in the millimeter wave range (Fernandez et al., 2015). In this frequency range, ozone presents two main emission lines which are traditionally used for its retrieval: 110.8 and 142.2 GHz. The transition strength of these lines leads to a fairly strong ozone signal throughout the stratosphere and mesosphere. There are a few ground-based ozone microwave radiometers sites in the world. Most of them are gathered under the NDACC, with permanent instruments located at observation stations in Ny-Alesund (Spitsbergen), Bern (Switzerland), Payerne (Switzerland), Mauna Loa (Hawaii), Lauder (New Zealand) and Rikubetsu (Japan). Other ozone radiometers are located in Thule (Greenland), Seoul (Korea), Kiruna (Sweden), Moscow (Russia) and in Antarctica.

As mentioned in section 1.6.2.1.3, FTIR measurements also provide vertical ozone profiles. Low-vertical-resolution profiles can be obtained from the temperature and pressure dependence of the absorption line shapes (Hassler et al., 2014). The advantage of the FTIR technique is that, for atmospheric gases such as ozone which have very narrow lines, an absolute calibration is not needed; the ozone absorption signatures are self-calibrated with the reference being the surrounding continuum.

³⁷ <http://ndacc-lidar.org/index.php?id=41/Instruments.htm>; visited on 30/11/2016

1.6.2.2 Remote sensing from space

1.6.2.2.1 Viewing geometry and operational wavelength range

The viewing geometry of satellite instruments enables particular aspects of the atmospheric composition to be probed (Burrows et al., 2011). Measurements are possible in nadir viewing mode, multiple viewing mode, limb viewing mode and occultation viewing mode (Figure 17; see Table 9 for examples of instruments).

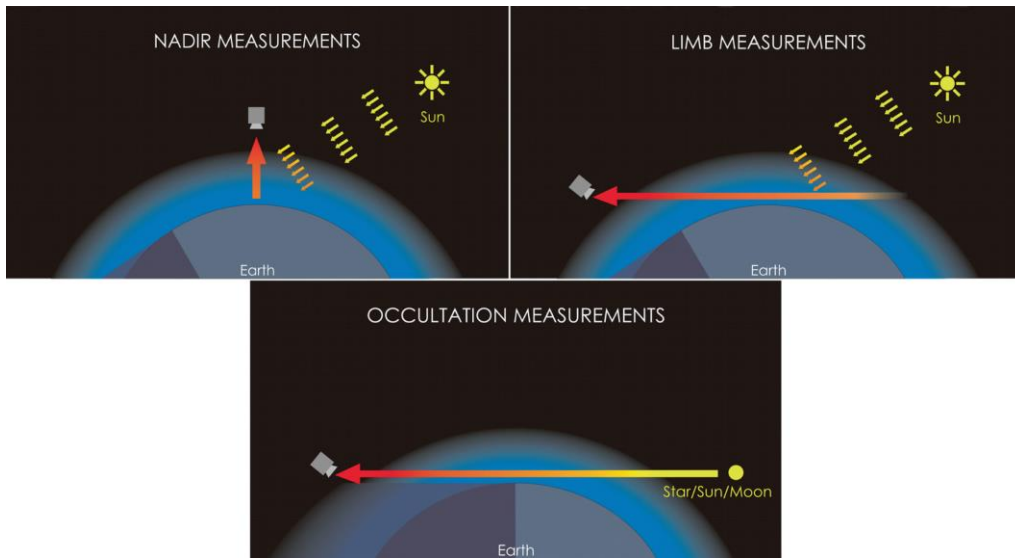


Figure 17 : A schematic representation of nadir (upper left), limb (upper right) and occultation (lower) viewing geometries used by SCIAMACHY (from Burrows et al., 2011).

Instruments in the nadir viewing mode (Figure 17; upper left) look down from space towards the nadir direction or close to it and observe radiation coming either from the Sun, back-scattered from the Earth's surface and the atmosphere or from emissions within the atmosphere (Burrows et al., 2011). They have a good spatial resolution, good signal to noise ratio and global coverage. Their vertical resolution however is poor.

Some instruments have several viewing directions (multiple viewing mode) and offer in addition to the nadir view, the advantage of multiple paths through the boundary layer, which is especially useful for aerosol retrieval (Burrows et al., 2011). The AOD is higher across longer atmospheric paths and the additional views provide a means to eliminate the effect of reflectance of land surfaces which often dominate the total reflectance. The multi-view instruments can also provide information about the height of aerosol plumes.

Instruments in limb viewing mode (Figure 17; upper right) analyze the light scattered from the Earth's rim (Burrows et al., 2011). By observing the limb at different tangent altitudes, vertical trace gas concentration profiles with a high vertical resolution can be inferred. The horizontal resolution of these type of instruments is poor, but higher than for occultation measurements.

Finally, some instruments observe the light of the rising or setting Sun, moon or stars through the atmosphere at different tangent altitudes (occultation viewing mode; Figure 17; lower) and deduce vertical trace gas concentration profiles (Burrows et al., 2011). They are self-

calibrating, have a high vertical resolution and a high signal to noise ratio. Their spatial coverage is limited as is their sensitivity to UV. Solar occultation works well in the middle and upper atmosphere where general transparency is high, but problems arise when clouds and heavy aerosol layers or strong absorbers are present in the path, as occurs in the troposphere.

Table 9 : Examples of instruments measuring in different viewing modes and in different wavelength region (adapted from Burrows et al., 2011). Between brackets is the property that can be measured. AOD, Ap, Q₀₃ and P₀₃ respectively stand for aerosol optical depth, aerosol profile, total ozone column and ozone profiles. Please refer to the list of acronyms for the full name of the instruments.

	NADIR	MULTIPLE VIEWS	LIMB	OCCULTATION
UV – VIS -NIR	AVHRR (AOD) BUV (Q ₀₃ , P ₀₃) CALIOP (Ap, AOD) GOME (Q ₀₃ , P ₀₃) GOME-2 (Q ₀₃ , P ₀₃) MERIS (AOD) MODIS (AOD) OMI (Q ₀₃ , P ₀₃ , AOD) OMPS (Q ₀₃ , P ₀₃) SBUV (Q ₀₃ , P ₀₃) SBUV-2 (Q ₀₃ , P ₀₃) SCIAMACHY (Q ₀₃ , P ₀₃) SeaWiFS (AOD) TOMS (Q ₀₃) TROPOMI (Q ₀₃ , P ₀₃)	ATSR-2 (AOD) AATSR (AOD) POLDER (AOD) MISR (AOD)	OSIRIS (P ₀₃) SCIAMACHY (Q ₀₃ , P ₀₃) OMPS (Q ₀₃ , P ₀₃)	Star occultation: GOMOS (P ₀₃) Solar occultation: POAM-II, -III (P ₀₃) SAGE-1, -2, -3 (P ₀₃) SCIAMACHY (Q ₀₃ , P ₀₃) ACE-MAESTRO (Ap, P ₀₃)
IR	IASI (Q ₀₃ , P ₀₃) TES (Q ₀₃ , P ₀₃)	AIRS (Q ₀₃ , P ₀₃) IASI (Q ₀₃ , P ₀₃)	CLAES (P ₀₃) HIRDLS (P ₀₃) ISAMS (P ₀₃) LIMS (P ₀₃) LRIR (P ₀₃) MIPAS (P ₀₃) TES (Q ₀₃ , P ₀₃)	ACE-FTS (P ₀₃) ILAS-I, -II (P ₀₃) HALOE (P ₀₃)
Microwave			MLS (P ₀₃) SMR (P ₀₃) SMILES (P ₀₃)	

Not only the viewing geometry, but also the wavelength range defines the measurement capabilities of satellites. A difference can be made between satellites measuring in the UV-VIS-NIR range, in the TIR range and in the microwave range (see Table 9 for examples of

instruments). In the UV-VIS-NIR region, thermal emission can usually be neglected so the measured spectral signatures can be directly related to the absorption spectra of different atmospheric trace gases within the chosen spectral range, which makes the spectral analysis usually reasonably straightforward (Burrows et al., 2011). An important advantage from satellite observations in the UV-VIS-NIR region is that information from all atmospheric height layers (including the near surface layers) can be obtained. In contrast to observations in the TIR or microwave, little or no information on the vertical distribution of a trace gas is obtained and the number of species which can be observed in this region is limited. When using the TIR spectral range to sound the atmosphere, a remote sensor onboard a satellite records the light passing through different atmospheric layers and from the radiance signal recorded, information on the vertical concentration of each atmospheric constituent absorbing at a given altitude can be extracted. The source can either be the thermal emission of the Earth-atmosphere system (nadir and limb viewing) or a section of the solar emission spectra (solar occultation). In the TIR, many molecules can be observed that cannot be measured in other spectral regions and measurements are possible both during day and night. In the TIR, there are problems with strong absorbers and with dark or cold surfaces. Instruments measuring in the microwave region, can measure through clouds and can distinguish between ice and water. They can give information on emissions and profiles.

1.6.2.2.2 UV measurements

Surface UV irradiance cannot be directly measured from space but satellite measurements can be used as input data to radiative transfer models, giving estimates of the surface UV radiation levels (Kujanpää & Kalakoski, 2015). Satellite UV products are associated with relatively large uncertainties which vary according to location, season, atmospheric situation and the characteristics of the satellite instruments (Bais et al., 2015). Known sources of errors that affect the accuracy of the derived surface UV irradiance include: absorption and scattering by tropospheric aerosols, inhomogeneities of clouds, assumptions or estimations of the surface reflectivity, variability of altitude within the sub-satellite pixel, various modeling parameterizations and inability of current satellites to distinguish between clouds and surfaces covered with snow and/or ice.

The first satellite UV radiation products were provided by the Total Ozone Mapping Spectrometer (TOMS) (Krotkov et al., 1998, 2001). TOMS is a nadir-viewing spectrometer that measures in the UV-VIS spectrum and has flown onboard Nimbus (1979-1993), Meteor-3 (1991-1994), ADEOS (1996-1997) and Earth Probe (1996-present). The TOMS UV algorithm for estimating surface UV irradiance from satellite measurements proceeds in two steps: first, the clear-sky radiation is calculated, and afterwards it is multiplied with the estimated cloud transmission factor (Herman et al., 1999; Krotkov et al., 1998, 2001). The clear-sky radiation in the UV spectral range is obtained from the satellite-derived spectral extraterrestrial solar irradiance (ATLAS-3 SUSIM) and TOMS measurements of total column ozone and scene reflectivity. The method is described in detail by Krotkov et al. (1998) and Herman et al. (1999).

Surface UV radiation estimates have also been provided by the Ozone Monitoring Instrument (OMI). OMI was launched in 2004 onboard the Aura satellite and observes the Earth's

backscattered radiation in the UV-VIS spectral region in nadir mode with a wide-field telescope feeding two imaging grating spectrometers³⁸. Its UV algorithm is based on the TOMS heritage (Ialongo et al., 2011). First, the algorithm estimates the surface irradiance under clear-sky conditions by using as inputs OMI satellite ozone data, climatological surface albedo elevation, solar zenith angle, and latitude-dependent climatological ozone and temperature profiles (Ialongo et al., 2011; Jégou et al., 2011). Afterwards the clear-sky irradiance is corrected by multiplying it with a cloud modification factor derived from OMI data that accounts for the attenuation of UV radiation by clouds and non-absorbing aerosols (Ialongo et al., 2011). The OMI UV algorithm does not include absorbing aerosols so OMI UV data are expected to show an overestimation for regions affected by absorbing aerosols.

The first Global Ozone Monitoring Experiment 2 (GOME-2) instrument was launched onboard MetOp-A in 2006. It is a nadir viewing spectrometer that measures in the UV-VIS part of the spectrum. The UV processing algorithm of the GOME-2 involves the gridding of GOME-2 total ozone data, the inversion of cloud optical depth from reflectance data, and finally the calculation of surface UV quantities from radiative transfer model look-up tables (Ialongo et al., 2011).

The Scanning Imaging Absorption Spectrometer for Atmospheric Cartography (SCIAMACHY) was designed for the global measurement of trace gases in the troposphere and stratosphere (Envisat, 2010) and was launched onboard Envisat. The instrument provides spectra measured from light transmitted, backscattered or reflected by trace gases in the atmosphere at relatively high resolution (0.2 nm to 0.5 nm) over the range 240 nm to 1700 nm, and in selected regions between 2000 nm and 2400 nm. The SCIAMACHY algorithm used to calculate the UVI applies a functional relation between this index, the local solar noon ozone fields and the solar zenith angle at local solar noon (Allaart et al., 2004). The UV index is a quantity valid for local solar noon and for clear-sky conditions. The daily erythemal UV doses have been validated for Europe through comparisons with ground-based measurement data stored in the European Database for UV Climatology and Evaluation (EDUCE) database (Van Geffen et al., 2005).

The Atmospheric Composition Satellite Application Facility (ACSAF) (formerly Ozone Monitoring Satellite Application Facility (O3MSAF)) of the European Organization for the Exploitation of Meteorological Satellites (EUMETSAT) also provides a surface UV product (surface UV index and daily doses), based on the total ozone column derived from the measurements of the GOME-2 instrument (Jégou et al., 2011; Kujanpää & Kalakoski, 2015). Cloud cover is taken into account by retrieving cloud optical depth from the channel 1 reflectance of the third Advanced Very High-Resolution Radiometer (AVHRR/3) instrument aboard both MetOp in the morning orbit and Polar Orbiting Environmental Satellites (POES) of the National Oceanic and Atmospheric Administration (NOAA) in the afternoon orbit. The AOD is currently taken from climatology (Kinne, 2007) and the surface albedo from the climatology of Tanskanen (2004).

³⁸ <https://aura.gsfc.nasa.gov/omi.html>; visited on 30/11/2016

1.6.2.2.3 AOD measurements

The retrieval of aerosol properties from satellite-based observations started in the 1970s and initially the retrievals were only obtained for measurements over water (Burrows et al., 2011). Retrievals over land only became available since the 2000s. The launch of lidars (e.g. Cloud-Aerosol Lidar with Orthogonal Polarization (CALIOP) onboard Cloud-Aerosol Lidar and Infrared Pathfinder Satellite Observation (CALIPSO)) in space has added a new dimension to satellite observation of aerosol properties by providing information on the vertical distribution of aerosols and clouds.

Aerosol retrieval is based on the comparison of the radiation received by an instrument at the TOA with that calculated using a radiative transfer model (RTM) for the same geometry and atmospheric conditions, for a range of aerosol models. By minimizing the difference between computed and observed radiances, the AOD can be determined. For the retrieval of aerosol properties, it is important to accurately detect the occurrence of clouds. In particular sub-visible and high cirrus clouds may disturb the signal and complicate the distinction between aerosols and clouds near cloud edges. The removal of land surface effects from the TOA radiation is also an important issue for aerosol retrievals. Generally, the quality of the satellite-derived AOD strongly depends on the retrieval's ability to remove scenes contaminated by clouds and to accurately account for reflectivity at the Earth's surface (Boucher et al., 2013).

A lot of satellites were not specifically designed to retrieve aerosol information (e.g. TOMS, GOME, SCIAMACHY, OMI, AVHRR, SeaWiFS, MERIS and ASTR) but their data has been used for aerosol products. Here we only discuss the instruments dedicated specifically for aerosol retrieval (MODIS, MISR, PARASOL and CALIOP). We also address the aerosol Climate Change Initiative (CCI) project from the European Space Agency (ESA), which aims at producing aerosol Climate Data Records (CDR) which satisfy the requirements on data quality and transparent documentation set by the Global Climate Observing System (GCOS). For aerosols over land, the first operational satellite dataset has been provided by the Moderate Resolution Imaging Spectrometer (MODIS) (Remer et al., 2005; Levy et al., 2007; Levy et al., 2010; Kleidman et al., 2012). MODIS is a nadir viewing multi-spectral radiometer and retrieves aerosol microphysical and optical properties over ocean and land (Nabat et al., 2013). It was launched first onboard Terra (since 1999, morning orbit) and later onboard Aqua (since 2002, afternoon orbit) satellites. It has 36 spectral bands from 0.4 μm to 14.4 μm with varying spatial resolutions (250 m, 500 m and 1 km). Kaufman et al. (1997) introduced the strategy for retrieving aerosols over land from MODIS and Levy et al. (2007) introduced a second algorithm for deriving optical properties over dark land surfaces. The traditional algorithms cover both ocean and land surfaces except deserts and have been applied to MODIS measurements with the objective to acquire a long data record (since 1999 for Terra and since 2002 for Aqua) at a $1^\circ \times 1^\circ$ resolution (Nabat et al., 2013). Over bright surfaces such as the Sahara, the "Deep Blue" algorithm is needed to retrieve aerosols, instead of the standard land algorithm which is based on finding dark targets. The Deep Blue algorithm relies on the blue wavelengths and libraries of surface reflectance. The aerosol products available over land include aerosol optical thickness at three visible wavelengths (470, 550 and 660 nm), a measure of the fraction of aerosol optical thickness attributed to the fine mode,

and several derived parameters including reflected spectral solar flux at the top of the atmosphere (Remer et al., 2005). Over the ocean, the aerosol optical thickness is provided in seven wavelengths: 470, 550, 660, 870, 1024, 1630 and 2130 nm. In addition, quantitative aerosol size information includes effective radius of the aerosol and quantitative fraction of optical thickness attributed to the fine mode.

The Multi-angle Imaging SpectroRadiometer (MISR) is a passive radiometer also launched onboard the Terra platform in 1999 into a sun-synchronous polar orbit (Kahn et al., 2005; Kahn et al., 2007; Kahn et al., 2010; Nabat et al., 2013). MISR combines high spatial resolution, a wide range of along-track view angles and high-accuracy radiometric calibration and stability (Kahn et al., 2010). Global coverage (to $\pm 82^\circ$ latitude) is obtained about once a week. MISR provides radiometrically and geometrically calibrated images at four wavelengths (446, 558, 672 and 866 nm) in nine different directions both over land and ocean. The MISR standard aerosol retrieval algorithm reports AOD (and aerosol type) at 17.6 km horizontal resolution, by analyzing MISR TOA radiances. The algorithm is based on a look-up table approach: it searches a database of TOA radiances simulated for the MISR channels, solar position and viewing geometries, assuming a range of candidate aerosol mixtures and optical depths and compares them with the observed radiances.

According to Nabat et al. (2013), the comparison between different satellites and AERONET highlights the quality of AQUA/MODIS and TERRA/MODIS, which both show relevant spatial and temporal aerosol variability. They have the smallest average root mean square error (rmse) and highest correlation. MISR AOD presents a similar spatial and temporal structure, but its score against AERONET is not as high as MODIS.

The POLARization and Directionality of the Earth's Reflectances (POLDER) instrument was launched onboard the Polarization and Anisotropy of Reflectances for Atmospheric Sciences coupled with Observations from a Lidar (PARASOL) satellite in 2005 (Tanré et al., 2011). The platform was launched as part of the A-train (consisting of Aqua, Aura, CALIPSO, CloudSat and PARASOL) and has a sun-synchronous orbit. Aerosol optical and microphysical properties are retrieved from POLDER measurements in a unique way thanks to its directional polarized measurements at 670 and 865 nm. POLDER total AOD is only available over ocean (Tanré et al., 2011). Since polarization is mainly sensitive to the presence of small particles, it allows deriving the optical depth of the fine mode only.

It is possible to assimilate the vertical profile of the extinction coefficient from the CALIOP sensor onboard the CALIPSO mission (Winker et al., 2009). CALIPSO was launched together with the CloudSat satellite in April 2006 and is now flying in formation with the A-train constellation of satellites. The primary instrument carried on the CALIPSO satellite is CALIOP, a near-nadir viewing two-wavelength (532 and 1064 nm) polarization-sensitive lidar. CALIOP is the first polarization lidar to provide global atmospheric measurements and as such offers new observational capabilities to the international scientific community. Lidar is the only technique giving high-resolution profiles of aerosols, and it is able to observe aerosol above bright surfaces, such as deserts and snow, and above bright clouds. Because lidar provides its own illumination, aerosol can be observed over the full globe—night as well as day—yielding a more complete dataset for the validation of regional and global aerosol models. CALIOP column AOD are obtained by integrating the aerosol extinction profile. The products are at a horizontal resolution of 5 km (for Version 3). Schuster et al. (2012) found a

CALIOP AOD (at 532 nm) bias of 13%, corresponding to an absolute bias of 0.029 relative to AERONET.

GCOS sets out observation requirements for satellites for aerosols as one Essential Climate Variable (ECV): the variables needed are AOD, SSA, vertical extinction profiles and layer height (Popp et al., 2016). For AOD at 550 nm, GCOS states the need for an accuracy better than 10% or 0.03 (whichever is larger), with a horizontal resolution of 5-10 km, a temporal resolution of 4 h and a stability of 0.01 per decade. A CDR is nominally required to contain a time series of 30 years or more. As individual satellite missions have shorter lifetimes, a CDR must be built from multiple data records. In the ESA CCI, the aerosol CCI project has worked on the development and qualification of several complementary aerosol CDRs. It has for example, produced a 17-year AOD CDR (based on ATSR-2 and AATSR data) (Popp et al., 2016).

The major goal of the aerosol CCI activity, which started in 2010, was to produce aerosols CDRs which satisfy the requirements on data quality and transparent documentation set by GCOS. Aerosol CCI focuses on European total column AOD retrieval algorithms. The overall concept for the qualification of AOD algorithms in aerosol_cci consists of three steps:

1. Several algorithm experiments conducted on a minimal statistically significant amount of data in order to understand the effects of major assumptions
2. A round robin exercise to evaluate the improved algorithms versus a more comprehensive independent ground-based data set and thus identify mature algorithms
3. The production of a complete validated one year ECV product for assessment by the climate model community.

Although AOD retrieval by satellite sensors shows some skill against more accurate sun photometer measurements such as those of AERONET, there are still large differences among satellite products in regional and seasonal patterns because of differences and uncertainties in calibration, sampling, cloud screening, treatment of the surface reflectivity and aerosol microphysical properties (e.g., Li et al., 2009; Kokhanovsky et al., 2010). The global but incomplete sampling of satellite measurements can be combined with information from global aerosol models through data assimilation techniques (e.g., Benedetti et al., 2009). The global mean AOD is not well constrained from satellite-based measurements and remains a significant source of uncertainty when estimating aerosol-radiation interactions. This highlights the importance of a ground-based network for measuring AOD (Boucher et al., 2013). Our thesis aims at contributing to this with the setting-up of a suitable method of AOD retrievals from Brewer instruments, which would benefit from the infrastructure network in place.

1.6.2.2.4 Ozone measurements

Satellite instruments can measure total ozone and/or ozone profiles in different viewing modes from the UV to the microwave spectral region (see Table 9). A discussion of all the instruments from Table 9 is out of the scope of this work. We will limit ourselves here to a few of the most important sensors. The ESA ozone CCI project will also be addressed shortly. Space-based measurements of the ozone column started in the 1970s with the (Solar) Backscatter Ultraviolet ((S)BUV) and TOMS series of instruments (Burrows et al., 2011;

Veefkind et al., 2006). The BUV and SBUV instruments (launched onboard Nimbus 4 in 1976 and onboard Nimbus 7 in 1979 respectively) measure the intensity in narrow spectral intervals (12 narrow bands between 250-340 nm³⁹), for which the atmospheric ozone absorption differs. From the BUV/SBUV data it is possible to retrieve information on the atmospheric ozone concentration profile, because the penetration depth into the atmosphere strongly depends on the absolute value of the ozone absorption cross-section and thus on wavelength. Typically, the received light at the shortest wavelengths has only “seen” the highest parts of the ozone layer whereas the longest wavelengths have seen the total column. Hence, the data at the shortest wavelengths are used to estimate the ozone concentration as a function of height, whereas the measurements at longer wavelengths are used to provide observations of the total ozone column. Like the BUV/SBUV instruments, the TOMS instruments observe the backscattered light in distinct wavelength intervals, but at longer wavelengths in the UV (from 312.5 to 380 nm), for which the light can penetrate the whole atmosphere (Burrows et al., 2011; Cracknell & Varotsos, 2014). TOMS observations thus yield the total ozone column.

The Solar Backscatter Ultraviolet Radiometer-2 (SBUV/2), onboard NOAA weather satellites, was designed to measure, on a global scale, total ozone concentrations and the vertical distribution of ozone in the Earth’s atmosphere. The instrument is a nadir-pointing, spectrally scanning, ultraviolet radiometer. The SBUV/2 measures solar irradiance and Earth radiance in the ultraviolet spectrum (160-400 nm). The SBUV/2 instruments have been monitoring the ozone layer continuously since 1985. Its predecessor, the SBUV instrument operated from 1978-1987, so there exists a continuous long-term record of measurements since November 1978⁴⁰ (Bhartia et al., 2013). The total ozone column is determined by measuring the scattered solar radiation from the atmosphere in the UV spectrum (Cracknell & Varotsos, 2014).

A completely new quality of the observed spectral information became available in 1995 with the launch of the first DOAS-type instrument, GOME-1, on the European Research Satellite ERS-2 (Burrows et al., 2011). GOME-1 was the first of a series of space instruments that measure the ultraviolet and visible part of the spectrum (between 240 and 790 nm) with a moderately high spectral resolution (between 0.2 and 0.4 nm)⁴¹. GOME-1 is a nadir viewing spectrometer which in its normal mode scans across-track in three steps and measures the solar radiation reflected from the Earth’s surface and the atmosphere (GOME, 2009). The field of view of each step can vary in size from 40 km x 40 km to 320 km x 40 km. In contrast to the few spectral intervals measured by BUV/SBUV and TOMS instruments, GOME spectra yield a plethora of spectral information (Burrows et al., 2011). Not only strong absorbers (e.g. O₃, H₂O, and O₂) but also weak absorbers can be retrieved (e.g. NO₂, BrO, OCIO, HCHO and SO₂). In addition, other quantities like aerosol extinction, cloud properties, surface albedo, vegetation properties, ocean color and indices characterizing the solar cycle are retrieved from the GOME measurements. The GOME instrument operated until 2011.

In 2002, the SCIAMACHY instrument was launched onboard Envisat. Compared to GOME, the SCIAMACHY spectra cover a wider wavelength range (240 nm to 1700 nm + selected

³⁹ <https://nssdc.gsfc.nasa.gov/nmc/experimentDisplay.do?id=1970-025A-05> ; visited 24/05/2018.

⁴⁰ <http://www.star.nesdis.noaa.gov/smcd/spb/ozone/>; visited on 30/11/2016

⁴¹ <https://earth.esa.int/web/guest/missions/esa-operational-eo-missions/ers/instruments/gome>; visited 14/6/2018

regions between 2000 nm and 2400 nm), facilitating measurements of different trace gases (e.g. CO₂, CH₄, and CO) despite low concentrations (Burrows et al. 2011). The large wavelength range is also ideally suited for the detection of clouds and aerosols. Another advantage is that the ground pixel size for the nadir viewing mode is appreciably reduced to 30 km x 60 km (and in a special mode to 15 km x 30 km). For the observation of tropospheric trace gases this is important, because their concentrations can exhibit strong spatial gradients. Smaller ground pixels are also less affected by clouds. SCIAMACHY has three different viewing geometries: nadir, limb, and sun/moon occultation. In nadir mode, the global distribution (total column values) of the atmospheric trace gases (such as ozone) and aerosols are observed. To obtain the altitude distribution of trace gases, SCIAMACHY performs observations in limb mode over an altitude range of 100 km, with a vertical resolution of 3 km. The DOAS technique is applied in sun and moon occultation measurements, where sun or moon are either tracked or a vertical scan over the complete sun/moon surface is performed. The obtained spectra can then be compared with suitable calibration spectra to yield the differential absorption of the atmosphere.

OMI, launched in 2004 onboard the Aura satellite, derives its heritage from the TOMS and GOME instrument. Compared to GOME and SCIAMACHY, it has a limited spectral range (270–500 nm), but a higher spatial resolution (up to 13 km x 25 km) in nadir viewing mode (Burrows et al., 2011). It can also measure many more atmospheric constituents than TOMS. The retrieval of the total ozone column is either based on the NASA-TOMS or the KNMI-DOAS method (Bhartia, 2002). The TOMS algorithm uses only two wavelengths (317.5 and 331.2 nm) and is applied to OMI to ensure continuity of the SBUV and TOMS data record. It is capable of producing total ozone columns with root mean square errors of about 2%. The errors are not necessarily randomly distributed over the globe and they typically increase with solar zenith angle and in the presence of heavy aerosol loading. The DOAS algorithm estimates the total ozone column using longer wavelengths (the 331.6 – 336.6 nm window) than those in the TOMS algorithm. It is less sensitive to disturbing effects by absorbing aerosols, SO₂ and calibration errors. The ozone column derived from the DOAS algorithm shows systematic seasonal and latitudinal differences when compared to ground-based measurements. OMI also provides ozone profile measurements using a technique called the optimal estimation technique (Rodgers, 2000).

In October 2006, the first of three instruments of a second generation of GOME instruments was launched on MetOp-A⁴² (Burrows et al., 2011). Compared to GOME-1, the GOME-2 instruments have an almost daily global coverage and much improved spatial resolution (80 km x 40 km). GOME-2 is used to get a detailed picture of the total atmospheric content of ozone and its vertical profile in the atmosphere⁴³. It also provides accurate information on the total column amount of NO₂, SO₂, water vapor, oxygen/oxygen dimer, bromine oxide and other trace gases, as well as aerosols.

The Infrared Atmospheric Sounding Interferometer (IASI) was designed for operational meteorology and for monitoring atmospheric chemistry and climate (Boynard et al., 2016) and

⁴² The Metop satellites carry a payload of eight instruments (among which GOME-2, IASI and AVHRR) for observing the planet. MetOp-B was launched in 2012 and MetOp-C is expected to be launched in September 2018.

⁴³ <http://www.eumetsat.int/website/home/Satellites/CurrentSatellites/Metop/MetopDesign/GOME2/index.html>; visited on 30/11/2016

combines the heritage of instruments dedicated to weather forecasting (such as the High-resolution Infrared Radiation Sounder, HIRS, and the Atmospheric InfraRed Sounder, AIRS) with that of tropospheric sounders dedicated to atmospheric chemistry and climate (e.g. the Interferometric Monitor for Greenhouse gases, IMG, the Tropospheric Emission Spectrometer, TES and the Atmospheric Chemistry Experiment, ACE-FTS) (Clerbaux et al., 2009). The instrument design of IASI resulted from compromises between the meteorology requirements (high spatial coverage) and the atmospheric chemistry needs (accuracy and vertical information for trace gases). IASI is a nadir viewing TIR Fourier transform spectrometer on board the MetOp satellites and measures the radiation emitted from the Earth's surface and absorbed and emitted by the atmosphere in the TIR spectral range, between 645 and 2760 cm^{-1} . IASI-A (on MetOp-A) and -B (on MetOp-B) instruments have been operational since October 2007 and March 2013 respectively. The spectral range was chosen to include the strong absorption features from CO_2 , O_3 , H_2O and CH_4 . Many other molecular absorptions occur within the IASI spectral range, from which the concentration of trace gases are retrieved (e.g. for N_2O , CO , HNO_3 , SO_2 -volcanoes, NH_3 , CH_3OH , ...). In addition, surface and cloud properties are derived from transparent windows. Ozone profiles and the total ozone column are retrieved using an optimal estimation algorithm. IASI shows as positive bias of ~3% for total ozone when compared to Brewer and Dobson measurements. For the vertical profile of ozone, the bias is generally less than 10%, however in the 10-25 km altitude range a positive bias of 10-15% has been reported (Boynard et al., 2016 and references therein).

The Tropospheric Monitoring Instrument (TROPOMI) was launched onboard the Sentinel 5 Precursor in October 2017. Its objective is to provide accurate and timely observations of key atmospheric species for services on air quality, climate and the ozone layer⁴⁴. TROPOMI is a space-borne nadir-viewing hyperspectral imager with four separate spectrometers covering non-overlapping wavelength bands between the ultraviolet and the shortwave infrared (270-320 nm, 320-490 nm, 710-775 nm, 2305-2385 nm) (TROPOMI ATBD, 2017). From the recorded spectra, it is possible to retrieve information on the total column densities and vertical profiles of a number of atmospheric trace gases like NO_2 , O_3 , CH_4 , CO and SO_2 . In addition, information relating to clouds, surface reflectance, and aerosols can be derived. Concerning ozone, TROPOMI provides the total column, the vertical profile and the tropospheric profile.

The Stratospheric Aerosol and Gas Experiments (SAGE II) operated on-board the Earth Radiation Budget Satellite (ERBS) from October 1984 until August 2005 (Damadeo et al., 2013). It uses the sun occultation technique to observe the Sun during sunrises and sunsets. Vertical slant path atmospheric transmission profiles are measured at a 1 km resolution in seven channels between 375 and 1030 nm and are inverted into profiles of ozone (Sofieva et al., 2017). Ozone is inferred primarily from spectral measurements near 600 nm and the resulting high quality profiles have random uncertainty less than 1% in the atmosphere.

⁴⁴ <http://www.tropomi.eu>; visited 17/7/2018

Similar to the aerosol CCI project, the ozone CCI project⁴⁵ is part of the ESA program on global monitoring of essential climate variables. The ozone CCI will develop three main product lines:

1. total ozone from nadir UV backscatter sensors
2. low-resolution ozone profiles from nadir UV backscatter sensors
3. stratospheric and upper-tropospheric ozone profiles from limb and occultation sensors.

During the first phase of the project, the ozone CCI project mostly concentrated on developing and demonstrating improved algorithms and methods, with the aim to define new baselines for the generation of consistent, state of the art and fully characterized long-term ozone data products derived from a complete suite of European nadir and limb-type sensors (Garane et al., 2018). During the second phase, the existing state-of-the-art ozone retrieval algorithms were further developed and applied to long time series of observations from all relevant ESA atmospheric chemistry sensors, with the aim to generate well-characterized and validated ozone data products that meet as closely as possible the GCOS and Climate Modelling User Group requirements. The most important users requirements were identified as (1) homogenized multi decadal records, (2) records with good vertical resolution in the (lower) stratosphere and (3) records with good horizontal resolution in the troposphere.

With respect to total ozone, 22 years of harmonized level-2 data records from GOME, OMI, SCIAMACHY and GOME-2 (A and B) sensors have been produced. The ESA-CCI total ozone Climate Research Data Package (CRDP) includes the level-2 products for each instrument (over the entire instrument lifetime) and a level-3 merged monthly mean gridded data set using GOME and OMI as long-term stability reference.

1.7 Aim of this work

According to IPCC, aerosols are one of the factors contributing to the uncertainties of climate change and their impact is largely determined by their physical and optical properties (IPCC, 2007). One of these optical properties, the Aerosol Optical Depth (AOD) describes the overall extinction of light by aerosols in the atmosphere. The global Brewer network has the potential to become a network for ground-based AOD measurements, making new observations sites available for aerosol monitoring. This is important especially for the satellite community who is always looking for more ground based stations to validate their AOD products.

It has already been shown that AOD can be retrieved from the Brewer direct sun measurements at the ozone wavelengths, but in this work, we will present a new method to retrieve AOD using a different type of measurements of the Brewer instrument. Sun scan measurements between 335 and 345 nm can be convoluted, using the band pass filter of the Cimel sun photometer, to obtain measurements at 340 nm. The advantage of using measurements at 340 nm is that ozone absorption is much lower at this wavelength compared to ozone absorption at the direct sun wavelengths (~306 to ~320 nm), enhancing the intensity at this wavelength. Also, comparison with the CIMEL sun photometer AOD measurements will become more straightforward, since no wavelength interpolation will be needed. The known Beer-Lambert law (section 3.1), which describes the attenuation of a beam of solar

⁴⁵ <http://www.esa-ozone-cci.org/?q=overview>; visited 14/6/2018

light while passing through the atmosphere, can be applied to our Brewer measurements (i.e. the intensity at 340 nm). One of the two unknown parameters in the linear Beer-Lambert equation is the extraterrestrial constant. The Langley Plot method (described in section 3.2) is a frequently used method to determine this constant using ground-based instrumentation and it will be applied here to determine the calibration factor of the instrument (which represents the extraterrestrial constant). A few criteria need to be set to determine the days for which Langley Plots can be created (section 3.2.1). Once the calibration factor is known, the individual AOD values at 340 nm ($\tau_{\text{aer},340}$) can be determined. There are many factors that can lead to uncertainties in the retrieved $\tau_{\text{aer},340}$ values and their possible influences have to be assessed in order to determine the overall uncertainty in $\tau_{\text{aer},340}$. A cloud screening method is needed to remove the influence of clouds from the measurements (section 4). Apart from the uncertainty analysis, the quality of the data can also be assessed by comparing them to quasi-simultaneous and collocated CIMEL $\tau_{\text{aer},340}$ measurements (section 5). A new $\tau_{\text{aer},340}$ time series for Uccle is now available for the 2006-2015 period. A first study of this time series includes an analysis of the weekly, monthly and seasonal behavior.

Within the scientific community, there has been concern about the UV radiation and its adverse effects (e.g. on human health) and it is important to monitor and understand its changes over time. Parameters known to influence UV irradiance at the ground are the global solar radiation, total ozone column and Aerosol Optical Depth and we want to study the relation between these parameters at Uccle to gain a better insight into observed UV changes and to assess possible future changes. The newly developed $\tau_{\text{aer},340}$ time series is not yet long enough to be used for statistical analysis, hence we decide to use the longer $\tau_{\text{aer},320}$ time series, obtained from the direct sun Brewer measurements. Erythemal UV dose, global solar radiation, total ozone column and $\tau_{\text{aer},320}$ data are available at Uccle for the 1991-2015 period. Linear trend analysis will allow us to study the changes of the individual parameters over time. A change point analysis will reveal possible discontinuities (of either instrumental or natural origin) in the time series. Finally, the multiple linear regression technique can be used to determine the individual influence of global solar radiation, total ozone column and $\tau_{\text{aer},320}$ on the erythemal UV dose at Uccle.

2. Instruments and location

In this section, the instruments that provide the measurements used in this work, are presented. Also, general information about the instrument's site is given.

This PhD work uses the sun scan measurements of a Brewer spectrophotometer (section 2.1) to retrieve the AOD at 340 nm ($\tau_{\text{aer},340}$). These values are studied and compared with $\tau_{\text{aer},340}$ values from a CIMEL sun photometer (section 2.2). The Brewer spectrophotometer's total ozone (Q_{O_3}), erythemal UV dose (D_{ery}^*) and $\tau_{\text{aer},320}$ time series are analyzed together with global radiation data (D_g^*) from pyranometers (section 2.3). Sunshine duration data for the cloud screening of $\tau_{\text{aer},340}$ and $\tau_{\text{aer},320}$ data is obtained from pyrheliometers (section 2.4).



Figure 18: Location of our measurement site (i.e. the Royal Meteorological Institute) at Uccle, Belgium⁴⁶.

All instruments are located at Uccle (50°48'N, 4°21'E, 100 m a.s.l., Figure 18), a residential suburb of Brussels about 100 km from the shore of the North Sea. As far as aerosols are concerned, the prevailing meteorological conditions determine whether the station is influenced by sea salt aerosols, by aerosols from urban activity or by continental type of aerosols (De Backer, 2009).

2.1 The Brewer spectrophotometer

Brewer spectrophotometers are a family of scientific instruments, which measure ground level intensities of the attenuated UV radiation in the solar spectrum. The instruments were originally developed in the 1980s to measure total O₃ (and to lesser extent SO₂) in the atmosphere. The retrieval of total column O₃ and SO₂ is inferred by examining the differential absorption of selected wavelengths in the UV-B portion of the spectrum (see Figure 19 for the absorption cross sections of O₃ and SO₂ at the Brewer ozone wavelengths). In addition, accurate spectral profiles of UV radiation in the 286.5 – 363 nm range (for the Mark III Brewer spectrophotometer) are measured. The instrument and its accompanying accessories are manufactured and marketed under license by Kipp&Zonen (Delft, The Netherlands) (Brewer, 1973; Kerr et al., 1988; Brewer MkIII Spectrophotometer Operator's Manual).

⁴⁶ www.googlemaps.com

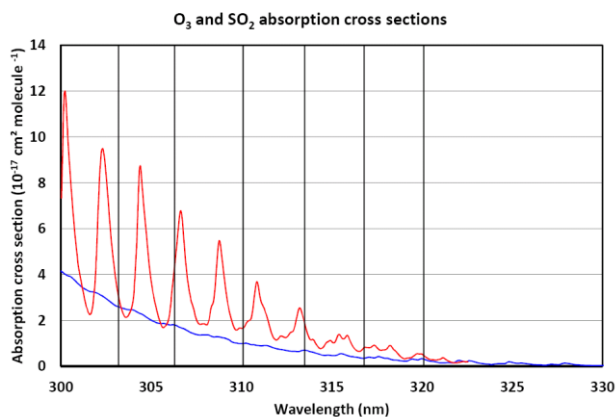


Figure 19 : Absorption cross sections (in $10^{-17} \text{ cm}^2 \text{ molecule}^{-1}$) for O_3 (in blue) and SO_2 (in red). The black vertical lines are positioned at the Brewer ozone measurement wavelengths (i.e. 303.2, 306.3, 310.1, 313.5, 316.8 and 320.1 nm).

For our work we have used the two Brewer spectrophotometers on the roof of the building of The Royal Meteorological Institute of Belgium (RMIB) in Uccle (Figure 20).



Figure 20: The two Brewer spectrophotometers on the roof of the RMIB building at Uccle. The instrument on the left is the double Brewer#178 and the one on the right is the single Brewer#016.

Brewer#016 is a single monochromator Mark II model, which was installed in Uccle in 1983. In 1989, the instrument was equipped with an automated azimuth and zenith pointing system, resulting in a higher observation frequency (Cheymol et al., 2006). The other instrument, Brewer#178, is a double monochromator Mark III, which was installed in September 2001. The most significant difference between a single and double Brewer is the presence of two spectrometers in a double Brewer, which is used to eliminate the stray light inside the instrument. In a single Brewer, a nickel sulfate (NiSO_4) filter is put in place in order to block light from longer wavelengths, but this does not eliminate all stray light. The following description of the Brewer instrument is valid for the double Brewer.

A complete Brewer system (Figure 21) is comprised of a Brewer spectrophotometer, a solar tracking system and computer equipment running Brewer control and data logging software.

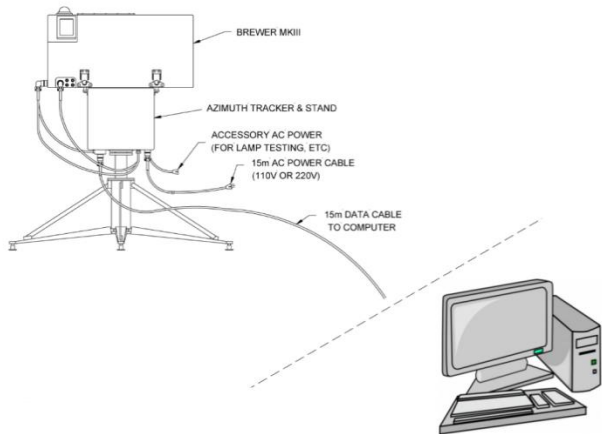


Figure 21: General set-up of a Brewer system (Brewer MkIII Spectrophotometer Operator's Manual) consisting of a Brewer spectrophotometer mounted on a solar tracking system and connected to a computer which runs the control and data logging software.

2.1.1 The spectrophotometer

Table 10: Brewer spectrophotometer MkIII instrument specifications (from Brewer MkIII Spectrophotometer Operator's Manual).

UV wavelengths	303.2 (Hg slit), 306.3, 310.1, 313.5, 316.8 and 320.1 nm
Mercury calibration	302.15 nm
Resolution	0.6 nm in UV
Stability	± 0.01 nm (over full temperature range)
Precision	0.006 ± 0.002 nm
Measurement range	286.5 to 363.0 nm
O₃ measurement accuracy	$\pm 1\%$ (for direct sun total ozone)

The spectrophotometer consists of fore-optics, a monochromator, a photomultiplier, electronics and a power supply (Figure 22).

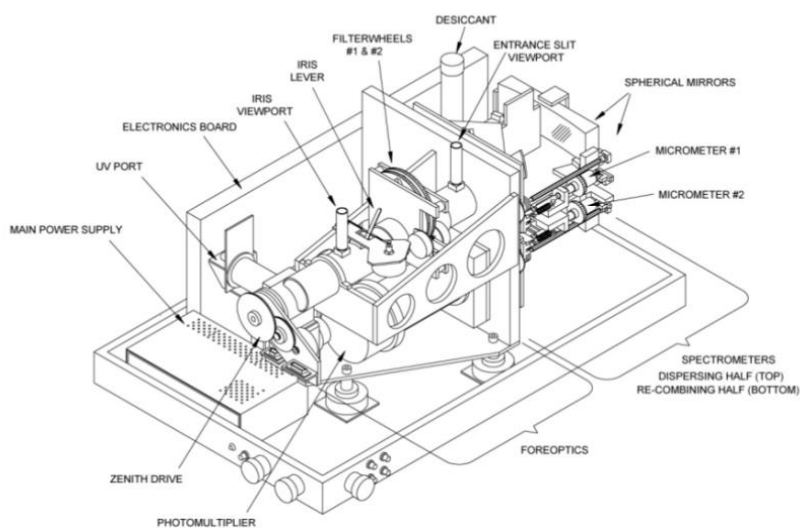


Figure 22: View of a Brewer MkIII with covers removed (Brewer MkIII Spectrophotometer Operator's Manual). It shows the foreoptics, spectrometer, photomultiplier, electronics and power supply.

To be fully flexible in azimuth direction, the Brewer needs to be mounted on an azimuth tracker (Brewer MkIII Spectrophotometer Operator's Manual). The optical assembly of a Brewer spectrophotometer is shown in Figure 23. Some measurement specifics are given in Table 10. The Brewer band pass function (with FWHM equal to 0.6 nm) is presented in Figure 24.

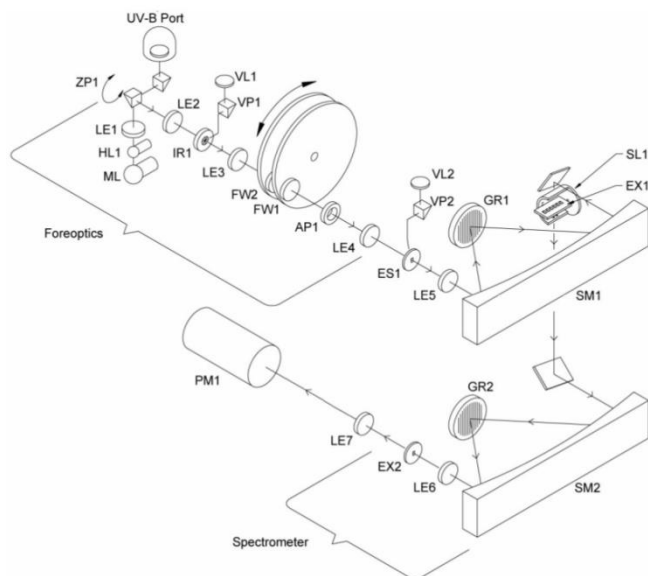


Figure 23: Optical elements of a double Brewer spectrophotometer (Brewer MkIII Spectrophotometer Operator's Manual). ZP1 refers to the zenith prism, HL1 is the quartz-halogen lamp, ML is the mercury discharge lamp and LE1-7 refer to the different lenses. FW1 and FW2 represent the two filter wheels. ES1 is the entry slit through which the light enters the spectrometer. SM1 and SM2 represent the spherical mirrors and GR1 and GR2 are the diffraction gratings of the two spectrometers. SL1 is the slit mask, EX1 and EX2 represent the exit slits and PM1 is the photomultiplier detector.

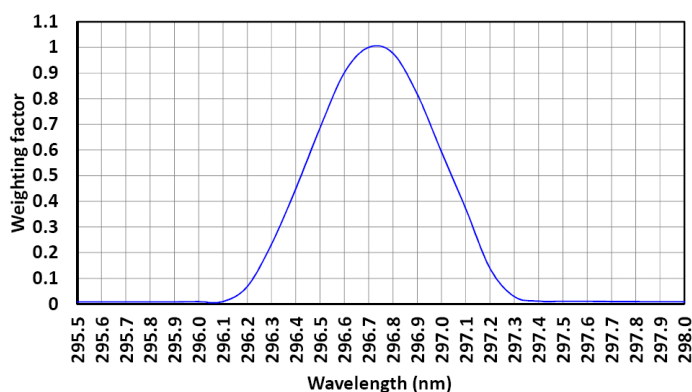


Figure 24 : Brewer band pass function, measured for Brewer#016 during the Calibration and Maintenance of Standards for Spectral UV Measurements (CAMSSUM) campaign in 1994.

The first element of the fore-optics is a reflecting zenith prism (ZP1 in Figure 23). The rotation of the prism allows the instrument to change the zenith angle of the observation (Figure 25). The zenith prism directs incoming light from the Sun, the sky or the test lamps onto the optical axis of the instrument. For zenith angles in the range 0° to 90° , the Sun or sky is viewed through an inclined quartz window. At zenith angle 180° , the spectrometer views the calibration lamps and at -90° the Teflon UV diffuser occupies the FOV.

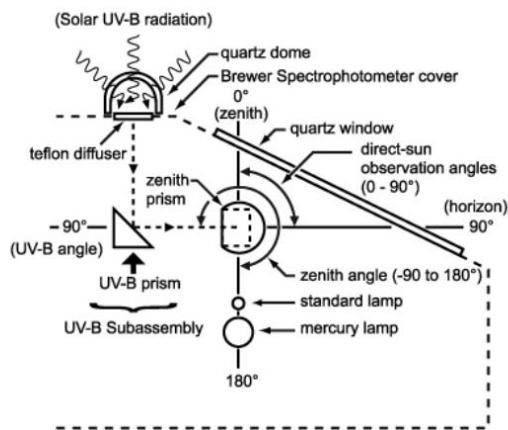


Figure 25: Zenith prism targets (Brewer MkIII Spectrophotometer Operator's Manual). The zenith prism can either select light from the Sun, the sky, the Teflon diffuser or the lamps and direct it onto the optical axis of the instrument.

There are two test lamps in the Brewer instrument. A quartz-halogen lamp (HL1 in Figure 23) provides a well-regulated light source which is used as a reference for sensitivity measurements. Beneath the halogen lamp is a mercury discharge lamp (ML in Figure 23), which provides a line source for wavelength calibration. Two filter wheels (FW1 and FW2 in Figure 23) are mounted in a filter wheel housing and are controlled by two stepper motors. The first filter wheel is used to switch between an open aperture (for moon and UV observations), two film polarizers (for all zenith sky and Umkehr measurements), a ground quartz disk (for direct sun and lamp measurements) and an opaque blank (for dark count measurements). The second filter wheel contains an open aperture and 5 neutral density filters to automatically adjust the light level entering the spectrometer. The monochromator has a vertical entrance slit (ES1 in Figure 23) through which the light enters after which it passes through a convex cylindrical-concave spherical lens (LE5 in Figure 23) that corrects for coma and astigmatic aberrations.

In the first spectrometer, the light is collimated by a spherical mirror (SM1 in Figure 23) onto a diffraction grating (GR1 in Figure 23) where it is dispersed. A second reflection on SM1 focuses the spectrum onto the focal plane of a slotted cylindrical slit mask (SL1 in Figure 23) positioned at the entrance of a second spectrometer. There are six exit slits (EX1 in Figure 23) positioned at the ozone operating wavelengths (303.2, 306.3, 310.1, 313.5, 316.8 and 320.1nm; with 0.6 nm resolution (Figure 24)) and 8 positions on the slit mask (six positions allow each slit to be open while others are blocked, one position blocks all slits for the dark count measurement and one position has two slits open blocking the remaining four used in a linearity test). Following wavelength selection by the slit mask, the light passes through the second spectrometer, where it is recombined and directed onto the exit slit (EX2 in Figure 23) plane. Light passing through the exit slit is collected on the cathode of a photomultiplier detector (PM1 in Figure 23). The photon pulses are amplified, discriminated and divided by 4, before being transmitted to a counter. The resulting photon count is registered in the corresponding wavelength channel.

2.1.2 Direct Sun (DS) ozone measurements

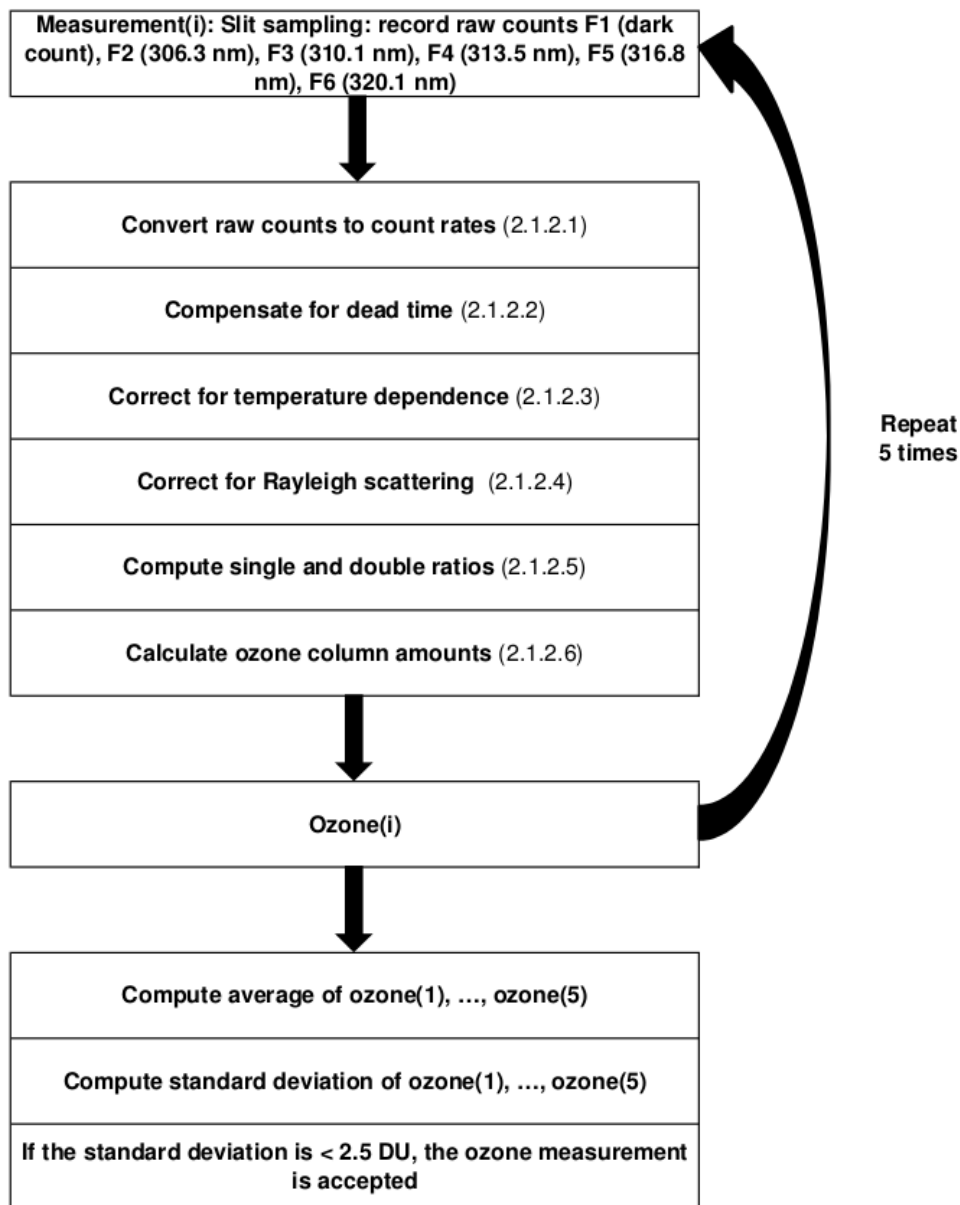


Figure 26 : Brewer DS ozone measurement sequence. One DS ozone observation consists of 5 measurements. One measurement is a set of 20 cycles on the slit mask, during which photon count data F1 to F6 are recorded. After each measurement, ozone is calculated. The final ozone value is the average of the 5 individual ozone values and is accepted only if the corresponding standard deviation is less than 2.5 DU.

During a DS ozone measurement, the Brewer zenith prism (ZP1 in Figure 23) and azimuth tracker are oriented towards the sun, the iris (IR1 in Figure 23) is closed, FW1 is rotated to the ground quartz disk, and FW2 is adjusted for maximum intensity. The measurement sequence is presented in Figure 26. A DS observation consists of five sets of 20 cycles of the slit mask (a measurement), each cycle taking a reading for $2 \cdot 0.14$ seconds on each wavelength. Photon count data for six wavelengths (303.2, 306.3, 310.1, 313.5, 316.8 and 320.1nm), and the dark count, are recorded for each of the five measurements. After each measurement, ozone is

calculated. The procedure is described in more detail in the following subsections (2.1.2.1 to 2.1.2.6). After the fifth measurement, all data is processed, resulting in a single summary set for the total observation. A DS measurement takes slightly more than three minutes to complete.

2.1.2.1 From raw data to count rates

Photon counts are stored in the F_i array. The dark count F_1 , which represents the registered counts without incident light, is subtracted from the operational wavelength counts (F_2 to F_6). After that, the result is scaled to produce count rates C_i in counts per second.

$$C_i = \frac{2 \cdot (F_i - F_1)}{CY \cdot IT} \quad i = 2, \dots, 6 \quad (23)$$

with

F_1 : dark count

F_i : registered counts at 306.3, 310.1, 313.5, 316.8 and 320.1 nm

CY: number of slit mask cycles

IT: integration time, predefined as 0.1147 s

2.1.2.2 Compensating for dead time

The dead time is defined as the time during which the photomultiplier is not able to count a second photon after detection of a first photon. The correction for dead time is required because the photon counting process is non-linear. A photon pulse generated by the photomultiplier has a finite width of about 30 ns. Thus, two or more photons arriving within 30 ns merge into a single pulse, which is generated as one count (Gao et al., 2010).

Poisson statistics are assumed so that for any observation at a true count rate C_0 , the observed count rate will be

$$C = C_0 \cdot e^{-C_0 \cdot T_1} \quad (24)$$

with

T_1 : the dead time of the photon counting system (determined by the dead time test; in s).

This equation is solved for C_0 by iterating nine times⁴⁷ on the expression

$$C_0 = C \cdot e^{C_0 \cdot T_1} \quad (25)$$

This compensation is performed for each of the five operational wavelengths. The dead time compensated count rates are normalized by computing the base-ten logarithm, then scaled by 10^4 , thus allowing integer arrhythmic.

⁴⁷ Fountoulakis et al. (2016b) state that after nine iterations, the expression converges to the corrected signal

2.1.2.3 Compensating for temperature and neutral density filter attenuation

Changes in the internal temperature of the Brewer instrument can affect the electronic, mechanical and optical parts, and subsequently the spectral response of each individual Brewer spectrophotometer (Fountoulakis et al., 2017). The temperature coefficients are determined during the initial calibration and are stored in the Brewer constant's file⁴⁸. If necessary, they can be recalculated by conducting a special test (Savastiouk, 2006) during which the instrument is subjected to a slow warm-up followed by a slow cooling-down, a process which is then repeated. By using the internal halogen lamp as a source of light, the intensities at operating wavelengths are measured regularly to record the instrument response at different temperatures.

The standard Brewer software operates under assumption that the neutral density filters used in the Brewer spectrophotometers attenuate all wavelengths equally. Each of the five neutral density filters has an assigned value that is used to compensate for its attenuation. (Savastiouk, 2006). For both Brewers at Uccle, these values have been determined experimentally (during calibration campaigns) and their values have been stored in the constant's file.

The count rates are corrected for the temperature and neutral filter attenuation dependence as follows:

$$C_{temp,i} = C_i + TC_i \cdot TE + AF_p \quad (26)$$

with

TC_i: the Brewer temperature coefficients (°C⁻¹)

TE: the instrument's temperature (in °C)

AF_p: the attenuation value of the neutral density filters at position p (read from the constant's file)

2.1.2.4 Compensating for Rayleigh scattering

For ozone calculations, the intensity at each slit is compensated for Rayleigh scattering using a universal set of Rayleigh scattering coefficients for all Brewer spectrophotometers, which is hard-coded in the software (Savastiouk, 2006). The values are adjusted according to the instrument location's altitude by the factor of the ratio between the site's normal atmospheric pressure P and the standard atmosphere pressure P_{std}.

$$C_{ray,i} = C_{temp,i} + \frac{\alpha_{R,i} \cdot m_R \cdot P}{P_{std}} \quad (27)$$

with

⁴⁸ Each Brewer spectrophotometer has a file containing the constants needed for operation and calculations. The file contains for example the values of the ozone temperature coefficients (TC_i) for the different slits, the neutral density filter attenuation values, the dead time, ...

- $\alpha_{R,i}$: Rayleigh scattering optical depth of a vertical path through the atmosphere normalized to the standard pressure
- P: the atmospheric pressure at the site of the instrument (a constant value of 1000 hPa is used for Uccle)
- P_{std}: standard atmospheric pressure (1013.25 hPa)
- m_R: the air mass for a layer of height 5 km above the Earth

$$m_R = \sec(\arcsin[k \cdot \sin(\theta_0)]) \quad (28)$$

with:

θ_0 : solar zenith angle

k: R/(R+Z)

R: radius of the Earth (6370 km)

Z: the effective altitude where molecular attenuation⁴⁹ occurs (5 km)

2.1.2.5 Computing single and double ratios

Four sets of single ratios are formed. As $C_{ray,i}$ is in logarithmic form, the ratios are written here as differences:

$$MS_4 = C_{ray,5} - C_{ray,2} \text{ (includes effects of O}_3 \text{ and SO}_2\text{)} \quad (29)$$

$$MS_5 = C_{ray,5} - C_{ray,3} \quad (30)$$

$$MS_6 = C_{ray,5} - C_{ray,4} \text{ (affected predominantly by O}_3\text{)} \quad (31)$$

$$MS_7 = C_{ray,6} - C_{ray,5} \quad (32)$$

Two higher order ratios are formed:

$$MS_8 = MS_4 - 3.2 \cdot MS_7 = -C_{ray,2} + 4.2 \cdot C_{ray,5} - 3.2 \cdot C_{ray,6} \quad (33)$$

$$MS_9 = MS_5 - 0.5 \cdot MS_6 - 1.7 \cdot MS_7 = -C_{ray,3} + 0.5 \cdot C_{ray,4} + 2.2 \cdot C_{ray,5} - 1.7 \cdot C_{ray,6} \quad (34)$$

The constant factors in the above equations were derived for a particular Brewer spectrophotometer to make MS₈ (SO₂ ratio) and MS₉ (O₃ ratio) little dependent on any linear trends in the spectrum while making MS₉ also independent of SO₂ absorption⁵⁰. These constants are currently used in the standard algorithm for calculating O₃ and SO₂ with all Brewer spectrophotometers (Savastiouk, 2006).

⁴⁹ Molecular attenuation is proportional to the number of molecules and the center of mass of the atmosphere (h≈5 km) is considered to be the height of molecular attenuation (Savastiouk & McElroy, 2005)

⁵⁰ Absorbing components in the atmosphere whose absorption is linear with wavelength will have no effect on the calculation of the total ozone column when using the defined weightings.

2.1.2.6 Determining O₃ from DS data

The O₃ amount, MS₁₁, is determined from the logarithms of the counts rates for the four longer wavelengths (i.e. C_{ray,3}, C_{ray,4}, C_{ray,5}, C_{ray,6}):

$$MS_{11} = \frac{MS_9 - B1}{A1 \cdot m_{O_3}} \quad (35)$$

with

MS₉: the double ratios calculated by Eq. 34 involving the wavelengths 310.1, 313.5, 316.8 and 320.1 nm

B1: the extraterrestrial coefficient for the O₃ wavelength, which can be obtained from comparison with a calibrated instrument or from the LPM (Redondas, 2007)

A1: the differential O₃ absorption coefficient for the O₃ wavelength combination (see also Eq. 54 and Eq. 55 in section 3.3.2)

m_{O₃}: the path lengthening factor for an ozone layer of height 22 km

$$m_{O_3} = \sec(\arcsin[k \cdot \sin(\theta_0)]) \quad (36)$$

with:

θ₀: solar zenith angle

k: R/(R+Z)

R: radius of the Earth (6370 km)

Z: the effective altitude where attenuation by ozone occurs: = 22 km⁵¹

2.1.3 UV measurements

The Brewer spectrophotometer is equipped with a UV dome to measure global UV-B using a thin disc of Teflon as a collector. The disc is mounted on top of the instrument under a quartz dome and is exposed to the global UV irradiance. For UV scans, only slit 1 is used (as opposed to ozone measurements where all slits are used). The grating is moved so that UV wavelengths from 286.5 to 363 nm can reach the photomultiplier. In its normal UV routine, the Brewer scans from 286.5 to 363 nm. The integration time is approximately 1 s for each wavelength, the sampling interval is 0.5 nm, and the scan takes about 8 min (Fioletov et al., 2002). The raw counts in the UV file are converted to counts per second and corrected for instrument dead time, dark count⁵² and temperature (similar as for the ozone retrieval). The corrected raw count rates C_λ are then divided by the instrument response values R_λ (Eq. 37):

$$E_\lambda = \frac{C_\lambda}{R_\lambda} \quad (37)$$

⁵¹ Savastiouk & McElroy (2005)

⁵² The average of the counts recorded at wavelengths ≤ 292 nm is subtracted from all other wavelengths to correct for the dark count (noise) and for part of the stray light.

with E_λ the spectral solar irradiance (in $\text{W m}^{-2} \text{nm}^{-1}$) at wavelength λ , C_λ the count rates (in counts s^{-1}) and R_λ the instrument responsivity (in counts $\text{s}^{-1} \text{W}^{-1} \text{m}^2 \text{nm}$). This responsivity is obtained by measuring the response of the Brewer to a source with known radiation (tungsten halogen lamps with a calibration certificate) (Eq. 38):

$$R_\lambda = \frac{C_{lamp,\lambda}}{E_{lamp,\lambda}} \quad (38)$$

with $C_{lamp,\lambda}$ the signal of the lamp (in counts s^{-1}) and $E_{lamp,\lambda}$ the irradiance of the lamp (in $\text{W m}^{-2} \text{nm}^{-1}$).

The spectral erythemal solar UV irradiance (in $\text{W m}^{-2} \text{nm}^{-1}$) ($E_{ery,\lambda}$) is calculated by multiplying Eq. 37 with the appropriate weighting values at each wavelength (CIE action spectrum; Table 5) (Eq. 39):

$$E_{ery,\lambda} = E_\lambda \cdot S_{er}(\lambda) \quad (39)$$

with E_λ the spectral solar irradiance (in $\text{W m}^{-2} \text{nm}^{-1}$) at wavelength λ and $S_{er}(\lambda)$ the CIE erythema reference action spectrum (no units).

The erythemal UV dose rate D_{ery} (in W m^{-2}) is calculated according to Eq. 40:

$$D_{ery} = \int_{250\text{nm}}^{400\text{nm}} E_\lambda \cdot S_{er}(\lambda) \quad (40)$$

From this, the erythemal daily dose D_{ery}^* (in J m^{-2}) can be determined using Eq. 41:

$$D_{ery}^* = \int_{t_{\min}}^{t_{\max}} D_{ery} \cdot dt \quad (41)$$

with t_{\min} and t_{\max} defining the time period over which the daily dose is measured.

The main limitation on the UV measurement performance of the Brewer is the uncertainty in the calibration of the instrument response to radiation at each wavelength⁵³.

2.1.4 AOD retrievals

Cheymol and De Backer (2003) developed a method to retrieve AOD values using the DS measurements at the five ozone wavelengths of the Brewer instrument. It was shown that this method generated good AOD values, comparable to the ones obtained by the CIMEL sun photometer (Figure 27). However, the Brewer and the CIMEL did not provide the AOD at exactly the same wavelength and some extrapolation was needed (Cheymol et al., 2006). The AOD at 320.1 nm ($\tau_{acr,320}$), retrieved from the DS measurements from Brewer#016, are used

⁵³ <http://kipponen-brewer.com/uv/measure-uv-radiation/>; visited on 28/9/17

in section 6 to study the long-term behavior of AOD and its relation to the erythemal UV dose at Uccle.

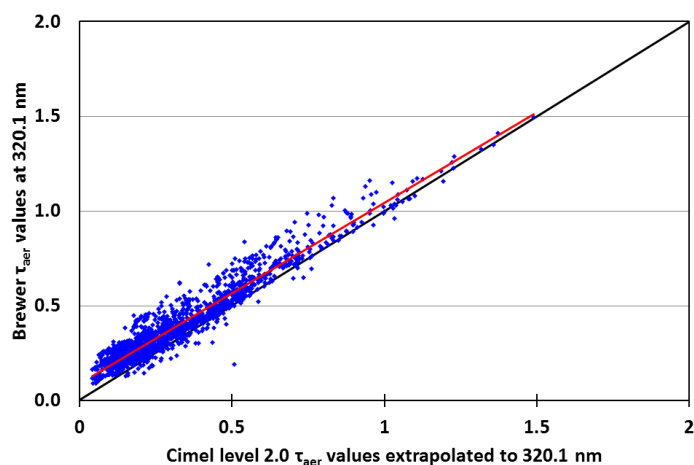


Figure 27 : Comparison of CIMEL level 2.0 τ_{aer} (originally at 340 nm, extrapolated to 320.1 nm using the Angström coefficient between 340 and 440 nm of the CIMEL) and Brewer DS AOD values at 320.1 nm ($\tau_{\text{aer},320}$) for the 1990-2015 period. The Pearson correlation, slope and intercept of the regression line are 0.960, 0.956 ± 0.007 and 0.088 ± 0.003 respectively.

This work presents a new method to derive AOD from Brewer measurements. Instead of using direct sun measurements, the already existing sun scan routine of Brewer#178 is adapted to perform scans between 335 and 345 nm with slit 1 (see Table 11 for differences between DS and SS measurements). The measuring wavelength step of this sun scan routine is 0.5 nm and one scan has a duration of 21 s. The spectral data obtained in this way are convoluted with the band pass function of the CIMEL sun photometer filter (Figure 29) in order to get the intensity at 340 nm. The data of this type, available since 17 August 2006, are then used for the retrieval of AOD at 340 nm ($\tau_{\text{aer},340}$). The Langley Plot Method, described in Cheymol & De Backer (2003), is adjusted (section 3.2) and applied to the sun scan data at 340 nm to generate $\tau_{\text{aer},340}$. The stability of the Brewer#178 wavelengths has been examined and the results show that the stability of this instrument is very good (Gröbner et al., 2006). This can be seen as a first justification of the application of the Langley Plot Method on the sun scan measurements of Brewer#178 for the retrieval of $\tau_{\text{aer},340}$. A more detailed discussion on the application of the LPM and the stability of the calibration factors is provided in section 3.2.

Table 11 : Comparison of the direct sun and sun scan measurements of the Brewer spectrophotometer

Direct sun measurements	Sun scan measurements
Zenith prism towards the sun	Zenith prism towards the sun
Iris closed	Iris closed
FW1 : ground quartz disk	FW1 : ground quartz disk
FW2 to select maximum intensity	FW2 to select maximum intensity
Wavelength selection using rotating slit mask Grating is fixed	Measurements taken over slit 1 Wavelength selection by moving the grating
Measurements at discrete wavelengths: 306.3, 310.1, 313.5, 316.8 and 320.1 nm	Measurement is a scan from 335 to 345 nm with a 0.5 nm increment

2.1.5 Calibration history

The calibration of the Brewer instrument comprises several checks of wavelength settings and relative instrument sensitivity at different wavelengths. In addition, each instrument must be calibrated at intervals of several years relative to a highly stable standard instrument to ensure the correctness of the extraterrestrial constants used with the instrument at different wavelengths at which the observations are made. Brewer#016 and #178 are calibrated with 50 W tungsten halogen lamps on a monthly basis and with 1000 W lamps during less frequent but regular intercomparisons (see Table 12). The instruments were also compared with the traveling QUASUME (Quality Assurance of Spectral UV Measurements in Europe) unit in 2004 (Gröbner et al., 2006).

Table 12 : Dates of intercomparison campaigns of the Brewer spectrophotometers at Uccle. For the first three calibration periods of Brewer#016, the specific dates are not known.

Intercomparison campaigns	
Brewer #016	Brewer #178
March 1989	
September 1994	
September 2001	
25/05/2003-30/05/2003	
14/05/2006-20/05/2006	
26/05/ 2008-30/05/2008	
10/05/2010-18/05/2010	
13/08/2012-17/08/2012	
25/04/2014-29/04/2014	
04/08/2016-09/08/2016	

2.2 The CIMEL sun photometer



Figure 28: CIMEL sun photometer at Uccle.

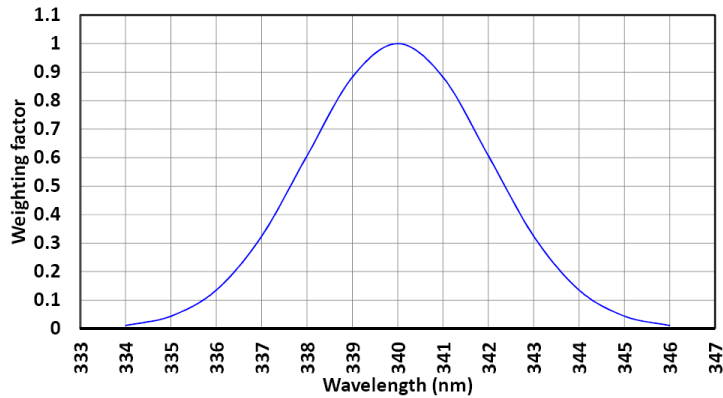


Figure 29 : CIMEL band pass filter with a FWHM of 4.756 nm (standard CIMEL sun photometer filter values; Barr Associates Inc.).

The CIMEL sun photometer (Figure 28), used in this study, belongs to the Belgian Institute of Space Aeronomy (BISA) and is located at approximately 100 m from the Brewer instrument. CIMEL sun photometers are automatic-tracking sun and sky scanning radiometers that make direct sun measurements with a 1.2° FOV at least every 15 minutes at 340, 380, 440, 500, 675, 870, 940 and 1020 nm. The direct sun measurements take 8 s to scan all eight wavelengths, with a motor-driven filter wheel positioning each filter in front of the detector. A sequence of three measurements taken 30 s apart are made resulting in three measurements at each wavelength within a 1 minute period. These solar extinction measurements are then used to compute AOD at each wavelength except 940 nm, which is used to retrieve precipitable water. The band pass filter of the CIMEL, which is used to convolute the Brewer sun scan measurements, is presented in Figure 29. The instruments are part of the AERONET global network (Holben et al., 2001). The accuracy of the AERONET AOD measurements at 340 nm is 0.02 (Eck et al., 1999). More detailed information on the CIMEL instrument can be found in Holben et al. (1998).

2.3 Pyranometer



Figure 30 : Pyranometer (CM11; Kipp&Zonen) at Uccle.

The pyranometer CM11 (Figure 30) is designed for measuring the irradiance on a plane surface, which results from the direct solar radiation and from the diffuse radiation incident from the hemisphere above (CM11 Operator's Manual). The pyranometer is a thermal sensor,

which converts the incoming radiation absorbed at the front side of the sensor into heat. The arising temperature difference between the front side and the back side, which is coupled to the ambient temperature, is measured by a thermo-coupling device and yields a voltage, which is proportional to the irradiation (Geuder et al., 2003). The rise of temperature is affected by wind, rain and thermal radiation losses to the environment. Therefore the detector is shielded by two glass domes. Glass domes allow equal transmission of the direct solar component for every position of the Sun on the celestial sphere (CM11 Operator's Manual).

2.4 Pyrheliometer

A pyrheliometer (Figure 31) is an instrument designed specifically to measure the direct beam solar irradiance with a FOV limited to 5° , also known as direct normal incidence (CH-1 pyrheliometer Operator's Manual). The 5° FOV is achieved by shaping the collimation tube with precision apertures and by the design of the detector. The front aperture is fitted with a quartz window to protect the instrument and to act as a filter that passes solar radiation between 200 and 4000 nm in wavelength. Pyrheliometers include a rain shield and integrated alignment aids. The sunshine duration measurements from the pyrheliometers in Uccle, are used for the cloud screening of the Brewer $\tau_{\text{aer},320}$ and $\tau_{\text{aer},340}$ values. According to WMO (1990)⁵⁴, sunshine duration during a given period is defined as the sum of the time for which the direct solar irradiance exceeds 120 W m^{-2} . Sunshine duration is expressed in seconds or hours.



Figure 31 : Pyrheliometer (model CH-1, Kipp&Zonen) at Uccle.

⁵⁴ Recommended by the Commission for Instruments and Methods of Observation at its tenth session (1989) through Recommendation 16

3. AOD retrieval method using sun scan Brewer measurements

Previous studies have already shown that AOD can be retrieved from Brewer spectrophotometers using their DS measurements at 306.3, 310.1, 131.5, 316.8 and 320.1 nm (e.g. Cheymol & De Backer, 2003). The novelty of the current study lies in the use of a different type of measurement for the retrieval of AOD. Indeed, instead of DS measurements, SS measurements (from 335 to 345 nm and convoluted using the CIMEL band pass filter to 340 nm; Figure 29) are used in this study. Retrieving the AOD at this wavelength allows for a better comparison with the collocated CIMEL sun photometer as an extrapolation from CIMEL to Brewer wavelengths is no longer needed (De Bock et al., 2010). Also, the signal to noise ratio is improved due to the lower absorption by ozone at 340 nm, increasing the intensity at this wavelength.

3.1 The Beer-Lambert law

The Beer-Lambert law was already discussed in section 1.2.2.4 and a generic expression for it was provided by Eq. 12. It describes the extinction of monochromatic radiation at a certain wavelength λ and can also be written as follows

$$I(\lambda) = I_0(\lambda) \exp(-m \cdot \tau_\lambda) \quad (42)$$

where $I(\lambda)$ is the radiation intensity (in $\text{W sr}^{-1} \text{m}^{-2}$), measured at the ground, after passing through a plane homogeneous layer over a relative optical path length m . $I_0(\lambda)$ is the initial radiation intensity before passing through the layer (in $\text{W sr}^{-1} \text{m}^{-2}$) and τ_λ is the total optical thickness at wavelength λ . This general equation can be applied to UV radiation from the Sun as it propagates through the atmosphere and reaches the ground where it is measured by the Brewer spectrophotometer (in our case through sun scan measurements). While passing through the atmosphere, the radiation of the Sun is subject to absorption and scattering through three different physical phenomena: (a) absorption by gases and for the wavelengths specific of the Brewer, this is ozone, (b) scattering by air molecules (Rayleigh scattering) and (c) extinction by aerosol particles. Eq. 42 can be applied to the signal received by the Brewer spectrophotometer (i.e. intensity at 340 nm) in the following manner:

$$S(\lambda) = K(\lambda) \cdot I_0(\lambda) \exp \left[-m_{O_3} \cdot \alpha_{O_3}(\lambda, T) \cdot Q_{O_3} - m_R \cdot \alpha_R(\lambda) \frac{P}{P_{std}} - \sec(\theta_0) \cdot \tau_{aer,340} \right] \quad (43)$$

with

$S(\lambda)$: the signal measured by the Brewer spectrophotometer at wavelength λ (in counts s^{-1})

$K(\lambda)$: a proportionality factor accounting for the instrument's response to the incoming solar radiation at wavelength λ ($\text{counts s}^{-1} \text{W}^{-1} \text{sr m}^2$) (i.e. what the

	instrument will measure in photon counts when radiation of a certain intensity reaches the instrument)
$I_0(\lambda)$:	the intensity outside the Earth's atmosphere at wavelength λ (in $\text{W sr}^{-1} \text{m}^{-2}$)
m_{O_3} :	the relative optical air mass (the path length relative to that at the zenith at sea level) of the ozone layer at a height of 22 km
$\alpha_{O_3}(\lambda, T)$:	the ozone absorption coefficient (in m^{-1}) at wavelength λ and temperature T
Q_{O_3} :	the equivalent thickness of the ozone layer (in DU)
m_R :	the relative optical air mass of the atmosphere in a thin layer assumed to be at an altitude of 5 km for Rayleigh scattering
$\alpha_R(\lambda)$:	Rayleigh scattering optical depth at wavelength λ of a vertical path through the atmosphere normalized to the standard pressure P_{std} (determined with the formula from Kneizys et al. 1980; Eq. 57).
P_{std} :	the standard pressure (1013.25 hPa)
P :	the station pressure (a constant value 1000 hPa is used for Uccle)
θ_0 :	the zenith angle of the Sun
λ :	wavelength; equal to 340 nm
$\tau_{\text{aer},340}$:	the aerosol extinction optical thickness at 340 nm of a vertical path through the atmosphere

When considering the absorption of gases, only ozone absorption is taken into account. The SO_2 and NO_2 absorption are not considered here, since they are very low compared to the O_3 absorption term, which is already small at 340 nm. The effect of not including them is further discussed in sections 3.3.4 and 3.3.5.

To eliminate the dependence of the $\tau_{\text{aer},340}$ retrieval on the effective ozone temperature, the ozone absorption coefficient $\alpha_{O_3}(\lambda, T)$ is computed using the effective ozone temperature T_{eff} as in Cheymol and De Backer (2003), thus accounting for the natural intra-annual variability of the stratospheric temperature. This effective ozone temperature is defined as the integral over altitude of the ozone-profile-weighted temperature (Eq. 44) and is calculated using ozone and temperature profiles from balloon soundings available at Uccle:

$$T_{\text{eff}} = \frac{\int_0^{\text{top}} T(z) O_3(z) dz}{\int_0^{\text{top}} O_3(z) dz} \quad (44)$$

with $T(z)$ the vertical temperature profile and $O_3(z)$ the vertical ozone profile.

Since the sun scans are convoluted with the CIMEL sun photometer band pass filter, we should (in theory) also convolute the Rayleigh scattering and the ozone absorption coefficients. The convolution was done for the Rayleigh scattering term and this caused only a small change in the retrieved $\tau_{\text{aer},340}$ values with a maximum difference of $\approx 2 \cdot 10^{-4}$ with respect to $\tau_{\text{aer},340}$ values calculated without a convoluted Rayleigh term. Since the contribution of the ozone absorption term to the computation of the $\tau_{\text{aer},340}$ values is very low compared to the Rayleigh contribution, we did not convolute the ozone absorption coefficient. This would lead to negligible changes in the $\tau_{\text{aer},340}$.

3.2 The Langley Plot Method

Langley extrapolation can be used to estimate the solar intensity at the top of the atmosphere I_0 (i.e. the Extra Terrestrial Constant = ETC) with ground-based instrumentation (Marenco, 2007). With this method, the effect of atmospheric attenuation is accounted for by observing the variation of ground-level direct sun intensity I when the air mass factor m varies during a morning or afternoon. On the assumption of a constant atmospheric total optical depth τ , the plot of $\ln(I)$ versus m is a straight line and its y-intercept represents $\ln I_0$:

$$\ln I(\lambda) = \ln I_0(\lambda) - m\tau_\lambda \quad (45)$$

As stated in Eq. 22, the total optical depth τ_λ in Eq. 45 is the sum of the aerosol (τ_{aer}), Rayleigh (τ_R), ozone (τ_{O_3}), SO_2 (τ_{SO_2}) and NO_2 (τ_{NO_2}) optical depths. Taking the logarithm of Eq. 43 gives Eq. 46 :

$$\ln[S(\lambda)] + m_{O_3} \cdot \alpha_{O_3}(\lambda, T) \cdot Q_{O_3} + m_R \cdot \alpha_R(\lambda) \frac{P}{P_{std}} = \ln[K(\lambda)I_0(\lambda)] - \tau_{aer,340} \sec(\theta_0) \quad (46)$$

Let us define:

$$Y = \ln[S(\lambda)] + m_{O_3} \cdot \alpha_{O_3}(\lambda, T) \cdot Q_{O_3} + m_R \cdot \alpha_R(\lambda) \frac{P}{P_{std}} \quad (47)$$

$$CF = \ln[K(\lambda)I_0(\lambda)] \quad (48)$$

With Eqs. 47-48, Eq. 46 can be simplified to a linear equation:

$$Y = CF - \tau_{aer,340} \cdot \sec(\theta_0) \quad (49)$$

Now, one AOD value ($\tau_{aer,340}$) and one calibration factor (CF) can be estimated per day by determining respectively the slope and intercept for each individual Langley Plot (Figure 32).

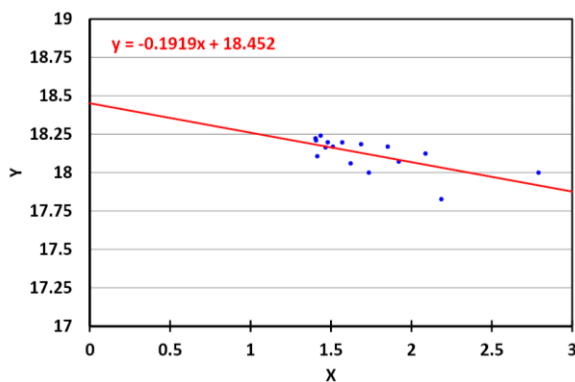


Figure 32 : Example of a Langley Plot (for 06/09/2006). The X-axis represents $\sec(\theta_0)$. The slope and intercept of the regression line are respectively $-\tau_{aer,340}$ and CF.

Physically, the calibration factor represents the extraterrestrial constant. By applying this method, $\tau_{\text{aer},340}$ is essentially determined as the residual of $\tau_{\text{aer},340} = \tau_{\text{tot},340} - \tau_{\text{R},340} - \tau_{\text{O}_3,340} - \tau_{\text{NO}_2,340} - \tau_{\text{SO}_2,340}$ (with $\tau_{\text{NO}_2,340}$ and $\tau_{\text{SO}_2,340}$ not considered here).

3.2.1 Selection of cloudless days

The quality of the linear regression depends on the range of the solar zenith angles covered during a certain day. Ideally, observations at both high and low solar zenith angles are needed, the atmospheric conditions (both the AOD and O_3) must remain stable over the day and clouds cannot be present (i.e. Gröbner & Meleti, 2004). This leads to different criteria for the selection of the days on which the LPM can be applied (i.e. Calibration quality Clear Days (CCD)). Cheymol et al. (2009) proposed the following criteria (for DS measurements):

1. The individual DS data for which the air mass is above 3 are removed
2. The range of solar zenith angles covered by valid DS observations for one day must be at least 20° .
3. The number of individual DS data must be at least 50 per day (i.e. 10 sequences of 5 measurements).
4. The total ozone column is retrieved for each measurement. For a set of 5 measurements, the average and standard deviation are computed (see section 2.1.2). Only sets with a standard deviation less than 2.5 DU are accepted.

Since in our case SS are used instead of DS measurements, these criteria have to be adapted. The test done on the ozone values (4th criterion) loses its significance since the DS ozone observations of Brewer#178 and the SS between 335 nm and 345 nm are not performed simultaneously. In this way, the presence of a DS ozone observation with a standard deviation less than 2.5 DU, made under cloudless circumstances, close (in time) to a SS measurement does not guarantee that this SS measurement was not influenced by clouds. Concerning the 2nd criterion, it has to be mentioned that the same SZA range can yield different ranges of air mass for different seasons. Since air mass range is a more important parameter for the quality control of the Langley Plots, the second criterion was changed so that a minimum range limit was placed on the optical air mass instead of on the SZA range. We retain the upper value of 3 for the air mass (1st criterion), since at higher air masses the intensities measured by the Brewer become much lower and the instrument becomes much more sensitive to stray light effects. This could thus bias the $\tau_{\text{aer},340}$ measurements. The remaining criterion (3) is applied to the SS instead of to DS measurements.

Manually verifying whether the selected days are indeed cloudless shows that these criteria are not sufficient. This is expected as the 4th criterion of Cheymol et al. (2009) (based on the standard deviation of ozone), which was there to filter out clouds, is removed. An additional criterion is therefore proposed. It is based on the ratio of the observed and expected intensity for a certain day. The observed intensity is obtained from the sun scans between 335 and 345 nm which are convoluted with the band pass function of the CIMEL sun photometer filter. The expected intensity (under cloudless circumstances) is calculated by the Tropospheric Ultraviolet and Visible Radiation Model (TUV model version 3.0; Madronich, 1993), which

uses the band pass function of the CIMEL sun photometer filter at 340 nm. The climatological monthly mean total ozone value and a default constant $\tau_{\text{aer},340}$ value (0.7777 as a standard value for polluted air as defined in the TUV program) are used as input parameters for the calculation of the monochromatic radiative transfer. The cloud optical depth and surface albedo are respectively set at 0 and 0.05. The ratio between the measured and simulated intensities $I_{\lambda}/I_{\lambda}^{\text{TUV}}$, is then calculated. For the calculation of the ratio, both the observed and the expected intensities are normalized to their maximum⁵⁵. Figure 33 shows the diurnal evolution of this ratio for a cloudless and for a cloudy day.

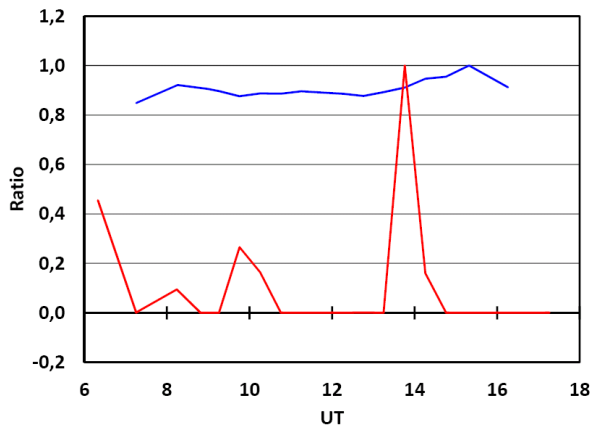


Figure 33: Ratio of the observed and expected intensity for a cloudless (5 August 2007; in blue) and for a cloudy (20 July 2008; in red) day at Uccle. The points that appear as null values are points for which the ratio is very small. This can be explained by the influence of clouds, which causes the observed intensity to be very low.

For clear days with stable atmospheric conditions, the ratio of the observed and expected intensity should be more or less constant throughout the day and close to 1. In this context, a day is considered cloudless if the maximum deviation of the individual ratios (of a day) from the mean ratio is smaller than 20% (different threshold values were tested, but the 20% value generated the best results, meaning that the selected cloudless days were in agreement with the observed cloudless days).

This leads to the following set of new criteria for the selection of CCD for the determination of the calibration factors with the LPM:

1. The sun scans for which the air mass is above 3 are removed.
2. The range of air masses covered by the sun scans for one day must be at least 1.
3. At least 10 sun scans per day have to remain after applying the first two criteria.
4. The maximum deviation of the individual ratios (of the observed and expected intensity) from the mean ratio for a certain day has to be smaller than 20%.

After applying these criteria, the calibration coefficients CF are calculated for each CCD (Table 13). Only 33 days out of a possible 3389 days (~1%) are selected as CCD as a result of the very strict criteria.

⁵⁵ i.e. the values are divided by the maximum value for that day

Table 13: List of calibration quality clear days and the individual CF for those days (for the 2006-2015 period).

DATE	CF	DATE	CF	DATE	CF	DATE	CF
20060906	18.32	20080511	18.54	20120723	18.53	20140416	18.50
20060921	18.27	20080701	18.56	20120810	18.56	20150630	18.69
20070404	18.42	20090815	18.47	20120908	18.54	20150710	18.71
20070422	18.44	20100310	18.43	20120909	18.35		
20070430	18.49	20100603	18.46	20130304	18.45		
20070501	18.36	20100922	18.33	20130420	18.44		
20070502	18.55	20101010	18.54	20130801	18.54		
20070805	18.51	20110521	18.34	20130905	18.47		
20080505	18.47	20110602	18.52	20140306	18.23		
20080508	18.52	20120315	18.40	20140309	18.33		

3.2.2 Stability of the Calibration Factors

The LPM selects CCDs that are used to determine the overall average CF of the instrument, which in turn is used to determine the individual $\tau_{aer,340}$ values for all available sun scan measurements using Eq. 50:

$$\tau_{aer,340} = \frac{CF - Y}{\sec(\theta_0)} \quad (50)$$

The variability in the CF, which for the largest part is caused by changes in the responsivity of the Brewer instrument ($K(\lambda)$), is studied here. As time passes and our time series becomes larger, the amount of available CCDs increases and the calculated CF changes. Table 13 shows the individual CCDs and their CF for the period 2006-2015. After an initial period with only a few CCDs, the average CF becomes more stable as the amount of CCDs increases. The average CF for the entire period is 18.46 and the standard deviation is equal to 0.11. The average CF did not change by more than 0.02 over the last 24 CCDs (after May 2008).

Instead of calculating an average CF for the entire period, we have also evaluated the possibility of using a moving average filter (with a length of 3 year; length empirically determined) to determine the CF that will be used in Eq. 50. This means that each year will have a different CF (instead of just one for the entire period) which allows a better tracking of both instrumental and environmental changes. The CF calculated in this way can be found in Table 14 and the CF of both methods (together with their standard deviation) are presented in Figure 34.

The $\tau_{aer,340}$ calculated using the average CF method and the moving average method have been compared to quasi simultaneous CIMEL level 2.0 data. The correlation coefficient, slope and intercept of the regression lines are quasi the same for both methods. In 51% of the cases we find that the moving average method gives a better agreement with CIMEL Level 2.0 values. From these results, it is hard to determine which of the two methods is better. However, based on the fact that the moving average method is better suited to take some instrumental changes into account, it is preferred to use this method to determine the CFs of the instrument. The comparison between the $\tau_{aer,340}$ from the Brewer retrieved in this work and the CIMEL is

described in Section 5.1. From Figure 34 and Table 13, it can be seen that the last two individual CF values (both in 2015) differ quite substantially from the previous ones. This could be the result of changes made during the calibration in April 2014 (such as increasing the high voltage of the photomultiplier). In this case, it might not be interesting to calculate the moving average using individual CF values from before and after the calibration. For this reason, we have decided to treat the last 3 years of data as preliminary data and propose that the CF be re-evaluated once the next series of individual calibration factors is known. In this way, it can be decided whether or not the outliers of 2015 are a result of calibration. Another possibility could be to determine a CF for each period between two calibrations. This can be part of future work.

Table 14: CF calculated using a moving average filter (based on 3 years).

Year	Moving average CF	Standard deviation
2006	18.42	0.10
2007	18.45	0.09
2008	18.48	0.06
2009	18.48	0.07
2010	18.44	0.08
2011	18.45	0.09
2012	18.47	0.08
2013	18.45	0.10
2014	18.49	0.15
2015	18.49	0.21

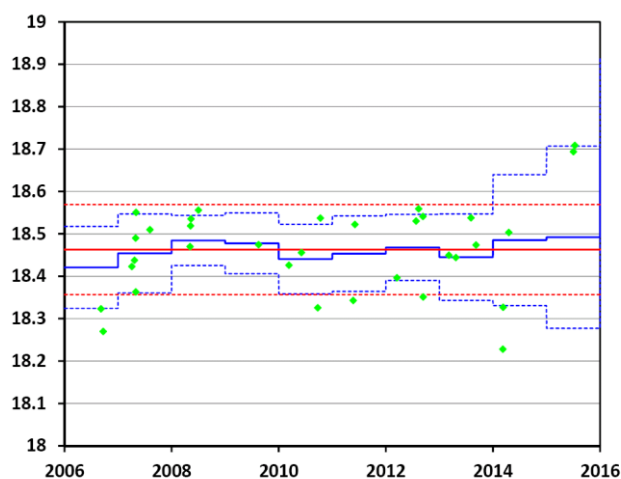


Figure 34: The individual CF (on the Y-axis) of the cloudless days are shown in green. The red solid line represents the average CF, calculated from the individual CF and the blue solid line shows the yearly CF calculated using a 3 year moving average. The dotted lines represent the standard deviation of the average CF (in red) and the moving average CF (in blue).

The CF should be as accurate as possible as an error in CF directly affects the calculated $\tau_{\text{aer},340}$. The relationship between a change in CF and the related change in $\tau_{\text{aer},340}$ can be described by Eq. 51 and is shown in Figure 35.

$$\Delta\tau_{aer,340} = \frac{\Delta CF}{airmass} \quad (51)$$

It is obvious from Eq. 51 and Figure 35 that the lower the air mass, the larger the effect on the retrieved $\tau_{aer,340}$ of a change in the calibration factor. For instance, at an air mass of 1, an error of 0.1 in the calibration factor causes an uncertainty of 0.1 in the calculated $\tau_{aer,340}$ (Figure 35). At an air mass of 3, this uncertainty decreases to around 0.033. Note that 75% of the $\tau_{aer,340}$ values between 2006 and 2015 were measured at air mass values between 1 and 2 (Figure 36). So for the lower $\tau_{aer,340}$ values within a period with a higher standard deviation in CF, there could be a considerably larger uncertainty in the $\tau_{aer,340}$.

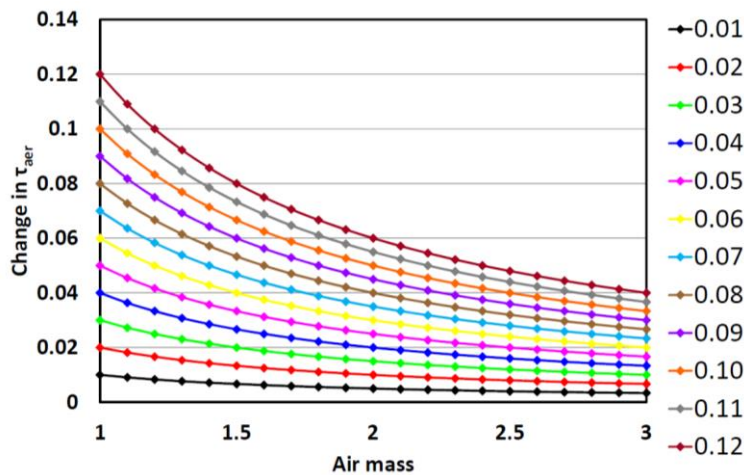


Figure 35 : Change in $\tau_{aer,340}$ at different air masses for different changes in Calibration Factor (represented by the different colors).

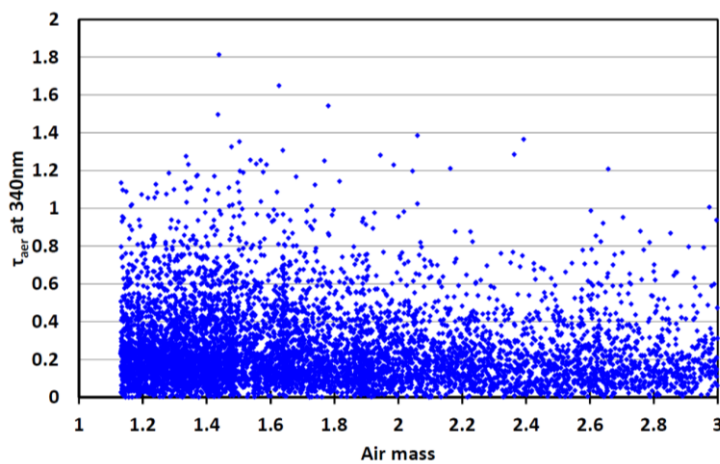


Figure 36 : Distribution of observed $\tau_{aer,340}$ between 2006 and 2015 over different air masses.

3.2.3 Basic requirements for the Langley Plot Method

Arola & Koskela (2004) state that there are four requirements that need to be fulfilled in order to allow the application of the LPM:

1. Direct radiation from the Sun is needed. This is not precisely the case, as diffuse radiation can enter the instrument's finite FOV. The magnitude of the effect depends on the FOV, the wavelength and the SZA. The Brewer FOV is 2.6° , which corresponds with a solid angle of $\sim 0.0257\%$ of the full hemispheric solid angle of 2π . This is not a very large fraction, however when the SZA (and the air mass) increases, the ratio of direct versus diffuse radiation strongly decreases and even a relatively small portion of diffuse radiation entering the FOV could already alter the Langley Plot. In this work, we consider the effect of diffuse radiation entering the Brewer's FOV reduced, as an upper air mass limit of 3 is used and our measurements are at a slightly higher wavelength in the UV (compared to the DS ozone wavelengths). As the wavelength increases, a smaller portion of the global radiation is received as diffuse radiation.
2. Monochromatic intensity is required. This is not exactly the case, as the Brewer measures through a slit function with FWHM of 0.6 nm (see Figure 24). This can cause a problem for the lower UV wavelengths where the ozone absorption changes rapidly and a small error in wavelength would result in a big change in ozone absorption coefficient, hence influencing the calculated AOD value. In this work, sun scan measurements between 335 and 345 nm are used and in this spectral region, the ozone absorption is negligible so we can consider the spectral resolution of 0.6 nm sufficiently high not to cause any problems.
3. The extraterrestrial conditions need to be stable, but this is naturally always the case.
4. The atmospheric conditions need to be constant, which is especially a challenge for urban locations. According to many authors (e.g. Diémoz et al., 2016, Terez and Terez, 2003), in situ Langley Plot ETC interpolation is fully reliable only at pristine and high altitude sites. At other sites, a long-term analysis of the data record on site should be performed (Diémoz et al., 2016), which is what is done at Uccle where the overall CF is determined using the long time series of individual CF.

3.3 Sources of uncertainty

As stated in section 3.2, $\tau_{aer,340}$ is calculated as the residual of the following equation:

$$\tau_{aer,340} = \tau_{tot,340} - \tau_{R,340} - \tau_{O_3,340} - \tau_{NO_2,340} - \tau_{SO_2,340} \quad (52)$$

Therefore, it is very important that all the individual components that compose the total optical depth are accurate. In the following section, the most important sources of uncertainty in the calculation of the $\tau_{aer,340}$ will be addressed.

3.3.1 Earth-Sun distance

A correction for the Earth-Sun distance has been included in our calculations, so this source of uncertainty does not apply to this research.

3.3.2 Uncertainties in the ozone term

The ozone term in the original equation is:

$$m_{O_3} \cdot \alpha_{O_3}(\lambda, T) \cdot Q_{O_3} \quad (53)$$

with

- m_{O_3} : ozone air mass
- $\alpha_{O_3}(\lambda, T)$: ozone absorption coefficient (in m^{-1})
- Q_{O_3} : equivalent ozone thickness (in DU)

From the above, it seems that the first component that can lead to uncertainty in the $\tau_{aer,340}$ retrieval is the equivalent ozone thickness, which is taken from the Brewer measurements. These measurements are known to have a 1% uncertainty or less (Fountoulakis et al., 2016a). In order to estimate the uncertainty propagating via an error on Q_{O_3} , the amount of ozone in the retrieval algorithm was changed with 1%. It was found that this had very little influence on the $\tau_{aer,340}$ values (Table 15). The observed maximum absolute changes were equal to $1.6 \cdot 10^{-4}$ and the absolute median value is about $6 \cdot 10^{-5}$, which is very low compared to the actual $\tau_{aer,340}$ values. Only for a few very small $\tau_{aer,340}$ values (< 0.02), the relative difference in the $\tau_{aer,340}$ is higher than 2% (Figure 37).

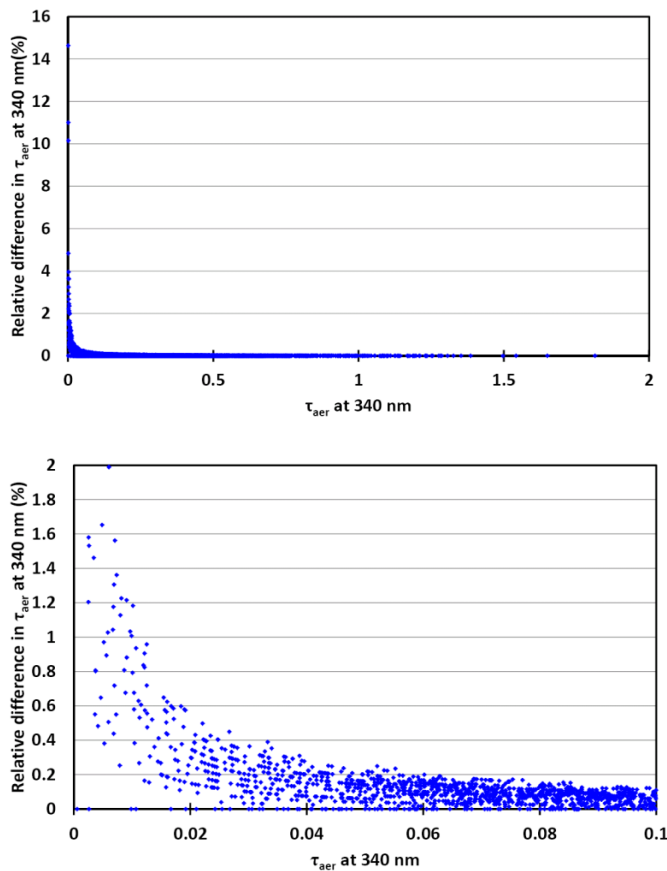


Figure 37 : Effect on the $\tau_{aer,340}$ of adding 1% to the total ozone amount. The figure on top shows the effect for all $\tau_{aer,340}$ values, whereas the figure on the bottom zooms in on $\tau_{aer,340}$ lower than 0.1 and limits the relative difference to 2%.

Another factor that might induce some uncertainty in the retrieved $\tau_{\text{aer},340}$ values is the height of the ozone layer that is used in the formula to determine the ozone air mass m_{O_3} . It is assumed to be constant at 22 km as described in section 2.1.2.6, whereas in reality, this value can fluctuate on a seasonal basis. In order to quantify this effect, we chose to investigate the influence on the $\tau_{\text{aer},340}$ of using an ozone height of 20 and 25 km (Table 15). As for the ozone thickness, we find a very small impact of the ozone air mass on the retrieved $\tau_{\text{aer},340}$ values. The absolute maximum difference in $\tau_{\text{aer},340}$ is equal to $1.2 \cdot 10^{-4}$ and $1.5 \cdot 10^{-4}$ for 20 and 25 km height respectively and the median values are also very low ($1 \cdot 10^{-5}$ and $-4 \cdot 10^{-5}$ respectively). Again, only for the $\tau_{\text{aer},340}$ values below 0.02 the relative difference becomes non-negligible, i.e. higher than 2%.

As mentioned in the literature (Arola & Koskela, 2004), the stratospheric effective ozone temperature should be used when calculating the ozone absorption coefficient $\alpha_{\text{O}_3}(\lambda, T)$ as this could otherwise also contribute to the $\tau_{\text{aer},340}$ uncertainty. The stratospheric effective ozone temperature is the convolution between the air temperature profile and the ozone profile (Cheymol & De Backer, 2003; Eq. 44). In the algorithm we have used, the effective ozone temperature is calculated using the information from the ozone soundings, performed three times a week at Uccle since 1969. Using this temperature (T_{deg}) and the Bass & Paur (1985) quadratic coefficients C_0 , C_1 and C_2 , the ozone cross section σ_{O_3} (in $\text{cm}^2 \text{ molecule}^{-1}$; Eq. 54) and ozone absorption coefficients α_{O_3} (in cm^{-1} ; Eq. 55) are then calculated as follows:

$$\sigma_{\text{O}_3}(\lambda, T_{\text{deg}}) = [C_0(\lambda) + C_1(\lambda)T_{\text{deg}} + C_2(\lambda)T_{\text{deg}}^2] \cdot 10^{-20} \quad (54)$$

$$\alpha_{\text{O}_3}(\lambda, T) = \frac{P_{\text{std}} \cdot N_a \cdot \sigma_{\text{O}_3}(\lambda, T_{\text{deg}})}{R_g \cdot T_{\text{std}}} \quad (55)$$

with

P_{std} : the standard pressure (= 1013.25 hPa)

N_a : Avogadro's number (= $6.0225 \cdot 10^{23} \text{ molecules} \cdot \text{mole}^{-1}$)

R_g : gas constant (= $8.314 \cdot \text{J} \cdot \text{K}^{-1} \cdot \text{mole}^{-1}$)

T_{std} : the standard temperature (= 273.15 K)

Over the last years, a lot of research has been performed, within the scientific ozone community, concerning the ozone absorption cross sections (σ_{O_3}). Redondas et al. (2014) compared five ozone cross-section data sets: three data sets that are based on measurements of Bass and Paur (quadratic temperature coefficients from the Integrated Global Atmospheric Chemistry Observations (IGACO) web page (IGQ4), the Brewer network operational calibration set (Bop), and the set used by Bernhard et al. (2005) in the reanalysis of the Dobson absorption coefficient values (B05)), one derived from Daumont, Brion and Malicet (DBM; Daumont et al., 1992; Brion et al., 1993; Malicet et al., 1995) and a new set determined by the Institute of Experimental Physics (IUP; Serdyuchenko et al., 2013; Gorshelev et al., 2013) University of Bremen. When comparing the results from the standard total ozone column algorithm for the Brewer instruments (obtained with Bop cross sections)

with the total ozone column obtained using the other cross sections, it was found that the IUP data set changes the total ozone column by -0.5% , the DBM data set by -3.2% , and the IGQ4 data set at -45°C by $+1.3\%$. The results were obtained using the European Dobson and Brewer reference instruments during the Izaña 2012 Absolute Calibration Campaign. The campaign also concluded that with the application of a common Langley calibration procedure and the choice of the IUP cross section, the differences between Brewer and Dobson retrieved total ozone columns vanished. On that basis, Redondas et al. (2014) advised on the future use of the IUP cross sections. A future change to the new IUP cross sections, would also impact the calculated $\tau_{\text{aer},340}$ values. At the time, it is hard to estimate the actual effect, but it will be less than the one caused by a 1% change in total ozone column.

Table 15 : Statistics of changes in $\tau_{\text{aer},340}$ caused by changes in ozone parameters. All values are in $10^{-4} \tau_{\text{aer},340}$.

	Minimum difference	Maximum difference	Average \pm standard deviation	Median
Total ozone column +1 %	-0.1	1.6	0.6 ± 0.3	0.6
Total ozone column -1 %	-1.6	0.2	-0.5 ± 0.4	-0.6
O₃ height = 20 km	-0.2	1.2	0.2 ± 0.2	0.1
O₃ height = 25 km	-0.1	-1.5	-0.4 ± 0.2	-0.4

3.3.3 Uncertainties in the Rayleigh term

The Rayleigh scattering term in the original equation is

$$-m_R \cdot \alpha_R(\lambda) \frac{P}{P_{\text{std}}} \quad (56)$$

with

m_R : Rayleigh air mass

$\alpha_R(\lambda)$: Rayleigh scattering optical depth of a vertical path through the atmosphere normalized to the standard pressure

P : Station pressure (at sea level) (hPa)

P_{std} : Standard pressure (at sea level) (hPa)

A first factor that can cause uncertainties in the $\tau_{\text{aer},340}$, is the station pressure P that is used in the retrieval algorithm. So far, a constant value of 1000 hPa is used for Uccle. In reality however, the station pressure is not constant. Also, the average pressure at Uccle is equal to 1016 hPa (calculated from monthly averages for the period 1981-2010). Changing the station pressure to 1016 hPa changes the $\tau_{\text{aer},340}$ with a maximum absolute value of 0.009 (Table 16). The relative differences are however non-negligible: for $\tau_{\text{aer},340}$ values ~ 0.5 , the relative difference is at 1.5% but it increases steeply for lower $\tau_{\text{aer},340}$ values (see Figure 38). For $\tau_{\text{aer},340}$ values lower than 0.2, the relative difference is already 5% or higher.

In the Rayleigh term, the height used for the calculation of the Rayleigh air mass is set to 5 km. As stated in Savastiouk & McElroy (2005), this value was chosen because it represents the centre of mass of the atmosphere which is considered to be the height of molecular attenuation. This value is of course not a constant and can deviate from the assumed 5 km. We

have tested the influence of changing the height to 4 and 6 km (Table 16). The absolute maximum difference is $\approx 1.2 \cdot 10^{-3}$ for heights of 4 and 6 km, which suggests a small impact overall. The relative difference in $\tau_{\text{aer},340}$ stays below 2% for $\tau_{\text{aer},340}$ values above 0.06.

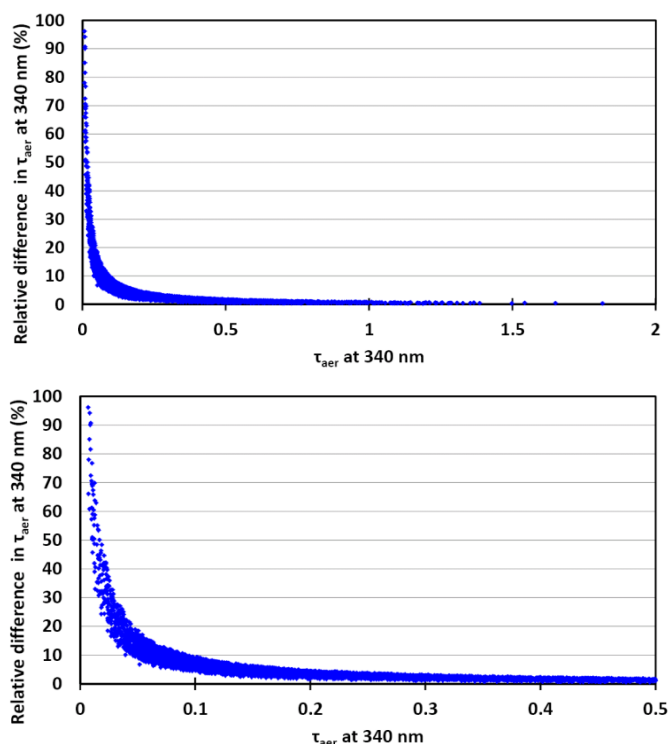


Figure 38: Relative difference in $\tau_{\text{aer},340}$ caused by changing the station pressure from 1000 to 1016 hPa. The figure on top shows the effect for all $\tau_{\text{aer},340}$ values, whereas the figure on the bottom zooms in on $\tau_{\text{aer},340}$ lower than 0.5.

Table 16: Statistics of changes in $\tau_{\text{aer},340}$ caused by changes in Rayleigh optical depth parameters. All values are in 10^{-3}

	Minimum difference	Maximum difference	Average \pm standard deviation	Median
Pressure : 1016 hPa	3.2	9.5	6.8 ± 1.3	6.9
Rayleigh height = 4 km	0.55	1.2	0.76 ± 0.12	0.73
Rayleigh height = 6 km	-0.54	-1.2	-0.78 ± 0.12	-0.75

Another possible source of uncertainty arises through the Rayleigh scattering optical depth coefficient $\alpha_R(\lambda)$ and hence the formula used to compute it. In the Brewer operator program, the values are hard coded, but the exact source is unknown. For the $\tau_{\text{aer},340}$ retrieval algorithm presented here, the formula from Kneizys et al. (1980) (Eq. 57) was used to determine the Rayleigh scattering optical depth coefficient at 340 nm:

$$\alpha_R(\lambda) = \frac{1}{\left[\lambda^4 \cdot \left(115.6406 - \frac{1.335}{\lambda^2} \right) \right]} \quad (57)$$

Other formulas have been found in literature (Teillet, 1990 ; Bodhaine et al., 1999) and are shown in

Table 17.

Table 17 : Formulas to calculate the Rayleigh scattering optical depth coefficient.

Source	Formula (wavelength in μm)
Leckner, 1978	$\alpha_R(\lambda) = 0.008735 \cdot \lambda^{-4.08}$
Moller, 1957	$\alpha_R(\lambda) = 0.00879 \cdot \lambda^{-4.09}$
Margraff & Griggs, 1969	$\alpha_R(\lambda) = 0.0088 \cdot \lambda^{(-4.15+0.2\lambda)}$
Fröhlich & Shaw, 1980	$\alpha_R(\lambda) = 0.00838 \cdot \lambda^{(-3.916-0.074\lambda-0.05/\lambda)}$
Hansen & Travis, 1974	$\alpha_R(\lambda) = 0.008569 \cdot \lambda^{-4} \cdot (1 + 0.0113 \cdot \lambda^{-2} + 0.00013 \cdot \lambda^{-4})$
Bodhaine et al., 1999	$\alpha_R(\lambda) = \frac{0.002152 \cdot (1.0455996 - 341.29061 \cdot \lambda^{-2} - 0.90230850 \cdot \lambda^2)}{1 + 0.002705889 \cdot \lambda^{-2} - 85.968563 \cdot \lambda^2}$

Table 18 shows the Rayleigh scattering optical depth coefficients at different wavelengths, calculated using the different formulas. These are obtained after convolution with the CIMEL slit function.

Table 18 : Rayleigh scattering optical depth coefficients calculated by different formulas compared to the hard coded values from the Brewer software (first column).

λ	Brewer	Leckner	Moller	Margraff & Griggs	Fröhlich & Shaw	Kneizys et al.	Hansen & Travis	Bodhaine
306.3	1.1214	1.0909	1.1108	1.1104	1.0740	1.1205	1.1051	1.1548
310.1	1.0638	1.0374	1.0562	1.0549	1.0190	1.0629	1.0486	1.0931
313.5	1.0154	0.9922	1.0101	1.0081	0.9728	1.0146	1.0011	1.0414
316.8	0.9717	0.9507	0.9678	0.9651	0.9304	0.9703	0.9575	0.9942
320.1	0.9302	0.9114	0.9276	0.9244	0.8903	0.9284	0.9163	0.9498
340.0	-----	0.7126	0.7248	0.7194	0.6897	0.7190	0.7101	0.7297

The effect on $\tau_{\text{aer},340}$ of using these different formulas for the calculation of the Rayleigh scattering coefficient is given in Table 19.

Table 19 : Statistics of changes in $\tau_{\text{aer},340}$ caused by changes in the calculation of the Rayleigh scattering optical depth coefficient. All values are in $10^{-3} \tau_{\text{aer},340}$.

	Minimum difference	Maximum difference	Average \pm standard deviation	Median
Bodhaine	3.1	9.3	6.6 ± 1.3	6.7
Leckner	-4.9	-1.6	-3.5 ± 0.7	-3.6
Moller	1.7	5.2	3.7 ± 0.7	3.8
Margraff & Griggs	0.2	0.8	0.5 ± 0.1	0.5
Fröhlich and Shaw	-23.7	-8.1	-17.0 ± 3.3	-17.2
Hansen & Travis	-6.9	-2.3	-4.9 ± 1.0	-5.0

While for some formulas (such as Marggraff & Griggs which provide similar Rayleigh scattering coefficients) the difference is low, for others (especially Fröhlich & Shaw), a median change of almost -0.02 on the $\tau_{\text{aer},340}$ was found, which is far from being negligible. Within the Brewer community (and more specifically within EUBREWNET), the decision was recently made to switch to the Bodhaine coefficients as a reference because these coefficients are also used within AERONET. The average effect on $\tau_{\text{aer},340}$ as compared to the results presented in this thesis is a bias of $6.6 \cdot 10^{-3}$.

3.3.4 Uncertainties by not including NO₂ in the calculations

For urban areas, the NO₂ concentrations can be large and will contribute to light extinction. Thus, the NO₂ should be taken into account for the $\tau_{\text{aer},340}$ calculation (Sellitto et al., 2006). In this work this has not been the case and we investigate in this section what bias this can have caused on the retrieved $\tau_{\text{aer},340}$. To do so, we have taken as reference the satellite values from NO₂ measured over De Bilt and Cabauw⁵⁶. The results are shown in Table 20. Since more than 90% of the values were lower than 0.75 DU for all three satellite instruments considered here (OMI, GOME and SCIAMACHY), a 0.75 DU column of NO₂ was included in the $\tau_{\text{aer},340}$ retrieval algorithm. The differences in $\tau_{\text{aer},340}$ with respect to the baseline calculation are smaller than $1 \cdot 10^{-5}$, which means that the impact on $\tau_{\text{aer},340}$ is negligible, which is probably due to the fact that Uccle is a suburban site, where NO₂ concentrations are not as high as at typical urban locations.

Table 20: NO₂ total columns from satellite retrievals for Cabauw and De Bilt (The Netherlands), expressed in DU.

CABAUW				
	Period	Average	Min	Max
OMI	20041001-20150617	0.49 DU	0.13 DU	2.67 DU
GOME 2	20070105-20150620	0.49 DU	0.08 DU	3.52 DU
SCIAMACHY	20020802-20120406	0.53 DU	0.07 DU	4.84 DU
DE BILT				
OMI	20041001-20150617	0.48 DU	0.14 DU	2.63 DU
GOME 2	20070105-20150620	0.49 DU	0.08 DU	3.52 DU
SCIAMACHY	20020802-20100406	0.52 DU	0.07 DU	4.84 DU

3.3.5 Uncertainties by not including SO₂ in the calculations

Similarly, the baseline retrieval scheme does not include SO₂ as an absorbing constituent. To study the effect of omitting SO₂, a low and a high amount of SO₂ have been added to the algorithm. The amount of SO₂ has been set equal to 2 DU (for h = 1 km) and 5 DU (for h = 8 km) (Table 21). For both the low and high SO₂ amounts, the relative difference is very small and less than 1% for nearly all cases.

Table 21: Statistics of changes in $\tau_{\text{aer},340}$ caused by changes in SO₂ amount. All values are in $10^{-5} \tau_{\text{aer},340}$.

	Minimum	Maximum	Average ±	Median

⁵⁶ available from: <http://www.temis.nl/airpollution/no2.html>

	difference	difference	standard deviation	
SO₂ = 2 DU	-3.0	9.0	0.0 ± 3.0	0.0
SO₂ = 5 DU	-4.0	9.0	2.0 ± 3.0	2.0

3.3.6 Instrumental issues

3.3.6.1 Internal polarization effect

It is known that the Brewer spectrophotometers have two polarization sensitive elements, i.e. the entrance window and the grating (Cede et al., 2006). This causes the sensitivity of the Brewer spectrophotometers for direct sun measurements to change with solar zenith angle. According to Cede et al. (2006), this effect is negligible for the lower solar zenith angles (SZA < 50°). However, at SZA = 60°, 70°, and 80° the Brewer's sensitivity is reduced by 1%, 4%, and 10%, relative to a SZA of 35°, when the direct solar irradiance is perpendicular to the entrance window. This will introduce systematic errors in Langley extrapolations (i.e. a 2–4% overestimation of the zero air mass CF) and in the retrieval of the AOD, with an overestimation of 0.01–0.04 (Cede et al. 2006). Hence, it is in theory necessary to correct the Brewer direct irradiance measurements for the SZA-polarization dependence. It has not been done in the algorithm presented here but, by setting an upper limit to the air mass or solar zenith angle (equal to respectively 3 and 1.23; see section 3.2.2), we limit this effect. This is similar to what was done in the research of Sellitto et al. (2006). Accounting for the effect of polarization will be part of future work.

3.3.6.2 Brewer temperature dependence

It is known that the photomultiplier tube of the Brewer spectrophotometer is sensitive to temperature changes inside the Brewer, which has an effect on the measurement sensitivity (Diémoz et al. 2016). This effect was quantified for the 5 ozone wavelengths and a correction has been applied for the calculation of the total ozone column. Berjón et al. (2017) have shown that the difference in total ozone is below 0.08 % for a mean diurnal temperature variation of 10°C. They also state that for absolute measurements such as AOD and UV, the temperature sensitivity should be analyzed separately. For the AOD retrieval at 340 nm in this work, no such analysis was performed and no temperature correction is currently in place hence the effect is consequently not accounted for in the results presented next.

3.3.6.3 Diffuse radiation entering the field of view

The sun scan measurements of the Brewer are performed with a finite FOV of 2.6°. This means that apart from direct irradiance, there will also be some fraction of diffuse irradiance entering the instrument (Arola & Koskela, 2004). This causes a systematic overestimation of the measured direct irradiance, which will influence the extraterrestrial constant determinations obtained with the Langley Plot (Arola & Koskela, 2004). This effect increases with the increasing solar zenith angle and air mass (as the ratio of direct to diffuse irradiance decreases) and decreases with wavelength. Arola and Koskela (2004) estimated the total optical depth (at an air mass of 4.5) to be underestimated by 0.0466 at 306.3 nm and by

0.0130 at 320.1 nm. Considering that the AOD retrieval for this work is at 340 nm and that an upper limit is used for the air mass values, the effect is expected to be much less.

3.3.6.4 Stray light

All spectroradiometers suffer from a degradation of the signal due to a small amount of light arriving from outside the intended wavelength (Arola & Koskela, 2004). The problem is called stray light, out-of-band leakage, or spectral scattering. It is caused by photons not following the desired path inside the monochromator due to scattering from the grating, the mirror, or the housing. The presence of two spectrometers in double Brewers eliminates the stray light, so this effect is not relevant for the presented AOD retrieval method.

3.3.6.5 Maintenance

The quartz window should be regularly cleaned to avoid the accumulation of dust on the window, which would influence the signal measured by the Brewer. The signal would be lower, leading to higher values of the $\tau_{\text{aer},340}$. For our Brewer instruments, the cleaning is done at irregular times.

3.3.7 Summary

Table 22 : Sources of uncertainty and their contributions to a first approximation of the overall $\tau_{\text{aer},340}$ uncertainty.

Source of uncertainty	Maximum change in $\tau_{\text{aer},340}$
$Q_{\text{O}_3} + 1\%$	$1.6 \cdot 10^{-4}$
Ozone airmass height = 25 km	$1.5 \cdot 10^{-4}$
Rayleigh airmass height = 6 km	$1.2 \cdot 10^{-3}$
Station pressure = 1016 hPa	$9.5 \cdot 10^{-3}$
Bodhaine Rayleigh scattering optical depth coefficients	$9.3 \cdot 10^{-3}$
$\text{SO}_2 = 5 \text{ DU}$	$9.0 \cdot 10^{-5}$

Among the several factors that act as a source of uncertainty in the $\tau_{\text{aer},340}$ retrieval, the most important ones come from the use of a constant station pressure, of ‘wrong’ Rayleigh scattering optical depth coefficients at 340 nm and from not accounting for the internal polarization effects. The overall effect of the different uncertainties on the τ_{aer} has not been quantified and will be the scope of future work. However, as a first approximation of this overall effect, we calculated the overall uncertainty as the square root of the sum of the

squares of the maximum individual errors $\sqrt{\sum_{i=1}^n (\varepsilon_i)^2}$ as detailed in Table 22. The result is an

overall maximum uncertainty in $\tau_{\text{aer},340}$ of 0.013. This result is only valid for $\tau_{\text{aer},340}$ values calculated with a total ozone error of 1%, an ozone airmass height of 25 km, a Rayleigh airmass height of 6 km, a constant station pressure of 1016 hPa, Rayleigh scattering optical depth coefficients determined with the Bodhaine formula and an SO_2 amount of 5 DU.

4. Cloud screening of AOD values

In section 3 it is explained how calibration quality clear days are selected which are then used to determine the CF through the LPM. The individual $\tau_{\text{aer},340}$ values are then retrieved using a 3-year moving average CF and Eq. 50. These individual $\tau_{\text{aer},340}$ values have not yet been screened for clouds, which is essential because they are only valid if they are retrieved in the absence of clouds between the Sun and the instrument as otherwise cloud optical depth would be measured. Therefore a general cloud screening technique is needed. This screening is different from the one to select the days for which the Langley plot method can be applied and is explained in the following chapter.

4.1 Initial cloud screening

An initial cloud screening algorithm was developed by De Bock et al. (2010). To avoid the influence of clouds, $\tau_{\text{aer},340}$ values were only calculated for the individual sun scans for which a DS observation (i.e. a cloudless observation) (made with Brewer#178) was available within a time period of 5 min. This reduced the total amount of individual $\tau_{\text{aer},340}$ data points from 38740 to 6496. However, not all cloud-perturbed measurements were excluded, which was obvious from the resulting $\tau_{\text{aer},340}$ values, some of which were clearly too high for Uccle (Figure 39).

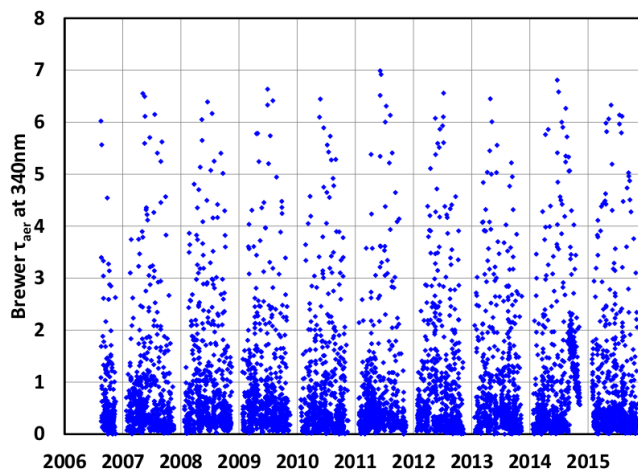


Figure 39 : Individual Brewer $\tau_{\text{aer},340}$ values with a direct sun measurement within a 5 minute time period.

The data were compared to quasi-simultaneous CIMEL level 2.0 (quality-assured and cloud screened) data (with a maximum time difference of 3 minutes) (Figure 40) and the Pearson correlation coefficient, slope and intercept of the regression line were 0.476, 0.915 ± 0.068 and 0.009 ± 0.026 respectively. Especially for Brewer values larger than 2, the agreement with the CIMEL was very bad so it was decided to automatically remove all Brewer $\tau_{\text{aer},340}$ values larger than 2 from the results on the assumption that they were influenced by clouds. This removed 609 data points from our Brewer $\tau_{\text{aer},340}$ data set but only three data points from

the comparison with the CIMEL which was slightly improved (i.e. the correlation coefficient, slope and intercept of the regression line were 0.723, 0.943 ± 0.036 and -0.019 ± 0.014 respectively). $\tau_{\text{aer},340}$ values higher than 1.5 were then checked manually and were removed when the scatter plot of the measured photon counts versus time showed that the $\tau_{\text{aer},340}$ values were calculated under cloudy circumstances. This only slightly improved the correlation coefficient to 0.789, whereas the slope and intercept of the regression line were a little worse (0.932 ± 0.029 and -0.024 ± 0.011 respectively).

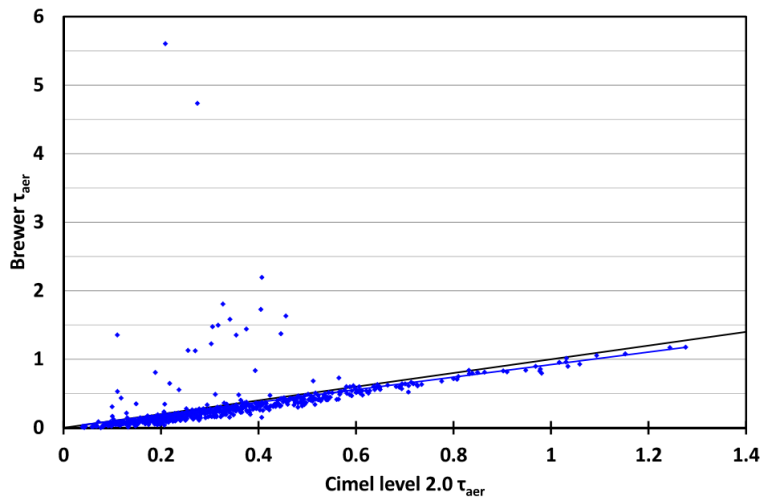


Figure 40 : Comparison between the Brewer and CIMEL $\tau_{\text{aer},340}$ values (maximum time difference of 3 minutes). The blue values (and the corresponding blue regression line) represent the $\tau_{\text{aer},340}$ values with a DS measurement within 5 minutes. The black line is the 'f(x)=x' line.

4.2 Improved cloud screening technique

As the initial cloud screening algorithm, described in section 4.1, which is totally based on the Brewer measurements, did not perform well, De Bock et al. (2014) have developed another sequence of criteria which simultaneously rely on other instruments. Specifically, the improved cloud screening method makes use of sunshine duration data from four pyrheliometers at Uccle and is also based on the assumption that the variability of the $\tau_{\text{aer},340}$ in the course of one day is either lower than 10% or lower than $0.08 \tau_{\text{aer},340}$ units. Figure 41 gives a schematic overview of the improved cloud screening sequence. First it is determined whether the individual $\tau_{\text{aer},340}$ measurements were taken within a 10 min interval of continuous sunshine. The measurements for which this is not the case are removed, after which more than two individual measurements per day must remain in order to continue. For each day, we then determine the maximum deviation to the median value. If this value is less than 0.08 (empirically determined), we accept all measurements for that day. However, if the maximum deviation exceeds 0.08, the relative standard deviation for that day is calculated. In case this value is less than 10 %, which would guarantee a given stability within the diurnal pattern of $\tau_{\text{aer},340}$, all the $\tau_{\text{aer},340}$ values for that day are kept. In the other case, the $\tau_{\text{aer},340}$ measurement with the largest contribution to the standard deviation is removed, as this measurement is most likely influenced by clouds. The median value will then be recomputed and the previous steps are repeated. Days with two or less individual $\tau_{\text{aer},340}$ measurements are excluded from the

results, since it does not make sense to calculate the deviation to the median and the standard deviation.

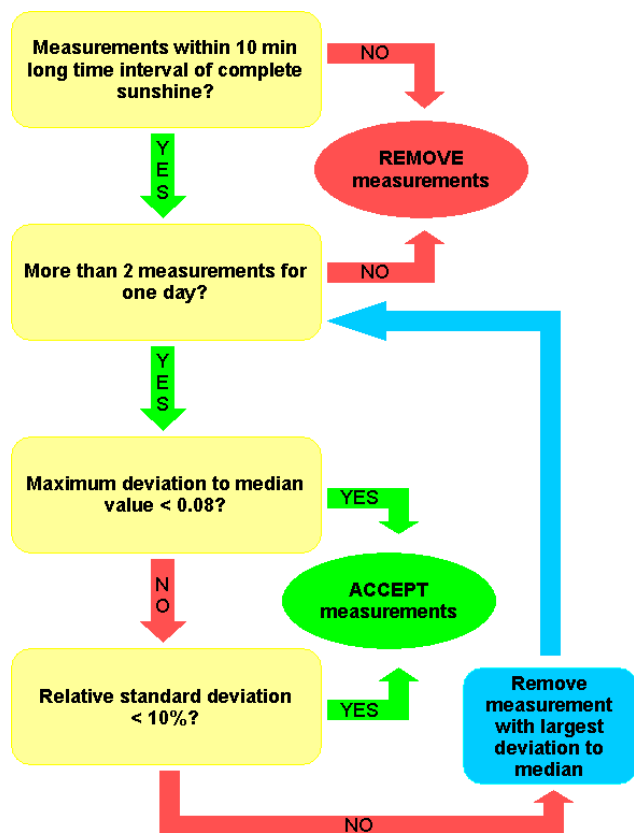


Figure 41: Improved cloud screening method (from De Bock et al., 2014).

The advantages of the improved cloud screening method are that it no longer automatically removes $\tau_{\text{aer},340}$ values larger than the arbitrary defined maximum level and the fact that it runs completely automatically, whereas the previous one needed manual verification afterwards. The disadvantage is the need of simultaneous observations between the pyrhelimeters and the Brewer. This method has now been applied not only to the τ_{aer} retrieval using SS measurements at 340 nm but also to the method using DS measurements at the ozone wavelengths. The cloud screened $\tau_{\text{aer},340}$ will be compared to quasi-simultaneous and co-located CIMEL level 2.0 quality-assured values in section 5.1 (Figure 42).

5. AOD data analysis

This section provides an analysis of the cloud screened $\tau_{\text{aer},340}$ retrieved from Brewer#178 SS measurements at Uccle with the method presented in section 3. The cloud screening is described in section 4. Section 5 is articulated around a comparison exercise between the Brewer $\tau_{\text{aer},340}$ retrieved simultaneously with the co-located CIMEL instrument (section 5.1) and the Brewer $\tau_{\text{aer},320}$ from the DS measurement mode (section 5.2) and a first analysis of the time evolution of these retrieved $\tau_{\text{aer},340}$ from the Brewer (section 5.3 and 5.4).

5.1 Comparison with CIMEL data

We compare the $\tau_{\text{aer},340}$ values obtained from the SS measurements of Brewer#178 with the measurements from the co-located CIMEL sun photometer (section 2.2). CIMEL Level 2.0 data are used here, which are quality-assured and cloud screened data. Only measurements from both instruments that are obtained within 3 minutes of each other are used for the comparison. In total this represents 1182 coupled data points for the period from 19/08/2006 until 02/11/2015. The result of the comparison is shown in Figure 42. Taken globally, the Pearson correlation coefficient, slope and intercept of the linear regression are respectively 0.972, 0.966 ± 0.007 and -0.060 ± 0.003 . While this highlights the excellent agreement between both instruments, we report on a systematic offset with the CIMEL $\tau_{\text{aer},340}$ being larger than the Brewer ones for 96% of all compared values (which is well seen in Figure 42 with quasi the total of all points being under the 1:1 line). For 82% of the data points, the residual between Brewer and CIMEL values is between -0.12 and 0.

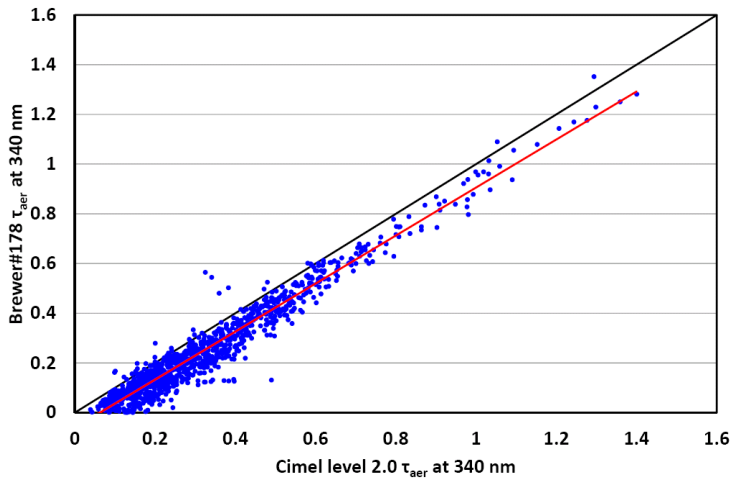


Figure 42: Comparison of $\tau_{\text{aer},340}$ from Brewer#178 and CIMEL values at Uccle. The black line represents the 'f(x)=x' line, whereas the red line represents the linear relation between Brewer and CIMEL values.

The bias and standard deviations (root mean square errors) are calculated as

$$\text{bias} = \frac{1}{N} \sum_{i=1}^N (\text{Brewer}_{\text{AOD}} - \text{Cimel}_{\text{AOD}}) \text{ and } \text{rmse} = \sqrt{\frac{1}{N} \sum_{i=1}^N (\text{Brewer}_{\text{AOD}} - \text{Cimel}_{\text{AOD}})^2} .$$

We find a low bias for the Brewer of -0.071 with an associated rmse equal to 0.086 taken the entire ~9

years record available. This is consistent with the results of Cheymol et al. (2009) who reported a bias of -0.07 of the Brewer#016 DS $\tau_{\text{aer},320}$ measurements over the CIMEL (with the CIMEL $\tau_{\text{aer},340}$ values shifted to 320 nm using the Angström's coefficient between 340 and 440 nm of the CIMEL). Table 23 shows the time evolution of the bias and correlation as yearly values: it can be clearly seen that 2010 and 2015 stand out as far as the bias is concerned with biases on the $\tau_{\text{aer},340}$ above 0.1 in absolute value. At the moment, we have no explanation for this behavior. 2006 also stands out with a much lower correlation coefficient of 0.89. This might be due to the fact that fewer Brewer $\tau_{\text{aer},340}$ data points are available for comparison in 2006 (as Brewer $\tau_{\text{aer},340}$ are only available since 19/08/2006). Note that there are no CIMEL data available for the year 2011 as the instrument was undergoing calibration.

Table 23 : Yearly biases and Pearson correlation coefficients for the Brewer-CIMEL $\tau_{\text{aer},340}$ comparison.

Year	Bias	Correlation
2006	-0.039	0.89
2007	-0.052	0.98
2008	-0.042	0.98
2009	-0.069	0.99
2010	-0.103	0.97
2011	N/A	N/A
2012	-0.052	0.99
2013	-0.070	0.98
2014	-0.075	0.95
2015	-0.113	0.94

Figure 43 (left panel) shows the residuals in function of air mass together with the WMO acceptance limits ($0.005 \pm \frac{0.010}{\text{airmass}}$) defined in WMO-GAW report number 162 (WMO, 2004). We found that only 3% of the values fall within the WMO limits, whereas a minimum of 95% is required to formally establish an intercomparison traceability (Kazadzis et al., 2014). If we consider the bias of -0.071 and correct our Brewer data according, the amount of data points within the WMO acceptance limits increases to 20% (Figure 43; right panel) but the scatter remains large. From Figure 43 and Table 24, it is seen that the residuals are larger for air masses between 1 and 2 and we have shown that they decrease as the air mass increases. This would be in agreement with Figure 35 where the effect of a change in CF is higher at lower air masses. We have therefore also tried to correct the Brewer data a posteriori using an air mass dependent correction factor. This however did not increase the amount of points within the WMO limits any further.

Table 24 : Brewer-CIMEL bias for different air mass ranges from 1 to 3, by steps of 0.5.

Air mass range	Bias
1.0-1.5	-0.099
1.5-2.0	-0.071
2.0-2.5	-0.043
2.5-3.0	-0.036

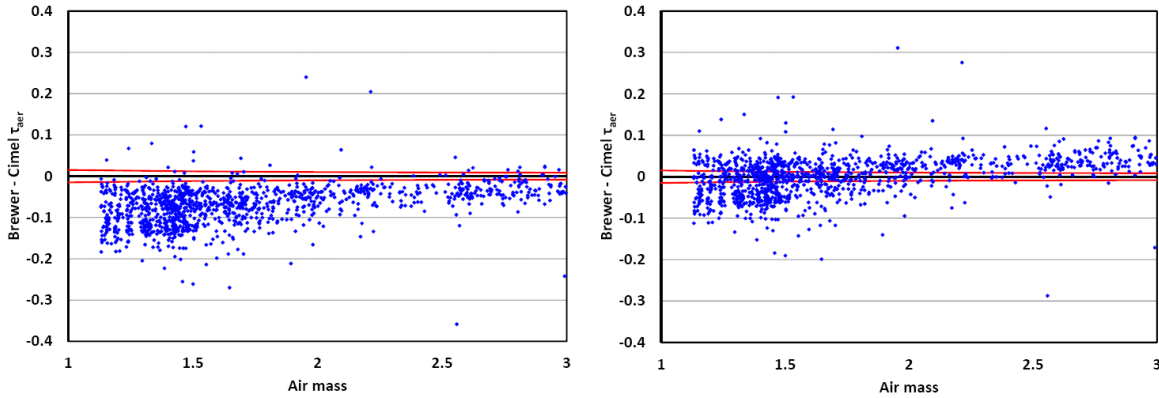


Figure 43 : Residuals (Brewer $\tau_{\text{aer},340}$ -CIMEL $\tau_{\text{aer},340}$) versus air mass. The red curved lines represent the acceptance limits fixed by WMO (2004). The plot on the left is made using the original Brewer $\tau_{\text{aer},340}$ data, whereas the Brewer data in the plot on the right side were corrected according to the 0.071 $\tau_{\text{aer},340}$ bias.

At the moment, it is assumed that part of the offset between the Brewer and CIMEL $\tau_{\text{aer},340}$ values is due to the uncertainty in the Brewer calibration factor CF. The fact that both instruments use different Rayleigh scattering coefficients, could also partly explain the offset (see discussion in section 3.3.3). Apart from that, it should be taken into account that the CIMEL values might also have unknown errors due to the manual screening before reaching their level 2.0 status.

Despite the presence of an offset between the Brewer and the CIMEL $\tau_{\text{aer},340}$ values, the overall correlation coefficient (0.972) is high enough to state that the Brewer spectrophotometer is largely sensitive to $\tau_{\text{aer},340}$ and it justifies its use in sun scan mode to expand the AOD retrieval network of instruments.

5.2 Comparison with Direct Sun $\tau_{\text{aer},320}$ measurements

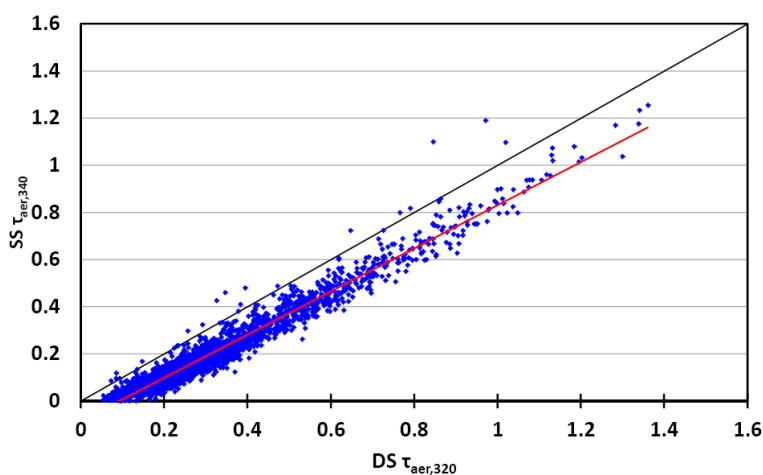


Figure 44 : Comparison of the $\tau_{\text{aer},340}$ values retrieved using the sun scan (SS) measurement mode and the $\tau_{\text{aer},320}$ values from the direct sun (DS) measurement mode. The Pearson correlation coefficient, slope and intercept of the regression line are 0.976, 0.915 ± 0.004 and -0.084 ± 0.002 respectively. The maximum time difference between two measurements is 3 minutes.

The $\tau_{\text{aer},340}$ measurements retrieved in the SS measurement mode are compared with the $\tau_{\text{aer},320}$ values determined in the DS measurement mode and Figure 44 shows the good agreement between the two measurement modes. The Pearson correlation coefficient, slope and intercept are equal to 0.976, 0.915 ± 0.004 and -0.084 ± 0.002 respectively. For the analysis in section 6, the $\tau_{\text{aer},320}$ from the DS measurement mode will be used as they are available for a longer time period.

5.3 Monthly and seasonal analysis

Table 25: Monthly climatological average $\tau_{\text{aer},340}$ at Uccle (2006-2015). The first column uses all available daily values to calculate the monthly means. The monthly values in the second column are only calculated when at least 10 daily values were available for that month.

	All data	Only months with minimum 10 daily values
January	0.25 ± 0.07	No data for this month
February	0.25 ± 0.12	0.21 ± 0.05
March	0.30 ± 0.08	0.31 ± 0.05
April	0.41 ± 0.12	0.40 ± 0.11
May	0.29 ± 0.11	0.30 ± 0.12
June	0.28 ± 0.07	0.28 ± 0.08
July	0.29 ± 0.07	0.27 ± 0.07
August	0.20 ± 0.06	0.22 ± 0.05
September	0.25 ± 0.07	0.24 ± 0.07
October	0.17 ± 0.04	0.16 ± 0.03
November	0.12 ± 0.06	No data for this month
December	No data for this month	No data for this month

Table 26: Same as in Table 25 for the seasonal climatological average $\tau_{\text{aer},340}$. Spring corresponds to March-April-May, summer to June- July- August, autumn to September- October-November and winter to December-January-February.

	All data	Using only months with minimum 10 daily values
Spring	0.34 ± 0.08	0.36 ± 0.08
Summer	0.24 ± 0.07	0.25 ± 0.06
Autumn	0.18 ± 0.04	0.21 ± 0.06
Winter	0.25 ± 0.11	0.21 ± 0.10

Table 25 and Table 26 respectively show the monthly and seasonal $\tau_{\text{aer},340}$ values measured at Uccle for the 2006-2015 period. The values in the first column of Table 25 are based on monthly means calculated as the mean of all available daily values. For the values in the second column, an extra constraint was added and monthly values are only calculated when at least 10 daily values were available for that month. This makes sure that the monthly value is more representative for the entire month. For the seasonal values in Table 26, the same distinction is made with the values in the second column being based on monthly values calculated for months with at least 10 daily values. (The discussion of the monthly and seasonal variation will use the values from the second column.)

On a monthly scale, the lowest values $\tau_{\text{aer},340}$ at Uccle are observed in October, whereas the highest values occur in April. On a seasonal scale, the highest values can be observed in spring (and summer) whereas autumn and winter values are clearly lower. Figure 45 gives the seasonal frequency distribution of $\tau_{\text{aer},340}$ at Uccle for the period from 1 September 2006 until 30 November 2015.

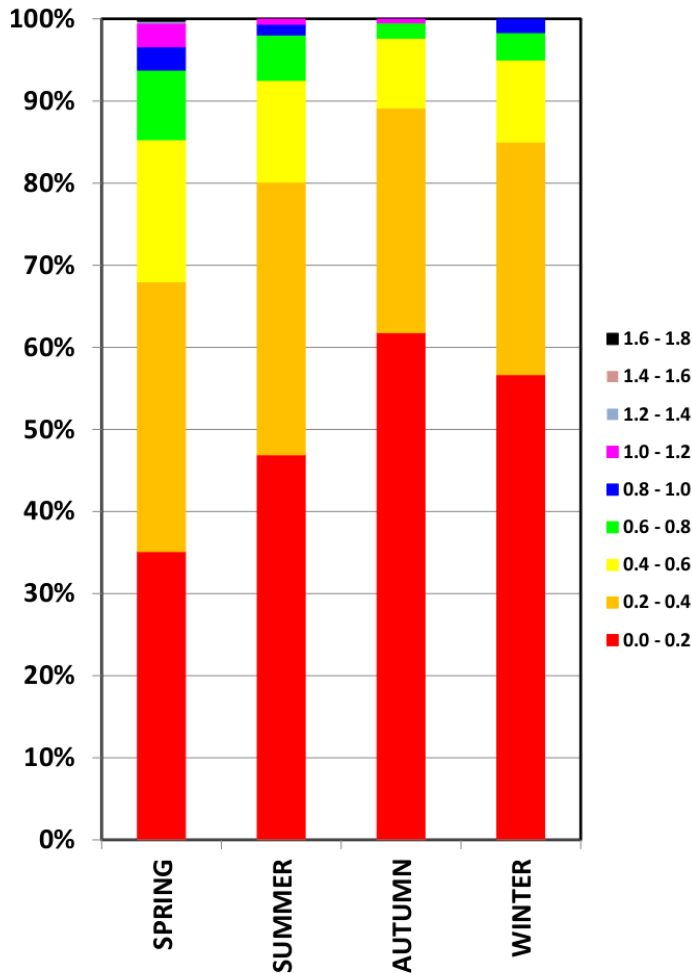


Figure 45: Seasonal frequency distribution of $\tau_{\text{aer},340}$ at Uccle from 1 September 2006 until 30 November 2015. The colors refer to the $\tau_{\text{aer},340}$, ranked by bins of 0.2 from 0 to 1.8.

There are clear differences between the different seasons. Spring is characterized by the largest spread in observed $\tau_{\text{aer},340}$ (from 0 to 1.8). For the other seasons, the spread is much lower: summer and autumn values stay below 1.2 and winter values do not reach values above 1.0. Low $\tau_{\text{aer},340}$ values occur most frequently during autumn and winter: respectively 62 and 57% of the $\tau_{\text{aer},340}$ at Uccle are below 0.2, which is in agreement with the results from Kazadzis et al. (2007) for Thessaloniki, Greece. In summer and spring, the amount of values lower than 0.2 decreases to respectively 47 and 35%. In spring, around 15% of the observed $\tau_{\text{aer},340}$ is higher than 0.6, whereas $\tau_{\text{aer},340}$ higher than 0.6 are much less often observed in summer (7%), autumn (2%) and winter (5%).

Overall, the obtained $\tau_{\text{aer},340}$ values from Brewer#178 at Uccle are consistent with other studies. Several studies that have investigated the seasonal variability of aerosols, reported for the Northern Hemisphere high AOD values during summer and spring and low AOD values in winter and autumn (e.g. Meleti and Cappellani, 2000; Behnert et al., 2004; Kim et al., 2006; Kazadzis et al., 2007; Estellés, 2008; Léon et al., 2009; Lyamani et al., 2010). In Valencia, maximum AOD values were observed (the data record extends here between 2002–2005) from June to September, whereas the minimum values occurred from October to February, mainly in December and January (Estellés, 2008). Behnert et al. (2004) observed two peak periods in the AOD values from Helgoland Island, Hamburg, Oostende and Lille. They occurred during spring (April–May) and summer (July–August). Studies in Ispra, Granada, M’Bour, Gwangju and Thessaloniki also show high AOD values in summer and low values in winter (Meleti and Cappellani, 2000; Kim et al., 2006; Kazadzis et al., 2007; Léon et al., 2009; Lyamani et al., 2010). The latitude and longitude of the places mentioned above are listed in Table 27.

Table 27 : Latitude and longitude of stations mentioned in section 5.3.

Location	Latitude	Longitude
Helgoland Island (Germany)	54°10' N	7°53' E
Hamburg (Germany)	53°34' N	9°56' E
Oostende (Belgium)	51°13' N	2°55' E
Uccle (Belgium)	50°48' N	4°21' E
Lille (France)	50°36' N	3°06' E
Ispra (Italy)	45°49' N	8°38' E
Granada (Spain)	37°10' N	35°35' E
Thessaloniki (Greece)	40°30' N	22°54' E
Beijing (China)	39°59' N	116°19' E
Valencia (Spain)	39°30' N	0°25' W
Gwangju (Korea)	35°13' N	126°50' E
M’Bour (Senegal)	16°58' N	14°23' E

Possible explanations for higher summer AODs are given by several authors. Behnert et al. (2004) attribute the summer peak values to the slowing down of air mass circulation in summer and the production of smog. This results in an accumulation of high aerosol concentrations above mid-latitude regions. Kaskaoutis et al. (2007) and Nabat et al. (2013) explain the higher summer AOD values at Ispra as a result of the absence of wet removal processes. According to Kazadzis et al. (2007), the enhanced evaporation and the higher temperatures during summer in Thessaloniki cause a rise in the turbidity of the boundary layer. Combined with stagnating weather systems, this leads to the formation of aerosols. The lower AOD values in winter are attributed to the significant amount of wet deposition of aerosols, which causes a cleaning of the atmosphere, as for example explained in Koelemeijer et al. (2006). They observed an anti-correlation (-0.41 for the region of Belgium and The Netherlands) between precipitation and mean monthly AOD. We similarly find an anti-correlation of -0.27 between the mean monthly $\tau_{\text{aer},340}$ and the monthly percentage of rain days at Uccle for a period between 2006 and 2015. In order to get a better view of the possible relationship between $\tau_{\text{aer},340}$ and precipitation, we divided the calculated $\tau_{\text{aer},340}$ values from

2006 to 2015 in two categories, “dry $\tau_{\text{aer},340}$ ” and “wet $\tau_{\text{aer},340}$ ”, based on the influence of precipitation on the values. We considered a single $\tau_{\text{aer},340}$ value to be wet if precipitation was observed on this day or on the previous day. If both days were precipitation-free, we considered the $\tau_{\text{aer},340}$ value to be representative for a dry day. Figure 46 shows the mean monthly $\tau_{\text{aer},340}$ for the dry and for the wet days. We would expect the wet $\tau_{\text{aer},340}$ to be lower than the dry $\tau_{\text{aer},340}$, however for some months (April, June and September) this is not the case. This could be due to the occurrence of local thunderstorms in these months, causing only local deposition of aerosols. Air flowing from other places can transport aerosol masses that were not influenced by these local thunderstorms and the measured $\tau_{\text{aer},340}$ can thus be higher than one would expect based on the precipitation associated with the thunderstorms. In winter, precipitation is mainly related to the passage of large frontal systems. The wet deposition of aerosols will thus be spread over a larger region.

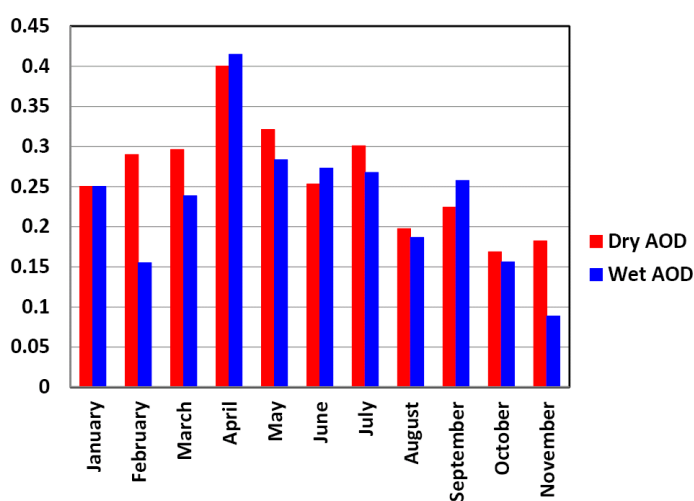


Figure 46: Mean monthly $\tau_{\text{aer},340}$ separated for dry and wet days at Uccle (2006-2015). See text for details.

According to Cheymol and De Backer (2003), a relation with a pollution cycle (i.e. emissions) or with a general circulation could also be an explanation for the annual cycle in AOD at Uccle. Chin et al. (2014) found that the AOD over polluted land regions generally varies with anthropogenic emissions but the magnitude of this association can be dampened by the presence of natural aerosols such as dust. They stated that the relation between emissions and AOD can be quite different from region to region and should be studied locally. To study the influence of emissions on $\tau_{\text{aer},340}$, we use annual country-level emissions of anthropogenic sectors for Europe from the European Environment Agency air pollutant emission data viewer⁵⁷, which provides access to the data contained in the European Union emission inventory report under the convention on Long-range Transboundary Air Pollution (LRTAP). We studied the annual emissions of BC, NH₃, NO_x, SO_x and PM₁₀ (Figure 47) and calculated their relative change over time and their correlation with $\tau_{\text{aer},340}$ at Uccle (Table 28). All emissions have decreased over time, with the decrease in SO_x being the largest (-88% over the 1990-2015 time series). We also found a decrease in the annual $\tau_{\text{aer},340}$ at Uccle for the

⁵⁷ www.eea.europa.eu/data-and-maps/data/data-viewers/air-emissions-viewer-lrtap; visited on 30/7/2017

2007-2015 period ⁵⁸ equal to -29%. There is a positive correlation (from 0.36 to 0.49) between all pollutants and $\tau_{\text{aer},340}$ on an annual scale, which affirms a link between changes in emissions and $\tau_{\text{aer},340}$. It is however difficult to use these results to confidently state that the annual variation in $\tau_{\text{aer},340}$ can be explained by changes in emissions.

However, it is known that certain emissions change on a seasonal scale. An example are the NH_3 emissions, which are mainly linked to agriculture (i.e. application of fertilizers on the fields). NH_3 plays a primary role in the formation of secondary particulate matter by reacting with sulfates and nitrates to form ammonium-containing aerosols (Wang et al., 2015). Due to an increase in agricultural activity in spring, NH_3 emissions are highest during this season, which is a possible explanation for the higher $\tau_{\text{aer},340}$ observed in spring.

Table 28 : Relative change in the emissions of NO_x , SO_x , NH_3 , PM_{10} and BC in Belgium over time. The third column presents the correlation of the emissions with $\tau_{\text{aer},340}$ at Uccle on an annual scale.

Pollutant	% change over time	Correlation with $\tau_{\text{aer},340}$
NO_x	- 52% (1990-2015)	0.36
SO_x	- 88% (1990-2015)	0.39
NH_3	- 44% (1990-2015)	0.37
PM_{10}	- 35% (2000-2015)	0.43
BC	- 53% (2000-2015)	0.49

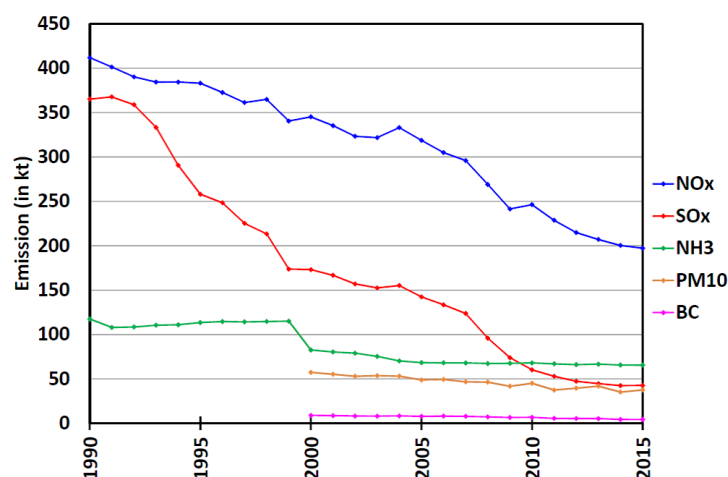


Figure 47 : Annual emission data of NO_x , SO_x , NH_3 , PM_{10} and BC between 1990 and 2015 for Belgium; based on data from European Environment Agency air pollutant emissions data viewer.

As reported in section 2, De Backer (2009) states that the prevailing meteorological conditions at Uccle determine whether our station is influenced by sea salt aerosols, by aerosols from urban activity or by continental type of aerosols, which will also have some influence on the $\tau_{\text{aer},340}$ values.

The mixing layer height (MLH) and its seasonal variation (with a smaller MLH in winter and autumn), could also be an explanation for the lower AOD in winter and autumn compared to summer and spring where the MLH is thicker. De Bock et al. (2010) calculated the correlation between the monthly mean MLH and the monthly mean $\tau_{\text{aer},340}$ (for the period between September 2006 and December 2009) and found a value of 0.701 for Uccle (red points in

⁵⁸ Data for 2016 are only available since September that year, so no annual mean $\tau_{\text{aer},340}$ was calculated for this year.

Figure 48). The correlation decreased strongly when the daily mean MLH and the daily mean $\tau_{\text{aer},340}$ are compared (correlation of 0.196; blue points in Figure 48).

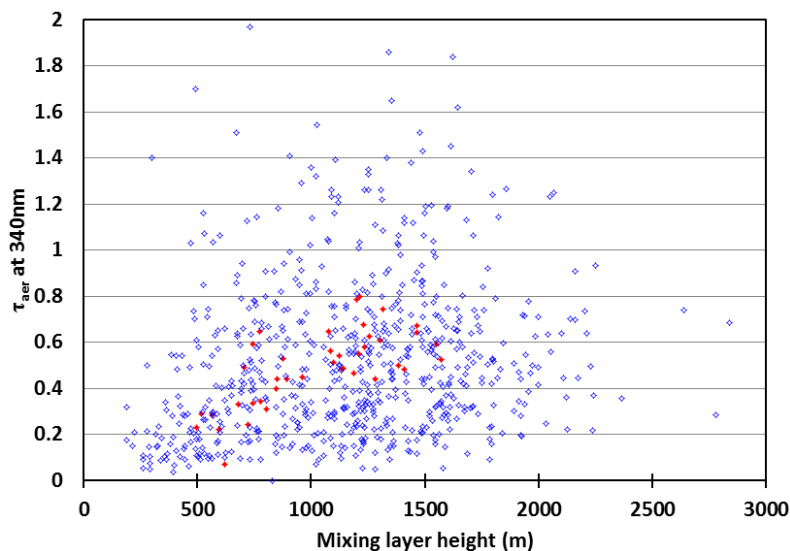


Figure 48 : Scatterplot of $\tau_{\text{aer},340}$ versus the mixing layer height at Uccle on a daily (blue points) and monthly scale (red points). The correlation for the red points is equal to 0.701, for the blue points, it is much lower (0.196).

5.4 Weekly periodicity

Table 29: Average $\tau_{\text{aer},340}$ at Uccle for the days of the week.

Day of week	Mean $\tau_{\text{aer},340} \pm$ standard deviation
Monday	0.26 ± 0.21
Tuesday	0.29 ± 0.22
Wednesday	0.28 ± 0.21
Thursday	0.30 ± 0.26
Friday	0.29 ± 0.24
Saturday	0.27 ± 0.21
Sunday	0.26 ± 0.20

Bäumer et al. (2008) and Xia et al. (2008) observed a weekly AOD cycle in Central Europe. They recorded the lowest values on Sunday and Monday, whereas higher values occurred between Wednesday and Saturday. This cycle is greater for the urban sites than for the rural sites. For our measurements in Uccle, there is no clear signal for such a weekly cycle (Table 29). The largest difference in mean $\tau_{\text{aer},340}$ values occurs between Monday and Thursday (respectively 0.26 versus 0.30). Because of the rather high standard deviation on the average values, this difference cannot be considered as a clear signal of a weekly cycle. It has to be taken into account here that Uccle is a suburban station and is probably less influenced by the difference in traffic between weekdays and weekends when compared to real urban stations.

6. Relationship between erythemal UV dose, global solar radiation, total ozone and AOD at Uccle

The main goal of this section is to gain more insight into the medium term behavior and changes of the erythemal UV dose at Uccle. The main geophysical parameters known to affect the levels of surface UV irradiance are ozone, clouds, surface reflectivity and aerosols (Bais et al., 2015; Fountoulakis et al., 2016a) and here we investigate the changes of these parameters over time and study their relationship with the UV irradiance measurements at Uccle.

At Uccle, an extensive dataset (spanning 25 years: 1991-2015) consisting out of all-sky erythemal UV dose (D_{ery}^* in J m^{-2}), all-sky global solar radiation (D_g^* in J m^{-2}), total ozone column (Q_{O_3} in DU) and clear-sky aerosol optical depth at 320.1 nm ($\tau_{aer,320}$) measurements, is available for analysis as detailed in the following sections. We use the $\tau_{aer,320}$ in this analysis as their time series is longer than the one for $\tau_{aer,340}$. The global solar radiation D_g^* can be used here as a proxy to estimate the effect of cloudiness on UV radiation (De Backer et al., 2009). We assume the surface reflectivity to be constant at Uccle since changes in surface reflectivity are only expected to play an important role for the levels of UV radiation over areas that are covered by ice or snow (Bais et al., 2015) and this is almost never the case at Uccle. Several statistical methods are applied to this dataset with the goal of studying the changes over time, evaluating the relationship between these parameters and attributing the variations in UV to changes in the other parameters. First, we investigate whether change points are present in any of our time series (of monthly anomalies) in section 6.2. After that, a linear trend analysis is applied to the monthly anomalies of the time series (both on a daily and seasonal time scale), and the results are compared with results found in the literature (section 6.3). Monthly anomalies are used here to reduce the influence of the seasonal cycle on the analysis and are calculated by subtracting the long-term monthly mean from the individual monthly means. A multiple linear regression (MLR) technique (with daily erythemal UV doses as the dependent variable and daily values of global solar radiation, total ozone column and aerosol optical depth at 320.1 nm as explanatory variables) is then carried out in section 6.4. It allows us to study the influence of the explanatory variables on the dependent variable on a daily and seasonal basis. The above described analysis was performed on a shorter time series (1991-2013) in De Bock et al. (2014).

6.1 Monthly anomalies

Since most statistical analysis tests, such as linear regression and change point tests, rely on independent and evenly distributed time series (e.g., Van Malderen and De Backer, 2010 and references therein), most data used in this part of the study are in their anomaly form. Monthly anomalies have indeed the advantage to reduce the influence of the seasonal cycle on the analysis and are calculated by subtracting, for each quantity, the long-term monthly mean from the individual monthly means. Monthly means are only calculated for months with at least 10 individual daily values. For D_{ery}^* , D_g^* and Q_{O_3} , accepting monthly means with only 10 daily individual values does not have an impact on the calculated trends, as respectively 85,

99 and 100% of the months consist of more than 20 individual daily values. For $\tau_{\text{aer},320}$ however, the number of available monthly mean values is dramatically reduced (from 114 to only 6 remaining values) when only accepting monthly means based on 20 individual values. There is a risk in accepting months with only 10 daily values, as those days could be concentrated at the beginning or end of a month, which could bias the calculated trend. However, the benefit of using 114 instead of 6 monthly mean values for $\tau_{\text{aer},320}$ trend calculations outweighs this potential bias. Note that for the multiple linear regression analysis, daily values are used instead of anomaly values.

6.2 Change point analysis

Change points are times of discontinuity in a time series (Reeves et al., 2007) and can either arise naturally or as a result of errors or changes in instrumentation, recording practices, data transmission, processing, etc. (Lanzante, 1996). A change point is said to occur at some point in the sequence if all the values up to and including it share a common statistical distribution and all those after the point share another. The most common change-point problem involves a change in the mean of the time series (Lanzante, 1996). There are different tests that can be used to detect a change point in a time series. In De Bock et al. (2014), the combination of three tests was used: the non-parametric Pettitt–Mann–Whitney (PMW) test (based on the ranks of the values in the sequence), the Mann–Whitney–Wilcoxon (MWW) test (a rank sum test) and the cumulative sum technique (CST). The details of these tests are described in Hoppe and Kiely (1999). Only the change points that exceeded the 90% confidence level were retained. The change points were determined for the monthly anomalies time series of D_{ery}^* , D_g^* , Q_{O_3} and $\tau_{\text{aer},320}$. When there is a clear and large-enough, statistically significant trend present in the time series, this automatically leads to the detection of a change point in the middle of the time series as, at this point, the change in the mean is large enough to be significant. In this case, it is necessary to detrend the time series, i.e., subtract the general trend from the time series.

De Bock et al. (2014) found a significant change point (observed by all three tests) around February/March 1998 in the D_{ery}^* and Q_{O_3} time series from 1991-2013. For Q_{O_3} , the mean before the change point was clearly lower than the one after the change point. As there was no change in the calibration constants of the Brewer instrument around 1998, the detected change points had no known instrumental cause. De Bock et al. (2014) assumed the detected change points had some natural/environmental cause and were related to each other. The change point in the Q_{O_3} time series corresponds with results found in literature where recent studies showed that ozone recovery started around 1997 (Steinbrecht et al., 2006; Reinsel et al., 2005).

In the current work, the change point analysis is repeated using the extended time series (1991-2015). However, the change points found by De Bock et al. (2014) are no longer detected when analyzing our longer time series (Figure 49). Therefore, we decide not to further discuss this analysis in this work.

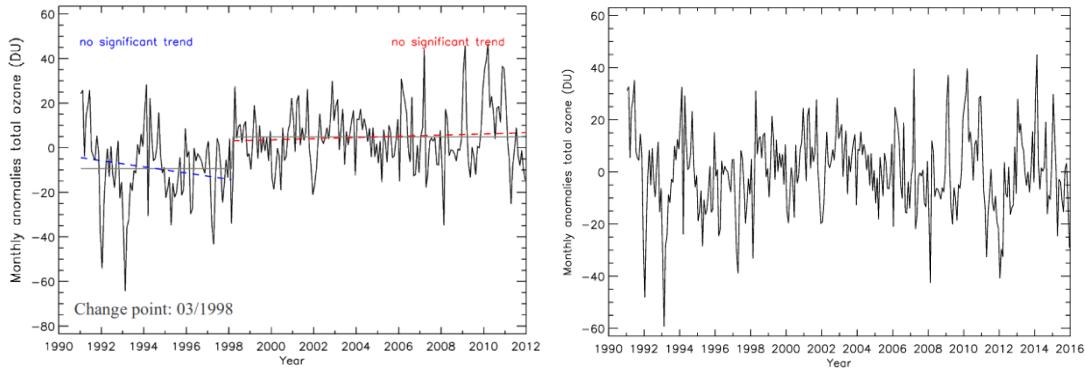


Figure 49 : Change point analysis of the total ozone time series. The plot on the left represents the ‘old’ time series (1990-2013) from De Bock et al. (2010) where a change point was detected around March 1998. The plot on the right shows the extended time series (1990-2015) for which no change point was detected.

6.3 Linear trend analysis

6.3.1 Method

Linear trends are calculated for the monthly anomalies of D_{ery}^* , D_g^* , Q_{O3} and $\tau_{aer,320}$. To determine the significance of the linear trends, the method described in Santer et al. (2000) is used. The least-squares linear regression estimate of the trend in $x(t)$, b , minimizes the squared differences between $x(t)$ and the regression line $\hat{x}(t)$:

$$\hat{x}(t) = a + b(t); t = 1, \dots, n_t \quad (58)$$

Whether a trend in $x(t)$ is significantly different from 0 is tested by computing the ratio t_b between the estimated trend (b) and its standard error (s_b):

$$t_b = \frac{b}{s_b} \quad (59)$$

Under the assumption that t_b is distributed as Student’s t , the calculated t ratio is then compared with a critical t value, t_{crit} , for a stipulated significance level α and n_{t-2} degrees of freedom (Santer et al., 2000). However, if the regression residuals are auto-correlated, the results of the regression analysis will be too liberal and the original approach must be modified. The method proposed in Santer et al. (2000) involves the use of an effective sample size n_e in the computation of the adjusted standard error and calculated t value, but also in the indexing of the critical t value. To test for autocorrelation in the residuals of a time series, the Durbin–Watson test is used (Durbin and Watson, 1971).

The linear trend analysis is also applied with similar methodology to the monthly anomalies of the extreme values (minima and maxima) of the variables, which are calculated by determining the lowest and highest measured value for each month. These trends are studied together with the relative frequency distribution of the daily mean values. This distribution is determined by using the minimum and maximum values of the entire study period as

boundaries and by dividing the range between the boundaries into a certain amount of bins of equal size. The daily values are distributed over the different bins, and the relative frequency (in percent) is calculated. This is done for two different time periods: 1991–2002 and 2003–2015. Additionally, the medians (calculated using the monthly values) for these periods are determined. In this way, it is possible to investigate whether there is a shift in the frequency distribution of the variables from the first period to the second one. Note that for the sake of clarity, the results of the analysis of the frequency distribution are only presented in case they show a significant shift in the data. In section 6.3.2 we discuss the results individually for the different parameters and in section 6.3.3 we discuss the results globally.

6.3.2 Results

Figure 50 shows the linear trends for the monthly anomaly time series of the erythemal UV dose, the global solar radiation, the total ozone column and the aerosol optical depth at 320.1 nm for the 1991-2015 period.

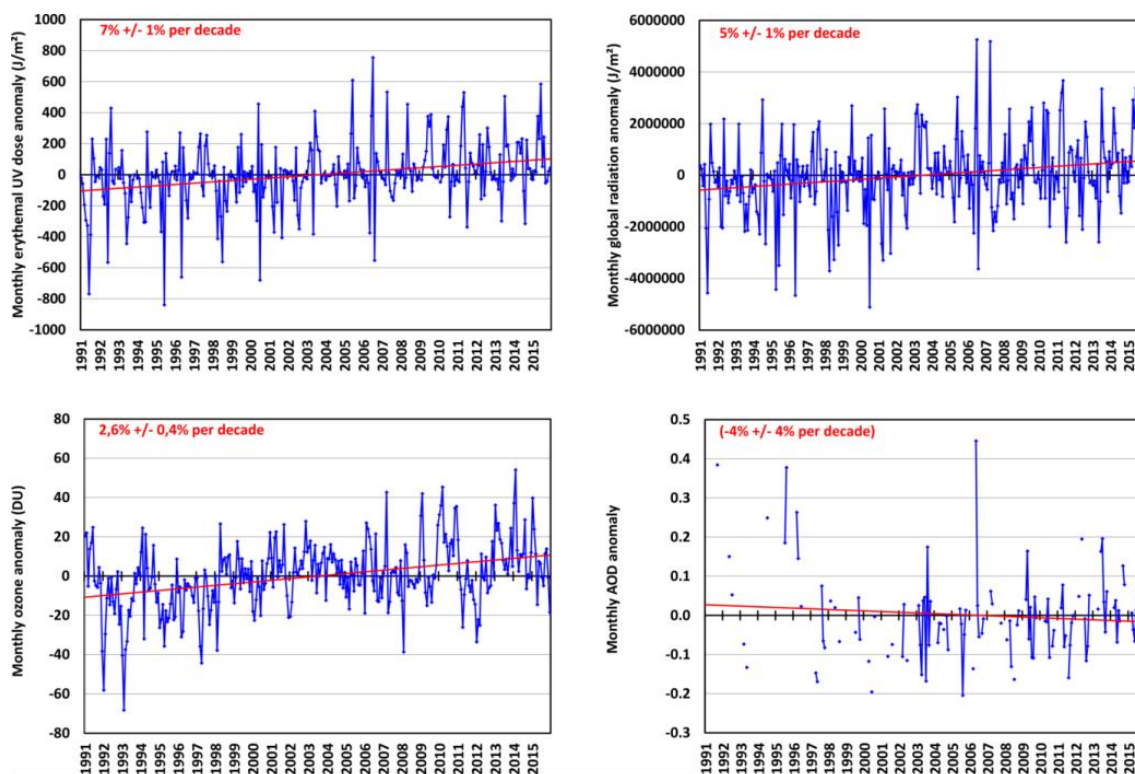


Figure 50: Trends of monthly anomalies at Uccle for erythemal UV dose (D_{ery}^* ; upper left panel), global solar radiation (D_g^* ; upper right panel), total ozone column (Q_{O_3} ; lower left panel) and aerosol optical depth at 320.1 nm ($\tau_{aer,320}$; lower right panel) for the time period 1991–2015. The blue lines represent the time series, whereas the red lines represent the trend over the time period.

6.3.2.1 Erythemal UV dose (D_{ery}^*)

A significant positive trend (at the 99% significance level) can be detected in the time series of monthly anomalies of D_{ery}^* (Figure 50, top left). These values increase by 7% ($\pm 1\%$) per decade. The seasonal trends are presented in Table 30. In spring (March, April and May),

summer (June, July and August) and autumn (September, October and November), D_{ery}^* increases significantly, whereas in winter (December, January and February) the trend is highly negative.

Table 30: Seasonal trends in erythemal UV dose at Uccle (1991-2015).

	Trend per decade	Significance
Spring	9% ± 2%	99%
Summer	6% ± 2%	99%
Autumn	7% ± 2%	95%
Winter	-10% ± 3%	99%

A significant positive trend has been found in the monthly anomalies of both the minimum and maximum values of D_{ery}^* . The minimum values show an increase of 8% ($\pm 4\%$) per decade and the maximum values increased by 6% ($\pm 1\%$) per decade (respectively significant at the 90 and 99% level). The increase in the median value from 1045 J m⁻² (1991–2002) to 1271 J m⁻² (2003–2015) shows that higher D_{ery}^* values are more frequent in the latter period.

6.3.2.2 Global radiation (D_g^*)

The values of D_g^* show an increase of 5% ($\pm 1\%$) per decade at the 99% significance level, which corresponds to an absolute change of +0.54 (± 0.14) W m⁻² per year for the observed time period (Figure 50, top right). On a seasonal scale, spring and autumn exhibit a significant positive trend (Table 31). The seasonal trends of D_g^* , although not significant in summer and winter, have the same sign as the seasonal D_{ery}^* trends. The trends of D_g^* however, are smaller than the D_{ery}^* trends, both on an annual and seasonal scale.

Table 31: Seasonal trends in global radiation at Uccle (1991-2015).

	Trend per decade	Significance
Spring	7% ± 2%	99%
Summer	3% ± 2%	Not
Autumn	5% ± 2%	95%
Winter	-2% ± 4%	Not

On the contrary to D_{ery}^* , we find a clear difference between the trends of the monthly anomalies of minimum and maximum values of D_g^* . Both trends are positive, but the increase in the minimum values (12% \pm 4% per decade at 99% significance level) is much larger than the one in the maximum values (3.1% \pm 0.6% per decade at 99% significance level). Study of the median values reveals the presence of an increase from 8883 kJ m⁻² (1991–2002) to 11140 kJ m⁻² (2003–2015). As the global radiation data are all-sky data, it is obvious that the minimum values are the ones that are influenced by clouds. The fact that the minimum values increase in time suggests that the cloud properties, i.e., their amount and/or water content, have decreased over the past 25 years.

6.3.2.3 Total ozone column (Q_{O_3})

The monthly anomalies of Q_{O_3} show a positive trend of 2.6% ($\pm 0.4\%$) per decade (significant at 99%) (Figure 50, bottom left). Significant positive trends occur in spring and summer (Table 32), with the trend in spring being the largest. Both the minimum and maximum Q_{O_3} values also increased significantly (99% level) and this at about the same rate: 2.9% ($\pm 0.5\%$) per decade for the minimum values and 3.3% ($\pm 0.5\%$) per decade for the maximum values over the past 25 years.

Table 32: Seasonal trends in total ozone column at Uccle (1991–2015).

	Trend per decade	Significance
Spring	3% \pm 1%	95%
Summer	1.7% \pm 0.6%	99%
Autumn	1.6% \pm 0.8%	NOT
Winter	4% \pm 2%	95%

A clear shift can be seen in the frequency distribution (Figure 51) of the daily Q_{O_3} values. During the second period (2003–2015), higher values are more frequent than during the previous period (1991–2002), which is supported by the increase in median values from 321 DU (1991–2002) to 334 DU (2003–2015). As the entire curve of the frequency distribution is shifted, not only the maximum but also the minimum values of the distribution have increased between the two periods. After a period with lower Q_{O_3} values in the 1990s, it seems that ozone has increased since then. Removing the Pinatubo period (1991–1993) from our analysis does not change the trend in Q_{O_3} significantly, which means that the observed increase in ozone is not very much related to the return of the stratosphere to pre-Pinatubo time but rather that it is more likely a result of the regulations of the Montreal Protocol.

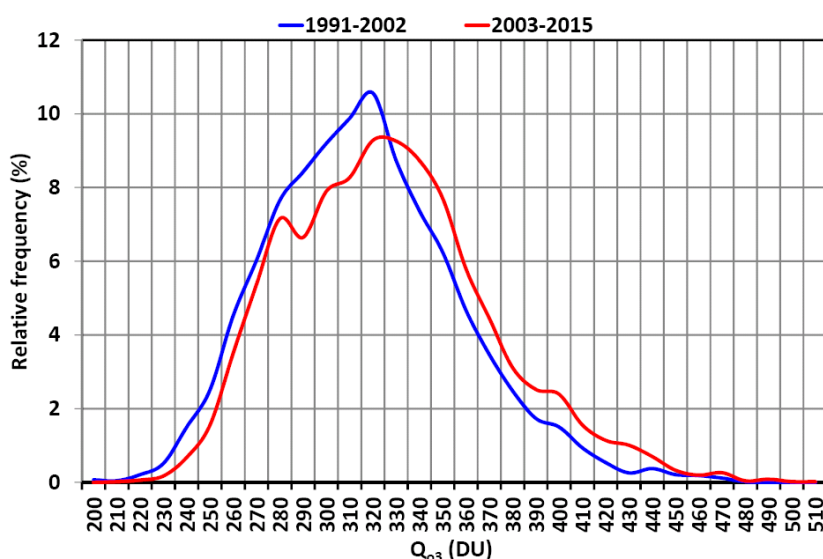


Figure 51 : Relative frequency distribution of daily total ozone column values for the two time periods: 1991–2002 (in blue) and 2003–2015 (in red).

As the Brewer only measures total ozone, it is impossible to use its measurements to determine whether there is a difference between tropospheric and stratospheric trends. However, the ozone sonde data from Uccle can help us to investigate the difference. From these measurements we find that, for the 1991-2015 time period, tropospheric ozone increased with 2% ($\pm 2\%$) per decade. This trend is not statistically significant. Total stratospheric ozone however shows a statistically significant trend of 3.2% ($\pm 0.5\%$) per decade.

Q_{O_3} trends are positive for each season, even for winter (as opposed to the negative winter trends observed in the D_{ery}^* and D_g^* time series). We would expect an increase in Q_{O_3} over these 25 years to be accompanied by a decrease in D_{ery}^* , which is not the case for the Uccle time series. This indicates that other variables might contribute to the change in D_{ery}^* and that the contribution of Q_{O_3} might be masked by the stronger influence of these other variables.

6.3.2.4 AOD at 320.1 nm ($\tau_{aer,320}$)

While the overall trends of D_{ery}^* , D_g^* and Q_{O_3} are all positive, the $\tau_{aer,320}$ values show a negative trend of -4% ($\pm 4\%$) per decade. This trend, however, is not significant (Figure 50, bottom right). While also not statistically significant, the seasonal trends (Table 33) show that the summer and autumn trends are negative, with the largest trend being retrieved during autumn. Due to a lack of sufficient clear-sky data, it was not possible to determine the winter trend for $\tau_{aer,320}$.

Table 33: Seasonal trends in AOD at 320.1 nm at Uccle (1991-2015).

	Trend per decade	Significance
Spring	1% \pm 6%	NOT
Summer	-13% \pm 7%	NOT
Autumn	-26% \pm 13%	NOT
Winter	Not enough data	Not enough data

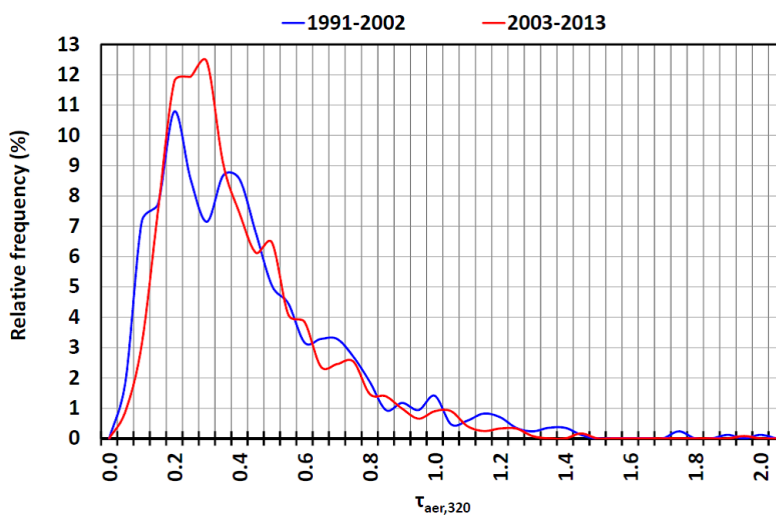


Figure 52: Relative frequency distribution of daily $\tau_{aer,320}$ values for the two time periods: 1991–2002 (in blue) and 2003–2015 (in red).

There are no significant changes in the minimum and maximum $\tau_{\text{aer},320}$ values over the 1991–2015 period. From the relative frequency distribution of the daily $\tau_{\text{aer},320}$ values (Figure 52), our results suggest that the frequency of lower $\tau_{\text{aer},320}$ values ($\tau_{\text{aer},320} < 0.4$) was higher during the second period (2003–2015) while the frequency of high $\tau_{\text{aer},320}$ values ($\tau_{\text{aer},320} > 0.7$) has followed the opposite evolution. This would be in agreement with the overall decrease in $\tau_{\text{aer},320}$ over the last 25 years. However, this cannot be confirmed from the median values, which did not change between the two periods.

6.3.3 Discussion of trends

6.3.3.1 Trends in UV radiation

Physically, UV trends can only be detected from direct UV measurements at the surface of the Earth. Changes in surface UV irradiance have been studied using ground-based measurements at different locations (e.g., den Outer et al., 2000; Sasaki et al., 2002; Bernhard et al., 2006; Fitzka et al., 2012; Zerefos et al., 2012; Eleftheratos et al., 2014). Sometimes ground-based measurements are combined with satellite retrievals (Herman et al., 1996; Matthijsen et al., 2000; Kalliskota et al., 2000; Ziemke et al., 2000; Zerefos et al., 2001; Fioletov et al., 2004; Williams et al., 2004). In addition to the surface UV data, reconstructed UV data can also be studied. Reconstructed data can be based on proxy data such as the abundance of ozone, solar irradiance, sunshine duration or regional reflectivity of the Earth–atmosphere system measured from space (Lindfors et al., 2003) and different reconstruction models have been used in the past. They all use various kinds of statistical or model approaches and different meteorological or irradiance data sets (Lindfors et al., 2007; Chubarova, 2008; Rieder et al., 2010; den Outer et al., 2010; Bais et al., 2011) and are either based on modeling of clear-sky UV irradiance or on empirical relationships between surface UV irradiance and the factors influencing the penetration of UV irradiance through the atmosphere (Kaurola et al., 2000; Trepte and Winkler, 2004). The uncertainties of the used parameters and the applied methodologies increase the uncertainty of the reconstructed UV irradiance when compared to actual surface UV measurements (Fountoulakis et al., 2016a). Some studies combine both models and observations to investigate possible UV irradiance changes (e.g., Kaurola et al., 2000).

Long-term UV trends for different locations around the world have been the subject of several research articles (e.g., den Outer et al., 2000; Zerefos et al., 2012; Eleftheratos et al., 2014), and it is interesting to investigate the consistency of the results obtained from Uccle in this work with these earlier studies, even though the time periods are not exactly the same. Trends (observed or modeled/reconstructed) reported in the literature, relevant for our work, are presented in Table 34. Looking at these trends, it can be seen that for the stations with comparable latitude to Uccle (45–55°N), the trends in UV range from -2.1 (Hradec Kralove) to +14.2% (Hoher Sonnblick) per decade which is consistent with the +7% ($\pm 1\%$) per decade that we measure at Uccle. The comparison has to be made with caution considering that not all trends in Table 34 are calculated in the same way as the one at Uccle. At Uccle, trends are indeed based on monthly anomalies, which are essentially calculated from daily doses. As such, all effects such as those from clouds are included in our analysis. This is not the case for

all values reported in Table 34. Furthermore some of the studies report trends at a certain fixed solar zenith angle, which does not cover the same range of effects as the daily sum does, and thus the trends may not be truly comparable.

Table 34: Trends of UV radiation at different stations from (a) Bais et al. (2007), (b) Krzýscin et al. (2011), (c) Smedley et al. (2012), (d) Fitzka et al. (2012), € den Outer et al. (2010) , (f) Chubarova (2008) and (g) Fountoulakis et al. (2016a).

Station, country	Latitude/longitude	Period	Trend/decade	Reference
Measured UV trends				
Uccle, Belgium	50°48'N, 4°21'E	1991-2015	+7% ($\pm 1\%$)	This work
Sodankylä, Finland	67.42°N/26.59°E	1990-2004	+2.1% (60° SZA)	(a)
Jokioinen, Finland	60.80°N/23.49°E	1996-2005	-1.9% (60° SZA)	(a)
Norrköping, Sweden	58.36°N/16.12°E	1996-2004	+12% (60° SZA)	(a)
Bilthoven, The Netherlands	52.13°N/5.20°E	1996-2004	+8.6% (60° SZA)	(a)
Belsk, Poland	51.83°N/20.81°E	1976-2008	+5.6%	(b)
Reading, United Kingdom	51.45°N/0.98°W	1993-2008	+6.6%	€
Hradec Kralove, Czech Republic	50.21°N/15.82°E	1994-2005	-2.1% (60° SZA)	(a)
Lindenberg, Germany	47.60°N/9.89°E	1996-2003	+7.7% (60° SZA)	(a)
Hoher Sonnblick, Austria	47.05°N/12.96°E	1997-2011	+14.2% (65° SZA)	(d)
Thessaloniki, Greece	40.63°N/22.95°E	1990-2004	+3.4% (60° SZA)	(a)
Thessaloniki, Greece	40.63°N/22.95°E	1994-2014	+3 to 4% (clear skies) +3.5 to 4.5% (all skies)	(g)
Reconstructed or modeled UV trends				
Sodankylä, Finland	67.42°N/26.59°E	1980-2006	+3.6%	€
Jokioinen, Finland	60.80°N/23.49°E	1980-2006	+2.8%	€
Norrköping, Sweden	58.36°N/16.12°E	1980-2006	+4.1%	€
Moscow, Russia	55.75°N/37.62°E	1980-2006	+6%	€
Bilthoven, The Netherlands	52.13°N/5.20°E	1980-2006	+2.9%	€
Hradec Kralove, Czech Republic	50.21°N/15.82°E	1980-2006	+5.2%	€
Lindenberg, Germany	47.60°N/9.89°E	1980-2006	+5.8%	€
Thessaloniki, Greece	40.63°N/22.95°E	1980-2006	+4.4%	€

On a more global scale, Zerefos et al. (2012) examined UV irradiance over selected sites in Canada, Europe and Japan between 1990 and 2011. The results, based on observations and modeling for all stations, showed an increase in UV irradiances of 3.7% ($\pm 0.5\%$) and 5.5% ($\pm 0.3\%$) per decade at respectively 305 and 325 nm. For Europe, only the trend at 325 nm (3.4% ($\pm 0.4\%$) per decade) was significant. The European Cooperation on Science and Technology (COST) 726 action⁵⁹ (Litynska et al., 2012) calculated trend values for European sites and

⁵⁹ www.cost726.org; visited 28/11/2016

concluded on a mean positive trend of 4.5% ($\pm 0.5\%$) per decade since 1980, which was derived from reconstruction models, based on measured total ozone and total solar irradiance. Bais et al. (2015) reported on linear trends in erythemal UV dose between 0 and +5% per decade between 50°S and 50°N over the period 1997–2010 based on TOMS and OMI satellite data. The range of trends shows the importance of local conditions and makes the comparison with the values calculated at Uccle difficult.

6.3.3.2 Trends in global solar radiation

Concerning the global solar radiation, the global consensus refers to the existence of a solar dimming period (characterized by a decrease in surface solar radiation) between 1970 and 1985 and a subsequent solar brightening period (characterized by an increase in surface solar radiation) (Norris and Wild, 2007; Solomon et al., 2007; Makowski et al., 2009; Stjern et al., 2009; Wild et al., 2009a/b; Sanchez-Lorenzo and Wild, 2012; Sanchez-Lorenzo et al., 2015). These two periods are highlighted not only by studies focusing on specific regions but also by studies focusing on worldwide datasets (Manara et al., 2016 and references therein).

The causes of these decadal variations are not completely clear, but it has been suggested that changes in the anthropogenic aerosols and cloud cover could be major causes (Garcia et al., 2014; Manara et al., 2016 and references therein). The increase in anthropogenic aerosol emissions in the 20th century in particular is thought to be the major cause of the observed decadal surface solar radiation (SSR) reduction until the 1980s, while measures to reduce air pollution in the late 20th century are possibly responsible for the renewed increase in SSR (Manara et al., 2016 and references therein). Nevertheless, the relative contribution of clouds and aerosols is not well quantified from the observations only (Manara et al., 2016). Several studies have been conducted with the objective to disentangle the two contributions by using global climate models, satellite derived products and ground-based observations. They identify aerosols as the dominating contributor to SSR variability on a decadal scale (Li et al., 2007; Zhang et al., 2015; Wild, 2016). Some studies underline the important contribution of clouds, especially on an interannual scale (Norris and Wild, 2007; Folini and Wild, 2011; Mateos et al., 2014; Parding et al., 2014).

Table 35 collects the trends in global solar radiation after 1985 over Europe as reported in the literature. The trend in D_g^* from GEBA (Global Energy Balance Archive⁶⁰) between 1987 and 2002 is equal to $+1.4 (\pm 3.4) \text{ W m}^{-2}$ per decade according to Norris and Wild (2007). This time series was extended by Sanchez-Lorenzo et al. (2015) who found a trend of $+3.2 \text{ W m}^{-2}$ per decade over the 1986–2012 period. Stjern et al. (2009) found a similar increase in the mean surface solar radiation over 11 stations in northwestern Europe of +4.4% between 1983 and 2003 and for Hamburg, Germany, which is the station closest to Uccle, they report a 8.8% trend for the entire period. Bais et al. (2013) found an upward trend of 3.3% per decade in shortwave downward solar irradiance received over Thessaloniki for the 1993–2011 period. In Wild et al. (2005), 421 sites of the Baseline Surface Radiation Network (BSRN), distributed globally, were analyzed and between 1992 and 2002, the change of all-sky surface solar radiation was estimated to 0.66 W m^{-2} per year. A similar large-scale study was conducted by

⁶⁰ http://www.iac.ethz.ch/groups/schaer/research/rad_and_hydro_cycle_global/geba/ visited on 28/9/2016

Wild et al. (2009b), who investigated the global solar radiation from 133 stations from GEBA/World Radiation Data Centre belonging to different regions in Europe: all time series showed an increase over the entire period, with a more pronounced upward trend since 2000. For the Benelux region, the linear trend between 1985 and 2005 amounts to $+0.42 \text{ W m}^{-2}$ per year, somewhat larger than the pan-European average trend of $+0.33 \text{ W m}^{-2}$ per year (or $+0.24 \text{ W m}^{-2}$ if the anomaly of the 2003 heat wave is excluded) (Wild et al. 2009b). The trend at Uccle calculated in this work is $+0.54 (\pm 0.14) \text{ W m}^{-2}$ per year (or $+5\% (\pm 1\%)$ per decade), which agrees within the error bars with the results from Wild et al. (2009). The differences could be related at least in part to the different time periods investigated: i.e. 1991-2015 in this work and 1985-2005 in Wild (2009b).

Table 35 : Observed trends in global radiation.

Region or station	Period	Trend	Reference
Uccle, Belgium	1991-2015	$+5\% (\pm 1\%)$ per decade $+0.54 (\pm 0.14) \text{ W m}^{-2}$ per year	This work
Pan-European (GEBA stations)	1987-2002	$+1.4 (\pm 3.4) \text{ W m}^{-2}$ per decade	Norris & Wild, 2007
	1986-2012	$+3.2 \text{ W m}^{-2}$ per decade	Sanchez-Lorenzo et al., 2015
Northwestern Europe (11 stations)	1983-2003	$+4.4\%$ (total trend)	Stjern et al., 2009
Hamburg, Germany	1983-2003	$+8.8\%$ (total trend)	Stjern et al., 2009
Thessaloniki	1993-2011	$+3.3\%$ per decade	Bais et al., 2013
Europe (421 stations)	1992-2002	$+0.66 \text{ W m}^{-2}$ per year	Solomon et al., 2007
Benelux	1985-2005	$+0.42 \text{ W m}^{-2}$ per year	Wild et al., 2009
Pan-European	1985-2005	$+0.33 \text{ W m}^{-2}$ per year $+2.5\%$ per decade	Wild et al., 2009b
Pan-European	1985-2005 (without 2003 heat wave)	$+0.24 \text{ W m}^{-2}$ per year $+1.8\%$ per decade	Wild et al., 2009b

6.3.3.3 Trends in total ozone

The changes in total ozone and the determination of its trends have been the subject of extensive scientific research since the discovery of ozone depletion. It is well established that ozone has decreased since 1980 to the mid-1990s as a consequence of anthropogenic emissions of ODSs and it is now thought that this period of decrease is followed by a period of increase which will need to be confirmed by extending the trends in the future (Steinbrecht et al., 2006; Harris et al., 2008; Vigouroux et al., 2008; Krzýscin and Borkowski, 2008; Herman, 2010; Bais et al., 2011; Bais et al., 2015; Solomon et al., 2016). According to the WMO (2014), the beginning of the period 1997-2014 coincides with the mid-latitude stratospheric peak values of the equivalent effective stratospheric chlorine (EESC), which refers to the sum of chlorine and bromine abundances originating from ODS tropospheric abundances, weighted to reflect their potential influence on ozone (Van Malderen et al., 2016). The turnaround in ozone trends after the mid-1990s could therefore be seen as a result

of the successful implementation of the Montreal protocol (Bais et al., 2015). However, even if an effect of the Montreal Protocol is suggested by the turnaround in the ozone trend, it is difficult to unambiguously attribute this to changes in ODSs because other factors also contribute to ozone variability and trends (Harris et al., 2008; Bais et al., 2015). These include large volcanic eruptions, long-term climate variability, changes in the stratospheric circulation and the 11-year solar cycle (Harris et al., 2008; Vigouroux et al., 2008). According to Rieder et al. (2013), the influence of dynamical features (such as the El Niño–Southern Oscillation, North Atlantic Oscillation and Quasi-Biennial Oscillation) on the ozone variability and trends can also not be neglected at a regional level.

Table 36: Trends of total ozone column at different stations from (a) Glandorf et al. (2005), (b) Smedley et al. (2012), (c) Bartlett and Webb (2000), (d) Bojkov et al. (1995), (e) Zerefos et al. (1997), (f) Fitzka et al. (2012), (g) Staehelin et al. (1998b), (h) Vigouroux et al. (2008) and (i) Fountoulakis et al. (2016a).

Station, country	Latitude/longitude	Period	Trend/decade	Reference
Uccle, Belgium	50°48'N, 4°21'E	1991-2015	+2.6% (\pm 0.4%)	This work
Sodankylä, Finland	67.42°N/26.59°E	1979–1998	-5.7%	(a)
Lerwick, United Kingdom	60.15°N/1.15°W	1979–1993	-5.8%	(b)
Reading, United Kingdom	51.45°N/0.98°W	1993–1997	-5.9%	(c)
Brussels, Belgium	50.84°N/4.36°E	1971–1994	-2.6%	(d)
Brussels, Belgium	Idem	1993–1996	-15%	(e)
Hradec Kralove, Czech Republic	50.21°N/15.82°E	1994–2005	-2.2%	(d)
Hohenpeisenberg, Germany	47.80°N/11.00°E	1968–1994	-3.5%	(d)
Hoher Sonnblick, Austria	47.05°N/12.96°E	1997–2011	+1.9%	(f)
Arosa, Switzerland	46.77°N/9.67°E	1964–1994	-2.7%	(d)
Arosa, Switzerland	Idem	1970–1996	-2.3%	(g)
Jungfrauoch, Switzerland	46.55°N/7.98°E	1995–2004	+4.1%	(h)
Thessaloniki, Greece	40.63°N/22.95°E	1993–1996	-4.0%	(e)
Thessaloniki, Greece	40.63°N/22.95°E	1990–1998	-4.5%	(a)
Thessaloniki, Greece	40.63°N/22.95°E	1994–2014	+0.8%	(i)

More specifically, for the period before the mid-1990s, studies report on decreasing ozone values at Brussels (Bojkov et al., 1995; Zerefos et al., 1997), Reading (Bartlett and Webb, 2000), Lerwick (Smedley et al., 2012), Arosa (Bojkov et al., 1995; Staehelin et al., 1998b), Hohenpeissenberg (Bojkov et al., 1995), Sodankylä (Glandorf et al., 2005) and Thessaloniki (Glandorf et al., 2005) (see Table 36). After the mid-1990s, the ozone evolution is characterized by a plateau or a limited increase (Bais et al., 2015). For example, Smedley et al. (2012) found no clear ozone trend in the 1993–2008 period for Reading. Ozone observations from a Brewer instrument at Hoher Sonnblick (Fitzka et al., 2012) showed a small but significant increase between 1997 and 2011. Similar behavior was reported for Jungfrauoch in Vigouroux et al. (2008). The trend of +2.6% per decade, found at Uccle for

the 1991-2016 period (see Figure 50), compares well with the one observed at Hoher Sonnblick, which is the only station with a time period comparable to the one at Uccle. Also, at Hoher Sonnblick, a decline in the frequency of low ozone events and increase in high ozone events was observed between 1994 and 2011 (Fitzka et al., 2014), similar to what is observed at Uccle (Figure 51).

We studied the trend in total ozone column before and after 1998⁶¹ and found a trend reversal in the Brewer#016 time series with a negative trend of -4 % (\pm 3%) per decade before 1998 and a positive trend of +1.4% (\pm 0.6%) per decade after 1998 (Figure 53).

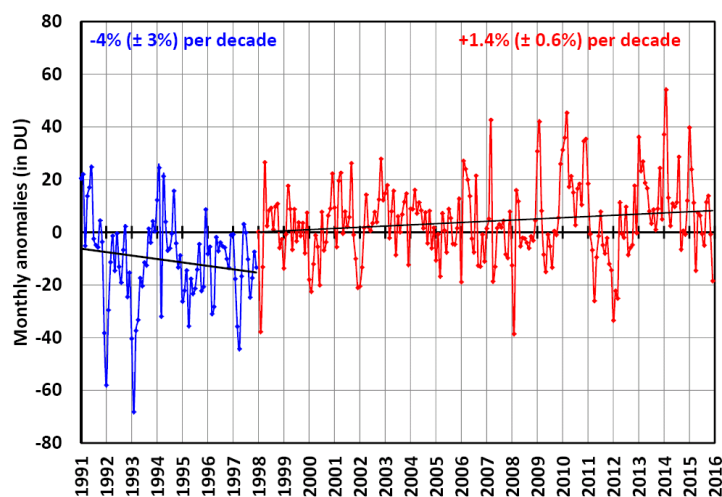


Figure 53 : Trend in monthly anomalies of total ozone for the period before and after 1998. The first period (1991-1997) is characterized by a negative trend of -4% (\pm 3%) per decade (not significant), whereas the trend in the second period (1998-2015) is positive and equal to +1.4% (\pm 0.6%) per decade. Both trends are not significant (tested at the 95% significance level).

This trend reversal is also present in the stratospheric ozone time series (based on data from the ozone sonde time series) at Uccle (Figure 54). For the period from 1991 up to 1998, a negative trend of -3% (\pm 4%) per decade (not significant) can be observed, followed by a positive trend from 1998 to 2015 of 1.9% (\pm 0.8%) per decade (significant at 90% significance level). Tropospheric ozone trends change from -13% (\pm 5%) per decade between 1991 and 1998 to +6% (\pm 1%) per decade between 1998 and 2015. (Both tropospheric trends are significant at the 95% significance level.)

⁶¹ 1998 was chosen based on the change point found in the 1991-2013 time series

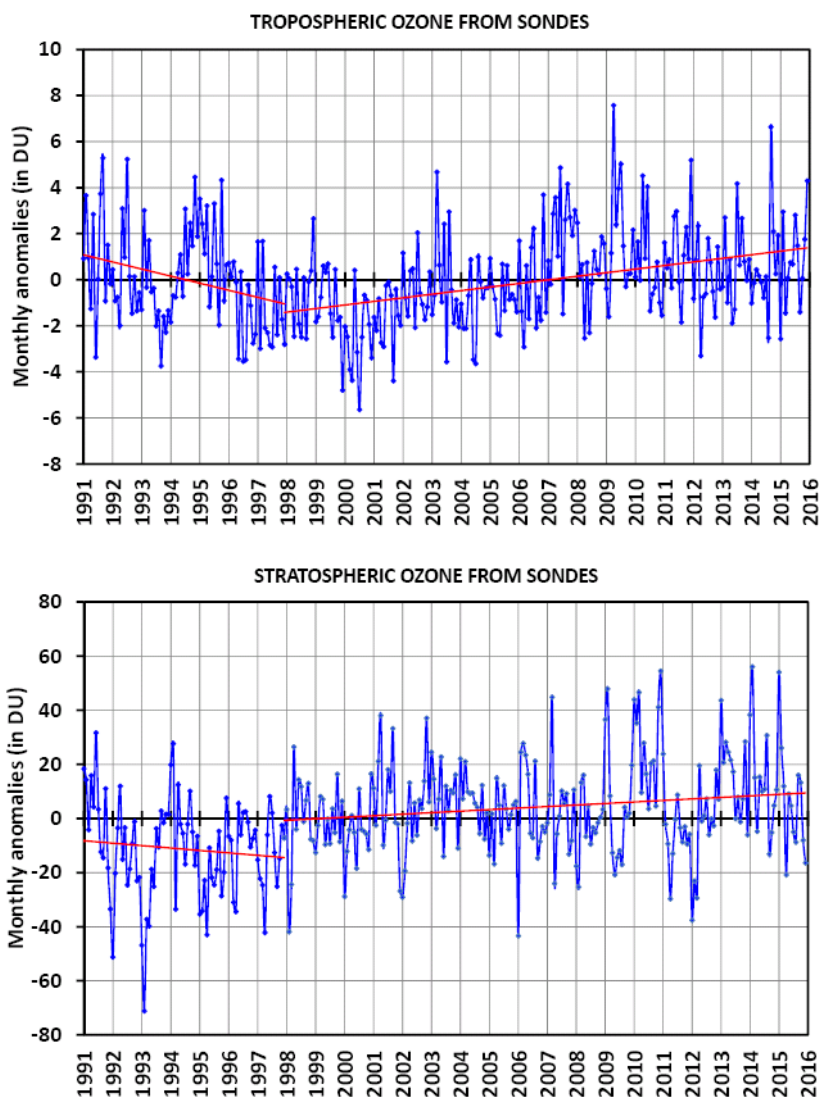


Figure 54 : Trends in monthly anomalies of tropospheric and stratospheric ozone for the period before and after 1998. Tropospheric ozone decreased with 13% ($\pm 5\%$) per decade for the 1991-1997 period and increased with 6% ($\pm 1\%$) per decade between 1998 and 2015. The trend in stratospheric ozone changes from a negative trend of -3% ($\pm 4\%$) per decade between 1991-1997 to a positive trend of +1.9% ($\pm 0.8\%$) per decade between 1998-2015.

6.3.3.4 Trends in AOD

Contrary to UV and ozone measurements, trend analysis studies of long time series of AOD are still very scarce. We have gathered in Table 37 some of the values found in the literature for European stations and find that the trend of $-4\% \pm 4\%$ per decade observed at Uccle, although not significant, lies within the range of most trends observed at other European stations. On a continental scale, Mishchenko and Geogdzhayev (2007) observed a significant decrease in AOD from 1991 to 2005 over much of Europe within the Global Aerosol Climatology Project (GACP⁶²) data. Alpert et al. (2012) used AOD measurements from MODIS and MISR satellites over the 189 largest cities in the world and reported a decreasing trend in AOD over European cities for the 2002–2010 period. The decadal trend observed by

⁶² <http://gacp.giss.nasa.gov/>

de Meij et al. (2012) over Europe between 2000 and 2009 was negative for MODIS (-30%), MISR (-9%) and AERONET (-25%). Zerefos et al. (2012), who investigated the AOD over Europe, Japan and Canada, discovered a general decline in AOD exceeding 10% per year. For Europe specifically, the trend of AOD varied between -16.6% ($\pm 6\%$) per decade when using the GACP data set and -42.8% ($\pm 5.7\%$) for the MODIS data set. Fountoulakis et al. (2016a) found a negative trend of -17% per decade for the 1990-2014 period in Thessaloniki.

Table 37: Relative trends of AOD at different stations from (a) Alpert et al. (2012), (b) Nyeki et al. (2012), (c) Fitzka et al. (2012), (d) Kazadzis et al. (2007) and (e) Fountoulakis et al. (2016a). MODIS-Terra, MODIS-Aqua and MISR measurements are represented by respectively “a”, “b” and “c” after the station name.

Station, country	Latitude/longitude	Period	Trend/decade	Reference
Uccle, Belgium	50°48'N, 4°21'E	1991-2015	-4% ($\pm 4\%$)	This work
Berlin (a), Germany	52.50° N/13.40° E	2002-2010	-20.5%	(a)
Berlin (b), Germany	52.50° N/13.40° E	2002-2010	-17.9%	(a)
Berlin I, Germany	52.50° N/13.40° E	2002-2010	-12.3%	(a)
Warsaw (a), Poland	52.30° N/21.00° E	2002-2010	-2.4%	(a)
Warsaw (a), Poland	52.30° N/21.00° E	2002-2010	-0.4%	(a)
Warsaw (a), Poland	52.30° N/21.00° E	2002-2010	12.9%	(a)
Ruhr Area (a), Germany	51.50° N/7.50° E	2002-2010	-15.7%	(a)
Ruhr Area (a), Germany	51.50° N/7.50° E	2002-2010	-9.3%	(a)
Ruhr Area (a), Germany	51.50° N/7.50° E	2002-2010	-9.3%	(a)
Paris (a), France	48.90° N/2.40° E	2002-2010	-8.1%	(a)
Paris (a), France	48.90° N/2.40° E	2002-2010	+5.0%	(a)
Paris (a), France	48.90° N/2.40° E	2002-2010	+9.8%	(a)
Hohenpeisenberg, Germany	47.80° N/11.00° E	1995-2010	-10.6%	(b)
Hohenpeisenberg, Germany	47.80° N/11.00° E	1997-2011	-5 to -6%	(c)
Barcelona (a), Spain	41.40° N/2.20° E	2002-2010	-8.8%	(a)
Barcelona (a), Spain	41.40° N/2.20° E	2002-2010	+4.2%	(a)
Barcelona (a), Spain	41.40° N/2.20° E	2002-2010	-2.3%	(a)
Thessaloniki, Greece	40.63° N/22.95° E	1997–2006	-29%	(d)
Thessaloniki, Greece	40.63° N/22.95° E	1990-2014	-17%	(e)
Madrid (a), Spain	40.40° N/3.70°W	2002-2010	-18.3%	(a)
Madrid (a), Spain	40.40° N/3.70°W	2002-2010	-10%	(a)
Madrid (a), Spain	40.40° N/3.70°W	2002-2010	-7.4%	(a)

This overall long-term AOD decrease over much of Europe is consistent with the supposed reversal from increasing to decreasing anthropogenic sulfur and black carbon emissions owing to the enactment of clean-air legislation in many countries (Mishchenko and Geogdzhayev, 2007; Chiaccio et al., 2011; Alpert et al., 2012; de Meij et al., 2012; Hsu et al., 2012; Nabat et al., 2013). This change occurred after 1988–1989, the time period when a maximum was reached in the emissions of sulfate aerosols over Europe (Chiaccio et al., 2011). The decrease in SO_x and BC can also be seen in the long time series of emissions over Belgium in Figure 47. Many scientists argue that the decadal changes in aerosols have influenced the amount of solar radiation reaching the surface of the Earth and that the decrease in aerosols has played a part in the switch from global dimming to global brightening, which occurred around 1980–1990 (Chiaccio et al., 2011). As discussed in the previous sections and according to Wild et

al. (2009b), the reduction of aerosols is likely to have played a role in the increase of surface UV during the 1990s but not after 2000. A likely explanation is that the decreases in cloudiness or cloud albedo have contributed to the increase in surface solar radiation over Europe beyond 2000, despite the stabilization of aerosol concentrations.

6.4 Multiple linear regression (MLR) analysis

6.4.1 Method

The goal of a MLR analysis is to determine the values of parameters for a linear function that cause this function to best describe a set of provided observations (Krishna Prasad et al., 2011). In this study, the MLR technique is used to go further in the analysis of the time evolution of D_{ery}^* , D_g^* , Q_{O_3} and $\tau_{aer,320}$ at Uccle by, rather than focusing on individual linear regression trends as in section 6.3, exploring whether there is a significant relationship between the various variables described. Specifically, we investigate the relation between D_{ery}^* and three explanatory variables (D_g^* , Q_{O_3} and $\tau_{aer,320}$) both on a daily and seasonal scale.

A linear model where the coefficients are determined with the least-squares minimization method is used. For the daily model, harmonic time series with a period of a year and half a year are included to account for variation in UV on these time scales as was done for example by Wespes et al. (2016) for their work on the ozone time series from IASI.

The general daily model is written as:

$$D_{ery}^* = Cst + a \cdot D_g^* + b \cdot Q_{O_3} + c \cdot \tau_{aer,320} + d \cdot \sin(\omega \cdot t) + e \cdot \cos(\omega \cdot t) + f \cdot \sin(2 \cdot \omega \cdot t) + g \cdot \cos(2 \cdot \omega \cdot t) + \varepsilon \quad (60)$$

with

D_{ery}^* :	erythemal UV dose (in $J \cdot m^{-2}$)
D_g^* :	normalized global solar radiation
Q_{O_3} :	normalized total ozone column
$\tau_{aer,320}$:	normalized AOD at 320.1 nm
$\omega = \frac{2\pi}{365.25}$	
t:	number of day
Cst:	constant term
a, b, c, d, e, f, g:	regression coefficients
ε :	error term

D_g^* , Q_{O_3} and $\tau_{aer,320}$ have been normalized following Eq. 61:

$$X_{norm} = 2 \cdot \left[\frac{X(t) - X_{median}}{X_{max} - X_{min}} \right] \quad (61)$$

For the seasonal model, the harmonic time series have no physical sense and are not included. The seasonal MLR model is written as:

$$D_{ery}^* = Cst + a \cdot D_g^* + b \cdot Q_{O_3} + c \cdot \tau_{aer,320} + \varepsilon \quad (62)$$

Although the attenuation of radiation by ozone is not linear (according to the Beer–Lambert law), we consider total ozone column as a linear independent variable, based on the limited variation of this variable throughout the year and throughout the different seasons. For the MLR analysis to produce trustworthy results, the distribution of the errors of the model should be normal (Williams et al., 2013). Non-normal errors may mean that the t and F statistics of the coefficients may not actually follow t and F distributions and that the model might underestimate reality. However, as stated in Williams et al. (2013), even if errors are not normally distributed, the sampling distribution of the coefficients will approach a normal distribution as sample size grows larger⁶³. As we have a large data set available at Uccle for the MLR analysis, we can assume that the distribution of the coefficients of the MLR model approaches normality.

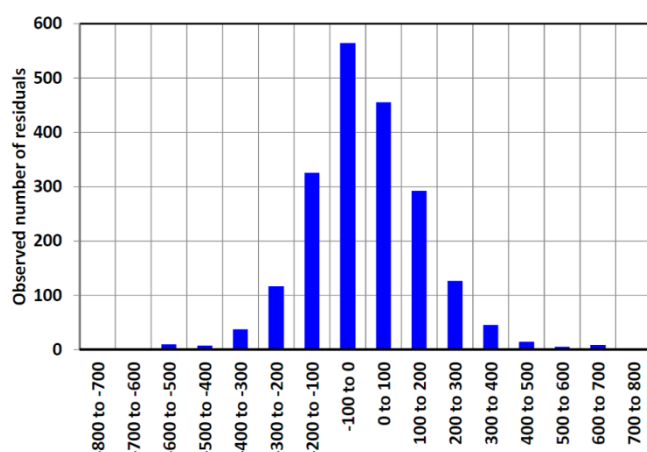


Figure 55 : Histogram of the residuals (in J m⁻²; presented on the x-axis) of MLR 1.

Visual inspection of the distribution of the residuals of MLR 1 (Figure 55) shows that they are indeed close to a normal distribution. The skewness (i.e. measure of asymmetry) and kurtosis (i.e. measure of peakedness) are respectively 0.29 and 1.57, which, according to West et al. (1996)⁶⁴, means that the distribution can be assumed normal.

The performance of the regression model and its parameters is evaluated through different statistical parameters. The adjusted R² value is the measure for the fraction of variation in D_{ery}^* explained by the regression, accounting for both the sample size and the number of explanatory variables. Compared to the R² value, the adjusted R² value only increases if a new variable has additional explanatory power. It is possible to test the null hypothesis that a

⁶³ Ghasemi & Zahediasi (2012) state that for sample sizes larger than 30-40, the sampling distribution tends to be normal regardless of the shape of the data

⁶⁴ West et al. (1996) proposed to use the following thresholds to determine whether a distribution is normal: the absolute skewness value should be smaller than 2 and the absolute kurtosis value should be smaller than 7.

regression coefficient is equal to 0, which would mean that the variable associated with this regression coefficient does not contribute to explaining the variation in D_{ery}^* . This is done by looking at the p-value. If we want to test whether a regression coefficient differs significantly from 0 at the 5% level, the p-value should be less than or equal to 0.05. The quantitative influence of the variation in the three parameters on the variation of D_{ery}^* is determined by multiplying the standard deviation of each parameter with its corresponding regression coefficient and dividing this by the average D_{ery}^* value (Mäder et al., 2007).

The mean bias error (MBE) and the mean absolute bias error (MABE) are calculated in order to evaluate the overall performance of the regression model. The MBE (given in %) provides the mean relative difference between modeled and measured values (Antón et al., 2009):

$$MBE = 100 \cdot \frac{1}{N} \sum_{i=1}^N \frac{D_{ery}^{*,modeled} - D_{ery_i}^{*,measured}}{D_{ery_i}^{*,measured}} \quad (63)$$

The MABE (given in %) reports on the absolute value of the individual differences between modeled and measured data (Antón et al., 2009):

$$MABE = 100 \cdot \frac{1}{N} \sum_{i=1}^N \frac{|D_{ery_i}^{*,modeled} - D_{ery_i}^{*,measured}|}{D_{ery_i}^{*,measured}} \quad (64)$$

Before applying the MLR technique to the Uccle time series, we have verified that the explanatory variables (D_g^* , Q_{O3} and $\tau_{aer,320}$) are independent variables. This was done by calculating the correlation coefficients between these parameters, which we found low enough (< 0.25) to consider these variables as independent. As opposed to the linear regression analysis method applied and discussed in section 6.3, the MLR is applied to daily values. For D_{ery}^* and D_g^* , the daily doses were used, whereas for Q_{O3} and $\tau_{aer,320}$ daily mean values were used.

Two different regression models are built and compared. The first model (MLR 1) is based on all 2007 data points between 1991 to 2015 and its overall performance is assessed using the same data set. However, it is known that there is a chance of over-fitting⁶⁵ when using the same data set to fit a model and assess this fit (Starkweather, 2011). In this case, the residuals of the model will be biased low. In order to assess the predictability of the model, a cross validation technique, which does not use the entire data set necessary to build the model, is employed. So, for the second model (MLR 2), the original dataset is randomly split in half. The first part of the data (i.e. the training set; which contains 1004 values between 1991 and 2015) is used to construct the MLR model, whereas the second part (i.e. the testing set; containing the remaining 1003 values between 1991 and 2015) is used for the validation of the predictive power of the MLR model.

⁶⁵ Over-fitting refers to when the model requires more information than the data can provide

6.4.2 Results

6.4.2.1 MLR analysis of daily D_{ery}^*

As just explained, MLR 1 is developed using the entire available data set, which contains 2007 simultaneous daily values of erythemal UV dose (D_{ery}^*) and daily normalized values of global solar radiation (D_g^*), total ozone (Q_{O3}) and aerosol optical depth at 320.1 nm ($\tau_{aer,320}$) between 1991 and 2015. MLR 2 uses a restricted training set of 1004 simultaneous daily values of these variables. In both cases, the amount of regression days was highly limited by the available $\tau_{aer,320}$ measurements.

Table 38: Comparison of the two different regression models MLR 1 and MLR 2. The table shows the multiple linear regression equations, the adjusted R^2 values and the relative changes in D_{ery}^* due to the different parameters. The performance of the models is given by the correlation, regression equation, MBE and MABE.

	MLR 1	MLR 2
Training data set	All data between 1991 – 2015	Half of the data between 1991-2015
Model equation (with D_{ery}^* in $J\ m^{-2}$)	$D_{ery}^* = 1972 + 1358 \cdot D_g^* - 599 \cdot Q_{O3} - 137 \cdot \tau_{aer,320} + 107 \cdot \sin(\omega t) - 744 \cdot \cos(\omega t) + 26 \cdot \sin(2\omega t) + 232 \cdot \cos(2\omega t) + \epsilon$	$D_{ery}^* = 1995 + 1446 \cdot D_g^* - 594 \cdot Q_{O3} - 107 \cdot \tau_{aer,320} + 87 \cdot \sin(\omega t) - 660 \cdot \cos(\omega t) + 24 \cdot \sin(2\omega t) + 233 \cdot \cos(2\omega t) + \epsilon$
Adjusted R^2	0.98	0.98
Relative change in D_{ery}^* due to		
D_g^*	33%	36%
Q_{O3}	-9%	-9%
$\tau_{aer,320}$	-2%	-1%
$\sin(\omega t)$	4%	3%
$\cos(\omega t)$	-21%	-19%
$\sin(2\omega t)$	1%	1%
$\cos(2\omega t)$	8%	8%
Validation		
Testing set	All data between 1991 – 2015	The other half of the data between 1991-2015 not used as training set
Correlation	0.99	0.99
Regression equation	$f(x) = 0.98x + 40.57$	$f(x) = 0.98x + 44.73$
MBE	-0.82%	-0.40%
MABE	10%	10%

The two models are compared in Table 38. We see that both models have an adjusted R^2 value of 0.98, which means that the explanatory variables explain 98% of the variation in daily D_{ery}^* . The coefficients of the model equations differ only slightly. The changes in D_{ery}^* caused by the variation of the explanatory variables are calculated by multiplying the standard deviation of each parameter with its corresponding regression coefficient and dividing this by

the average value of D_{ery}^* . The resulting values for both models are also provided in Table 38. The results show that in both models D_g^* (~35%) and the harmonic time series have the biggest influence on D_{ery}^* , followed by Q_{O_3} (~9%); $\tau_{aer,320}$ contributes marginally (~1-2%). MLR 1 is validated using the same data set that was used to build the regression model itself, whereas MLR 2 is validated using the remaining data, i.e. which are not used as training set. The results of the validation is provided in Table 38, Figure 56 and Figure 57. The regression equations and correlation coefficients of both models reveal a good agreement between the models and reality with correlation coefficients of 0.99. Both models have a minor tendency to underestimate the measurements, which is shown by the slightly negative MBE values (-0.82% and -0.40% for MLR 1 and MLR 2 respectively). Especially the very low and very high D_{ery}^* are underestimated as can be seen from Figure 57. The MABE, which is a useful measure to evaluate the overall performance of the model, equals 10% for both models, implying that D_{ery}^* is reproduced by the models with a mean error of 10 %.

Figure 56 and the upper panel of Figure 57 show that, in some cases, negative D_{ery}^* doses are modeled, which is unphysical. This is the case only during winter, when the D_g^* values are indeed very low and when Q_{O_3} are at the same time moderate to high. The bottom panel of Figure 57 shows the fit residual. Clearly, the residual shows a slight seasonal variation. Therefore, it was decided to apply the multiple regression analysis on a seasonal scale to see if these seasonal models provide better results.

Overall, MLR 1 and MLR 2 perform equally and only small differences can be found (Table 38, Figure 56 and Figure 58). However, depending on the objective, one of the models could be chosen over the other. For instance, when assessing the overall performance of the model, MLR 1 gives the most comprehensive picture, but for a more general study of the predictability, MLR 2 should be used.

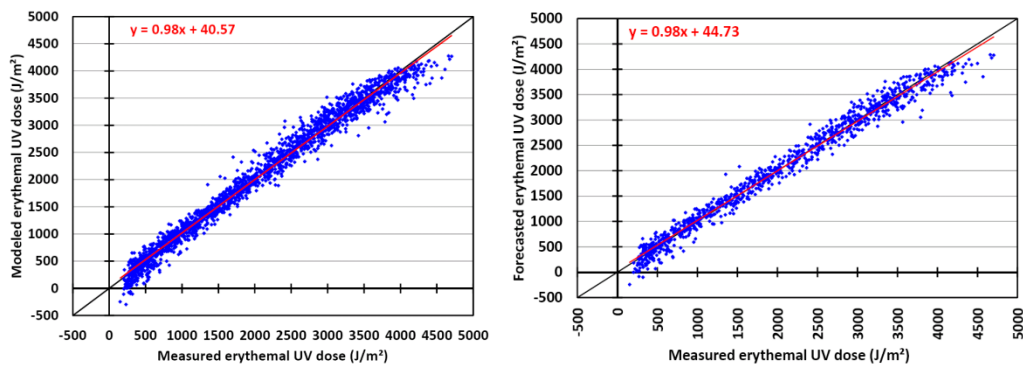


Figure 56 : Scatterplots of the measured and modeled erythemal UV doses at Uccle for the 1991–2015 period. The red line represents the regression line of the data and the black line is the $f(x)=x$ line. The plot on the left side represents the validation of MLR 1 and the one on the right side represents the validation of MLR 2.

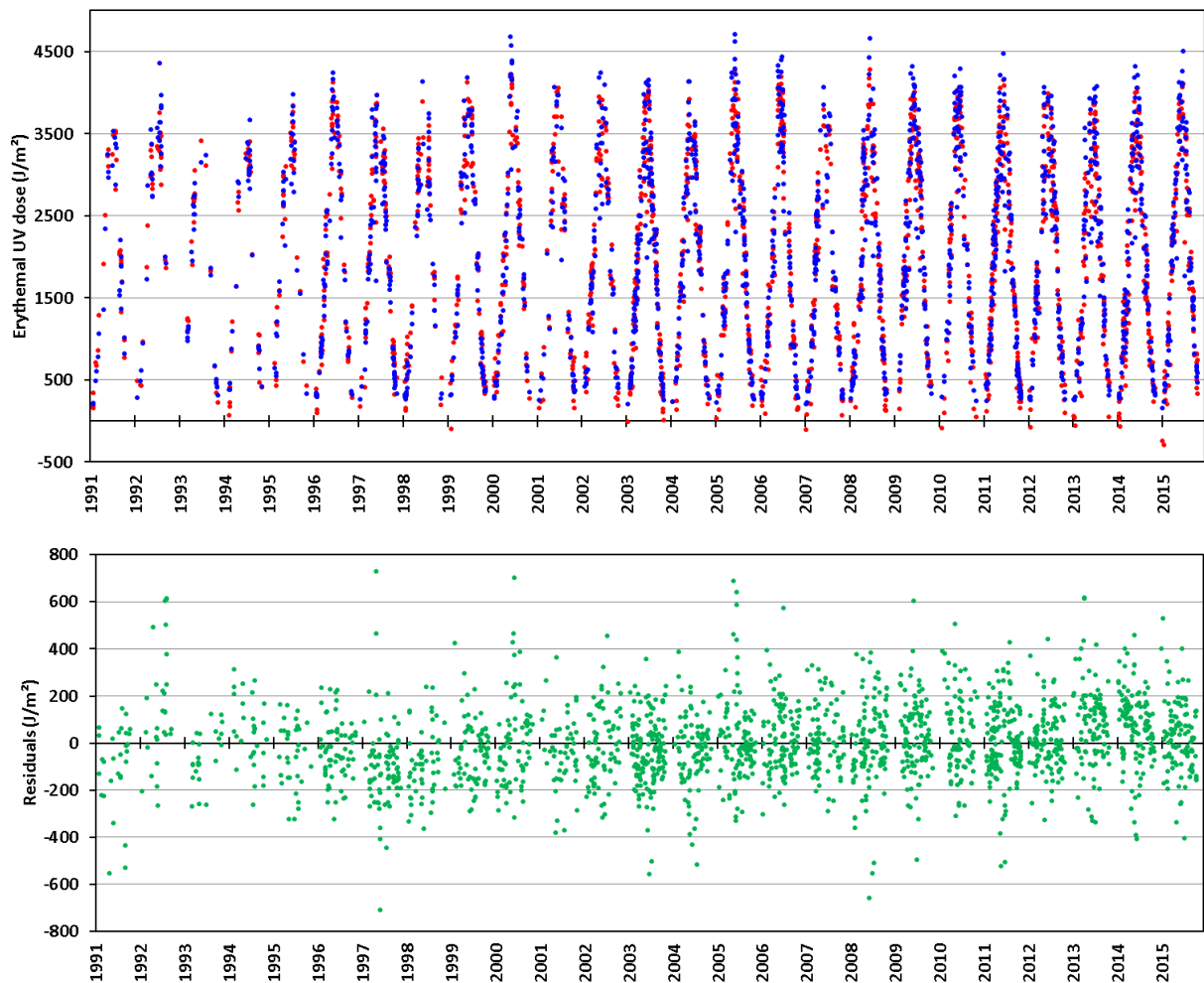


Figure 57 : Upper panel: measured (in blue) and modeled (MLR 1) (in red) erythemal UV values for the 1991-2015 period. Lower panel: residuals for the same period. The results for MLR 2 are similar and not shown.

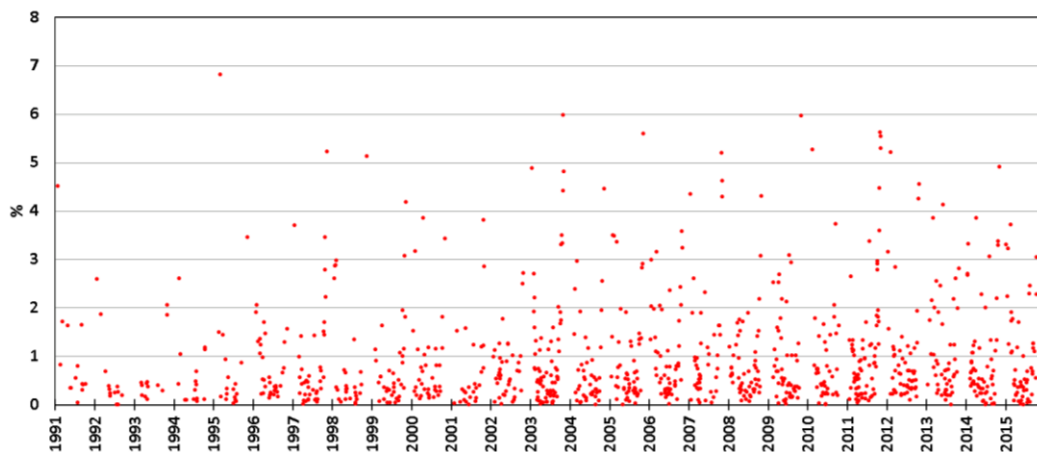


Figure 58 : Relative difference between the absolute residuals of MLR 1 and MLR 2.

6.4.2.2 Seasonal MLR analysis of D_{ery}^*

For the seasonal models, Eq. 62 is used. The harmonic terms are not included in the regression equations as this has no physical sense. As in the previous section, a difference is

made between MLR 1 and MLR 2. The results from fitting D_{ery}^* with the seasonal models are provided in Table 39 and Figure 59.

Table 39 : Comparison of the different seasonal regression models MLR 1 and MLR 2. The table shows the multiple linear regression equations, the adjusted R² values and the relative changes in D_{ery}^* due to the different parameters. The performance of the models is given by the correlation, regression equation, MBE and MABE.

	MLR 1	MLR 2
Training data set	All data between 1991 – 2015	Half of the data between 1991-2015
SPRING		
Model equation (with D_{ery}^* in J m⁻²)	$D_{ery}^* = 2008 + 2109 * D_g^* - 629 * Q_{O3} + 113 * \tau_{aer,320} + \epsilon$	$D_{ery}^* = 1987 + 2161 * D_g^* - 586 * Q_{O3} + 102 * \tau_{aer,320} + \epsilon$
Adjusted R²	0.90	0.91
Relative change in D_{ery}^* due to		
D_g^*	38%	38%
Q_{O3}	-8%	-7%
$\tau_{aer,320}$	2%	1%
Validation		
Testing set	All data between 1991 – 2015	The other half of the data between 1991-2015 not used as training set
Correlation	0.95	0.94
Regression equation	$f(x)=0.90x+199.50$	$f(x)=0.92x+141.38$
MBE	1%	-0.7%
MABE	14%	15%
SUMMER		
Model equation (with D_{ery}^* in J m⁻²)	$D_{ery}^* = 2513 + 1933 * D_g^* - 729 * Q_{O3} - 131 * \tau_{aer,320} + \epsilon$	$D_{ery}^* = 2497 + 1958 * D_g^* - 770 * Q_{O3} - 120 * \tau_{aer,320} + \epsilon$
Adjusted R²	0.86	0.87
Relative change in D_{ery}^* due to		
D_g^*	17%	19%
Q_{O3}	-4%	-4%
$\tau_{aer,320}$	-1%	-1%
Validation		
Testing set	All data between 1991 – 2015	The other half of the data between 1991-2015 not used as training set
Correlation	0.93	0.92
Regression equation	$f(x)=0.86x+470.27$	$f(x)=0.86x+441.37$
MBE	0.5%	0.07%
MABE	6%	6%
AUTUMN		
Model equation (with D_{ery}^* in J m⁻²)	$D_{ery}^* = 2040 + 1939 * D_g^* - 180 * Q_{O3} + 209 * \tau_{aer,320} + \epsilon$	$D_{ery}^* = 2034 + 1930 * D_g^* - 197 * Q_{O3} + 204 * \tau_{aer,320} + \epsilon$
Adjusted R²	0.94	0.94

Relative change in D_{ery}^* due to		
D_g^*	53%	53%
Q_{O_3}	-3%	-3%
$\tau_{aer,320}$	4%	4%
Validation		
Testing set	All data between 1991 – 2015	The other half of the data between 1991-2015 not used as training set
Correlation	0.97	0.97
Regression equation	$f(x)=0.94x+67.01$	$f(x)=0.93x+85.20$
MBE	0.4%	2%
MABE	13%	13%
WINTER		
Model equation (with D_{ery}^* in $J m^{-2}$)	$D_{ery}^* = 1204 + 973 * D_g^* - 171 * Q_{O_3} + 93 * \tau_{aer,320} + \epsilon$	$D_{ery}^* = 1244 + 1016 * D_g^* - 183 * Q_{O_3} + 116 * \tau_{aer,320} + \epsilon$
Adjusted R^2	0.82	0.82
Relative change in D_{ery}^* due to		
D_g^*	31%	32%
Q_{O_3}	-14%	-16%
$\tau_{aer,320}$	4%	4%
Validation		
Testing set	All data between 1991 – 2015	The other half of the data between 1991-2015 not used as training set
Correlation	0.91	0.90
Regression equation	$f(x)=0.82x+79.48$	$f(x)=0.90x+53.78$
MBE	2%	3%
MABE	13%	14%

All seasonal models (both for MLR 1 and MLR 2) perform well in estimating the measured D_{ery}^* values. For all seasons, more than 80% of the total variation in D_{ery}^* is explained by the combination of D_g^* , Q_{O_3} and $\tau_{aer,320}$, as can be concluded from the adjusted R^2 values in Table 39. The correlation between the modeled and measured values varies between 0.91 in winter and 0.97 in autumn for MLR 1 and between 0.90 in winter and 0.97 in autumn for MLR 2. Consistent with the daily regression model, the MBE values show that each model only has a slight tendency (always below 3%) to overestimate the measured values (except for the spring MLR 2 model where the MBE is slightly negative at -0.7%). The summer models perform best, with an absolute mean model error of only 6%. This is confirmed by Figure 60, which shows the relative residuals for MLR 1 for the four seasons. The models for the other seasons have much higher relative residuals and a mean model error amounting 15%.

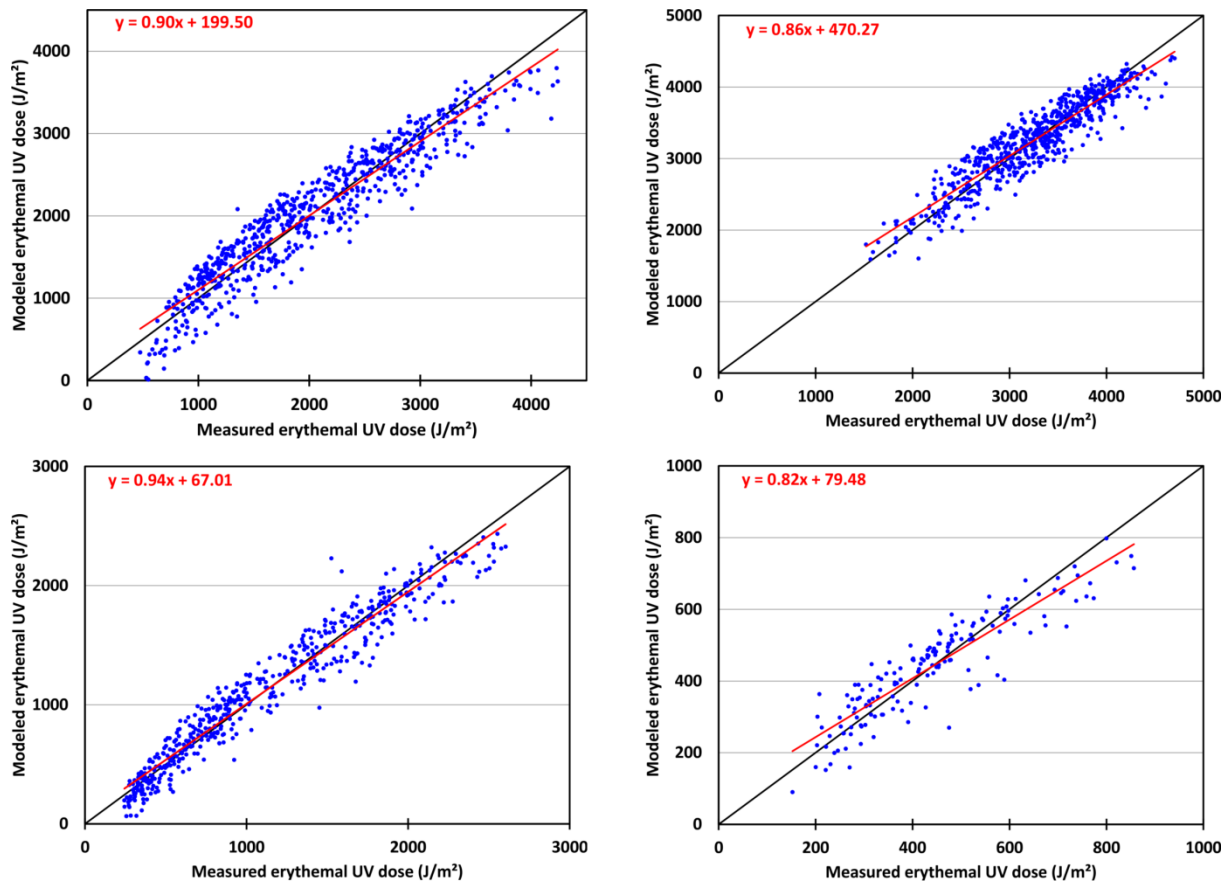


Figure 59: Scatterplots of the measured and modeled erythemal UV doses at Uccle for the 1991–2015 period for spring (upper left panel), summer (upper right panel), autumn (lower left panel) and winter (lower right panel). The red lines represent the regression lines of the data, and the black lines are the $f(x)=x$ lines. The plots here represent the results for MLR 1. The MLR 2 results are similar and not shown.

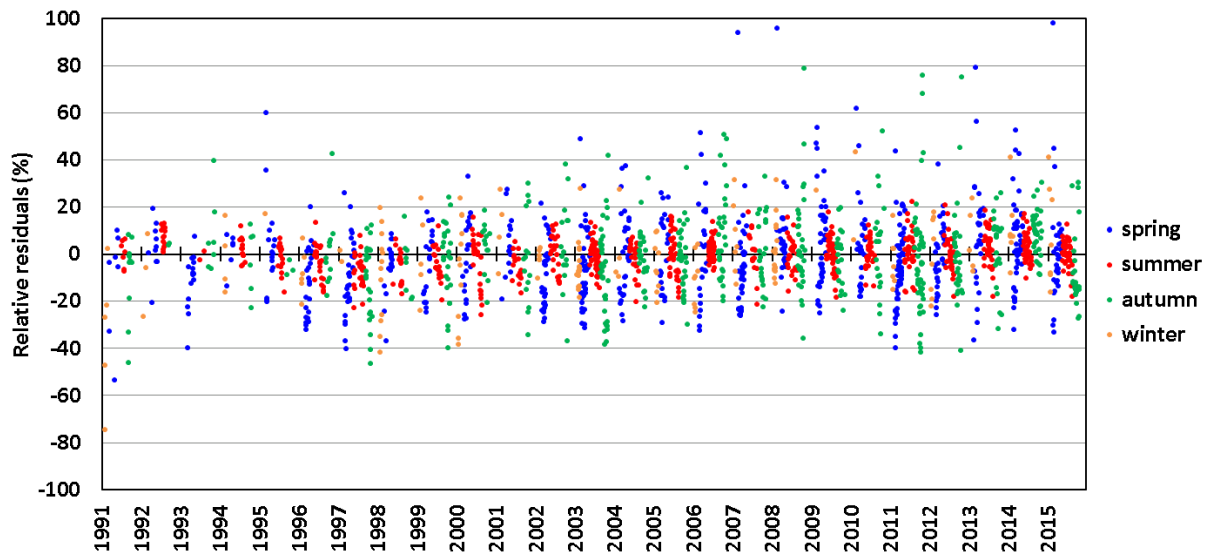


Figure 60 : Same as the lower panel of Figure 57 for the seasonal multiple regression models. The colors represent the different seasons: blue – spring; red – summer; green – autumn; and orange – winter. The plot is valid for MLR 1. Results for MLR 2 are not shown here, but are similar.

The magnitude of the influence of each parameter on D_{ery}^* is given in Table 39. For both models, we find that changes in the variation of D_g^* are the most important and lead to changes

in D_{ery}^* between 17% (in summer) and 53% (in autumn). The influence of the variation in Q_{O3} and $\tau_{aer,320}$ is much smaller. Throughout all seasons, the influence of Q_{O3} on D_{ery}^* is negative and changes in the variation of Q_{O3} lead to negative changes in D_{ery}^* (from -3% in autumn to -16% in winter). The influence of a change in variation of $\tau_{aer,320}$ varies from a -1% to 4% change in D_{ery}^* . $\tau_{aer,320}$ and D_g^* have their lowest contribution in summer. Q_{O3} on the other hand has the lowest contribution in summer and autumn. These findings confirm those from the daily analysis. As D_g^* appears to have by far the largest influence on D_{ery}^* , an important question that needs to be addressed is whether Q_{O3} and $\tau_{aer,320}$ are actually necessary to capture the variation in D_{ery}^* . This was investigated by performing the MLR analysis using (1) only D_g^* , (2) D_g^* combined with Q_{O3} , (3) D_g^* combined with $\tau_{aer,320}$ and (4) only Q_{O3} as explanatory variables for MLR 1. The results are compiled in Table 40, which gives the adjusted R^2 , the MABE and correlation coefficients for the different combinations.

Table 40: Results of MLR analysis with only D_g^* , D_g^* combined with Q_{O3} , D_g^* combined with $\tau_{aer,320}$ and only Q_{O3} as explanatory variables.

	D_g^*	$D_g^* + Q_{O3}$	$D_g^* + \tau_{aer,320}$	Q_{O3}
Adjusted R^2				
Spring	0.87	0.90	0.87	0.10
Summer	0.82	0.85	0.82	0
Autumn	0.93	0.94	0.94	0
Winter	0.65	0.81	0.65	0.08
MABE (in %)				
Spring	14.34	13.61	14.25	42.72
Summer	6.47	5.98	6.41	16.67
Autumn	13.99	14.03	13.16	73.94
Winter	16.56	13.37	16.28	32.41
Correlation modeled and measured UV values				
Spring	0.93	0.95	0.93	0.32
Summer	0.91	0.92	0.91	0.003
Autumn	0.97	0.97	0.97	0.086
Winter	0.81	0.90	0.81	0.29

From the sensitivity analysis (Table 40), it becomes clear that $\tau_{aer,320}$ only has a minor contribution to the regression model (i.e. the MBE decreases only slightly whereas the adjusted R^2 and correlation remain the same) and that, to describe the changes in D_{ery}^* , $\tau_{aer,320}$ is not needed. One possible explanation is that the influence of $\tau_{aer,320}$ is already partly included in the D_g^* parameter (see also section 6.4.3). Q_{O3} seems a more relevant explanatory variable, as the adjusted R^2 increases for all seasons (especially in winter) and the MABE of the models decreases, except in autumn, when combining D_g^* and Q_{O3} . The correlation between modeled and measured values does not change much, except in winter (from 0.81 when using only D_g^* to 0.90 when combining D_g^* and Q_{O3}). It is important to mention that the developed regression models are only valid for Uccle. For other sites, the atmospheric conditions will differ and it might be necessary to include all three parameters in the regression models in order to explain the observed variation in D_{ery}^* . As the results for MLR 2

are very similar to the ones from MLR 1, they are not shown here, but they can be found in appendix A.

6.4.3 Discussion of the results

Most studies aiming at quantifying the effects of different variables on the amount of UV irradiance reaching the ground, have relied on empirical models with UV irradiance (or a related quantity) as a dependent variable (Díaz et al., 2000; Fioletov et al., 2001; de La Casinière et al., 2002; Foyo-Moreno et al., 2007; Antón et al., 2009; De Backer, 2009; Huang et al., 2011; Krishna Prasad et al., 2011; El Shazly et al., 2012). Most of these models use ozone (either total or slant column) as an independent variable together with cloud related parameters (e.g. global solar radiation, daily sunshine fraction, global broadband hemispherical transmittance, clearness index) and geometrical parameters (e.g. solar zenith angle, optical air mass, declination). Some models also include meteorological parameters (such as the dew point temperature; Fioletov et al., 2001). Information on aerosols however is not frequently used in models. Fioletov et al. (2001) recognized that not including (absorbing) aerosols into their model was probably the major source of error of their model as this type of aerosols can substantially reduce UV irradiance. El Shazly et al. (2012) used the aerosol index as one of their independent variables.

The influence of global radiation (D_g^*), total ozone (Q_{O_3}) and AOD at 320.1 nm ($\tau_{aer,320}$) on the erythemal UV dose (D_{ery}^*) at Uccle has been studied here. Specifically for the Uccle station, De Backer (2009) already studied the relation between these parameters for the 1990-2007 period. He found a high positive correlation between D_{ery}^* and D_g^* , which varied between 0.9 in winter and around 1 in summer. Q_{O_3} was found to be negatively correlated with D_{ery}^* (-0.2 in winter and -0.5 in summer) and it was shown that the influence of Q_{O_3} on D_{ery}^* was reduced under cloudy conditions. Finally, a negative correlation was also found between D_{ery}^* and $\tau_{aer,320}$. The current study extends the analysis from De Backer (2009) by constructing MLR models with the goal to model the variation in D_{ery}^* both on a daily and seasonal scale. We have shown that D_g^* was the parameter with the biggest influence on D_{ery}^* , followed by Q_{O_3} and $\tau_{aer,320}$, whatever the temporal scale considered.

D_g^* can serve as a proxy for cloudiness. From the results of the MLR analysis it was shown that an increase in D_g^* (or a decrease in cloudiness) would lead to an increase in D_{ery}^* . Generally, clouds are known to lead to the attenuation of UV radiation, however in certain conditions they can also lead to an enhancement of UV radiation (Bais et al., 2015). Reductions of irradiance depend on cloud cover, depth and type (water/ice) and can be moderated by surface reflectivity. In the presence of clouds, scattering increases due to reflections on cloud edges, hence increasing the diffuse component and reducing the direct component of UV (Jégou et al., 2011). In low cloud cover conditions the increase of diffuse radiation is not sufficient to compensate the decrease of the direct component. In general the UV radiation decreases from clear-sky condition until a cloud cover of about 25%. From this threshold to a cloud cover of 65%, the situation reverses and the diffuse radiation leads to an increase in UV radiation. In situations of significant broken cloud cover (i.e. between 50 and

80%), the average amount of direct and diffuse radiations becomes up to 10% larger than the clear sky value. When approaching overcast conditions, the direct component of radiation vanishes completely, resulting in UV radiation half of clear sky values (Jégou et al., 2011).

The influence of Q_{O_3} on D_{ery}^* was found to be less but negative in the daily and seasonal models. It is well known from many previous studies that UV radiation is inversely correlated with total ozone (Bais et al., 2015 and references therein) and the results at Uccle are a further demonstration of this. From the seasonal MLR models, we find that the influence of ozone is bigger in winter and spring. This is due to the variation in ozone itself, which is largest during winter and early spring.

The influence of the $\tau_{aer,320}$ in the MLR models is quite small and including this parameter in the analysis might even not be necessary. There could be two possible explanations for this. First, although the correlation between $\tau_{aer,320}$ and D_g^* is small enough to allow them to be used as independent variables in the MLR analysis, it is not equal to zero, which means that some small part of the influence of $\tau_{aer,320}$ might already be included in the D_g^* term. Second, the interaction of UV with aerosols is very complex and changes in AOD cannot fully explain the changes in UV without taking into account the absorption efficiency of the aerosols (i.e. the SSA) for which no measurements are currently available at Uccle. For example, decreases in the SSA (i.e. greater absorption efficiency) counteract the effect of decreases in the AOD (Fountoulakis et al., 2016a). In the future, it may be appropriate to add the SSA as an explanatory variable to the MLR model.

7. Conclusion and outlook

The majority of the work in this PhD is based on the work previously presented in two papers: De Bock et al. (2010) and De Bock et al. (2014). In the first part of this work, the method developed during this thesis to retrieve AOD from Brewer sun scan measurements at 340 nm ($\tau_{\text{aer},340}$) was described and explained. The Beer-Lambert law was applied to the signal received by the Brewer spectrophotometer with two unknown parameters: the calibration factor CF (which represents the extraterrestrial constant) and the aerosol optical depth $\tau_{\text{aer},340}$. Calibration quality clear days (CCD) were selected and used to apply the Langley Plot Method on the measurements. This method has allowed us to determine the CF for each CCD. A 3 year running mean was then applied to the resulting individual calibration factors which led to one CF for each year. Using these values, the individual $\tau_{\text{aer},340}$ were calculated. The uncertainties caused by different sources have been characterized and it was concluded that the dominating error source was related to the use of a constant station pressure. The use of ‘wrong’ Rayleigh absorption coefficients and not accounting for the internal polarization effects are additional sources of errors that propagate on the $\tau_{\text{aer},340}$ retrievals but they generally contribute less. A first approximation of the uncertainty resulted in an overall maximum uncertainty in $\tau_{\text{aer},340}$ of 0.013. This result is only valid for $\tau_{\text{aer},340}$ values calculated with a total ozone error of 1%, an ozone airmass height of 25 km, a Rayleigh airmass height of 6 km, a constant station pressure of 1016 hPa, Rayleigh scattering optical depth coefficients determined with the Bodhaine formula and an SO₂ amount of 5 DU.

A cloud screening method was developed to filter out clouds from the Brewer $\tau_{\text{aer},340}$ data record. This method made use of sunshine duration data from four pyrhemometers at Uccle and was also based on the assumption that the variability of $\tau_{\text{aer},340}$ in the course of one day is either lower than 10% or lower than 0.08 $\tau_{\text{aer},340}$ units. Using this new methodology, a time series of cloud screened $\tau_{\text{aer},340}$ from the Brewer measurements was obtained. (This new cloud screening has now also been applied to the $\tau_{\text{aer},320}$ values retrieved using the DS Brewer measurements.)

For validation purpose, the $\tau_{\text{aer},340}$ time series has been compared to quasi-simultaneous values from the collocated CIMEL sun photometer. The results showed a very good agreement with correlation, slope and intercept of the linear regression respectively of 0.972, 0.978 ± 0.007 and 0.077 ± 0.002 . A systematic offset between both datasets was found however (the Brewer measurements being biased low), which might be due to uncertainties in the CF of the Brewer or to uncertainties in the manual screening of the CIMEL values. Despite the presence of an offset, the overall correlation coefficient is high enough to state that the Brewer spectrophotometer is largely sensitive to $\tau_{\text{aer},340}$ and it justifies its use in sun scan mode to expand the AOD retrieval capabilities of the global Brewer network. The new $\tau_{\text{aer},340}$ data record will be useful for the satellite community to validate their AOD products.

The $\tau_{\text{aer},340}$ time series from the Brewer showed a seasonal behavior with higher values in spring and summer and lower values in autumn and winter and this was tentatively explained by the seasonal behavior of the mixing layer height (being smaller in autumn and winter), the increase of wet removal processes in winter and the increased production of smog in summer. There is also a possible link with the local pollution cycle and meteorological conditions. No weekly cycle was present in the AOD data from Uccle.

In the second part of this work, the long-term behavior (1991-2015) of the erythemal UV dose D_{ery}^* , the global solar radiation D_g^* , total ozone column Q_{O_3} and AOD (at 320.1 nm) $\tau_{\text{aer},320}$ at Uccle was studied. It was shown that the time series of D_{ery}^* , D_g^* and Q_{O_3} all showed an increase of respectively 7%, 5% and 2.6% per decade, whereas $\tau_{\text{aer},320}$ decreased (insignificantly) with 4% per decade. Overall, our results agreed with previous findings from literature. We applied a multiple linear regression technique to go further in the analysis of the time evolution of D_{ery}^* , D_g^* , Q_{O_3} and $\tau_{\text{aer},320}$ at Uccle in order to explore whether there is a significant relationship between the various variables described. Specifically, we investigated the relation between D_{ery}^* and three explanatory variables (D_g^* , Q_{O_3} and $\tau_{\text{aer},320}$) both on a daily and seasonal scale. A big advantage of using this analysis method is that it allows us to determine the individual influence of the explanatory variables on D_{ery}^* . Two different regression models were built. A first model (MLR 1) was based on all 2007 data points between 1991 to 2015 and was validated using the same data set. In this way the overall performance of the model was assessed. In order to assess the predictability of the model, a second model (MLR 2) was built, with the original dataset randomly split in half. The first part of the data (i.e. the training set; which contained 1004 values between 1991 and 2015) was used to construct the MLR model, whereas the second part (i.e. the testing set; containing the remaining 1003 values between 1991 and 2015) was used for the validation of the predictive power of the MLR model. From the performed multiple linear regression analysis, we could conclude that the global radiation has the largest influence on erythemal UV dose, followed by ozone and AOD. The influence of D_g^* was positive for the daily and seasonal models, whereas the influence of Q_{O_3} was negative, as expected as ozone is an absorber of UV radiation. It proved more complicated to assess the influence of $\tau_{\text{aer},320}$ on the erythemal UV dose which overall was found by the MLR to be weak if not negligible. In the overall daily model, the influence was negative, whereas for the seasonal models the influence was positive (except for summer). These results, although only valid for Uccle, clearly highlight the difficulty in attributing changes in UV to changes in AOD without taking into account the absorption efficiency of the aerosols. Leaving out $\tau_{\text{aer},320}$ as an explanatory variable did not furthermore change the performance of the models. In the future, it might be worthwhile using other parameters (such as the SSA) to determine the influence of aerosols on the erythemal UV dose at the ground. In the next decades, ozone, aerosols and clouds are projected to undergo important changes which may alter the levels of the surface UV irradiance with important impacts on human health and the balance of ecosystems (Fountoulakis et al., 2016a and references therein). It is therefore important to keep monitoring these parameters in order to be able to understand their exact impact on UV irradiance.

In the future, the AOD retrieval method using the Brewer sun scan measurements, as described in this PhD, could be implemented at other Brewer stations, thus extending the observational capacities of the Brewer network and the global ground-based AOD observation network. Each Brewer site might however need to develop its own cloud screening procedures, depending on its available ancillary measurements. Also, the criteria for the selection of CCD might need to be adjusted for some sites (e.g. for high latitude sites, the air mass limit should be higher than 3 as otherwise too little measurements will remain).

As the results of the linear trend analysis and the multiple linear regression analysis presented in this work are only valid for Uccle, it would be very interesting to extend the analysis to other stations that have the same (or similar) measurements available in order to compare the differences between these stations and to study local influences on changes in UV irradiance at the ground. Also, instead of using daily values for the variables in the MLR analysis, using simultaneous diurnal values can lead to an even better characterization of the changes in UV irradiance.

More specific future work will include alterations to some of the calculations of the different parameters needed for the LPM. Following the guidelines of Redondas et al. (2014), new ozone cross sections (i.e. the ones from the Institute of Experimental Physics (IUP), University of Bremen) should be used. For the Rayleigh scattering coefficients, the formula from Bodhaine et al. (1999) is preferred as this is also used within the AERONET network and will also become a standard within Eubrewnet. The internal polarization effect should be taken into account in the future as it is known that not doing so introduces systematic errors in Langley extrapolations. The temperature sensitivity of the Brewer should also be analyzed. The selection criteria of the Langley Plot Days could be further refined by e.g. only using measurements with a neutral density filter attenuation of at least 10^1 to remove measurements under thick clouds and at very high air masses. Also, the individual Langley Plots used to calculate the Calibration Factor should be investigated in more detail (e.g. to avoid using days with AOD changes symmetrical around noon). A more detailed analysis and quantification of the uncertainties of the proposed AOD retrieval will also be the subject of future work. To get a more comprehensive insight in the changes of erythemal UV dose, including extra parameters to the MLR analysis will be needed. An example of such a parameter would be the Single Scattering Albedo, which we can determine from the measurements of the aethalometer and nephelometer at Uccle.

References

Ahrens, C.D., *Meteorology today – An introduction to weather, climate and environment – Eight edition*, Thomson Brooks/Cole, USA, ISBN-13: 978-0-495-10581-7, 2007.

Alexandrov, M. D., Lacis, A., Carlson, B. E., and Cairns, B.: Remote sensing of atmospheric aerosols and trace gases by means of Multifilter Rotating Shadowband Radiometer. Part I: Retrieval algorithm, *J. Atmos. Sci.*, 59(3), 524–543, doi: 10.1175/1520-0469(2002)059<0524:RSOAAA>2.0.CO;2, 2002.

Alexandrov, M. D., Marshak, A., Cairns, B., Lacis, A., and Carlson, B. E.: Automatic cloud screening algorithm for MFRSR data, *Geophys. Res. Lett.*, 31(4), L04118, doi: 10.1029/2003GL019105, 2004.

Allaart, M., van Weele, M., Fortuin, P., and Kelder, H.: An Empirical model to predict the UV-index based on Solar Zenith Angle and Total Ozone, *Meteorol. Appl.*, 11(1), 59–65, doi: 10.1017/S1350482703001130, 2004.

Alpert, P., Shvainshtein, O., and Kishcha, P.: AOD trends over megacities based on space monitoring using MODIS and MISR, *Am. J. Clim. Change*, 1(3), 117–131, doi: 10.4236/ajcc.2012.13010, 2012.

Andreae, M. O., Jones, C. D. and Fox, P. M.: Strong present-day aerosol cooling implies a hot future, *Nature*, 435, 1187–1190, doi: 10.1038/nature03671, 2005.

Antón, M., Serrano, A., Cancillo, M. L., and García, J. A.: An empirical model to estimate ultraviolet erythematous transmissivity, *Ann. Geophys.*, 27, 1387–1398, doi: 10.5194/angeo-27-1387-2009, 2009.

Arecchi, A.V., Messadi, T., Koshel, R.J.: *Field Guide to Illumination*, SPIE Press, Bellingham, Washington, USA, ISBN: 9780819467683, 2007.

Arola, A. and Koskela, T.: On the sources of bias in aerosol optical depth retrieval in the UV range, *J. Geophys. Res.*, 109 (D08209), doi: 10.1029/2003JD004375, 2004.

Augustine, J.A., Hodges, G.B., Dutton, E.G., Michalsky, J.J. and Cornwall, C.R.: An aerosol optical depth climatology for NOAA's national surface radiation budget network (SURFRAD), *J. Geophys. Res.*, 113, D11204, doi: 10.1029/2007JD009504, 2008.

Bais, A. F.: Absolute spectral measurements of direct solar ultraviolet irradiance with a Brewer spectrophotometer, *Appl. Optics*, 36(21), 5199–5204, doi: 10.1364/AO.36.005199, 1997.

Bais, A. F., Kazadzis, S., Meleti, C., Kouremeti, N., Kaurola, J., Lakkala, K., Slaper, H., den Outer, P. N., Josefsson, W., Feister, U., and Janouch, M.: Variability in spectral UV irradiance at seven European stations, edited by: Gröbner J., One century of UV radiation research. Proceedings of the UV conference, Davos, Switzerland, July 2007, 1, 27–28, 2007.

Bais, A. F., Tourpali, K., Kazantzidis, A., Akiyoshi, H., Bekki, S., Braesicke, P., Chipperfield, M. P., Dameris, M., Eyring, V., Garny, H., Iachetti, D., Jöckel, P., Kubin, A., Langematz, U., Mancini, E., Michou, M., Morgenstern, O., Nakamura, T., Newman, P. A., Pitari, G., Plummer, D. A., Rozanov, E., Shepherd, T. G., Shibata, K., Tian, W., and Yamashita, Y.: Projections of UV radiation changes in the 21st century: impact of ozone recovery and cloud effects, *Atmos. Chem. Phys.*, 11, 7533–7545, doi: 10.5194/acp-11-7533-2011, 2011.

Bais, A.F., Drosoglou, Th., Meleti, C., Tourpali, K. and Kouremeti, N.: Changes in surface shortwave solar irradiance from 1993 to 2011 at Thessaloniki (Greece), *Int. J. Climatol.*, 33, 13, 2871-2876, doi: 10.1002/joc.3636, 2013.

Bais, A.F., McKenzie, R.L., Bernhard, G., Aucamp, P.J., Ilyas, M., Madronich, S. and Tourpali, K.: Ozone depletion and climate change: impacts on UV radiation, *Photochemical and Photobiological Sciences*, 14, 19-52, doi: 10.1039/c4pp90032d, 2015.

Barret, B., De Mazière, M. and Demoulin, P.: Retrieval and characterization of ozone profiles from solar infrared spectra at the Jungfraujoch, *J. Geophys. Res.*, 107, D24, 4788, doi: 10.1029/2001JD001298, 2002.

Bartlett, L. M. and Webb, A. R.: Changes in ultraviolet radiation in the 1990s: Spectral measurements from Reading, England, *J. Geophys. Res.*, 105 (D4), 4889–4893, doi: 10.1029/1999JD900493, 2000.

Bass, A. M. and Paur, R.J.: The ultraviolet cross-sections of ozone, I, The measurements, in *Atmospheric Ozone*, edited by C.S. Zerefos and A. Ghazi, pp. 606 – 610, D. Reidel, Norwell, Mass., 1985.

Bates, D.R. and Nicolet, M.: The photochemistry of atmospheric water vapor, *J. Geophys. Res.*, 55, 3, 301-327, doi: 10.1029/JZ055i003p00301, 1950.

Bäumer, D., Rinke, R., and Vogel, B.: Weekly periodicities of Aerosol Optical Thickness over Central Europe – evidence of an anthropogenic direct aerosol effect, *Atmos. Chem. Phys.*, 8, 83–90, doi: 10.5194/acp-8-83-2008, 2008.

Behnert, I., Matthias, V., and Doerffer, R.: Aerosol optical thickness and its spectral dependence derived from sun photometer measurements over the southern North Sea coastal region, *Optica pura y aplicada*, 37(3), 3253–3257, 2004.

Benedetti, A., Morcrette, J.-J., Boucher, O., Dethof, A., Engelen, R.J., Fisher, M., Flentje, H., Huneeus, N., Jones, L., Kaiser, J.W., Kinne, S., Mangold, A., Razinger, M., Simmons, A.J. and Suttie, M.: Aerosol analysis and forecast in the European Centre for Medium-Range Weather Forecasts Integrated Forecast System: 2. Data assimilation, *J. Geophys. Res.*, 114 (D13205), doi: 10.1029/2008JD011115, 2009.

Berjón, A., Redondas, A., Sildoja, M.-M., Nevas, S., Wilson, K., León-Luis, S.F., el Gawhary, O. and Fountoulakis, I.: Characterization of the instrument temperature dependence of Brewer total ozone column measurements, *Atmos. Meas. Tech. Discuss.*, doi: 10.5194/amt-2017-406, 2017.

Bernhard, G., Evans, R. D., Labow, G. J., and Oltmans, S. J.: Bias in Dobson total ozone measurements at high latitudes due to approximations in calculations of ozone absorption coefficients and air mass, *J. Geophys. Res.*, 110 (D10305), doi: 10.1029/2004JD005559, 2005.

Bernhard, G., Booth, C. R., Ebrahimian, J. C., and Nichol, S. E.: UV climatology at McMurdo Station, Antarctica, based on Version 2 data of the National Science Foundation's Ultraviolet Radiation Monitoring Network, *J. Geophys. Res.*, 111 (D11201), doi: 10.1029/2005JD005857, 2006.

Bhartia, P.K.: OMI Algorithm Theoretical Basis Document - OMI ozone products (version 2.0), Maryland, USA, 2002.

Bhartia, P.K., McPeters, R.D., Flynn, L.E., Taylor, S., Kramarova, N.A., Frith, S., Fisher, B. and DeLand, M.: Solar Backscatter UV (SBUV) total ozone and profile algorithm, *Atmos. Meas. Tech.*, 6, 2533-2548, doi: 10.5194/amt-6-2533-2013, 2013.

Bodhaine, B.A., Wood, N.B., Dutton, E.G. and Slusser, J.R.: On Rayleigh optical depth calculations, *J. Atmos. Oceanic Technology*, 16, 1854-1861, doi: 10.1175/1520-0426(1999)016<1854:ORODC>2.0.CO;2, 1999.

Bojkov, R. D., Bishop, L., and Fioletov, V. E.: Total ozone trends from quality-controlled ground-based data (1964–1994), *J. Geophys. Res.*, 100 (D12), 25867–25876, doi: 10.1029/95JD02907, 1995.

Bornman, J.F., Barnes, P.W., Robinson, S.A., Ballaré, C.L., Flint, S.D. and Caldwell, M.M.: Solar ultraviolet and ozone depletion driven climate change: effects on terrestrial ecosystems, *Photochem. Photobiol. Sci.*, 14, 88-107, doi: 10.1039/C4PP90034K, 2015.

Boucher, O., Randall, D., Artaxo, P., Bretherton, C., Feingold, G., Forster, P., Kerminen, V.-M., Kondo, Y., Liao, H., Lohmann, U., Rasch, P., Satheesh, S.K., Sherwood, S., Stevens, B. and Zhang, X.Y.: Clouds and Aerosols. In: *Climate Change 2013: The Physical Science Basis. Contribution of Working Group I to the Fifth Assessment Report of the Intergovernmental Panel on Climate Change* [Stocker, T.F., D. Qin, G.-K. Plattner, M.

Tignor, S.K. Allen, J. Boschung, A. Nauels, Y. Xia, V. Bex and P.M. Midgley (eds.)]. Cambridge University Press, Cambridge, United Kingdom and New York, NY, USA, 2013.

Boynard, A., Hurtmans, D., Koukouli, M.E., Goutail, F., Bureau, J., Safieddine, S., Lerot, C., Hadji-Lazaro, J., Wespes, C., Pommereau, J.-P., Pazmino, A., Zyrichidou, I., Balis, D., Barbe, A., Mikhailenko, S.N., Loyola, D., Valks, P., Van Roozendael, M., Coheur, P.-F. and Clerbaux, C.: Seven years of IASI ozone retrievals from FORLI: validation with independent total column and vertical profile measurements, *Atmos. Meas. Tech.*, 9, 4327-4353, doi: 10.5194/amt-9-4327-2016, 2016.

Bokoye, A.I., Royer, A., O'Neil, N.T., Cliché, P., Fedosejevs, G., Teillet, P.M and McArthur, L.J.B.: Characterization of atmospheric aerosols across Canada from a ground-based sunphotometer network: AEROCAN, *Atmosphere-Ocean*, 39(4), 429-456, doi: 10.1080/07055900.2001.9649687, 2001.

Brasseur, G. and Solomon, S.: *Aeronomy of the middle atmosphere: chemistry and physics of the stratosphere and mesosphere*, D. Reidel Publishing Company, Dordrecht, 1986.

Brewer, A. W. and Milford, J. R.: The Oxford-Kew Ozone Sonde, *P. Roy. Soc. Lond. A Mat.*, 256, 470–495, doi: 10.1098/rspa.1960.0120, 1960.

Brewer, A.W.: A replacement for the Dobson spectrophotometer, *Pure and Appl. Geophys.*, 106-108, 919-927, 1973.

Brewer MkIII spectrophotometer Operator's Manual, Kipp&Zonen BV, Delft, The Netherlands.

Brion, J., Chakir, A., Daumont, D., Malicet, J., and Parisse, C.: High-resolution laboratory absorption cross section of O₃: Temperature effect, *Chem. Phys. Lett.*, 213, 610–612, 1993.

Burrows, JP, Platt, U and Borrell, P.: *The Remote Sensing of Tropospheric Composition from Space*, Springer Verlag, Berlin Heidelberg, ISBN: 978-3-642-14790-6, doi: 10.1007/978-3-642-14791-3, 2011.

Campanelli, M., Estellés, V., Tomasi, C., Nakajima, T., Malvestuto, V. and Martínez-Lozano, J.A.: Application of the SKYRAD Improved Langley plot method for the in situ calibration of CIMEL Sun-sky photometers, *App. Opt.*, 46, 14, 2688-2702, 2007.

Campanelli, M., Estelles, V., Diemoz, H., Kouremeti, N., Kazadzis, S., Becker, R., Vergari, S. and Dietrich, S.: The SKYNET radiometer Network: Aerosol Optical Depth retrieval performance at the ERC-IV campaign and long-term comparison against GAW-PFR and AERONET standard instruments, *WMO Technical Conference on Meteorological and Environmental Instruments and Methods of Observation (CIMO TECO 2016)*, 2016.

Casper, J.K.: Greenhouse gases: worldwide impacts, ISBN 978-1-4381-2740-8, New York, 2010.

Cazorla, A., Shields, J. E., Karr, M. E., Olmo, F. J., Burden, A., and Alados-Arboledas, L.: Technical Note: Determination of aerosol optical properties by a calibrated sky imager, *Atmos. Chem. Phys.*, 9, 6417–6427, doi:10.5194/acp-9-6417-2009, 2009.

Cede, A., Kazadzis, S., Kowalewski, M., Bais, A., Kouremeti, N., Blumthaler, M., and Herman, J.: Correction of direct irradiance measurements of Brewer spectrophotometers due to the effect of internal polarization, *Geophys. Res. Lett.*, 33, L02806, doi:10.1029/2005GL024860, 2006.

CH-1 pyrheliometer Operator's Manual, Kipp&Zonen BV, Delft, The Netherlands.

Chapman, S.: A theory of upper-atmospheric ozone, *Memoirs of the Royal Meteorological Society*, vol. III, No 26, pp 103-125, 1930.

Che, H., Zhang, X., Chen, H., Damiri, B., Goloub, P., Li, Z., Zhang, X., Wei, Y., Zhou, H., Dong, F., Li, D., and Zhou, T.: Instrument calibration and aerosol optical depth validation of the Chinese Aerosol Remote Sensing Network, *J. Geophys. Res.*, 114, D03206, doi:10.1029/2008JD011030, 2009.

Cheyamol, A. and De Backer, H.: Retrieval of the aerosol optical depth in the UV-B from Brewer ozone measurements over a long time period 1984–2002, *J. Geophys. Res.*, 108(D24), 4800, doi:10.1029/2003JD003758, 2003.

Cheyamol, A., De Backer, H., Josefsson, W., and Stübi, R.: Comparison and validation of the aerosol optical depth obtained with the Langley plot method in the UV-B from Brewer Ozone Spectrophotometer measurements, *J. Geophys. Res.*, 111, D16202, doi:10.1029/2006JD007131, 2006.

Cheyamol, A., Gonzalez Sotelino, L., Lam, K. S., Kim, J., Fioletov, V., Siani, A. M., and De Backer, H.: Intercomparison of Aerosol Optical Depth from Brewer Ozone spectrophotometers and CIMEL sunphotometers measurements, *Atmos. Chem. Phys.*, 9, 733–741, doi:10.5194/acp-9-733-2009, 2009.

Chiaccio, M., Ewen, T., Wild, M., Chin, M., and Diehl, T.: Decadal variability of aerosol optical depth in Europe and its relationship to the temporal shift of the North Atlantic Oscillation in the realm of dimming and brightening, *J. Geophys. Res.*, 116, D02108, doi:10.1029/2010JD014471, 2011.

Chin, M., Diehl, T., Tan, Q., Prospero, J. M., Kahn, R. A., Remer, L. A., Yu, H., Sayer, A. M., Bian, H., Geogdzhayev, I. V., Holben, B. N., Howell, S. G., Huebert, B. J., Hsu, N. C., Kim, D., Kucsera, T. L., Levy, R. C., Mishchenko, M. I., Pan, X., Quinn, P. K., Schuster, G.

L., Streets, D. G., Strode, S. A., Torres, O., and Zhao, X.-P.: Multi-decadal aerosol variations from 1980 to 2009: a perspective from observations and a global model, *Atmos. Chem. Phys.*, 14, 3657-3690, <https://doi.org/10.5194/acp-14-3657-2014>, 2014.

Chubarova, N. Y.: UV variability in Moscow according to long term UV measurements and reconstruction model, *Atmos. Chem. Phys.*, 8, 3025–3031, [doi:10.5194/acp-8-3025-2008](https://doi.org/10.5194/acp-8-3025-2008), 2008.

Clerbaux, C., Boynard, A., Clarisse, L., George, M., Hadji-Lazaro, J., Herbin, H., Hurtmans, D., Pommier, M., Razavi, A., Turquety, S., Wespes, C., and Coheur, P.-F.: Monitoring of atmospheric composition using the thermal infrared IASI/MetOp sounder, *Atmos. Chem. Phys.*, 9, 6041-6054, <https://doi.org/10.5194/acp-9-6041-2009>, 2009.

CM11 pyranometer Operator's Manual, Kipp&Zonen BV, Delft, The Netherlands.

Cordero, R. R., Seckmeyer, G., Pissulla, D., and Labbe, F.: Exploitation of spectral direct UV irradiance measurements, *Metrologia*, 46, 19–25, [doi:10.1088/0026-1394/46/1/003](https://doi.org/10.1088/0026-1394/46/1/003), 2009.

Cracknell, A.P. & Varotsos, C.A.: Satellite systems for atmospheric ozone observations, *International Journal of Remote Sensing*, Vol. 35, No. 15, 5566-5597, [doi:10.1080/01431161.2014.945013](https://doi.org/10.1080/01431161.2014.945013), 2014.

Cooper, O.R., Parrish, D.D., Ziemke, J., Balashov, N.V., Cupeiro, M., Galbally, I.E., Gilge, S., Horowitz, L., Jensen, N.R., Lamarque, J.-F., Naik, V., Oltmans, S.J., Schwab, J., Shindell, D.T., Thompson, A.M., Thouret, V., Wang, Y and Zbinden, R.M.: Global distribution and trends of tropospheric ozone: An observation-based review, *Elementa: Science of the Anthropocene*, 2, [doi:10.12952/journal.elementa.000029](https://doi.org/10.12952/journal.elementa.000029), 2014.

Damadeo, R. P., Zawodny, J. M., Thomason, L. W., and Iyer, N.: SAGE version 7.0 algorithm: application to SAGE II, *Atmos. Meas. Tech.*, 6, 3539-3561, <https://doi.org/10.5194/amt-6-3539-2013>, 2013.

Daumont, Brion, J., Charbonnier, J., and Malicet, J.: Ozone UV spectroscopy I: Absorption cross-sections at room temperature, *J. Atmos. Chem.*, 15, 145–155, 1992.

Dayou, J., Chang, J.H.W. & Sentian, J.: Ground-Based Aerosol Optical Depth Measurement using Sunphotometers, *SpringerBriefs in Applied Sciences and Technology*, Springer Singapore, ISBN 978-981-287-100-8, [doi:10.1007/978-981-287-101-5](https://doi.org/10.1007/978-981-287-101-5), 2014.

De Backer, H.: Time series of daily erythemal UV doses at Uccle, Belgium, *Int. J. Remote Sens.*, 30(15), 4145–4145, [doi:10.1080/01431160902825032](https://doi.org/10.1080/01431160902825032), 2009.

De Bock, V., De Backer, H., Mangold, A., and Delcloo, A.: Aerosol optical depth measurements at 340 nm with a Brewer spectrophotometer and comparison with CIMEL sunphotometer observations at Uccle, Belgium. *Atmos. Meas. Tech.*, 3, 1577–1588, doi:10.5194/amt-3-1577-2010, 2010.

De Bock, V., De Backer, H., Van Malderen, R., Mangold, A., and Delcloo, A.: Relations between erythemal UV dose, global solar radiation, total ozone column and aerosol optical depth at Uccle, Belgium. *Atmos. Chem. Phys.*, 14, 12251–12270. Doi:10.5194/acp-14-12251-2014, 2014.

de La Casinière, A., Lamine Touré, M., Masserot, D., Cabot, T., and Pinedo Vega, J. L.: Daily doses of biologically active UV radiation retrieved from commonly available parameters, *Photochem. Photobiol.*, 76, 171–175, doi:10.1562/0031-9655(2002)0760171DDOBAU2.0.002, 2002.

de Meij, A., Pozzer, A., and Lelieveld, J.: Trend analysis in aerosol optical depths and pollutant emission estimates between 2000 and 2009, *Atmos. Environ.*, 51, 75–85, doi:10.1016/j.atmosenv.2012.01.059, 2012.

Den Outer, P. N., Slaper, H., Matthijsen, J., Reinen, H. A. J. M., and Tax, R.: Variability of ground-level ultraviolet: Model and Measurement, *Radiat. Prot. Dos.*, 91, 105–110, 2000.

Den Outer, P. N., Slaper, H., Kaurola, J., Lindfors, A., Kazantzidis, A., Bais, A. F., Feister, U., Junk, J., Janouch, M., and Josefsson, W.: Reconstructing of erythemal ultraviolet radiation levels in Europe for the past 4 decades, *J. Geophys. Res.*, 115, D10102, doi:10.1029/2009JD012827, 2010.

Díaz, S., Deferrari, G., Martinioni, D., and Oberto, A.: Regression analysis of biologically effective integrated irradiances versus ozone, clouds and geometric factors, *J. Atmos. Sol-Terr. Phys.*, 62, 629–638, doi:10.1016/S1364-6826(00)00055-9, 2000.

Diémoz, H., Eleftheratos, K., Kazadzis, S., Amiridis, V. and Zerefos, C.S.: Retrieval of aerosol optical depth in the visible range with a Brewer spectrophotometer in Athens, *Atmos. Meas. Tech.*, 9, 1871–1888, doi: 10.5194/amt-9-1871-2016, 2016.

Diffey, B. L.: Solar ultraviolet radiation effects on biological systems, *Phys. Med. Biol.*, 36(3), 299–328, doi:10.1088/0031-9155/36/3/001, 1991.

Diffey, B.L.: Sources and measurement of ultraviolet radiation, *Methods*, 28, 1, 4-13, 2002.

Dobson, G. M. B.: Observers' handbook for the ozone spectrophotometer, *Ann. Int. Geophys. Year*, 5, Part 1, 46-89, Pergamon Press, 1957.

Duflot, V., Baray, J.-L., Payen, G., Marquestaut, N., Posny, F., Metzger, J.-M., Langerock, B., Vigouroux, C., Hadji-Lazaro, J., Portafaix, T., De Mazière, M., Coheur, P.-F., Clerbaux, C., and Cammas, J.-P.: Tropospheric ozone profiles by DIAL at Maïdo Observatory (Reunion Island): system description, instrumental performance and result comparison with ozone external data set, *Atmos. Meas. Tech.*, 10, 3359-3373, <https://doi.org/10.5194/amt-10-3359-2017>, 2017.

Dunlea, E.J., Herndon, S.C., Nelson, D.D., Volkamer, R.M., Lamb, B.K., Allwine, E.J., Grutter, M., Ramos Villegas, C.R., Marquez, C., Blanco, S., Cardenas, B., Kolb, C.E., Molina, L.T., Molina, M.J.: Technical note: Evaluation of standard ultraviolet absorption ozone monitors in a polluted urban environment, *Atmos. Chem. Phys.*, 6, 3163-3180, 2006.

Durbin, J. and Watson, G. S.: Testing for serial correlation in least squares regression III, *Biometrika*, 58, 1–19, 1971.

Dütsch, H.: The photochemistry of stratospheric ozone, *Quartely J. Roy. Meteorol. Soc.*, 94, 402, 483-497, 1968.

Eck, T. F., Holben, B. N., Reid, J. S., Dubovik, O., Smirnov, A., O'Neill, N. T., Slutsker, I., and Kinne, S.: Wavelength dependence of the optical depth of biomass burning, urban, and desert dust aerosols, *J. Geophys. Res.*, 104(D24), 31333–31349, doi:10.1029/1999JD900923, 1999.

Eleftheratos, K., Kazadzis, S., Zerefos, C. S., Tourpali, K., Meleti, C., Balis, D., Zyrichidou, I., Lakkala, K., Feister, U., Koskela, T., Heikkilä, A., and Karhu, J. M.: Ozone and Spectroradiometric UV Changes in the Past 20 Years over High Latitudes, *Atmos. Ocean*, doi:10.1080/07055900.2014.919897, 2014.

El Shazly, S. M., Kassem, Kh. O., Hassan, A. A., and El-Nobi, E. F.: An empirical model to estimate UV index in some upper Egypt regions, *Resour. Environ.*, 2, 216–227, doi:10.5923/j.re.20120205.05, 2012.

Envisat-1 products specifications volume 15: SCIAMACHY products specifications Issue 3/L, IDEAS-SER-IPF-SPE-0398, 2010.

Estellés, V., Martinez-Lozano, J. A., Utrillas, M. P., and Campanelli, M.: Columnar aerosol properties in Valencia (Spain) by ground-based Sun photometry, *J. Geophys. Res.*, 112, D11201, doi:10.1029/2006JD008167, 2008.

Farman, J. C., Gardiner, B. G. and Shanklin, J. D.: Large losses of total ozone in Antarctica reveal seasonal ClO_x/NO_x interaction, *Nature*, 315, 207-210, 1985.

Feister, U., Grewe, R. and Gericke, K.: A method for correction of cosine errors in measurements of spectral UV irradiance, *Solar Energy*, 60 (6), 313-332, 1997.

Fernandez, S., Murk, A. and Kämpfer, N.: GROMOS-C, a novel ground-based microwave radiometer for ozone measurement campaigns, *Atmos. Meas. Tech.*, 8, 2649–2662, doi:10.5194/amt-8-2649-2015, 2015.

Fioletov, V. E., McArthur, L. J. B., Kerr, J. B., and Wardle, D. I.: Long-term variations of UV-B irradiance over Canada estimated from Brewer observations and derived from ozone and pyranometers measurements, *J. Geophys. Res.*, 106, 23009–23027, doi:10.1029/2001JD000367, 2001.

Fioletov, V.E., Kerr, J.B., Wardle, D.I., Krotkov, N. and Herman, J.R.: Comparison of Brewer ultraviolet irradiance measurements with total ozone mapping spectrometer satellite retrievals, *Opt. Eng.*, 41 (12), 3051-3061, 2002.

Fioletov, V. E., Kimlin, M. G., Krotkov, N., McArthur, L. J. B., Kerr, J. B., Wardle, D. I., Herman, J. R., Meltzer, R., Mathews, T. W., and Kaurola, J.: UV index climatology over the United States and Canada from ground-based and satellite estimates, *J. Geophys. Res.*, 109, D22308, doi:10.1029/2004JD004820, 2004.

Fitzka, M., Simic, S., and Hadzimustafic, J.: Trends in spectral UV radiation from long-term measurements at Hoher Sonnblick, Austria, *Theor. Appl. Climatol.*, 110, 585–593, doi:10.1007/s00704-012-0684-0, 2012.

Fitzka, M., Hadzimustafic, J. and Simic, S.: Total ozone and umkehr observations at Hoher Sonnblick 1994-2011: climatology and extreme events, *J. Geophys. Res.*, 119, 739-752, 2014.

Folini, D. and Wild, M.: Aerosol emissions and dimming/brightening in Europe: Sensitivity Studies with ECHAM5-HAM, *J. Geophys. Res.-Atmos.*, 116, 1–15, doi:10.1029/2011JD016227, 2011.

Forster, P., Ramaswamy, V., Artaxo, P., Berntsen, T., Betts, R., Fahey, D.W., Haywood, J., Lean, J., Lowe, D.C., Myhre, G., Nganga, J., Prinn, R., Raga, G., Schulz, M. and Van Dorland, R.: Changes in Atmospheric Constituents and in Radiative Forcing. In: *Climate Change 2007: The Physical Science Basis. Contribution of Working Group I to the Fourth Assessment Report of the Intergovernmental Panel on Climate Change* [Solomon, S., D. Qin, M. Manning, Z. Chen, M. Marquis, K.B. Averyt, M.Tignor and H.L. Miller (eds.)]. Cambridge University Press, Cambridge, United Kingdom and New York, NY, USA, 2007.

Fountoulakis, I., Bais, A.F., Fragkos, K., Meleti, C., Tourpali, K. and Zempila, M.M.: Short and long term variability of spectral solar UV irradiance at Thessaloniki, Greece: effects of changes in aerosols, total ozone and clouds, *Atmos. Chem. Phys.*, 16, 2493-2505, doi: 10.5194/acp-16-2493-2016, 2016a.

Fountoulakis, I., Redondas, A., Bais, A. F., Rodriguez-Franco, J. J., Fragkos, K., and Cede, A.: Dead time effect on the Brewer measurements: correction and estimated uncertainties, *Atmos. Meas. Tech.*, 9, 1799-1816, <https://doi.org/10.5194/amt-9-1799-2016>, 2016b.

Fountoulakis, I., Redondas, A., Lakkala, K., Berjon, A., Bais, A. F., Doppler, L., Feister, U., Heikkila, A., Karppinen, T., Karhu, J. M., Koskela, T., Garane, K., Fragkos, K., and Savastiouk, V.: Temperature dependence of the Brewer global UV measurements, *Atmos. Meas. Tech.*, 10, 4491-4505, <https://doi.org/10.5194/amt-10-4491-2017>, 2017.

Foyo-Moreno, I., Alados, I., and Alados-Arboledas, L.: Adaptation of an empirical model for erythemal ultraviolet irradiance, *Ann. Geophys.*, 25, 1499-1508, doi:10.5194/angeo-25-1499-2007, 2007.

Frohlich, C. and Shaw, G.E.: New determination of Rayleigh scattering in the terrestrial atmosphere, *Appl. Opt.*, 19, 1773-1775, 1980.

Gao, W., Schmoldt, D., Slusser, J. R. (Eds.): *UV Radiation in Global Climate Change, Measurements, Modeling and Effects on Ecosystems*, ISBN 978-3-642-03313-1, 2010.

Garane, K., Lerot, C., Coldewey-Egbers, M., Verhoelst, T., Koukouli, M. E., Zyrichidou, I., Balis, D. S., Danckaert, T., Goutail, F., Granville, J., Hubert, D., Keppens, A., Lambert, J.-C., Loyola, D., Pommereau, J.-P., Van Roozendaal, M., and Zehner, C.: Quality assessment of the Ozone_cci Climate Research Data Package (release 2017) – Part 1: Ground-based validation of total ozone column data products, *Atmos. Meas. Tech.*, 11, 1385-1402, <https://doi.org/10.5194/amt-11-1385-2018>, 2018.

García, R. D., Cuevas, E., García, O. E., Cachorro, V. E., Pallé, P., Bustos, J. J., Romero-Campos, P. M., and de Frutos, A. M.: Reconstruction of global solar radiation time series from 1933 to 2013 at the Izaña Atmospheric Observatory, *Atmos. Meas. Tech.*, 7, 3139-3150, <https://doi.org/10.5194/amt-7-3139-2014>, 2014.

Geuder, N., Trieb, F., Schillings, C., Meyer, R. and Quaschnig, V.: Comparison of different methods for measuring solar irradiation data, 3rd international conference on experiences with automatic weather stations, 19-21 february 2003, Torremolinos, Spain, 2003.

Ghasemi, A. and Zahediasi, S.: Normality tests for statistical analysis: a guid for non-statisticans, *Int. J. Endocrinol. Metab.*, 10, 2, 486-489, doi: 10.5812/ijem.3505, 2012.

Glandorf, M., Arola, A., Bais, A., and Seckmeyer, G.: Possibilities to detect trends in spectral UV irradiance, *Theor. Appl. Climatol.*, 81, 33–44, doi:10.1007/s00704-004-0109-9, 2005.

GOME: Product specification document for GOME Level 1 products: radiances/irradiances and cloud properties, DLR, ER-PS-DLR-GO-0016, Iss./Rev.5/A, 2009.

Gorshelev, V., Serdyuchenko, A., Weber, M., Chehade, W., and Burrows, J. P.: High spectral resolution ozone absorption cross-sections – Part 1: Measurements, data analysis and comparison with previous measurements around 293 K, *Atmos. Meas. Tech. Discuss.*, 6, 6567–6611, doi:10.5194/amtd-6-6567-2013, 2013.

Gröbner, J. and Meleti, C.: Aerosol optical depth in the UVB and visible wavelength range from Brewer spectrophotometer direct irradiance measurements: 1991–2002, *J. Geophys. Res.*, 109, D09202, doi:10.1029/2003JD004409, 2004.

Gröbner, J., Blumthaler, M., Kazadzis, S., Bais, A., Webb, A., Schreder, J., Seckmeyer, G., and Rembges, D.: Quality assurance of spectral solar UV measurements: results from 25 UV monitoring sites in Europe, 2002 to 2004, *Metrologia*, 43, S66, doi:10.1088/0026-1394/43/2/S14, 2006.

Hansen, J.E. and Travis, L.D.: Light scattering in planetary atmospheres, *Space Sci. Rev.*, 16, 527, 1974.

Harris, N. R. P., Ancellet, G., Bishop, L., Hofmann, D. J., Kerr, J.B., McPeters, R.D., Prendez, M., Randel, W.J., Staehelin, J., Subbaraya, B.H., Volz-Thomas, A., Zawodny, J. and Zerefos, C.S.: Trends in stratospheric and free tropospheric ozone, *J. Geophys. Res.*, 102, 1571-1590, 1997.

Harris, N. R. P., Kyrö, E., Staehelin, J., Brunner, D., Andersen, S.-B., Godin-Beekmann, S., Dhomse, S., Hadjinicolaou, P., Hansen, G., Isaksen, I., Jrrar, A., Karpetchko, A., Kivi, R., Knudsen, B., Krizan, P., Lastovicka, J., Maeder, J., Orsolini, Y., Pyle, J. A., Rex, M., Vanicek, K., Weber, M., Wohltmann, I., Zanis, P., and Zerefos, C.: Ozone trends at northern mid- and high latitudes – a European perspective, *Ann. Geophys.*, 26, 1207–1220, doi:10.5194/angeo-26-1207-2008, 2008.

Hartmann, D.L., Klein Tank, A.M.G., Rusticucci, M., Alexander, L.V., Brönnimann, S., Charabi, Y., Dentener, F.J., Dlugokencky, E.J., Easterling, D.R., Kaplan, A., Soden, B.J., Thorne, P.W., Wild, M. and Zhai, P.M.: Observations: Atmosphere and Surface. In: *Climate Change 2013: The Physical Science Basis. Contribution of Working Group I to the Fifth Assessment Report of the Intergovernmental Panel on Climate Change* [Stocker, T.F., D. Qin, G.-K. Plattner, M. Tignor, S.K. Allen, J. Boschung, A. Nauels, Y. Xia, V. Bex and P.M. Midgley (eds.)]. Cambridge University Press, Cambridge, United Kingdom and New York, NY, USA, 2013.

Hassler, B., Petropavlovskikh, I., Staehelin, J., August, T., Bhartia, P. K., Clerbaux, C., Degenstein, D., Mazière, M. D., Dinelli, B. M., Dudhia, A., Dufour, G., Frith, S. M., Froidevaux, L., Godin-Beekmann, S., Granville, J., Harris, N. R. P., Hoppel, K., Hubert, D., Kasai, Y., Kurylo, M. J., Kyrölä, E., Lambert, J.-C., Levelt, P. F., McElroy, C. T., McPeters, R. D., Munro, R., Nakajima, H., Parrish, A., Raspollini, P., Remsberg, E. E., Rosenlof, K. H., Rozanov, A., Sano, T., Sasano, Y., Shiotani, M., Smit, H. G. J., Stiller, G., Tamminen, J.,

Tarasick, D. W., Urban, J., van der A, R. J., Veeffkind, J. P., Vigouroux, C., von Clarmann, T., von Savigny, C., Walker, K. A., Weber, M., Wild, J., and Zawodny, J. M.: Past changes in the vertical distribution of ozone – Part 1: Measurement techniques, uncertainties and availability, *Atmos. Meas. Tech.*, 7, 1395-1427, <https://doi.org/10.5194/amt-7-1395-2014>, 2014.

Haywood, J. and Boucher, O.: Estimates of the direct and indirect radiative forcing due to tropospheric aerosols: a review, *Reviews of Geophysics*, 38 (4), 513-543, 2000.

Hegglin, M.I. (Lead Author), Fahey, D.W., McFarland, M., Montzka, S.A. and Nash, E.R.: Twenty Questions and Answers About the Ozone Layer: 2014 Update, Scientific Assessment of Ozone Depletion: 2014, 84 pp., World Meteorological Organization, Geneva, Switzerland, 2015.

Held, I.M. and Soden, B.J.: Water vapor feedback and global warming, *Annu. Rev. Energy Environ.* 25, 441-475, 2000.

Hendrick, F., Pommereau, J.-P., Goutail, F., Evans, R.D., Ionov, D., Pazmino, A., Kyrö, E., Held, G., Eriksen, P., Dorokhov, V., Gil, M. Van Roozendaal, M.: NDACC/SAOZ UV-visible total ozone measurements: improved retrieval and comparison with correlative ground-based and satellite observations, *Atmos. Chem. Phys.*, 11, 5975–5995, doi:10.5194/acp-11-5975-2011, 2011.

Herman, J. R., Bhartia, P. K., Ziemke, J., Ahmad, Z., and Larko, D.: UV-B increases (1979–1992) from decreases in total ozone, *Geophys. Res. Lett.*, 23, 2117–2120, doi:10.1029/96GL01958, 1996.

Herman, J. R., Krotkov, N., Celarier, E., Larko, D. and Labow, G.: Distribution of UV radiation at the Earth's surface from TOMS-measured UV-backscattered radiances, *J. Geophys. Res.*, 104, 12059–12076, 1999.

Herman, J. R.: Global increase in UV irradiance during the past 30 years (1979–2008) estimated from satellite data, *J. Geophys. Res.*, 115, D04203, doi:10.1029/2009JD012219, 2010.

Holben, B. N., Eck, T.F., Slutsker, I., Tanré, D., Buis, J.P., Setzer, A., Vermote, E., Reagan, J.A., Kaufman, Y., Nakajima, T., Lavenue, F., Jankowiak, I. and Smirnov, A.: AERONET – A federated instrument network and data archive for aerosol characterization. *Remote Sens. Environ.*, 66, 1–16, 1998.

Holben, B. N., Tanré, D., Smirnov, A., Eck, T. F., Slutsker, I., Abuhassan, N., Newcomb, W. W., Schafer, J. S., Chatenet, B., Lavenue, F., Kaufman, Y. J., Vande Castle, J., Setzer, A., Markham, B., Clark, D., Frouin, R., Halthore, R., Karneli, A., O'Neill, N. T., Pietras, C., Pinker, R. T., Voss, K., and Zibordi, G.: An emerging ground-based aerosol climatology:

Aerosol optical depth from AERONET, *J. Geophys. Res.*, 106(D11), 12067–12097, doi:10.1029/2001JD900014, 2001.

Hoppe, H. and Kiely, G.: Precipitation over Ireland: observed change since 1940, *Phys. Chem. Earth B*, 24, 91–96, 1999.

Hsu, N.C., Gautam, R., Sayer, A.M., Bettenhausen, C., Li, C., Jeong, M.J., Tsay, S.-C. and Holben, B.N.: Global and regional trends of aerosol optical depth over land and ocean using SeaWiFS measurements from 1997 to 2010, *Atmos. Chem. Phys.*, 12, 8037-8053, doi: 10.5194/acp-12-8037-2012, 2012.

Huang, M., Jiang, H., Ju, W., and Xiao, Z.: Ultraviolet radiation over two lakes in the middle and lower reaches of the Yangtze river, China: An innovative model for UV estimation, *Terr. Atmos. Ocean. Sci.*, 22, 491–506, doi:10.3319/TAO.2011.05.02.01(A), 2011.

Hudson, R. D. and Reed, E. I (Eds.): *The stratosphere: Present and future*, NASA Ref. Pub. 1049, Washington, D.C., 432 pp., 1979.

Hülsen, G., Gröbner, J., Bais, A., Blumthaler, M., Disterhoft, P., Johnsen, B., Lantz, K. O., Meleti, C., Schreder, J., Vilaplana Guerrero, J. M., and Ylianttila, L.: Intercomparison of erythemal broadband radiometers calibrated by seven UV calibration facilities in Europe and the USA, *Atmos. Chem. Phys.*, 8, 4865-4875, <https://doi.org/10.5194/acp-8-4865-2008>, 2008.

Ialongo, I., Arola, A., Kujanpää, J., and Tamminen, J.: Use of satellite erythemal UV products in 149 pectrome the global UV changes, *Atmos. Chem. Phys.*, 11, 9649-9658, <https://doi.org/10.5194/acp-11-9649-2011>, 2011.

Intergovernmental Panel on Climate Change 2007: *The physical science, Technical summary of the working group I report*, Cambridge University Press, New York, 2007.

ISO 17166:1999, *Erythema reference action spectrum and standard erythema dose*, 1999.

Jacobs, L., Emmerechts, J., Nawrot, T., Nemery, B. & het milieu- en gezondheidsconsortium: *Eindrapportering onderzoeksluiken Steunpunt Milieu en Gezondheid 2007-2011*, 2011.

Jégou, F., Godin-Beekman, S., Corrêa, M.P., Brogniez, C., Auriol, F., Peuch, V.H., Haeffelin, M., Pazmino, A., Saiag, P., Goutail, F. and Mahé, E.: Validity of satellite measurements used for the monitoring of UV radiation risk on health, *Atmos. Chem. Phys.*, 11, 13377–13394, doi:10.5194/acp-11-13377-2011, 2011.

Kahn, R. A., Gaitley, B. J., Martonchik, J. V., Diner, D. J., Crean, K. A. and Holben, B.: Multiangle Imaging Spectroradiometer (MISR) global aerosol optical depth validation based on 2 years of coincident Aerosol Robotic Network (AERONET) observations, *J. Geophys. Res.*, 110, D10S04, 2005.

Kahn, R. A., Garay, M.J., Nelson, D.L., Yau, K.K., Bull, M.A., Gaitley, B.J., Martonchik, J.V. and Levy, R.C.: Satellite-derived aerosol optical depth over dark water from MISR and MODIS: Comparisons with AERONET and implications for climatological studies, *J. Geophys. Res.*, 112, D18205, 2007.

Kahn, R.A., Gaitley, B.J., Garay, M.J., Diner, D.J., Eck, T.F., Smirnov, A. and Holben, B.N.: Multiangle Imaging SpectroRadiometer global aerosol product assessment by comparison with the Aerosol Robotic Network, *J. Geophys. Res.*, 115, D23209, doi:10.1029/2010JD014601, 2010.

Kalliskota, S., Kaurola, J., Taalas, P., Herman, J., Celarier, E. A., and Krotkov, N. A.: Comparison of daily UV doses estimated from Nimbus 7/TOMS measurements and ground-based spectroradiometric data, *J. Geophys. Res.*, 105, 5059–5067, doi:10.1029/1999JD900926, 2000.

Kaskaoutis, D. G., Kambezidis, H. D., Hatzianastassiou, N., Kosmopoulos, P. G., and Badarinath, K. V. S.: Aerosol climatology: on the discrimination of aerosol types over four AERONET sites, *Atmos. Chem. Phys. Discuss.*, 7, 6357–6411, doi:10.5194/acpd-7-6357-2007, 2007.

Kaufman, Y. J., Tanré, D., Remer, L.A., Vermote, E.F., Chu, A. and Holben, B.N.: Operational remote sensing of tropospheric aerosol over land from EOS moderate resolution imaging spectroradiometer, *J. Geophys. Res.*, 102(D14), 17,051–17,067, doi:10.1029/96JD03988, 1997.

Kaufman, Y. J., Tanré, D., and Boucher, O.: A satellite view of aerosols in the climate system, *Nature*, 419, 215–223, doi:10.1038/nature01091, 2002.

Kaurola, J., Taalas, P., Koskela, T., Borkowski, J., and Josefsson, W.: Long-term variations of UV-B doses at three stations in northern Europe, *J. Geophys. Res.*, 105, 20813–20820, doi:10.1029/2000JD900258, 2000.

Kazadzis, S., Bais, A., Kouremeti, N., Gerasopoulos, E., Garane, K., Blumthaler, M., Schallhart, B., and Cede, A.: Direct spectral measurements with a Brewer spectroradiometer: absolute calibration and aerosol optical depth retrieval, *Appl. Optics*, 44(9), 1681–1690, doi:10.1364/AO.44.001681, 2005.

Kazadzis, S., Bais, A., Amiridis, V., Balis, D., Meleti, C., Kouremeti, N., Zerefos, C. S., Rapsomanikis, S., Petrakakis, M., Kelesis, A., Tzoumaka, P., and Kelektoglou, K.: Nine years of UV aerosol optical depth measurements at Thessaloniki, Greece, *Atmos. Chem. Phys.*, 7, 2091–2101, doi:10.5194/acp-7-2091-2007, 2007.

Kazadzis, S., Kouremeti, N., Bais, A., Kazantzidis, A., and Meleti, C.: Aerosol forcing efficiency in the UVA region from spectral solar irradiance measurements at an urban environment, *Ann. Geophys.*, 27, 2515–2522, doi:10.5194/angeo-27-2515-2009, 2009.

Kazadzis, S., Veselovskii, I., Amiridis, V., Gröbner, J., Suvorina, A., Nyeki, S., Gerasopoulos, E., Kouremeti, N., Taylor, M., Tsekeri, A., and Wehrli, C.: Aerosol microphysical retrievals from precision filter radiometer direct solar radiation measurements and comparison with AERONET, *Atmos. Meas. Tech.*, 7, 2013–2025, doi:10.5194/amt-7-2013-2014, 2014.

Kerr, J. B., Asbridge, I. A., and Evans, W. F. J.: Intercomparison of total ozone measured by the Brewer and Dobson spectrophotometer at Toronto, *J. Geophys. Res.*, 93(D9), 11129–11140, doi:10.1029/JD093iD09p11129, 1988.

Kerr, J.B. and Seckmeyer, G. (lead authors), Bais, A.F., Bernhard, G., Blumthaler, M., Diaz, S.B., Krotkov, N., Lubin, D., McKenzie, R.L., Sabziparvar, A.A. and Verdebout, J.: Surface ultraviolet radiation: past and future, Chapter 5 in *Scientific Assessment of Ozone Depletion: 2002*, Global Ozone Research and Monitoring Project, Report nr. 47, Geneva, 2003.

Kerr, J.B.: Understanding the factors that affect surface ultraviolet radiation, *Optical Engineering*, 44 (4), 2005.

Kim, J. E., Kim, Y. J., and He, Z.: Temporal variation and measurement uncertainty of UV aerosol optical depth measured from April 2002 to July 2004 at Gwangju, Korea, *Atmos. Res.*, 81, 111–123, doi:10.1016/j.atmosres.2005.11.006, 2006.

Kim, J. E., Ryu, S. Y., and Kim, Y. J.: Determination of radiation amplification factor of atmospheric aerosol from the surface UV irradiance measurement at Gwangju, Korea, *Theor. Appl. Climatol.*, 91, 217–228, doi:10.1007/s00704-006-0285-x, 2008.

Kinne, S.: Towards an observation-tied AOD climatology, presentation in AT2 Aerosol Workshop, Bremen, Germany, 2007.

Kirchhoff, V. W. J. H., Silva, A. A., Costa, C. A., Paes Leme, N., Pañao, H. G., and Zaratti, F.: UV-B optical thickness observations of the atmosphere, *J. Geophys. Res.*, 106(D3), 2963–2973, doi:10.1029/2000JD900506, 2001.

Kleidman, R. G., Smirnov, A., Levy, R. C., Mattoo, S. and Tanré, D.: Evaluation and wind speed dependence of MODIS aerosol retrievals over open ocean, *IEEE Trans. Geosci. Remote Sens.*, 50, 429–435, 2012.

Kneizys, F.X., Shettle, E.P., Gallery, W.O., Chetwynd, J.H., Abreu, L.W., Selby, J.E.A., Fenn, R.W. and McClatchey, R.A.: Atmospheric transmittance/radiance: Computer Code LOWTRAN 5, AFGL TR-80-0067, AD088215, 1980.

Kobayashi, J. and Toyama, Y.: On various methods of measuring the vertical distribution of atmospheric ozone (III) – carbon iodine type chemical ozonesonde, *Pap. Meteorol. Geophys.*, 17, 113–126, 1966.

Koelemeijer, R. B. A., Homan, C. D., and Matthijsen, J.: Comparison of spatial and temporal variations of aerosol optical thickness and particulate matter over Europe, *Atmos. Environ.*, 40, 5304–5315, doi:10.1016/j.atmosenv.2006.04.044, 2006.

Kokhanovsky, A. A., Deuzé, J. L., Diner, D. J., Dubovik, O., Ducos, F., Emde, C., Garay, M. J., Grainger, R. G., Heckel, A., Herman, M., Katsev, I. L., Keller, J., Levy, R., North, P. R. J., Prikhach, A. S., Rozanov, V. V., Sayer, A. M., Ota, Y., Tanré, D., Thomas, G. E., and Zege, E. P.: The inter-comparison of major satellite aerosol retrieval algorithms using simulated intensity and polarization characteristics of reflected light, *Atmos. Meas. Tech.*, 3, 909–932, 2010.

Kondratyev, K. Y.: *Radiation in the atmosphere*, 1-912, Academic Press Inc, New York, USA, 1969.

Komhyr, W. D.: Electrochemical concentration cells for gas analysis, *Ann. Geophys.*, 25, 203–210, 1969.

Krishna Prasad, N. V., Niranjana, K., Sarma, M. S. S. R. K., and Madhavi, N.: Regression analysis of biologically effective UV-B irradiance versus ozone at Visakhapatnam, *Int. J. Phys. Sci.*, 6, 7838–7843, doi:10.5897/IJPS11.581, 2011.

Krotkov, N., Bhartia, P.K., Herman, J.R., Fioletov, V. and Kerr, J.: Satellite estimation of spectral surface UV irradiance in the presence of tropospheric aerosols: 1. Cloud-free case, *J. Geophys. Res.*, 103, 8779–8793, 1998.

Krotkov, N. A., Herman, J.R., Bhartia, P.K., Fioletov, V. and Ahmad, Z.: Satellite estimation of spectral surface UV irradiance: 2. Effects of homogeneous clouds and snow, *J. Geophys. Res.*, 106, 11743–11760, 2001.

Krzyścin, J. W. and Borkowski, J. L.: Variability of the total ozone trend over Europe for the period 1950–2004 derived from reconstructed data, *Atmos. Chem. Phys.*, 8, 2847–2857, doi:10.5194/acp-8-2847-2008, 2008.

Krzyścin, J. W., Sobolwieski, P. S., Jaroslowski, J., Podgórski, J., and Rajewska-Wiech, B.: Erythemal UV observations at Belsk, Poland, in the period 1976–2008: data homogenization, climatology and trends, *Acta Geophys.*, 59, 155–182, doi:10.2478/s11600-010-0036-3, 2011.

Kujanpää, J. and Kalakoski, N.: Operational surface UV radiation product from GOME-2 and AVHRR/3 data, *Atmos. Meas. Tech.*, 8, 4399–4414, <https://doi.org/10.5194/amt-8-4399-2015>, 2015.

Laj, P., Klausen, J., Bilde, M., Plaß-Duelmer, C., Pappalardo, G., Clerbaux, C., Baltensperger, U., Hjorth, J., Simpson, D., Reimann, S., Coheur, P.-F., Richter, A., De Maziere, M., Rudich, Y., McFiggans, G., Tørseth, K., Wiedensohler, A., Morin, S., Schulz, M. and Zardini, A.: Measuring atmospheric composition change, *Atmos. Env.*, 43, 5351-5414, doi:10.1016/j.atmosenv.2009.08.020, 2009.

Lanzante, J. R.: Resistant, Robust and Non-parametric techniques for the analysis of climate data: theory and examples, including applications to historical radiosonde station data, *Int. J. Climatol.*, 16, 1197–1226, doi:10.002/(SICI)1097-0088(199611)16:11<1197::AID-JOC89>3.0.CO;2-L, 1996.

Leckner, B.: The spectral Distribution of solar radiation at the Earth's surface-elements of a model, *Sol. Energy*, 20, 143-150, 1978.

Léon, J.-F., Derimian, Y., Chiapello, I., Tanré, D., Podvin, T., Chatenet, B., Diallo, A., and Deroo, C.: Aerosol vertical distribution and optical properties over M'Bour (16.96°W; 14.39° N), Senegal from 2006 to 2008, *Atmos. Chem. Phys.*, 9, 9249–9261, doi:10.5194/acp-9-9249-2009, 2009.

Levy, C.L., Remer, L.A., Mattoo, S., Vermote, E.F., Kaufman, Y.J.: Second-generation operational algorithm: Retrieval of aerosol properties over land from inversion of Moderate Resolution Imaging Spectroradiometer spectral reflectance, *J. Geophys. Res.*, 112, D13211, doi:10.1029/2006JD007811, 2007.

Levy, R. C., Remer, L. A., Kleidman, R. G., Mattoo, S., Ichoku, C., Kahn, R. and Eck, T. F.: Global evaluation of the Collection 5 MODIS dark-target aerosol products over land, *Atmos. Chem. Phys.*, 10, 10399–10420, 2010.

Li, Z., Xia, X., Cribb, M., Mi, W., Holben, B., Wang, P., Chen, H., Tsay, S.-C., Eck, T. F., Zhao, F., Dutton, E. G. and Dickerson, R. E.: Aerosol optical properties and their radiative effects in northern China, *J. Geophys. Res. Atmos.*, 112, 1–11, doi:10.1029/2006JD007382, 2007.

Li, Z., Zhao, X., Kahn, R., Mishchenko, M., Remer, L., Lee, K.-H., Wang, M., Laszlo, I., Nakajima, T., and Maring, H.: Uncertainties in satellite remote sensing of aerosols and impact on monitoring its long-term trend: A review and perspective, *Ann. Geophys.*, 27, 2755–2770, 2009.

Lindfors, A. V., Arola, A., Kaurola, J., Taalas, P., and Svenøe, T.: Longterm erythemal UV doses at Sodankylä estimated using total ozone, sunshine duration, and snow depth, *J. Geophys. Res.*, 108, 4518, doi:10.1029/2002JD003325, 2003.

Lindfors, A., Kaurola, J., Arola, A., Koskela, T., Lakkala, K., Josefsson, W., Olseth, J. A., and Johnsen, B.: A method for reconstruction of past UV radiation based on radiative transfer

modeling: applied to four stations in northern Europe, *J. Geophys. Res.*, 112, D23201, doi:10.1029/2007JD008454, 2007.

Litynska, Z., Koepke, P., De Backer, H., Gröbner, J., Schmalwieser, A., and Vuilleumier, L.: COST action 726 final report: Long term changes and climatology of UV radiation over Europe, ISBN 978-92-898-0052-5, Luxembourg: Publications office of the European Union, doi:10.2831/12065, 2012.

Liu, S. C., McKeen S. A., and Madronich, S.: Effect of anthropogenic aerosols on biologically active ultraviolet radiation, *Geophys. Res. Lett.*, 18(12), 2265–2268, doi:10.1029/91GL02773, 1991.

Lohmann, U.: Possible aerosol effects on ice clouds via contact nucleation, *J. Atmos. Sci.*, 59(3), 647–656, 2002a.

Lohmann, U.: A glaciation indirect aerosol effect caused by soot aerosols, *Geophys. Res. Lett.*, 29, 4, doi: 10.1029/2001GL014357, 2002b.

Lohmann, U. and Feichter, J.: Global indirect aerosol effects: a review, *Atmos. Chem. Phys.*, 5, 715–737, doi:10.5194/acp-5-715-2005, 2005.

Lucas, R.M., Norval, M., Neale, R.E., Young, A.R., de Gruijl, F.R., Takizawa, Y. and van der Leun, J.C.: The consequences for human health of stratospheric ozone depletion in association with other environmental factors, *Photochem. Photobiol. Sci.*, 14, 53-87, doi: 10.1039/C4PP90033B, 2015.

Lyamani, H., Olmo, F. J., and Alados-Arboledas, L.: Physical and optical properties of aerosols over an urban location in Spain: seasonal and diurnal variability, *Atmos. Chem. Phys.*, 10, 239–254, doi:10.5194/acp-10-239-2010, 2010.

Mäder, J.A., Staehelin, J., Brunner, D., Stahel, W.A., Wohltmann, I. and Peter, T.: Statistical modeling of total ozone: Selection of appropriate explanatory variables, *J. Geophys. Res.*, 112, D11, doi: 10.1029/2006jd007694, 2007.

Madronich, S.: UV radiation in the natural and perturbed atmosphere, in: Teveni, M. (Ed.), *Environmental Effects of Ultraviolet Radiation*, Lewis, Boca Raton, FL., 17–69, 1993.

Makowski, K., Jaeger, E. B., Chiacchio, M., Wild, M., Ewen, T., and Ohmura, A.: On the relationship between diurnal temperature range and surface solar radiation in Europe, *J. Geophys. Res.*, 114, D00D07, doi :10.1029/2008JD011104, 2009.

Malicet, Daumont, D., Charbonnier, J., Parrisé, C., Chakir, A., and Brion, J. : Ozone UV spectroscopy. II. Absorption cross-sections and temperature dependence, *J. Atmos. Chem.*, 21, 263–273, 1995.

Manara, V., Brunetti, M., Celozzi, A., Maugeri, M., Sanchez-Lorenzo, A. and Wild, M.: Detection of dimming/brightening in Italy from homogenized all-sky and clear-sky surface solar radiation records and underlying causes (1959-2013), *Atmos. Chem. Phys.*, 16, 11145-11161, doi: 10.5194/acp-16-11145-2016, 2016.

Marenco, F., Santacesaria, V., Bais, A. F., Balis, D., di Sarra, A., Papayannis, A., and Zerefos, C.: Optical properties of tropospheric aerosols determined by lidar and spectrophotometric measurements (Photochemical Activity and Solar Ultraviolet Radiation campaign), *Appl. Optics*, 36(27), 6875–6886, doi:10.1364/AO.36.006875, 1997.

Marenco, A., Thouret, V., Nédélec, P., Smit, H., Helten, M., Kley, D., Karcher, F., Simon, P., Law, K., Pyle, J., Poschmann, G., Von Wrede, R., Hume, C. and Cook, T.: Measurement of ozone and water vapor by Airbus in-service aircraft: The MOZAIC airborne program, an overview, *J. Geophys. Res.*, 3, D19, 25631–25642, doi: 10.1029/98JD0097, 1998.

Marenco, F., di Sarra, A., and Di Luisi, J.: Methodology for determining aerosol optical depth from Brewer 300-320nm ozone measurements, *Appl. Optics*, 41(9), 1805–1814, doi:10.1364/AO.41.001805, 2002.

Marenco, F.: On Langley plots in the presence of a systematic diurnal aerosol cycle centered at noon: A comment on recently proposed methodologies, *J. Geophys. Res.*, 112, d06205, doi:10.1029/2006JD007248, 2007.

Margraff, W.A. and Griggs, M.: Aircraft measurements and calculations of the total downward flux of solar radiation as a function of altitude, *J. Atmos. Sci.*, 26, 469-477, 1969.

Mateos, D., Sanchez-Lorenzo, A., Antón, M., Cachorro, V. E., Calbó, J., Costa, M. J., Torres, B., and Wild, M.: Quantifying the respective roles of aerosols and clouds in the strong brightening since the early 2000s over the Iberian Peninsula, *J. Geophys. Res.-Atmos.*, 119, 10382–10393, doi:10.1002/2014JD022076, 2014.

Matthijsen, J., Slaper, H., Reinen, A. J. M. H., and Velders, G. J. M: Reduction of solar UV by clouds: A comparison between satellite-derived cloud effects and ground-based radiation measurements, *J. Geophys. Res.*, 105, 5069–5080, doi:10.1029/1999JD900937, 2000.

McArthur, L.J.B., Halliwell, D.H., Niebergall, O.J., O'Neill, N.T., Slusser, J.R. and Wehrli, C.: Field comparison of network Sun photometers, *J. Geophys. Res.*, 108, D19, doi: 10.1029/2002JD002964, 2003.

McKinlay, A.F. and Diffey, B.L.: A Reference Action Spectrum for Ultraviolet Induced Erythema in Human Skin, *CIE Journal*, 6, 17-22, 1987.

McPeters, R. D. and Labow, G. J.: An assessment of the accuracy of 14.5 years of Nimbus 7 TOMS version 7 ozone data by comparison with the Dobson network, *Geophys. Res. Lett.*, 23, 3695-3698, 1996a.

McPeters, R. D., Hollandsworth, S. M., Flynn, L. E., Herman, J. R. and Seftor, C. J.: Long-term ozone trends derived from the 16-year combined Nimbus 7/Meteor 3 TOMS version7 record, *Geophys. Res. Lett.*, 23, 3699-3702, 1996b.

Meleti, C. and Cappellani, F.: Measurements of aerosol optical depth at Ispra: Analysis of the correlation with UV-B, UV-A and total solar irradiance, *J. Geophys. Res.*, 105(D4), 4971–4978, doi:10.1029/1999JD900459, 2000.

Mishchenko, M. I. and Geogdzhayev, I. V.: Satellite remote sensing reveals regional tropospheric aerosol trends, *Opt. Express*, 15, 7423–7438, doi:10.364/OE.15.007423, 2007.

Molina, M.J. and Rowland, F.S., Stratospheric sink for chlorofluoromethanes: chlorine atom-catalysed destruction of ozone, *Nature*, 249, 810-812, 1974.

Moller, F.: *Strahlung in der Unteren Atmosphere*, Handbuch der Physik, Flugge, S. (Ed.), Springer-Verlag, New York, 1957.

Mulcahy, J. P., O’Dowd, C. D. and Jennings, S. G.: Aerosol optical depth in clean marine and continental northeast Atlantic air, *J. Geophys. Res.*, 114, D20204, doi:10.1029/2009JD011992, 2009.

Myrhe, G.: Consistency between satellite derived and modeled estimates of the direct aerosol effect, *Science*, 325(187), 187–190, doi:10.1126/science.1174461, 2009.

Myhre, G., Shindell, D., Bréon, F.-M., Collins, W., Fuglestedt, J., Huang, J., Koch, D., Lamarque, J.-F., Lee, D., Mendoza, B., Nakajima, T., Robock, A., Stephens, G., Takemura, T. and Zhang, H.: Anthropogenic and Natural Radiative Forcing. In: *Climate Change 2013: The Physical Science Basis. Contribution of Working Group I to the Fifth Assessment Report of the Intergovernmental Panel on Climate Change* [Stocker, T.F., D. Qin, G.-K. Plattner, M. Tignor, S.K. Allen, J. Boschung, A. Nauels, Y. Xia, V. Bex and P.M. Midgley (eds.)]. Cambridge University Press, Cambridge, United Kingdom and New York, NY, USA, 2013.

Nabat, P., Somot, S., Mallet, M., Chiapello, I., Morcrette, J.J., Solmon, F., Szopa, S., Dulac, F., Collins, W., Ghan, S., Horowitz, L.W., Lamarque, J.F., Lee, Y.H., Naik, V., Nagashima, T., Shindell, D. and Skeie, R.: A 4-D climatology (197-2009) of the monthly tropospheric aerosol optical depth distribution over the Mediterranean region from a comparative evaluation and blending of remote sensing and model products, *Atmos. Meas. Tech.*, 6, 1287-1314, doi: 10.5194/amt-6-1287-2013, 2013.

Nawrot, T.S., Nemmar, A. and Nemery, B.: Air pollution: to the heart of the matter, *European Heart Journal*, 27, 2269-2271, 2006.

Newman, P. A., Oman, L. D., Douglass, A. R., Fleming, E. L., Frith, S. M., Hurwitz, M. M., Kawa, S. R., Jackman, C. H., Krotkov, N. A., Nash, E. R., Nielsen, J. E., Pawson, S., Stolarski, R. S., and Velders, G. J. M.: What would have happened to the ozone layer if chlorofluorocarbons (CFCs) had not been regulated?, *Atmos. Chem. Phys.*, 9, 2113-2128, <https://doi.org/10.5194/acp-9-2113-2009>, 2009.

Norris, J. R. and Wild, M.: Trends in aerosol radiative effects over Europe inferred from observed cloud cover, solar “dimming”, and solar “brightening”, *J. Geophys. Res.*, 112, D08214, doi:10.1029/2006JD007794, 2007.

Nyeki, S., Halios, C. H., Baum, W., Eleftheriadis, K., Flentje, H., Gröbner, J., Vuilleumier, L., and Wehrli, C.: Ground-based aerosol optical depth trends at three high-altitude sites in Switzerland and southern Germany from 1995 to 2010, *J. Geophys. Res.*, 117, D18202, doi:10.1029/2012JD017493, 2012.

Ozone Trends Panel (OTP): Report of the international ozone trends panel, WMO Rep. 18, World Meteorol. Organ., Geneva, 1988.

Parding, K., Olseth, J. A., Dagestad, K. F., and Liepert, B. G.: Decadal variability of clouds, solar radiation and temperature at a high-latitude coastal site in Norway, *Tellus B*, 66, 25897, doi:10.3402/tellusb.v66.25897, 2014.

Petropavlovskikh, I., Evans, R., McConville, G., Oltmans, S., Quincy, D., Lantz, K., Disterhoft, P., Stanek, M and Flynn, L.: Sensitivity of Dobson and Brewer Umkehr ozone profile retrievals to ozone cross-sections and stray light effects, *Atmos. Meas. Tech.*, 4, 1841–1853, doi:10.5194/amt-4-1841-2011, 2011.

Philipona, R., Dürr, B., Ohmura A. and Ruckstuhl, C.: Anthropogenic greenhouse forcing and strong water vapor feedback increase temperature in Europe, *Geophys. Res. Lett.*, 32, L19809, doi:10.1029/2005GL023624, 2005.

Popp, T., de Leeuw, G., Bingen, C., Brühl, C., Capelle, V., Chedin, A.; Clarisse, L., Dubovik, O., Grainger, R., Griesfeller, J., Heckel, A., Kinne, S., Klüser, L., Kosmale, M., Kolmonen, P., Lelli, L., Litvinov, P., Mei, L., North, P., Pinnock, S., Povey, A., Robert, C., Schulz, M., Sogacheva, L., Stebel, K., Stein Zweers, D., Thomas, G., Tilstra, L.G., Vandenbussche, S., Veefkind, P., Vountas, M., Xue, Y.: Development, Production and Evaluation of Aerosol Climate Data Records from European Satellite Observations (Aerosol_cci), *Remote Sens*, 8, 421, doi: 10.3390/rs8050421, 2016.

Raghavendra Kumar, K., Narasimhulu, K., Balakrishnaiah, G., Suresh Kumar Reddy, B., Rama Gopal, K., Reddy, R. R., Satheesh, S. K., Krishna Moorthy, K., and Suresh Babu, S.:

A study on the variations of optical and physical properties of aerosols over a tropical semi-arid station during grassland fire, *Atmos. Res.*, 95, 77–87, doi:10.1016/j.atmosres.2009.08.012, 2010.

Ramanathan, V., Crutzen, P. J., Kiehl, J. T., and Rosenfeld, D.: Aerosols, climate and the hydrological cycle, *Science*, 294, 2119–2121, doi:10.1126/science.1064034, 2001.

Raval, A. & Ramanathan, V.: Observational determination of the greenhouse effect, *Science*, 342, 758-761, 1989.

Redondas, A.: Ozone absolute Langley calibration, The Tenth Biennial WMO Consultation on Brewer Ozone and UV Spectrophotometer Operation, Calibration and Data Reporting, Edited by C. T. McElroy and E. W. Hare, Gaw Report. No. 176, WMO TD No. 1420, 12–14, 2007.

Redondas, A., Evans, R., Stuebi, R., Köhler, U. and Weber, M.: Evaluation of the use of five laboratory-determined ozone absorption cross sections in Brewer and Dobson retrieval algorithms, *Atmos. Chem. Phys.*, 14, 1635–1648, doi:10.5194/acp-14-1635-2014, 2014.

Reeves, J., Chen, J., Wang, X. L., Lund, R., and Lu, Q. Q.: A review and comparison of changepoint detection techniques for climate data, *J. Appl. Meteorol. Clim.*, 46, 900–915, doi:10.1175/JAM2493.1, 2007.

Reichler, T., Dameris, M. and Sausen, R., Determining the tropopause height from gridded data, *Geophys. Res. Lett.*, 30(20), 2042, doi:10.1029/2003GL018240, 2003.

Reinsel, G.C., Miller, A.J., Weatherhead, E.C., Flynn, L.E., Nagatani, R.M., Tiao, G.C and Wuebbles, D.J.: Trend analysis of total ozone data for turnaround and dynamical contributions, *J. Geophys. Res.*, 110, D16, doi: 10.1029/2004JD004662, 2005.

Reid, J.P. and Sayer, R.M.: Chemistry in the clouds: the role of aerosols in atmospheric chemistry, *Sci. Prog.*, 85, 3, 263-296, 2002.

Remer, L. A., Kaufman, Y.J, Tanré, D., Mattoo, S., Chu, D.A., Martins, J.V., Li, R.-R., Ichoku, C., Levy, R.C., Kleidman, R.G., Eck, T.F., Vermote, E. and Holven, B.N.: The MODIS aerosol algorithm, products, and validation, *J. Atmos. Sci.*, 62, 947–973, 2005.

Rieder, H. E., Holawe, F., Simic, S., Blumthaler, M., Krzyscin, J. W., Wagner, J. E., Schmalwieser, A. W., and Weihs, P.: Reconstruction of erythemal UV-doses for two stations in Austria: a comparison between alpine and urban regions, *Atmos. Chem. Phys.*, 8, 6309–6323, doi:10.5194/acp-8-6309-2008, 2008.

Rieder, H. E., Staehelin, J., Weihs, P., Vuilleumier, L., Maeder, J. A., Holawe, F., Blumthaler, M., Lindfors, A., Peter, T., Simic, S., Spichtinger, P., Wagner, J. E., Walker, D., and Ribatet,

M.: Relationship between high daily erythemal UV doses, total ozone, surface albedo and cloudiness: An analysis of 30 years of data from Switzerland and Austria, *Atmos. Res.*, 98, 9–20, doi:10.1016/j.atmosres.2010.03.006, 2010.

Rieder, H. E., Frossard, L., Ribatet, M., Staehelin, J., Maeder, J. A., di Rocco, S., Davison, A. C., Peter, T., Weihs, P., and Holawe, F.: On the relationship between total ozone and atmospheric dynamics and chemistry at midlatitudes – Part 2: The effects of the El Niño/Southern Oscillation, volcanic eruptions and contributions of atmospheric dynamics and chemistry to long-term total ozone changes, *Atmos. Chem. Phys.*, 13, 165–179, doi:10.5194/acp-13-165-2013, 2013.

Rodgers, C.D: *Inverse Methods For Atmospheric Sounding: Theory and Practice*, Series on Atmospheric, Oceanic and Planetary Physics (Vol. 2), World Scientific, ISBN: 978-981-02-2740-1, 256 pp., 2000.

Rowland, F. S. and Molina, M.J. : Chlorofluoromethanes in the environment, *Rev. Geophys. Space Phys.*, 13, 1-35, 1975.

Ryer, A.D.: *The light measurement handbook*, Technical Publications Dept., International Light Technologies, USA, ISBN 0-9658356-9-3, 1997.

Saha, K., *The Earth's atmosphere, its physics and dynamics*, Springer-Verlag Berlin Heidelberg, ISBN: 9787-3-540-78426-5, 2008.

Sanchez-Lorenzo, A. and Wild, M.: Decadal variations in estimated surface solar radiation over Switzerland since the late 19th century, *Atmos. Chem. Phys.*, 12, 8635–8644, doi:10.5194/acp-12-8635-2012, 2012.

Sanchez-Lorenzo, A., Wild, M., Brunetti, M., Guijarro, J.A., Hakuba, M.Z., Calbó, J., Mystakidis, S. and Bartok, B.: Reassessment and update of long-term trends in downward surface shortwave radiation over Europe (1939-2012), *J. Geophys. Res. Atmos.*, 120, 9555-9569, doi: 10.1002/2015JD023321, 2015.

Santer, B. D., Wigley, T. M. L., Boyle, J. S., Gaffen, D. J., Hnilo, J. J., Nychka, D., Parker, D. E., and Taylor, K. E.: Statistical significance of trends and trend differences in layer-average atmospheric temperature time series, *J. Geophys. Res.*, 105, 7337–7356, doi:10.1029/1999JD901105, 2000.

Sasaki, M., Takeshita, S., Oyanagi, T., Miyake, Y., and Sakata, T.: Increasing trend of biologically active solar ultraviolet-B irradiance in mid-latitude Japan in the 1990s, *Opt. Eng.*, 41, 3062–3069, doi:10.1117/1.1516823, 2002.

Savastiouk, V. and McElroy, C.T.: Brewer spectrophotometer total ozone measurements made during the 1998 middle atmosphere nitrogen trend assessment (MANTRA) campaign, *Atmosphere-Ocean*, 43, 4, 315-324, 2005.

Savastiouk, V.: Improvements to the direct-sun ozone observations taken with the Brewer spectrophotometer, PhD thesis, York University, Toronto, Ontario, Canada, 2006.

Schuster, G. L., Vaughan, M., MacDonnell, D., Su, W., Winker, D., Dubovik, O., Lapyonok, T. and Trepte, C.: Comparison of CALIPSO aerosol optical depth retrievals to AERONET measurements, and a climatology for the lidar ratio of dust, *Atmos. Chem. Phys.*, 12, 7431–7452, doi:10.5194/acp-12-7431-2012, 2012.

Serdyuchenko, A., Gorshelev, V., Weber, M., Chehade, W., and Burrows, J. P.: High spectral resolution ozone absorption cross-sections – Part 2: Temperature dependence, *Atmos. Meas. Tech. Discuss.*, 6, 6613–6643, doi: 10.5194/amtd-6-6613-2013, 2013.

Seinfeld, J.H. and Pandis, S.N.: *Atmospheric Chemistry and Physics: from air pollution to climate change*, John Wiley & Sons, inc., New York, ISBN: 0-471-17815-2, 1998.

Sellitto, P., di Sarra, A., Siani, A.M.: An improved algorithm for the determination of aerosol optical depth in the ultraviolet spectral range from Brewer spectrophotometer observations, *J. Opt. A: Pure Appl. Opt.*, 8, 849–855, doi:10.1088/1464-4258/8/10/005, 2006.

Smedley, A. R. D., Rimmer, J. S., Moore, D., Toumi, R., and Webb, A. R.: Total ozone and surface UV trends in the United Kingdom: 1979–2008, *Int. J. Climatol.*, 32, 338–346, doi:10.1002/joc.2275, 2012.

Sofieva, V. F., Kyrölä, E., Laine, M., Tamminen, J., Degenstein, D., Bourassa, A., Roth, C., Zawada, D., Weber, M., Rozanov, A., Rahpoe, N., Stiller, G., Laeng, A., von Clarmann, T., Walker, K. A., Sheese, P., Hubert, D., van Roozendaal, M., Zehner, C., Damadeo, R., Zawodny, J., Kramarova, N., and Bhartia, P. K.: Merged SAGE II, Ozone_cci and OMPS ozone profile dataset and evaluation of ozone trends in the stratosphere, *Atmos. Chem. Phys.*, 17, 12533-12552, <https://doi.org/10.5194/acp-17-12533-2017>, 2017.

Solomon, S.: Stratospheric ozone depletion: a review of concepts and history, *Review of Geophysics*, 37, 3, 275-316, 1999.

Solomon, S., Qin, D., Manning, M., Alley, R. B., Berntsen, T., Bindoff, N. L., Chen, Z., Chidthaisong, A., Gregory, J. M., Hegerl, G. C., Heimann, M., Hewitson, B., Hoskins, B. J., Joos, F., Jouzel, J., Kattsov, V., Lohmann, U., Matsuno, T., Molina, M., Nicholls, N., Overpeck, J., Raga, G., Ramaswamy, V., Ren, J., Rusticucci, M., Somerville, R., Stocker, T. F., Whetton, P., Wood, R. A. and Wratt, D.: Technical Summary, in: *Climate Change 2007: The Physical Science Basis. Contribution of Working Group I to the Fourth Assessment Report of the Intergovernmental Panel on Climate Change*, edited by: Solomon, S., Qin, D., Manning, M., Chen, Z., Marquis, M., Averyt, K. B., Tignor, M., and Miller, H. L., Cambridge University Press, Cambridge, United Kingdom and New York, NY, USA, 19–91, 2007.

Solomon, S., Ivy, D.J., Kinnison, D., Mills, M.J., Neely III, R.R. and Schmidt, A.: Emergence of healing in the Antarctic ozone layer, *Science*, doi:10.1126/science.aae0061, 2016.

Sørensen, B.: *Renewable energy: Physics, Engineering, Environmental impacts, economics and planning*, Academic Press, ISBN: 978-0-12-375025-9, 2010.

Staehelin, J., Renaud, A., Bader, J., McPeters, R., Viatte, P., Hoegger, B., Bugnion, V., Giroud, M. and Schill, H.: Total ozone series at Arosa (Switzerland): Homogenization and data comparison, *J. Geophys. Res.*, 103, 5827-5841, 1998a.

Staehelin, J., Kegel, R., and Harris, N. R. P.: Trend analysis of the homogenized total ozone series of Arosa (Switzerland) 1926–1996, *J. Geophys. Res.*, 103, 8389–8399, doi:10.1029/97JD03650 , 1998b.

Starkweather, J.: *Cross Validation techniques in R : A brief overview of some methods, packages, and functions for assessing prediction models*, https://it.unt.edu/sites/default/files/crossvalidation1_jds_may2011.pdf (visited 11/1/2018), 2011.

Steinbrecht, W., Claude, H., Schönenborn, F., McDermid, I. S., Leblanc, T., Godin, S., Song, T., Swart, D. P. J., Meijer, Y. J., Bodeker, G. E., Connor, B. J., Kämpfer, N., Hocke, K., Calisesi, Y., Schneider, N., de la Noë, J., Parrish, A. D., Boyd, I. S., Brühl, C., Steil, B., Giorgetta, M. A., Manzini, E., Thomason, L. W., Zawodny, J. M., McCormick, M. P., Russell III, J. M., Bhartia, P. K., Stolarski, R. S., and Hollandsworth-Frith, S. M.: Long-term evolution of upper stratospheric ozone at selected stations of the Network for the Detection of Stratospheric Change (NDSC), *J. Geophys. Res.*, 111, D1027, doi:10.1029/2005JD006454, 2006.

Stjern, C. W., Egill Kristjánsson, J., and Hansen, A. W.: Global dimming and global brightening: an analysis of surface radiation and cloud cover data in northern Europe, *Int. J. Climatol.*, 29, 643–653, doi:10.1002/joc.1735, 2009.

Stolarski, R.S. and Cicerone, R.J., Stratospheric chlorine: a possible sink for ozone, *Canadian J. Chemistry*, 52, 1610-1615, 1974.

Stolarski, R. S., Bloomfield, P., McPeters, R. D. and Herman, J. R.: Total ozone trends deduced from Nimbus 7 TOMS data, *Geophys. Res. Lett.*, 18, 1015-1018, 1991.

Tanré, D., Bréon, F.M., Deuzé, J.L., Dubovik, O., Ducos, F., François, P., Foloub, P., Herman, M., Lifermann, A. and Waquet, F.: Remote sensing of aerosols by using polarized, directional and spectral measurements with the A-train: The PARASOL mission, *Atmos. Meas. Tech.*, 4, 1383-1395, doi:10.5194/amt-4-1383-2011, 2011.

Tanskanen, A.: Lambertian surface albedo climatology at 360 nm from TOMS data using moving time-window technique. Proc. XX Quadrennial Ozone Symposium, 1–8 June, Kos, Greece., 1159–1160, 2004

Teillet, P.M.: Rayleigh optical depth comparisons from various sources, *Appl. Opt.*, 29 (13), doi: 10.1364/AO.29.001897, 1990.

Terez, E.I. and Terez, G.A.: A method to determine atmospheric optical depth using observations of direct solar radiation, *J. Geophys. Res.*, 108, D22, 4704, doi: 10.1029/2003JD003829, 2003.

Tevini, M. and Teramura, H. A.: UV-B effects on terrestrial plants, *Photochem. Photobiol.*, 50, 479–487, doi:10.1111/j.1751-1097.1989.tb05552.x, 1989.

Tilley, D.R.: Spectral transformities for solar radiation reaching the Earth, in Brown, M., Odum, H.T., Tilley, D. and Ulgiati, S. (eds.) *Emergy Synthesis 2: Theory and Applications of the Emergy Methodology*, The Center for Environmental Policy Department of Environmental Engineering Sciences, University of Florida, 2003.

Trepte, S. and Winkler, P.: Reconstruction of erythemal UV irradiance and dose at Hohenpeissenberg (1968–2001) considering trends of total ozone, cloudiness and turbidity, *Theor. Appl. Climatol.*, 77, 159–171, doi:10.1007/s00704-004-0034-y, 2004.

TROPOMI: Algorithm theoretical basis document for the TROPOMI L01b data processor (issue 8.0.0), S5P-KNMI-L01B-0009-DS, 2017.

Unger, N., Menon, S., Koch, D. M., and Shindell, D. T.: Impacts of aerosol-cloud interactions on past and future changes in tropospheric composition, *Atmos. Chem. Phys.*, 9, 4115–4129, doi:10.5194/acp-9-4115-2009, 2009.

Vanicek K, Frei T, Litynska Z and Schmalwieser A.: UV-index for the public; A guide for publication and interpretation of solar UV Index forecasts for the public prepared by the Working Group 4 of the COST-713 Action “UV-B Forecasting”; *Eur. Coop. in the Field of Sci. and Tech. Res.*, Brussels, 2000.

van Geffen, J., van der A, R., van Weele, M., Allaart, M., and Eskes, H.: Surface UV radiation monitoring based on GOME and SCIAMACHY, *Proceedings of the ENVISAT and ERS Symposium*, 6-10 September 2004, Salzburg, Austria, ESA publication SP-572, 2005.

Van Malderen, R. and De Backer, H.: A drop in upper tropospheric humidity in autumn 2001, as derived from radiosonde measurements at Uccle, Belgium, *J. Geophys. Res.*, 115, D20114, doi:10.1029/2009JD013587, 2010.

Van Malderen, R., Allaart, M., De Backer, H., Smit, H.G.J. and De Muer, D.: On instrumental errors and related correction strategies of ozonesondes: possible effect on calculated ozone trends for the nearby sites Uccle and De Bilt, *Atmos. Meas. Tech.*, 9, 3793-3816, doi: 10.5194/amt-9-3793-2016, 2016.

Veefkind, P.J., de Haan, J.F., Brinksma, E.J., Kroon, M. and Levelt, P.F.: Total Ozone from the Ozone Monitoring Instrument (OMI) using the DOAS technique, *IEEE transactions on geoscience and remote sensing*, 44, 5, 1239-1244, doi: 10.1109/TGRS.2006.871204, 2006.

Viatte, C., Schneider, M., Redondas, A., Hase, F., Eremenko, M., Chelin, P., Flaud, J.-M., Blumenstock, T. and Orphal, J.: Comparison of ground-based FTIR and Brewer O₃ total column with data from two different IASI algorithms and from OMI and GOME-2 satellite instruments, *Atmos. Meas. Tech.*, 4, 535–546, doi:10.5194/amt-4-535-2011, 2011.

Vigouroux, C., De Mazière, M., Demoulin, P., Servais, C., Hase, F., Blumenstock, T., Kramer, I., Schneider, M., Mellqvist, J., Strandberg, A., Velasco, V., Notholt, J., Sussmann, R., Stremme, W., Rockmann, A., Gardiner, T., Coleman, M., and Woods, P.: Evaluation of tropospheric and stratospheric ozone trends over Western Europe from ground-based FTIR network observations, *Atmos. Chem. Phys.*, 8, 6865–6886, doi:10.5194/acp-8-6865-2008, 2008.

Wang, S., Nan, J., Shi, C., Fu, Q., Goa, S., Wang, D., Ciu, H., Saiz-Lopez, A. and Zhou, B.: Atmospheric ammonia and its impacts on regional air quality over the megacity of Shanghai, China, *Scientific Reports*, 5, doi: 10.1038/srep15842, 2015.

Weatherhead, C. E., Reinsel, G. C., Tiao, G. C., Meng, X.-L., Choi, D., Cheang, W.-K., Keller, T., DeLuisi, J., Wuebbles, D. J., Kerr, J. B., Miller, A. J., Oltmans, S. J., and Frederick, J. E.: Factors affecting the detection of trends: Statistical considerations and applications to environmental data, *J. Geophys. Res.*, 103, 17149–17161, doi:10.1029/98JD00995, 1998.

Wespes, C., Hurtmans, D., Emmons, L.K., Safieddine, S., Clerbaux, C., Edwards, D.P. and Coheur, P.-F.: Ozone variability in the troposphere and the stratosphere from the first 6 years of IASI observations (2008-2013), *Atmos. Chem. Phys.*, 16, 5721-5743, doi: 10.5194/acp-16-5721-2016, 2016.

West S.G., Finch J.F. and Curran P.J.: Structural equation models with nonnormal variables: problems and remedies. In RH Hoyle (Ed.). *Structural equation modeling: Concepts, issues and applications*. Newbery Park, CA: Sage, 56-75, 1996.

World Health Organization, World Meteorological Organization, United Nations Environment Programme & International Commission on Non-Ionizing Radiation Protection: *Global solar UV index : a practical guide*, Geneva, 2002.

Wild, M., Gilgen, H., Roesch, A., Ohmura, A., Long, C.N., Dutton, E.G. Forgan, B., Kallis, A., Russak, V. and Tsvetkov, A.: From dimming to brightening: decadal changes in solar radiation at Earth's surface, *Science*, 308, 5723, 847-850, doi: 10.1126/science.1103215, 2005.

Wild, M.: Global dimming and brightening: a review, *J. Geophys. Res.*, 114, D00D16, doi:10.1029/2008JD011470, 2009a.

Wild, M., Trüssel, B., Ohmura, A., Long, C. N., König-Langlo, G., Dutton, E. G., and Tsvetkov, A.: Global dimming and brightening: an update beyond 2000, *J. Geophys. Res.*, 114, D00D13, doi:10.1029/2008JD011382, 2009b.

Wild, M., Folini, D., Schär, C., Loeb, N., Dutton, E.G. and König-Langlo, G.: The global energy balance from a surface perspective, *Clim. Dyn.*, 40, 3107-3134, doi:10.1007/s00382-012-1569-8, 2013.

Wild, M.: Decadal changes in radiative fluxes at land and ocean surfaces and their relevance for global warming, *WIREs Clim. Change*, 7, 91-107, doi:10.1002/wcc.372, 2016.

Williams, J. E., den Outer, P. N., Slaper, H., Matthijsen, J., and Kelfkens, G.: Cloud induced reduction of solar UV-radiation: A comparison of ground-based and satellite based approaches, *Geophys. Res. Lett.*, 31, L03104, doi:10.1029/2003GL018242, 2004.

Williams, M. N., Grajales, C. A. G. and Kurkiewicz, D: Assumptions of Multiple Regression: Correcting Two Misconceptions. *Practical Assessment, Research & Evaluation*, 18(11), 2013.

Wilson, R. and Spengler, J.: *Particles in our air concentrations and health effects*, Harvard University Press, Cambridge, USA, 1996.

Winker, D.M., Vaughan, M.A., Omar, A. Hu, Y. Powell, K.A., Liu, Z., Hunt, W.H. and Young, S.A.: Overview of the CALIPSO mission and CALIOP data processing algorithms, *Journal of Atmospheric Oceanic Technology*, 26, 2310-2323, doi: 10.1175/2009JTECHA1281.1, 2009.

World Meteorological Organization (WMO), *Meteorology A Three-Dimensional Science: Second Session of the Commission for Aerology*, WMO Bulletin IV(4), WMO, Geneva, 134–138, 1957.

World Meteorological Organization (WMO): *Atmospheric Ozone 1985, Global Ozone Research and Monitoring Project*, Report No. 16,, Geneva, Switzerland, 1985.

World Meteorological Organization (WMO): *Commission for instruments and methods of observation, Abridged final report of the tenth session*, Brussels, 11-22 September 1989, ISBN: 92-63-10727-0, 1990.

World Meteorological Organization/United Nations Environment Programme (WMO/UNEP), Scientific Assessment of Ozone Depletion: 1991, Rep. 25, Geneva, 1991.

World Meteorological Organization/United Nations Environment Programme (WMO/UNEP), Scientific Assessment of Ozone Depletion: 1994, Rep. 37, Geneva, 1994.

WMO, WMO/CEOS Report on a Strategy for Integrating Satellite and Ground based Observations of Ozone (WMO TD. No. 1046), report nr. 140, 2001.

WMO: WMO/GAW experts workshop on a global surface-based network for long term observations of column aerosol optical properties, report nr. 162, 2004.

WMO/GAW: Instruments to measure solar ultraviolet radiation part 3: multi-channel filter instruments (WMO TD. No. 1537), report nr 190, 2010a.

WMO/GAW: Instruments to measure solar ultraviolet radiation part 4: Array spectroradiometers (WMO TD. No. 1538), report nr 191, 2010b.

World Meteorological Organization (WMO): Scientific Assessment of Ozone Depletion: 2014, World Meteorological Organization, Global Ozone Research and Monitoring Project—Report No. 55, 416 pp., Geneva, Switzerland, 2014.

Xia, X., Eck, T. F., Holben, B. N., Philippe, G., and Chen, H.: Analysis of the weekly cycle of aerosol optical depth using AERONET and MODIS data, *J. Geophys. Res.*, 113, D14217, doi:10.1029/2007JD009604, 2008.

Zerefos, C. S., Balis, D. S., Bais, A. F., Gillotay, D., Simon, P. C., Mayer, B., and Seckmeyer, G.: Variability of UV-B at four stations in Europe, *Geophys. Res. Lett.*, 24, 1363–1366, 1997.

Zerefos, C., Balis, D., Tzortziou, M., Bais, A., Tourpali, K., Meleti, C., Bernhard, G., and Herman, J.: A note on the interannual variations of UV-B erythemal doses and solar irradiance from groundbased and satellite observations, *Ann. Geophys.*, 19, 115–120, doi:10.5194/angeo-19-115-2001, 2001.

Zerefos, C. S., Tourpali, K., Eleftheratos, K., Kazadzis, S., Meleti, C., Feister, U., Koskela, T., and Heikkilä, A.: Evidence of a possible turning point in solar UV-B over Canada, Europe and Japan, *Atmos. Chem. Phys.*, 12, 2469–2477, doi:10.5194/acp-12-2469-2012, 2012.

Zhang, X., Xia, X., and Xuan, C.: On the drivers of variability and trend of surface solar radiation in Beijing metropolitan area, *Int. J. Climatol.*, 35, 452–461, doi:10.1002/joc.3994, 2015.

Ziemke, J. R., Chandra, S., Herman, J., and Varotsos, C.: Erythemally weighted UV trends over northern latitudes derived from Nimbus 7 TOMS measurements, *J. Geophys. Res.*, 105,

7373–7382, 2000.

Zong, Y., Brown, S.W., Johnson, B.C., Lykke, K.R. and Ohno, Y.: Simple spectral stray light correction method for array spectroradiometers, *Appl. Opt.*, 45, 6, 1111-1119, 2006.

Zuk-Golaszewska, K., Upadhyaya, M.K. and Golaszewski, J.: The effect of UV-B radiation on plant growth and development, *Plant Soil Environ.*, 49 (3), 135-140, 2003.

Appendices

Appendix A: Seasonal MLR 2 results

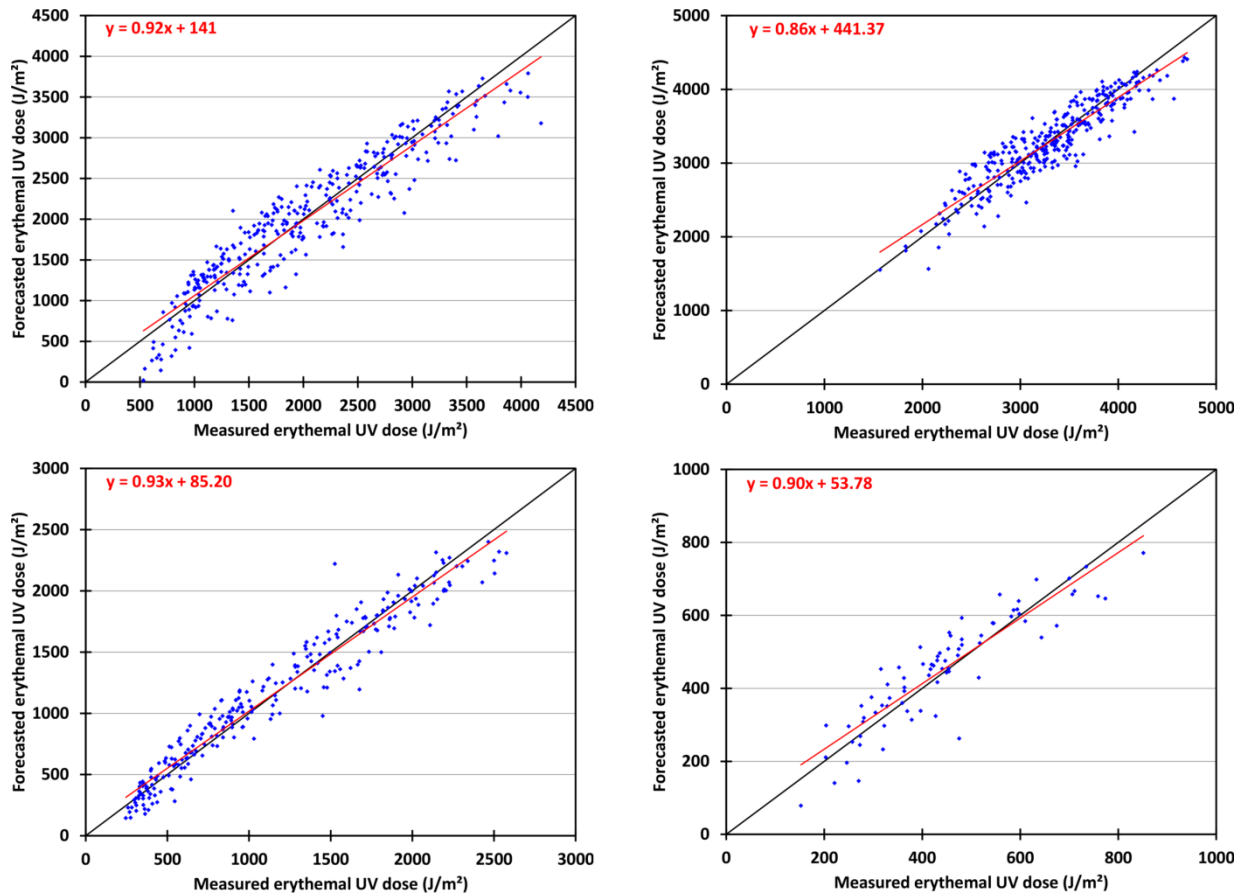


Figure 61: Scatterplots of the measured and modeled (MLR 2) erythemal UV doses at Uccle for the 1991–2015 period for spring (upper left panel), summer (upper right panel), autumn (lower left panel) and winter (lower right panel). The red lines represent the regression lines of the data, and the black lines are the $f(x)=x$ lines.

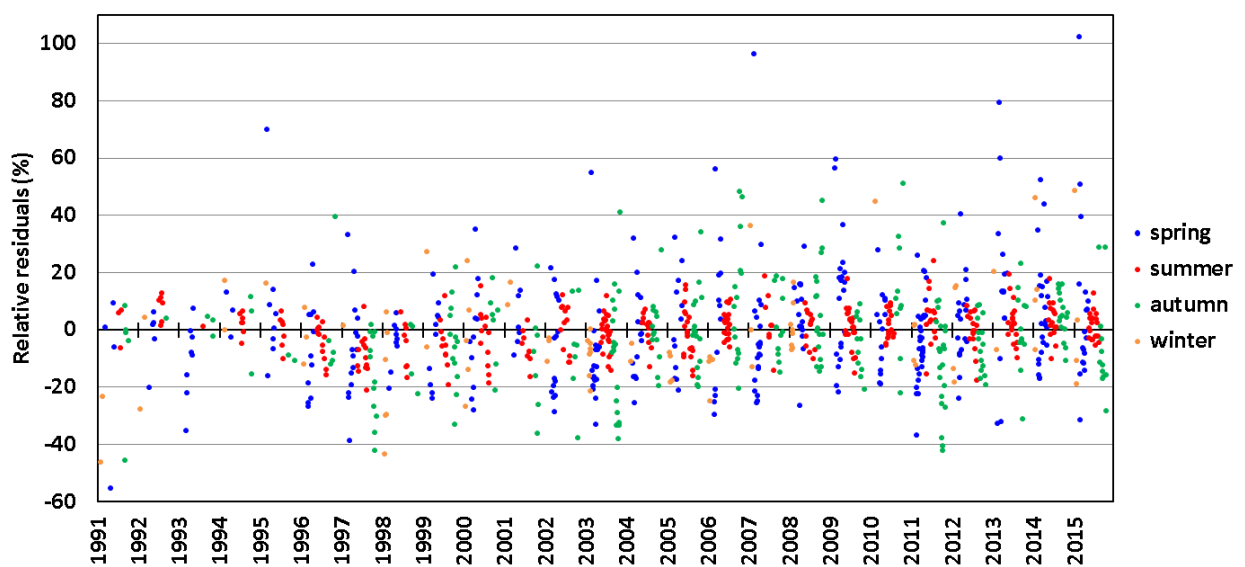


Figure 62 : Same as Figure 60 for MLR 2. The colors represent the different seasons: blue – spring; red – summer; green – autumn; and orange – winter.

Table 41: Results of MLR 2 analysis with only S_g , S_g combined with Q_{O3} , S_g combined with τ_{aer} , only Q_{O3} and Q_{O3} combined with τ_{aer} as explanatory variables

	S_g	$S_g + Q_{O3}$	$S_g + \tau_{aer}$	Q_{O3}
Adjusted R²				
Spring	0.88	0.91	0.88	0.08
Summer	0.83	0.87	0.83	0
Autumn	0.93	0.93	0.94	0
Winter	0.63	0.81	0.63	0.09
Spring	15.32	14.62	15.23	43.79
Summer	6.25	5.9	6.21	15.07
Autumn	13.28	13.66	12.4	72.6
Winter	15.54	13.76	15.57	31.74
Spring	0.92	0.94	0.92	0.34
Summer	0.90	0.91	0.90	0.04
Autumn	0.97	0.97	0.97	0.11
Winter	0.82	0.90	0.83	0.25

Appendix B: Table of quantities and constants mentioned in this work

QUANTITIES		
	Symbol	Unit
Temperature	T	Kelvin (K)
Effective ozone temperature	T_{eff}	Kelvin (K)
Wavelength	λ	Meter (m)
Frequency	ν	Hertz (Hz)(= s^{-1})
Wavenumber	$\tilde{\nu}$	m^{-1}
Potential vorticity	PV	1 PVU (Potential Vorticity Unit) = $10^{-6} \text{K} \cdot \text{kg}^{-1} \cdot \text{m}^2 \cdot \text{s}^{-1}$
Plane angle	θ	Radian
Solid angle	ω	Steradian (sr)
Surface	A	m^2
Radiant flux	Φ	Watt ($1 \text{ W} = 1 \text{ J} \cdot \text{s}^{-1}$)
Spectral flux	Φ_{λ}	$\text{W} \cdot \text{m}^{-1}$
Intensity (=spectral radiance)		
- Source	I_s	$\text{W} \cdot \text{sr}^{-1}$
- Observer	I	$\text{W} \cdot \text{m}^{-2}$
Spectral intensity		
- Source	$I_{s,\lambda}$	$\text{W} \cdot \text{sr}^{-1} \cdot \text{m}^{-1}$
- Observer	I_{λ}	$\text{W} \cdot \text{m}^{-2} (\text{m}^{-1})$
Extraterrestrial Constant (ETC)	$I_0(\lambda)$	$\text{W} \cdot \text{m}^{-2}$
Irradiance		
- Source	E_s	$\text{W} \cdot \text{m}^{-2}$
- Observer	E	$\text{W} \cdot \text{m}^{-2}$
Spectral irradiance		
- Source	$E_{s,\lambda}$	$\text{W} \cdot \text{m}^{-3}$
- Observer	E_{λ}	$\text{W} \cdot \text{m}^{-2} (\text{m}^{-1})$
Blackbody spectral irradiance	$E_{B,\lambda}$	$\text{W} \cdot \text{m}^{-3}$
Blackbody irradiance	E_B	$\text{W} \cdot \text{m}^{-2}$
Radiance	L_s	$\text{W} \cdot \text{sr}^{-1} \cdot \text{m}^{-2}$
Spectral radiance	$L_{s,\lambda}$	$\text{W} \cdot \text{sr}^{-1} \cdot \text{m}^{-3}$
Extinction coefficient	α_e	m^{-1}
Scattering coefficient	α_s	m^{-1}
Absorption coefficient	α_a	m^{-1}
Ozone absorption coefficient	$\alpha_{\text{O}_3}(\lambda, T)$	m^{-1}
Total optical depth	τ	(dimensionless)
Scattering total optical depth	τ_s	(dimensionless)
Absorption total optical depth	τ_a	(dimensionless)
Aerosol optical depth (AOD)	τ_{aer}	(dimensionless)
- at 320 nm	$\tau_{\text{aer},320}$	
- at 340 nm	$\tau_{\text{aer},340}$	
Rayleigh optical depth	τ_R	(dimensionless)
Optical depth from absorption by gases (general)	τ_g	(dimensionless)

- by ozone	τ_{O_3}	
- by NO ₂	τ_{NO_2}	
- by SO ₂	τ_{SO_2}	
Particle number concentration	N	molecules·cm ⁻³
Extinction cross section	$\sigma_e(\lambda)$	cm ² ·molecule ⁻¹
Absorption cross section	$\sigma_a(\lambda)$	cm ² ·molecule ⁻¹
Scattering cross section	$\sigma_s(\lambda)$	cm ² ·molecule ⁻¹
Ozone cross section	$\sigma_{O_3}(\lambda, T_{deg})$	cm ² ·molecule ⁻¹
Solar zenith angle	θ_0	° (degrees)
Air mass	m	(dimensionless)
- For Rayleigh scattering	m_R	
- For ozone absorption	m_{O_3}	
Registered Brewer counts	$F_i (i = 2,6)$	counts
Dark count	F_1	counts
Number of slit mask cycles	CY	(dimensionless)
Count rates (for ozone calculations)	C_i	counts·s ⁻¹
- True count rate	C_0	
- Temperature corrected	$C_{i,temp}$	
- Rayleigh corrected	$C_{i,ray}$	
Corrected count rates (for UV)	C_λ	
Brewer temperature coefficients	TC_i	°C ⁻¹
Brewer instrument temperature	TE	°C
Attenuation value of neutral density filter	AF_p	(dimensionless)
Brewer responsivity (for UV)	R_λ	Counts·s ⁻¹ ·W ⁻¹ ·m ² ·nm
Signal calibration lamp	$C_{lamp,\lambda}$	Counts·s ⁻¹
Irradiance calibration lamp	$E_{lamp,\lambda}$	W·m ⁻² ·nm ⁻¹
Spectral erythemal solar UV irradiance	$E_{ery,\lambda}$	W·m ⁻² ·nm ⁻¹
Erythemal UV dose rate	D_{ery}	W·m ⁻²
Erythemal daily UV dose	D_{ery}^*	J·m ⁻²
Global solar radiation	D_g^*	J·m ⁻²
Total ozone column (TOC)	Q_{O_3}	DU
Signal measured by the Brewer	$S(\lambda)$	counts·s ⁻¹
Proportionality factor for the Brewer	$K(\lambda)$	counts·s ⁻¹ ·W ⁻¹ ·m ²
Calibration factor	CF	s ⁻¹
CONSTANTS		
Planck's constant	h	6.626 · 10 ⁻³⁴ · J · s
Speed of light in vacuum	c	2.9979 · 10 ⁸ · m · s ⁻¹
Boltzmann constant	k_B	1.38064852 · 10 ⁻²³ · J · K ⁻¹
Stefan-Boltzmann constant	k_{SB}	5.671 · 10 ⁻⁸ · W · m ⁻² · K ⁻⁴
Solar constant	S_0	1360 W·m ⁻²
	k_{er}	40 m ² ·W ⁻¹
Radius of the Earth	R	6370 km
Station pressure for Uccle	P	1000 hPa
Standard pressure	P_{std}	1013.25 hPa
CIE erythema action spectrum	$Ser(\lambda)$	Dimensionless (see table 5)

Bass & Paur quadratic coefficients (at 340 nm)	C_0	$1.81094 \cdot 10^{-1}$
	C_1	$1.169180 \cdot 10^{-3}$
	C_2	$3.916970 \cdot 10^{-6}$
Avogadro's number	N_a	$6.0225 \cdot 10^{23} \cdot \text{molecules} \cdot \text{mole}^{-1}$
Gas constant	R_g	$8.314 \cdot \text{J} \cdot \text{K}^{-1} \cdot \text{mole}^{-1}$
Standard temperature	T_{std}	273.15 K
Brewer integration time	IT	0.1147 s

Appendix C: list of publications

Peer-reviewed papers

De Bock, V., De Backer, H., Mangold, A. and Delcloo, A.: Aerosol Optical Depth measurements at 340 nm with a Brewer spectrophotometer and comparison with CIMEL observations at Uccle, Belgium, *Atmos. Meas. Tech.*, 3, 1577-1588, doi:10.5194/amt-3-1577-2010, 2010.

De Bock, V., De Backer, H., Van Malderen, R., Mangold, A. and Delcloo, A.: Relations between erythemal UV dose, global solar radiation, total ozone column and aerosol optical depth at Uccle, Belgium, *Atmos. Chem. Phys.*, 14, 12251-12270, doi:10.5194/acp-14-12251-2014, 2014.

Gielen, C., Van Roozendaal, M., Hendrick, F., Pinardi, G., Vlemmix, T., De Bock, V., De Backer, H., Fayt, C., Hermans, C., Gillotay, D. and Wang, P.: A simple and versatile cloud-screening method for MAX-DOAS retrievals, *Atmos. Meas. Tech.*, 7, 3509-3527, doi:10.5194/amt-7-3509-2014, 2014.

Zerefos, C. S., Eleftheratos, K., Kapsomenakis, J., Solomos, S., Inness, A., Balis, D., Redondas, A., Eskes, H., Allaart, M., Amiridis, V., Dahlback, A., De Bock, V., Diémoz, H., Engelmann, R., Eriksen, P., Fioletov, V., Gröbner, J., Heikkilä, A., Petropavlovskikh, I., Jarosławski, J., Josefsson, W., Karppinen, T., Köhler, U., Meleti, C., Repapis, C., Rimmer, J., Savinykh, V., Shiroto, V., Siani, A. M., Smedley, A. R. D., Stanek, M., and Stübi, R.: Detecting volcanic sulfur dioxide plumes in the Northern Hemisphere using the Brewer spectrophotometers, other networks, and satellite observations, *Atmos. Chem. Phys.*, 17, 551-574, <https://doi.org/10.5194/acp-17-551-2017>, 2017.

López-Solano, J., Redondas, A., Carlund, T., Rodríguez-Franco, J. J., Diémoz, H., León-Luis, S. F., Hernández-Cruz, B., Guirado-Fuentes, C., Kouremeti, N., Gröbner, J., Kazadzis, S., Carreño, V., Berjón, A., Santana-Díaz, D., Rodríguez-Valido, M., De Bock, V., Moreta, J. R., Rimmer, J., Smedley, A. R. D., Boulkelia, L., Jepsen, N., Eriksen, P., Bais, A. F., Shiroto, V., Vilaplana, J. M., Wilson, K. M., and Karppinen, T.: Aerosol optical depth in the European Brewer Network, *Atmos. Chem. Phys.*, 18, 3885-3902, <https://doi.org/10.5194/acp-18-3885-2018>, 2018.

Posters

De Bock V. and De Backer, H.: Comparison of AOD values at 340nm from Brewer#178 and CIMEL measurements at Uccle, Belgium, WMO-GAW Brewer Users Group Meeting, Aosta, Italy, 20-26, September 2009.

Maenhaut, W., Wang, W., Chi, X., Raes, N., Cafmeyer, J., Cheymol, A., Delcloo, A., De Bock, V. and De Backer, H.: Measurements on Atmospheric Aerosols and of the Aerosol

Optical Depth during 2006 at Uccle, Belgium, 11th Science Conference of the International Global Atmosphere Chemistry (IGAC) Project, Halifax, Canada, July 11-16, 2010.

De Bock, V., De Backer, H., Mangold, A. and Delcloo, A.: Aerosol Optical Depth measurements at 340 nm with a Brewer spectrophotometer and comparison with CIMEL sunphotometer observations at Uccle, Belgium, 3rd MeteoClim PhD Symposium on Meteorology and Climatology, Uccle, Belgium, November 5, 2010.

De Bock, V., De Backer, H. and Mangold, A.: Improved cloud screening for Aerosol Optical Depth measurements with a Brewer spectrophotometer, European Aerosol Conference, Manchester, United Kingdom, September 4-9, 2011.

Nikitidou, E., De Bock, V., De Backer, H. and Kazantzidis, A.: Estimation of aerosol optical properties and their effect on UV irradiance at Uccle, Belgium, 11th EMS Annual Meeting / 10th European Conference on Applications of Meteorology (ECAM), Berlin, Germany, September 12-16, 2011.

Mangold, A., Mano, M.-J., Namsaraev, Z., De Backer, H., De Bock, V., Hermans, C., Gorodetskaya, I., Maenhaut, W., Atmospheric composition research at the Belgian Antarctic research station Princess Elisabeth with emphasis on aerosol particle characterisation, IPY 2012 Conference, From Knowledge to Action, Montréal, Canada, 22-27 April 2012.

Nikitidou, E., De Bock, V., De Backer, H. and Kazantzidis, A.: Aerosols optical properties and their effect on the UV solar irradiance at Uccle, Belgium, International Radiation Symposium 2012, Berlin, Germany, 6-10 August, 2012.

De Bock, V., De Backer, H. and Van Malderen, R.: Analysis of an extensive time series of UV irradiation and AOD measurements in the UV-B region at Uccle, Belgium, International Radiation Symposium 2012, Berlin, Germany, 6-10 August, 2012.

De Bock, V., De Backer, H. and Van Malderen, R.: Analysis of an extensive time series of UV irradiation and AOD measurements in the UV-B region at Uccle, Belgium, Quadrennial Ozone Symposium 2012, Toronto, Canada, 26-31 August, 2012.

De Bock, V., De Backer, H. and Mangold, A.: Retrieval of Single Scattering Albedo values from Brewer spectrophotometer irradiance measurements at Uccle, Belgium, European Aerosol Conference 2012, Granada, Spain, 2-7 September, 2012.

Mangold, A. De Backer, H., De Bock, V., Hermans, C., Gorodetskaya and Maenhaut, W.: Physical and optical properties of atmospheric aerosol in Eastern Antarctica, European Aerosol Conference 2012, Granada, Spain, 02-07 September, 2012.

De Bock, V., Delcloo, A., Mangold, A. and De Backer, H.: Modeling of aerosol optical properties with CHIMERE and OPAC and validation with Brewer and CIMEL measurements at Brussels, Belgium, European Aerosol Conference 2013, Prague, Czech Republic, 1-6 September, 2013.

Mangold, A., De Backer, H., Delcloo, A., De Bock, V., Hermans, C., Gorodetskaya, I., and W. Maenhaut: Seasonal physical and optical properties of atmospheric aerosol at Princess Elisabeth station, East Antarctica, European Aerosol Conference 2013, Prague, Czech Republic, 1-6 September, 2013.

Mangold, A., Van Malderen, R., De Backer, H., Delcloo, A., De Bock, V., Gorodetskaya, I., Wex, H., and Hermans, C.: Observations of atmospheric composition, clouds and precipitation in Dronning Maud Land, East Antarctica, MOZAIC–IAGOS Scientific Symposium on Atmospheric Composition Observations by Commercial Aircraft: 20th Anniversary, Toulouse, 12-15 May, 2014.

De Bock, V., De Backer, H. and Mangold, A.: Aerosol Optical Depth retrieval from Brewer spectrophotometers at Uccle, Belgium, Eubrewnet open congress/14th WMO-GAW Brewer Users Group Meeting, Tenerife, 24-28 March, 2014.

De Bock, V., Mangold, A., De Backer, H. and Delcloo, A.: Aerosol optical properties during a 2014 smog period at Uccle, Belgium, European Aerosol Conference, Milan, Italy, 6-11 September, 2015.

Mangold, A., De Backer, H., De Bock, V., Delcloo, A., Hermans, C., Gorodetskaya, I., Herenz, P., Henning, S. and Wex, H.: Atmospheric aerosol properties at Princess Elisabeth station, East Antarctica,: seasonality and indication of new particle formation, European Aerosol Conference 2015, Milan, Italy, 6-11 September, 2015.

Mangold, A., Laffineur, Q., De Bock, V., Hermans, C., Gielen, C., Gorodetskaya, I., Herenz, P., Wex, H., Verhasselt, K., Oosterbos, S., Kuppens, S. and De Backer, H.: Atmospheric aerosol characterisation at Princess Elisabeth station, East Antarctica, BNCCGG-BNCAR Symposium, Unlocking a continent: Scientific research at the Belgian Princess Elisabeth Station Antarctica 2008-2016, Brussels, Belgium, 29 April, 2016.

Mangold, A., Laffineur, Q., Van Malderen, R., De Bock, V., Hermans, C., Nys, K. and De Backer, H.: Analysis of total ozone and UV radiation and of vertical profile measurements of temperature, humidity and wind data at Princess Elisabeth Station, East Antarctica, BNCCGG-BNCAR Symposium, Unlocking a continent: Scientific research at the Belgian Princess Elisabeth Station Antarctica 2008-2016, Brussels, Belgium, 29 April, 2016.

Gielen, C., Van Roozendael, M., Hermans, C., Hendrick, F., Fayt, C., De Backer, H., Mangold, A., De Bock, V., Laffineur, Q., Van Lipzig, N., Souverijns, N., Gorodetskaya, I., Lhermitte, S. and Gossart, A.: Aerosol and ozone measurements from the recently installed MAX-DOAS instrument at the Princess Elisabeth Station in the framework of the AEROCLOUD project, BNCCGG-BNCAR Symposium, Unlocking a continent: Scientific research at the Belgian Princess Elisabeth Station Antarctica 2008-2016, Brussels, Belgium, 29 April, 2016.

Fountoulakis, I., Bais, A.F., Lakkala, K., Toth, Z., De Bock, V., Diémoz, H., Doppler, L., Feister, U., Fragkos, K., Gröbner, J., Heikkilä, A., Karppinen, T., Koskela, T., San Atanasio,

J.M., Siani, A.M. and Smedley, A.R.D.: Temperature dependence of the Brewer spectral UV and total ozone column measurements, Quadrennial Ozone Symposium, Edinburgh, United Kingdom, 4-9 September, 2016.

De Bock, V., Mangold, A., Delcloo, A., Hermans, C. and De Backer, H.: Measurements of aerosol optical properties at a suburban site in Belgium, European Aerosol Conference 2017, , Zürich, Switzerland, 27 August – 1 September, 2017.

Mangold, A., Q. Laffineur, H. De Backer, V. De Bock, A. Delcloo, C. Hermans, C. Gielen, P. Herenz, and Wex, H.: Atmospheric aerosol and CCN properties in Dronning Maud Land, East Antarctica, European Aerosol Conference 2017, Zürich, Switzerland, 27 August – 1 September, 2017.

De Bock, V., Tilstra, G., Tuinder, O., Mangold, A., Laffineur, Q. and Delcloo, A.: Validation of the aerosol absorbing height (AAH) products from GOME-2 instruments on-board MetOp-A and MetOp-B within the framework of the AC SAF, Eumetsat conference, Rome, Italy, 2-6 October, 2017.

Laffineur, Q., A. Delcloo, A. Mangold, V. De Bock and De Backer, H.: Misidentification of smoke plumes over Europe: joint use of ceilometer measurements with dispersion model increases their identification, European Geosciences Union General Assembly 2018, Vienna, Austria, 8-13 April, 2018.

Talks

De Bock, V.: AGACC-II: Advanced exploitation of Ground-based measurements for Atmospheric Chemistry and Climate applications - II: RMI project results, RMI conference, Uccle, Belgium, December 10, 2014

De Bock V.: Brewer AOD retrieval at RMI using DS measurements, COST ES1207-Eubrewnet WG meeting, Santa Cruz de Tenerife, January 27-28, 2015.

Articles:

De Bock et al. (2010)

De Bock et al. (2014)

Aerosol Optical Depth measurements at 340 nm with a Brewer spectrophotometer and comparison with Cimel sunphotometer observations at Uccle, Belgium

V. De Bock, H. De Backer, A. Mangold, and A. Delcloo

Royal Meteorological Institute of Belgium, Ringlaan 3, 1180 Brussels, Belgium

Received: 28 May 2010 – Published in Atmos. Meas. Tech. Discuss.: 29 June 2010

Revised: 10 November 2010 – Accepted: 10 November 2010 – Published: 19 November 2010

Abstract. The Langley Plot Method (LPM) is adapted for the retrieval of Aerosol Optical Depth (AOD) values at 340 nm from Brewer#178 sun scan measurements between 335 and 345 nm (convoluted with the band pass function of the Cimel sunphotometer filter at 340 nm) performed in Uccle, Belgium. The use of sun scans instead of direct sun measurements simplifies the comparison of the AOD values with quasi-simultaneous Cimel sunphotometer values. Also, the irradiance at 340 nm is larger than the one at 320.1 nm due to lower ozone absorption, thus improving the signal to noise ratio. For the selection of the cloudless days (from now on referred to as calibration quality clear days), a new set of criteria is proposed. With the adapted method, individual clear sky AOD values, for which the selection criteria are also presented in this article, are calculated for a period from September 2006 until the end of August 2010. These values are then compared to quasi-simultaneous Cimel sunphotometer measurements, showing a very good agreement (the correlation coefficient, the slope and the intercept of the regression line are respectively 0.974, 0.968 and 0.011), which proves that good quality observations can be obtained from Brewer sun scan measurements at 340 nm. The analysis of the monthly and seasonal Brewer AODs at Uccle is consistent with studies at other sites reporting on the seasonal variation of AODs in Europe. The highest values can be observed in summer and spring, whereas more than 50% of the winter AODs are lower than 0.3. On a monthly scale, the lowest AOD are observed in December and the highest values occur in June and April. No clear weekly cycle is observed for Uccle. The current cloud-screening algorithm is still an issue,

which means that some AOD values can still be influenced by scattered clouds. This effect can be seen when comparing the calculated monthly mean values of the Brewer with the AERONET measurements.

1 Introduction

Aerosols are particles in the solid or liquid phase that are suspended in the atmosphere and have an important influence on the atmospheric chemistry and physics (Cheymol and De Backer, 2003; Raghavendra Kumar et al., 2010). They affect the tropospheric chemical composition, they can reduce visibility and they have important impacts on human health (Unger et al., 2009; Lyamani et al., 2010; Raghavendra Kumar et al., 2010). Aerosols also influence the Earth's radiation budget in a direct, semi-direct and indirect manner. The scattering and absorption of short and long wave radiation is called the direct effect (Ramanathan et al., 2001; Kaufman et al., 2002; Andreae et al., 2005; Myrhe, 2009). The semi-direct effect describes the warming of the boundary layer, through the absorption of radiation by aerosols, which can lead to evaporation of clouds. This will allow more solar radiation to reach the surface (Ramanathan et al., 2001; Cazorla et al., 2009). The indirect effect concerns the ability of aerosols to act as cloud condensation nuclei which influences the microphysical and optical properties of clouds, thus changing the radiative and precipitation properties and the lifetime of clouds (Ramanathan et al., 2001; Kaufman et al., 2002; Lohmann, 2002; Lohmann and Feichter, 2005; Unger et al., 2009). Because of a lack of information concerning the temporal and spatial distribution of aerosols, they are key



Correspondence to: V. De Bock
(veerle.debock@meteo.be)

contributors to the uncertainties in current climate studies (Andreae et al., 2005; IPCC, 2007).

The influence of aerosols on ultraviolet (UV) radiation has received a lot of attention in research, since the impact of UV radiation on human health, the biosphere and atmospheric chemistry strongly depends on the characteristics and quantity of aerosol in the atmosphere. An overexposure to UV-B radiation can lead to serious health damage for humans such as skin cancer, accelerated aging of skin, cataract, photokeratitis (snow blindness) and changes in the immune system (Rieder et al., 2008; Cordero et al., 2009). UV-B radiation also has adverse effects on terrestrial plants (Tevini and Teramura, 1989; Cordero et al., 2009) and on other elements of the biosphere (Diffey, 1991). The increase of anthropogenic aerosols in non-urban areas of the industrialized countries since the industrial revolution is supposed to have decreased the biologically active UV radiation by 5 to 18% (Liu et al., 1991). Accuracy in UV prediction can be improved if the role of aerosols on surface UV radiation is clarified (Kim et al. 2008). However, little information is available on the optical properties of atmospheric aerosols in the UV spectral region, compared to the visible spectral range (Sellitto et al., 2006).

To gain a better understanding of the effect of aerosols in the UV, knowledge of the parameters that determine the optical and physical properties of aerosols is essential (Cazorla et al., 2009; Kazadzis et al., 2009). One of these parameters is the Aerosol Optical Depth (AOD), an integral measurement of the combined aerosol scattering and absorption in the atmospheric column (Mulcahy et al., 2009). When assessing the recovery of the ozone layer, knowledge of the AOD is of high importance. Without such knowledge, it is very likely that a change in surface UV irradiance is attributed to a change in ozone amount, whereas it could actually be the result of an increase or decrease in aerosol load. Several reports have been written on the retrieval of AOD in the UV range. For example, Taylor et al. (2008) and Corr et al. (2009) use MFRSR (Multi Filter Rotating Shadowband Radiometer) measurements for this retrieval. Research also shows that the standard Brewer direct sun (DS) measurements allow AOD retrieval at the wavelengths used for ozone determination (mainly 320.1 nm). Some authors base their retrieval on the absolute calibration of the solar spectral irradiance measured by the Brewer (Bais, 1997; Marengo et al., 1997; Kazadzis et al., 2005) whereas others use the Langley extrapolation method to determine the absolute calibration of the irradiance (Kirchhoff et al., 2001; Marengo et al., 2002; Cheymol and De Backer, 2003). Arola and Koskela (2004) discussed the systematic errors in the AOD retrieval from Brewer DS measurements, which led to improvements of the conventional Langley Plot Method (e.g. Cheymol et al., 2009).

Several authors studied the spatial and temporal patterns in AOD. Both Bäumer et al. (2008) and Xia et al. (2008) reported a weekly cycle in AOD for Central Europe (45–

55° N; 0–20° E). Seasonal patterns in AOD with maximum values in spring and summer and minimum values in autumn and winter are observed in many studies (Meleti and Cappellani, 2000; Behnert et al., 2004; Kim et al., 2006; Estellés, 2008; Remer et al., 2008; Che et al., 2009; Léon et al., 2009; Lyamani et al., 2010). Gröbner and Meleti (2004) studied long-term trends in AOD at Ispra and detected a decrease between 1991 and 1997, followed by a stabilization in the AOD values. Kazadzis et al. (2007) however, reported on a statistically significant (99% level) decrease in AOD for Thessaloniki after 1997. Hatzianastassiou et al. (2009) studied the spatial distribution of AOD over the Mediterranean basin and found significant geographical variation of AOD within the study area (e.g. large AOD values over North Africa and smaller values in relatively remote oceanic areas such as Crete island).

In this paper, we present an adapted and improved method for the retrieval of AOD values. Instead of using the standard direct sun measurements from the Brewer instrument dedicated to ozone retrieval (which are performed at 5 specific wavelengths) (as in Cheymol and De Backer, 2003), we will use sun scan measurements between 335 and 345 nm, convoluted with the band pass function of the Cimel sunphotometer filter at 340 nm, to obtain AOD values at 340 nm. This will allow for a direct comparison between these retrieved AOD values and the AODs from the Cimel sunphotometer at the same wavelength. Information about the used instruments and the measurement location is included in Sect. 2. The method applied for the retrieval of the Brewer AOD values is described in Sect. 3. The resulting AOD values are compared with Cimel sunphotometer measurements in Sect. 4. Also, the temporal patterns in AOD are discussed and compared to results of other studies.

2 Instruments and location

In this study, we make use of the measurements of a Brewer spectrophotometer and a Cimel sunphotometer. Both instruments are located in Uccle, a residential suburb of Brussels about 100 km from the shore of the North Sea. The prevailing meteorological conditions will determine whether the station is influenced by sea salt aerosols, by aerosols from urban activity or by continental type of aerosols (De Backer, 2009).

The Brewer spectrophotometer was developed in the early 1980s to measure total ozone in the atmosphere from UV-B radiation (Brewer, 1973; Kerr et al., 1988). The instrument records raw photon counts of the photomultiplier at five wavelengths (306.3, 310.1, 313.5, 316.8 and 320.1 nm) using a blocking slit mask, which opens successively one of the five exit slits. The five exit slits are scanned twice within 1.6 s and this is repeated 20 times. The whole procedure is repeated five times for a total of about three minutes. The total ozone column is obtained from a combination of measurements at 310.1, 313.5, 316.8 and 320.1 nm weighted with a

predefined set of constants chosen to minimize the influence of SO₂ and linearly varying absorption features such as from clouds or aerosols (Gröbner and Meleti, 2004). RMIB (Royal Meteorological Institute of Belgium) has two Brewers on the roof of its building in Uccle (50°48' N, 4°21' E, 100 m a.s.l.). Brewer#016 is a single monochromator Mark II model that was installed in Uccle in 1983. In 1989, the instrument was equipped with an automated azimuth and zenith pointing system, resulting in a higher observation frequency (Cheymol et al., 2006). Brewer#178 is a double monochromator Mark III that was installed in September 2001. In addition to the standard observation routines, an additional routine was developed to be able to determine the AOD at 340 nm with the double monochromator Brewer. More precisely, the sun scan routine was adapted to perform scans between 335 nm and 345 nm with slit 1. The measuring wavelength step of this sun scan routine is 0.5 nm and one scan has a duration of 21 s. For comparison with Cimel AOD products, the obtained spectral data are convoluted with the band pass function of the Cimel sunphotometer filter (Full Width at Half Maximum of the filter is 4.756 nm) (standard Cimel sunphotometer filter values; Barr Associates Inc.). The data of this type, available since 17 August 2006, will be used for the retrieval of AOD at 340 nm. The stability of the Brewer#178 wavelengths has been examined and the results show that the stability of this instrument is very good (Gröbner et al. 2006). This justifies the application of the Langley Plot Method (Sect. 3) on the sun scan measurements of Brewer#178 for the retrieval of AOD.

The Cimel sunphotometer, which belongs to BISA (Belgium Institute of Space Aeronomy), is located at approximately 100 m from the Brewer instrument. It is an automatic sun-sky scanning filter radiometer allowing the measurements of the direct solar irradiance at wavelengths 340, 380, 440, 500, 670, 870, 940 and 1020 nm. These solar extinction measurements are used to compute aerosol optical depth at each wavelength except for the 940 nm channel, which is used to retrieve total atmospheric column precipitable water in centimeters. The instrument is part of the AERONET network (<http://aeronet.gsfc.nasa.gov/>; Holben et al., 2001). The accuracy of the AERONET AOD measurements at 340 nm is 0.02 (Eck et al. 1999).

3 Method

To derive the AOD at 340 nm from the measurements described above, we apply the Langley Plot Method (LPM), in a similar way as described in Cheymol and De Backer (2003), to the weighted irradiances. The Langley Plot Method is a linear regression technique that can be used for the retrieval of the Aerosol Optical Depth from direct radiation measurements. This method can only be applied on cloud-free days and for each cloud-free day, one AOD value and one calibration factor (CF) will be estimated. Due to the

low number of completely cloud-free days, we only applied the LPM once for the entire period. The mean calibration factor (calculated from the individual values for the cloud-free days) will be used to calculate the Aerosol Optical Depth for each individual measurement. The basics of this method and the deviations from the algorithm in Cheymol and De Backer (2003) will be described here. More details on the LPM can be found in Marengo et al. (2002) and in Cheymol and De Backer (2003).

3.1 Basic equation

An important difference between this work and the one by Cheymol and De Backer (2003) is that the latter uses the direct sun (DS) measurements at five specific wavelengths (320.1 nm being the largest) from the Brewer instrument for the received signal values, whereas here we use sun scans between 335 and 345 nm, convoluted with the band pass function of the Cimel sunphotometer filter at 340 nm. The use of the sun scans is an important improvement that simplifies the comparison of the AOD values, since it is no longer necessary to extrapolate the Cimel AOD values to the Brewer wavelength. Moreover, due to the convolution with the Cimel sunphotometer band pass filter, we compare physically exactly the same quantity. Another advantage is that the intensity of the retrieved signal at this wavelength is larger due to the lower absorption by ozone, improving the signal to noise ratio. The signal, received by the Brewer instrument, follows Beer's law (using the notations as in Cheymol and De Backer, 2003):

$$S(\lambda) = K(\lambda)I_0(\lambda)\exp[-\mu\alpha(\lambda, T)\Omega - m\beta(\lambda)\frac{P}{P_{\text{std}}} - \delta(\lambda)\sec(z_a)], \quad (1)$$

with $S(\lambda)$ the received signal, $K(\lambda)$ the proportionality factor of the instrument's response to the incoming solar radiation at wavelength λ , $I_0(\lambda)$ the irradiance outside the earth's atmosphere at wavelength λ , μ the relative optical air mass (the path length relative to that at the zenith at sea level) of the ozone layer at height=22 km, $\alpha(\lambda, T)$ the ozone absorption coefficient at wavelength λ and temperature T , Ω the equivalent thickness of the ozone layer, m the relative optical air mass of the atmosphere in a thin layer assumed to be at an altitude of 5 km for Rayleigh scattering, $\beta(\lambda)$ the Rayleigh scattering coefficient, P_{std} the standard pressure (1013.25 hPa), P the station pressure (1000 hPa), $\delta(\lambda)$ the aerosol extinction optical thickness of a vertical path through the atmosphere and z_a the zenith angle of the sun.

This law reflects that, while passing through the atmosphere, the direct beam at the top of the atmosphere is subject to absorption and scattering through three different physical phenomena: (a) absorption by ozone, (b) scattering by air molecules (Rayleigh scattering) and (c) extinction by aerosol particles. The SO₂ absorption is not considered here, since this term is very low compared to the ozone absorption

term, which is already small at 340 nm. To eliminate the dependence of the AOD retrieval on the effective ozone temperature, the ozone absorption coefficient is computed using the effective ozone temperature (as in Cheymol and De Backer, 2003). This effective ozone temperature is calculated using ozone and temperature profiles from balloon soundings available at Uccle. Since the sun scans are convoluted with the Cimel sunphotometer band pass filter, we should also convolute the Rayleigh scattering and the ozone absorption coefficients. The convolution was done for the Rayleigh scattering term and this caused only a small change in the retrieved AOD values with a maximum difference of 0.00023 with respect to AOD values calculated without a convoluted Rayleigh term. Since the contribution of the ozone absorption term to the computation of the AOD values is very low compared to the Rayleigh contribution, we did not convolute the ozone absorption coefficient. This would lead to negligible changes in the AOD.

3.2 Langley plot method

Taking the logarithm of Eq. (1) gives Eq. (2):

$$\begin{aligned} \ln[S(\lambda)] + \mu\alpha(\lambda)\Omega + m\beta(\lambda)\frac{P}{P_{\text{std}}} \\ = \ln[K(\lambda)I_0(\lambda)] - \delta(\lambda)\sec(z_a) \end{aligned} \quad (2)$$

Let us define:

$$Y = \ln[S(\lambda)] + \mu\alpha(\lambda)\Omega + m\beta(\lambda)\frac{P}{P_{\text{std}}}, \quad (3)$$

$$\text{CF} = \ln[K(\lambda)I_0(\lambda)], \quad (4)$$

$$A = \delta(\lambda), \quad (5)$$

$$X = \sec(z_a). \quad (6)$$

With Eqs. (3–6), Eq. (2) can be simplified to

$$Y = \text{CF} - A * X \quad (7)$$

Now, one AOD value (A) and one calibration factor (CF) can be estimated per day. The quality of the linear regression depends on the range of the solar zenith angles covered during a certain day. Good observations at both high and low solar zenith angles are needed and the atmospheric conditions must remain stable over the day. This leads to different criteria for the selection of the days on which the LPM can be applied (calibration quality clear days). Cheymol et al. (2009) proposed the following criteria:

1. The individual DS data for which the air mass is above 3 are removed.
2. The range of solar zenith angles (SZA) covered by valid DS observations for one day must be at least 20° .
3. The number of individual DS data must be at least 50 per day (i.e. 10 sequences of 5 observations).

4. The ozone column and its standard deviation are computed on each group of 5 individual DS measurements for each wavelength. Data are accepted if the standard deviation is lower than 2.5 DU.

Since in our case sun scans are used instead of DS measurements, these criteria have to be adapted. The test done on the ozone values (4th criterion) loses its significance since the ozone observations of Brewer#178 and the sun scans between 335 nm and 345 nm are not performed simultaneously. Clouds are thus able to influence the irradiance measurements during the sun scan, while the closest ozone observations (in time) could be made under cloudless conditions. Concerning the 2nd criterion, it has to be mentioned that the same SZA range can yield different ranges of air mass for different seasons. Since air mass range is a more important parameter for the quality control of the Langley Plots, the 2nd criterion was changed so that a minimum range limit was placed on the optical air mass instead of on the SZA range. We will retain the upper value of 3 for the air mass (1st criterion), since at higher air masses the irradiances measured by the Brewer become much lower and the instrument becomes much more sensitive to stray light effects. This could thus bias the AOD measurements. The remaining criteria are applied to the sun scans instead of to DS measurements.

Manually verifying whether the selected days are indeed cloudless showed that these criteria were not sufficient. An additional criterion is therefore proposed. It is based on the ratio of the observed and expected irradiance for a certain day. The observed irradiance is obtained from the sun scans between 335 and 345 nm that are convoluted with the band pass function of the Cimel sunphotometer filter. The expected irradiance (under cloudless circumstances) is calculated by the Tropospheric Ultraviolet and Visible Radiation Model (TUV model version 3.0; Madronich, 1993), which uses the band pass function of the Cimel sunphotometer filter at 340 nm. The climatological monthly mean total ozone value and a default constant AOD value (0.7777 as a standard value for polluted air) are used as input parameters for the calculation of the monochromatic radiative transfer. The cloud optical depth and surface albedo are respectively 0 and 0.05. If a certain day is cloudless and the atmospheric conditions are stable, the ratio of the irradiance should be more or less constant throughout the day. For the calculation of the ratio, both the observed and the expected irradiance are normalized to their maximum. (Figure 1 shows the calculated ratios for a cloudless and for a cloudy day.) In this context, a day is considered cloudless if the maximum deviation of the individual ratios (of a day) from the mean ratio is smaller than 20% (different threshold values were tested, but the 20% value generated the best results, meaning that the selected cloudless days were in agreement with the observed cloudless days).

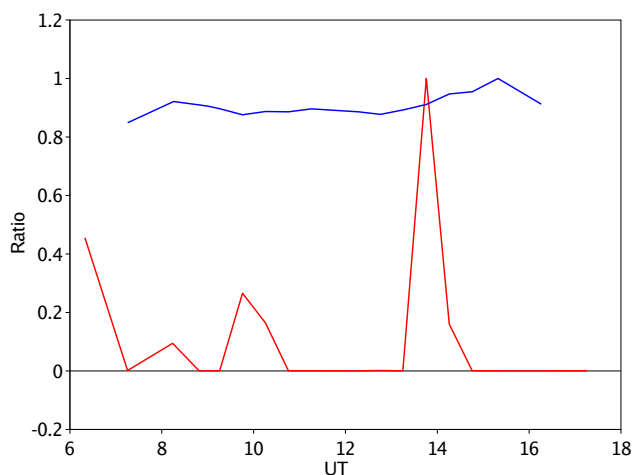


Fig. 1. Ratio of the observed and expected irradiance for a cloudless (5 August 2007; in blue) and for a cloudy (20 July 2008; in red) day at Uccle. The points that appear as null values are points for which the ratio is very small. This can be explained by the influence of clouds, which causes the observed irradiance to be very low.

This leads to the following set of criteria for the selection of calibration quality clear days (CCD=Criteria Calibration Days) for the determination of the calibration factors with the Langley Plot Method:

1. The sun scans for which the air mass is above 3 are removed.
2. The range of air masses covered by the sun scans for one day must be at least 1.
3. At least 10 sun scans per day have to remain after applying the first two criteria.
4. The maximum deviation of the individual ratios (of the observed and expected irradiance) from the mean ratio for a certain day has to be smaller than 20%.

After applying these criteria, the calibration coefficients are calculated for each selected calibration quality clear day (Table 1). From this calibration coefficient, the mean value is calculated which will be used as mean calibration coefficient of the instrument. With this mean calibration coefficient, the AOD can now be calculated for each individual observation. Since we only apply the Langley Plot Method once for the entire period, the stability of the calibration factor of the instrument can not be calculated. However, the UV-lamp tests of the Brewer instrument, showing that the instrument is very stable, indicate that the same is true for the calibration factor of the instrument. To avoid the influence of clouds that might remain on the calculated AOD values, we only calculated AOD values for the individual sun scans for which a direct sun observation, made with Brewer#178, is available

Table 1. List of selected calibration quality clear days from September 2006 until the end of August 2010 with their calibration factor. The mean calibration factor is calculated from these values.

Date	Calibration Factor
6 Sep 2006	18.485
21 Sep 2006	18.386
4 Apr 2007	18.463
22 Apr 2007	18.527
30 Apr 2007	18.599
1 May 2007	18.434
2 May 2007	18.646
5 May 2008	18.631
8 May 2008	18.593
11 May 2008	18.649
1 Jul 2008	18.568
29 May 2009	18.692
15 Aug 2009	18.584
10 Mar 2010	18.654
23 May 2010	18.638
3 Jun 2010	18.520

within a time period of 5 min. It has to be mentioned that this however does not exclude all cloud-perturbed measurements. This is shown in the resulting AOD values, some of which seemed too high to be reliable. As the definition of simple criteria to detect cloud interference in the UV is complex (Dürr and Philipona, 2004) we propose at this stage only a manual method to exclude this cloud contamination. The application of a more sophisticated and automated method will be the subject of a subsequent study. Figure 2 shows the scatter plot of the Brewer AOD measurements and the corresponding Cimel sunphotometer measurements (with a maximum time difference of 30 min). There is a good agreement between Brewer and Cimel for Brewer AOD values lower than 2. When the Brewer AODs become larger than 2, there is virtually no agreement with the Cimel sunphotometer measurements. Based on this result, we decided to automatically remove all Brewer AOD values larger than 2 from our results on the assumption that they were influenced by clouds. No Cimel values were removed, since these values are already cloud-screened.

A set of criteria to select the individual clear sky AOD values (from all the calculated AOD values), can now be defined (CICA = Criteria Individual Clear sky AOD):

1. A direct sun observation must be available for each individual AOD measurement within a time period of 5 min.
2. Each individual AOD value must be lower than 2. Larger values are removed from the results.

The remaining Brewer AOD values were compared to quasi-simultaneous Cimel AODs at 340 nm (AERONET level 2.0 data). Only quasi-simultaneous measurements of

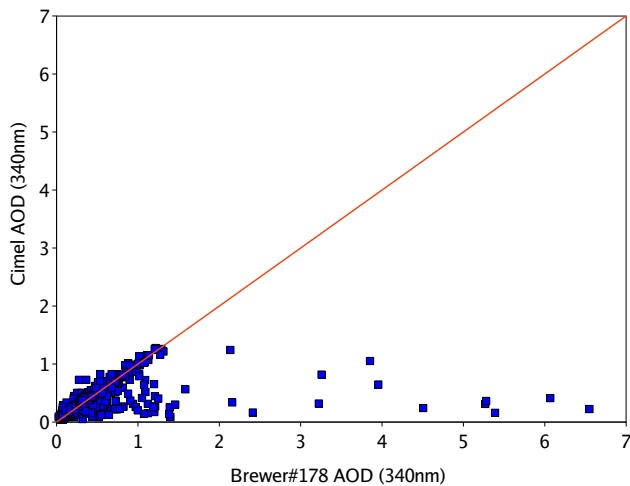


Fig. 2. Scatter plot of the Brewer and Cimel AOD at 340 nm (time period for the comparison is 30 min). The red curve represents $f(x) = x$.

both instruments (with a maximum time difference of 3 min) are considered. The AOD values from Brewer#178 at 320 nm were also compared to quasi-simultaneous Cimel values. A second order fit of $\ln(\text{AOD})$ to $\ln(\lambda)$ (using the AERONET data from 500, 440, 380 and 340 nm) was used to estimate the Cimel AOD values at 320 nm.

4 Results and discussion

4.1 Comparison between Brewer spectrophotometer and Cimel sunphotometer measurements

For the comparison with the AOD values from the Cimel sunphotometer, the Brewer#178 sun scan measurements at 340 nm from September 2006 until the end of August 2010 were used. For this period, a total of 16 calibration quality clear days (Table 1) were selected using CCD (as mentioned in Sect. 3.2) combined with individual inspection. The mean calibration factor (CF) for these days is 18.567 ± 0.089 . With this calibration coefficient, the individual clear sky AOD values (according to CICA) are calculated, using the Brewer#178 sun scans. The applied method resulted in 2951 AODs at 340 nm for a period from 1 September 2006 to 31 August 2010. The uncertainty in the calibration coefficient (0.089) causes an uncertainty of 0.08 in the AOD measurements. Only quasi-simultaneous measurements from the Brewer and Cimel (level 2.0 data from AERONET) were used for comparison. From the 2951 individual Brewer AODs, only 251 measurements had a quasi-simultaneous Cimel measurement. The comparison of the Brewer and Cimel AODs at 340 nm had a correlation coefficient of 0.860 (Fig. 3). Selecting only those Brewer AOD observations with a concurrent Cimel sunphotometer observation (maximum

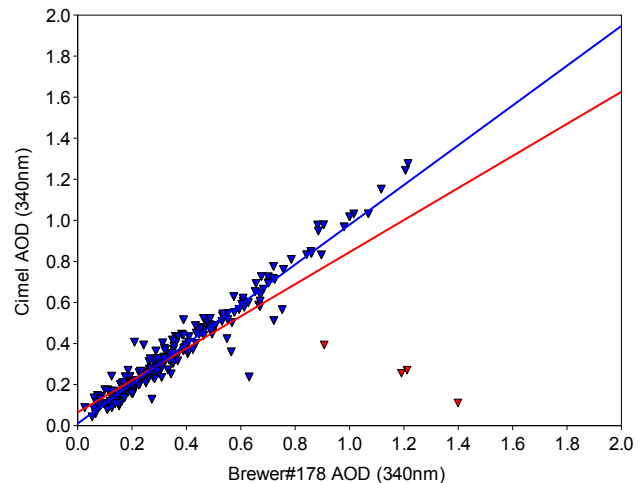


Fig. 3. Comparison of the Brewer and Cimel AOD values at 340 nm (time period for the comparison is 3 min). The red curve ($f(x) = 0.781x + 0.065$) represents the regression line of all the data. The blue curve ($f(x) = 0.968x + 0.011$) shows the regression line of the data without the outliers.

time difference of 3 min) and with a quasi-simultaneous DS measurement (maximum time difference of 5 min) automatically eliminates most of the cloudy conditions. The scatter plot of the compared AODs still showed the presence of a few outliers (highlighted in red in Fig. 3), causing the rather low correlation coefficient compared to the one obtained by Cheymol et al. (2009) (correlation coefficient of 0.96 for the comparison between Brewer#016 at 320 nm and Cimel at 340 nm). These remarkable outliers require further examination. We consider a single point in the scatter plot to be an outlier if the difference in AOD between Brewer and Cimel measurements is bigger than 0.5. This is the case for less than 2% of the compared values which made us question those individual Brewer measurements for which the difference was higher than 0.5. All the sun scan measurements of days with an outlier were plotted. Figure 4 shows the theoretical and the observed relative intensity of the irradiance for a day on which an outlier was present (13 September 2006). The figure clearly shows that the outlier measurement (highlighted in red) is influenced by clouds. This justifies the removal of this point from the comparison. Similar checks were performed for the other outliers and it turned out that for those outliers, the Brewer measurements were made under cloud-perturbed circumstances. Then a comparison was made excluding these outliers. This resulted in a much higher correlation coefficient of 0.974. The slope is 0.968 ± 0.014 and the intercept is 0.011 ± 0.006 (Fig. 3), confirming a good linear agreement between the AOD measurements of both instruments. The agreement between the AODs at 340 nm is better than at 320 nm (Fig. 5), where the correlation is 0.900, the slope 0.863 ± 0.021 and the intercept 0.025 ± 0.010 . This shows that good quality AOD

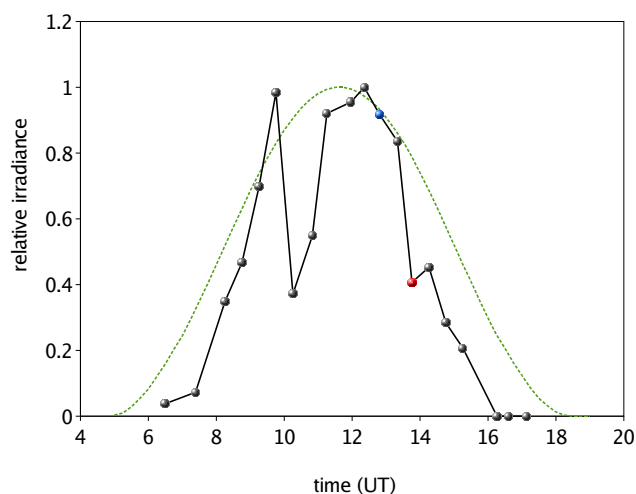


Fig. 4. Sun scan measurements of Brewer#178 on a day for which an outlier was present (13 September 2006). The green dashed line represents the theoretical values, based on the output of the TUV model, whereas the black line represents the observed relative intensity of the irradiance. The highlighted points (red and blue) represent the points for which the comparison with the Cimel measurements was done (which means there was a Cimel observation within a time period of 3 min). The difference between the Brewer and Cimel measurements was larger than 0.5 for the red point, which was considered to be an outlier. From this plot, it is clear that this outlier measurement is strongly influenced by clouds.

observations can be obtained at 340 nm from Brewer#178 sun scan measurements with the proposed method. A comparison is also made between the monthly mean AOD values (Fig. 7) from the Brewer and Cimel measurements. For some months, the difference between the monthly values is rather high. For example in March 2008, the mean monthly Cimel AOD was 0.16, whereas for the Brewer instrument, the monthly mean was 0.54. For 13 months (out of the analyzed 27 months) the difference between the monthly AOD values of the two instruments is larger than 0.2. The mean monthly AOD values of the Brewer instrument are most likely upper limits, since some individual AOD measurements (that constitute to these values) can still be highly biased as a result of cloud perturbation. This thus causes the large differences in mean monthly values between the two instruments. It also shows that the used cloud-screening method needs further improvement.

4.2 AOD variability in Uccle on different timescales

A total of 2951 individual AOD measurements from Brewer#178 were calculated for the period from 1 September 2006 to 31 August 2010 and the values were examined for possible variations on seasonal, monthly and weekly timescales. Some of the individual AOD values were questionable, especially the values larger than 1.5. When Brewer and Cimel measurements were compared, these values were

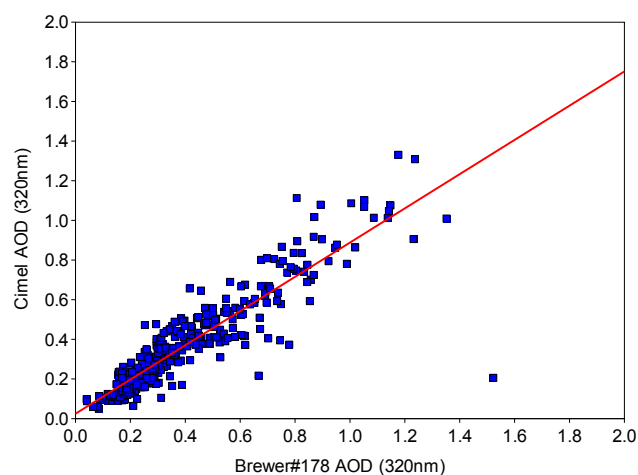


Fig. 5. Comparison of the Brewer#178 and Cimel AOD values at 320 nm. The red line is the linear regression curve ($f(x) = 0.863x + 0.025$) of the comparison.

automatically removed from the results because the Brewer AOD values larger than 1.5 did not have a concurrent Cimel measurement. However, for the study of the individual values in the whole archive (which are not compared to the Cimel data) it is required to manually check the data for cloud-perturbed measurements. For each day with an AOD measurement higher than 1.5, a plot was made of the measured irradiances (photon counts) from the Brewer instruments. If the relative irradiance is much lower than one would expect, the measurement is perturbed (by clouds) and the individual AOD value will thus be removed from the results. So, next to the automatic cloud-screening (using CICA), a manual check is done for the individual AOD values larger than 1.5. An objective method to remove observations affected by clouds is under development. The outlier values from the comparison with the Cimel are also not included in the analyzed dataset. The remaining 2834 individual AOD values were used to study variability on different time scales.

4.2.1 Seasonal and monthly variability

Many studies that investigate the seasonal variability of aerosols, report high AODs during summer (June, July, August) and spring (March, April, May) and low AODs in winter (December, January, February) and autumn (September, October, November). In Valencia (Spain), maximum AOD values were observed (between 2002–2005) from June to September, whereas the minimum values occurred from October to February (mainly in December and January) (Estellés, 2008). Behnert et al. (2004) observed two peak periods in the AOD values from Helgoland Island, Hamburg, Oostende and Lille. They occurred during spring (April–May) and summer (July–August). Studies in Ispra (Italy),

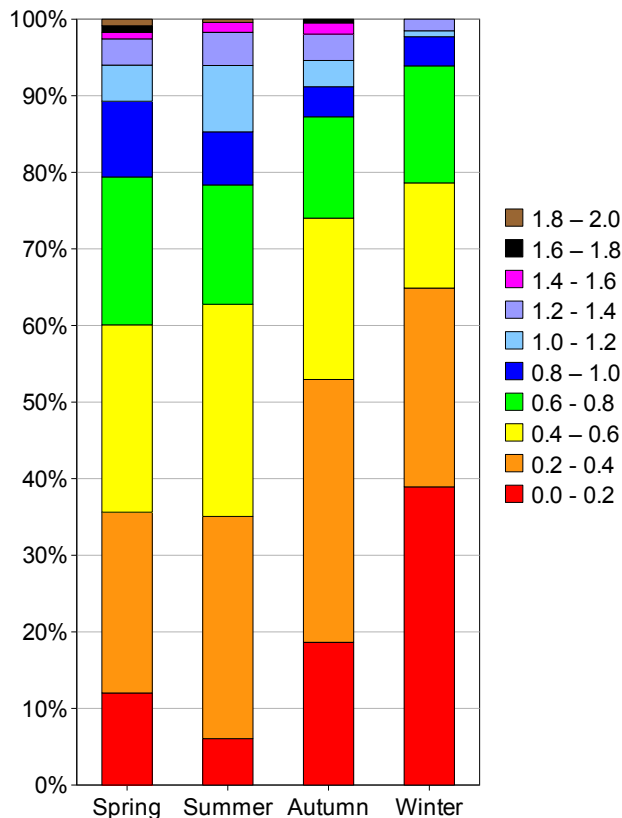


Fig. 6. Seasonal frequency distribution of AOD values at 340 nm at Uccle from 1 September 2006 to 31 August 2010.

Granada (Spain), M'Bour (Senegal), Gwangju (Korea) and Thessaloniki (Greece) also show high AOD values in summer and low values in winter (Meleti and Cappellani, 2000; Kim et al., 2006; Kazadzis et al., 2007; Léon et al., 2009; Lyamani et al., 2010). (The latitude and longitude of the places mentioned in this article can be found in Table 2.)

The obtained AODs from Brewer#178 at Uccle are consistent with these studies. Figures 6 and 7 display the seasonal and monthly variation in AOD values for Uccle. The highest values can be observed in summer (respectively $0.63(\pm 0.35)$, $0.59(\pm 0.34)$, $0.53(\pm 0.27)$ and $0.58(\pm 0.37)$ for 2007, 2008, 2009 and 2010) and spring (respectively $0.55(\pm 0.32)$, $0.58(\pm 0.35)$, $0.63(\pm 0.38)$ and $0.51(\pm 0.30)$ for 2007, 2008, 2009 and 2010). In winter more than 50% of the AODs at Uccle are below 0.3, which is in agreement with the results from Kazadzis et al. (2007) for Thessaloniki, Greece. On a monthly scale (Fig. 7), the lowest AODs are observed in December (respectively $0.07(\pm 0.02)$, $0.23(\pm 0.14)$ and $0.21(\pm 0.13)$ for 2007, 2008 and 2009), whereas the highest values occur in June ($0.79(\pm 0.38)$) in 2007 and April ($0.74(\pm 0.31)$) in 2008 and $0.78(\pm 0.41)$ in 2009).

Possible explanations for the higher summer AODs are given by several authors. Behnert et al. (2004) attribute the summer peak values to the slowing down of air mass cir-

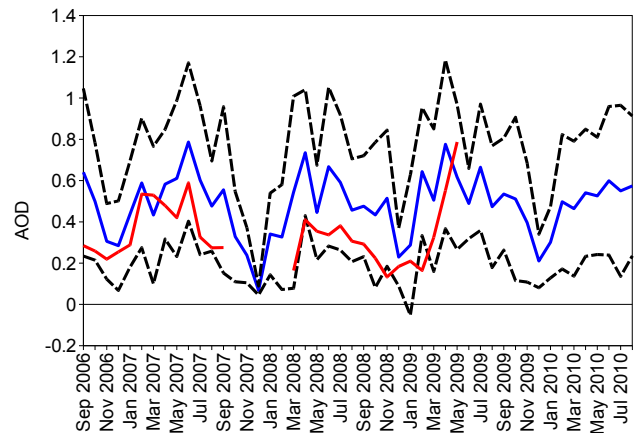


Fig. 7. Monthly variation in AOD (at 340 nm) at Uccle (based on data from September 2006 until the end of August 2010). The blue line is the mean seasonal value, whereas the dashed black lines represent the mean value \pm its standard deviation. For December 2007, the mean monthly value is based on only 3 individual AOD values (which were accidentally very close). This explains the low standard deviation for this month. The AERONET level 2.0 monthly means are shown in red.

Table 2. List of places mentioned in this article with their latitude and longitude.

Location	Latitude	Longitude
Uccle (Belgium)	50°48' N	4°21' E
Oostende (Belgium)	51°13' N	2°55' E
Lille (France)	50°36' N	3°06' E
Helgoland Island (Germany)	54°10' N	7°53' E
Hamburg (Germany)	53°34' N	9°56' E
Ispra (Italy)	45°49' N	8°38' E
Valencia (Spain)	39°30' N	0°25' W
Granada (Spain)	37°10' N	35°35' E
Thessaloniki (Greece)	40°30' N	22°54' E
Beijing (China)	39°59' N	116°19' E
Gwangju (Korea)	35°13' N	126°50' E
M'Bour (Senegal)	16°58' N	14°23' E

ulation in summer and the production of smog. This results in an accumulation of high aerosol concentrations above midlatitude regions. Kaskaoutis et al. (2007) explain the higher summer AODs at Ispra as a result of the absence of wet removal processes. According to Kazadzis et al. (2007), the enhanced evaporation and the higher temperatures during summer in Thessaloniki cause a rise in the turbidity of the boundary layer. Combined with stagnating weather systems, this will lead to the formation of aerosols. In winter, there is a significant amount of wet deposition of aerosols, which will cause a cleaning of the atmosphere and therefore lower AOD values. Koelemeijer et al. (2006) also state that

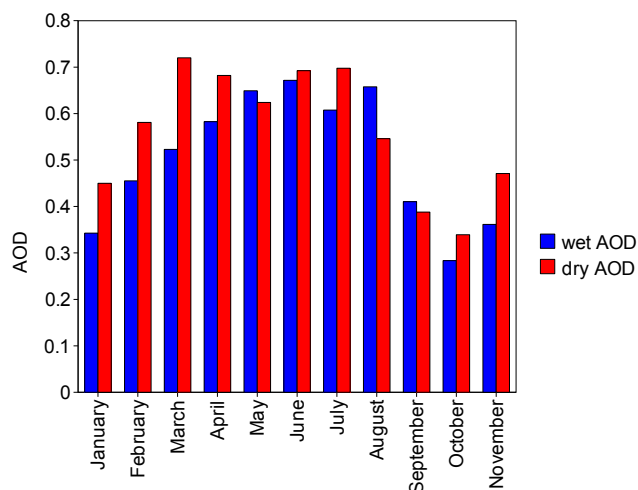


Fig. 8. Mean monthly AOD values (at 320 nm from Brewer#016) for dry and wet days for a time period from 1984 to 2009.

high precipitation in winter leads to low AOD values. They observed an anti-correlation (-0.41 for the region of Belgium and The Netherlands) between precipitation and mean monthly AOD. We calculated a correlation of -0.24 between the mean monthly AOD and the monthly percentage of rain days at Uccle for a period between 1984 and 2009. The used AOD values are calculated from Brewer#016 observations at 320 nm, since our time series from Brewer#178 at 340 nm is too short. In order to get a better view of the possible relationship between AOD and precipitation, we divided the calculated AOD values from 1984 to 2009 in two categories, “dry AODs” and “wet AODs”, based on the influence of precipitation on the values. We considered a single AOD value to be wet if precipitation was observed on this day or on the previous day. If both days were precipitation-free, we considered the AOD value to be representative for a dry day. Figure 8 shows the mean monthly AOD for the dry and for the wet days. It can be seen that during late autumn, winter and early spring (November–April) the dry AODs are clearly higher than the wet values. The difference is less obvious for the late spring, summer and early autumn months. This could be due to the rather frequent occurrence of local thunderstorms in these seasons, causing only local deposition of aerosols. Air flowing from other places can transport aerosol masses that were not influenced by these local thunderstorms and the measured AOD can thus be higher than one would expect based on the precipitation associated with the thunderstorms. In winter, precipitation is mainly related to the passage of large frontal systems. The wet deposition of the aerosols will thus be spread over a larger region. According to Cheymol and De Backer (2003), a relation with a pollution cycle or with a general circulation could be an explanation of the annual cycle in AOD at Uccle. The seasonal variation of the mixing layer height, which is smaller

Table 3. Mean AOD values at 340 nm and their standard deviations for each day of the week.

Day of the week	Mean AOD
Monday	0.49 ± 0.29
Tuesday	0.50 ± 0.34
Wednesday	0.53 ± 0.32
Thursday	0.51 ± 0.35
Friday	0.52 ± 0.30
Saturday	0.52 ± 0.36
Sunday	0.50 ± 0.37

in winter and autumn, could be another explanation for the lower AOD in winter and autumn compared to summer and spring where the mixing layer height is thicker. The correlation between the monthly mean mixing layer height and the monthly mean AOD is 0.701 for Uccle. The correlation decreased strongly when the daily mean mixing layer height and the daily mean AOD are compared (correlation of 0.196).

4.2.2 Weekly periodicity

Bäumer et al. (2008) and Xia et al. (2008) observed a weekly AOD cycle in Central Europe. They recorded the lowest values on Sunday and Monday, whereas higher values occurred between Wednesday and Saturday. This cycle is greater for the urban sites than for the rural sites. For our measurements in Uccle, there is no clear signal for such a weekly cycle (Table 3). The largest difference in mean AOD value occurs between Monday and Wednesday (respectively 0.49 versus 0.53). Because of the rather high standard deviation on the average values, we can not state that this difference is a clear signal of a weekly cycle.

5 Summary and conclusions

Aerosols are the most important source of uncertainty in current climate change research (IPCC, 2007). Therefore knowledge of optical and physical properties of aerosols, such as the Aerosol Optical Depth, is essential to gain a better understanding in their effects. In this perspective, an adapted method was developed to retrieve AOD values at 340 nm from Brewer#178 sun scan measurements at Uccle, which allowed for a direct comparison with AOD values from the co-located Cimel sunphotometer at the same wavelength. The retrieval of the Brewer AOD values was based on the Langley Plot Method (as described in Cheymol and De Backer, 2003). For this linear regression technique, the calibration quality clear days in the time period for which the AOD is to be calculated, have to be selected. The criteria from Cheymol et al. (2009) had to be adapted so that they could be applied on sun scan measurements instead of

direct sun measurements. Also, a new criterion, based on the ratio of the observed and expected irradiance for a certain day, was added since the adapted criteria were not sufficient. This led to a new set of criteria for the selection of the calibration quality clear days (CCD). The selected days were then used to determine the mean calibration coefficient of the instrument. With this coefficient, the individual clear sky AOD values (selected using CICA) were calculated from the Brewer sun scans. These values were then compared to the AOD values from the Cimel sunphotometer. After removing the outliers from the comparison, the correlation between the Brewer#178 and Cimel measurements was 0.974, the slope was 0.968 ± 0.014 and the intercept was 0.011 ± 0.006 . This proves that there is a very good linear agreement between the AOD measured by both instruments and that good quality AOD observations can be obtained at 340 nm from the sun scans of Brewer#178. The seasonal and monthly variability of the Brewer AODs is consistent with other studies that report on higher AOD values during spring and summer and lower values in autumn and winter. No clear weekly cycle is present for the measurements in Uccle.

Still some AOD measurements perturbed by clouds may exist, which are not removed by the automatic and manual cloud-screening. Currently, the automatic cloud-screening selects the sun scan measurements that have a direct sun measurement within a time period of 5 min for the calculation of the AOD. The individual AOD measurements larger than 2 are automatically removed from the results, since these values are very unlikely for our location. During the manual screening, AOD values larger than 1.5 are removed when the scatter plot of the measured irradiance (i.e. photon counts) shows that the AODs are calculated under cloudy circumstances. The influence of scattered clouds on our measurements is still an issue for the calculation of the AOD values and the current cloud-screening algorithm has to be improved to further increase the quality and reliability of the data.

Acknowledgements. This research was performed under the project AGACC contract SD/AT/01B of the Belgian Science Policy. We thank Christian Hermans (Belgian Institute for Space Aeronomy, Belgium) for establishing and maintaining the AERONET site at Uccle. Our thanks also go to Roeland Van Malderen (Royal Meteorological Institute of Belgium, Belgium) for his constructive advice concerning data analysis and interpretation. The authors would like to acknowledge the anonymous reviewers for their constructive comments and suggestions.

Edited by: O. Torres

References

- Andreae, M. O., Jones, C. D. and Fox, P. M.: Strong present-day aerosol cooling implies a hot future, *Nature*, 435, 1187–1190, doi:10.1038/nature03671, 2005.
- Arola, A. and Koskela, T.: On the sources of bias in aerosol optical depth retrieval in the UV range, *J. Geophys. Res.*, 109, D08209, doi:10.1029/2003JD004375, 2004.
- Bais, A. F.: Absolute spectral measurements of direct solar ultraviolet irradiance with a brewer spectrophotometer, *Appl. Optics*, 36(21), 5199–5204, doi:10.1364/AO.36.005199, 1997
- Bäumer, D., Rinke, R., and Vogel, B.: Weekly periodicities of Aerosol Optical Thickness over Central Europe – evidence of an anthropogenic direct aerosol effect, *Atmos. Chem. Phys.*, 8, 83–90, doi:10.5194/acp-8-83-2008, 2008.
- Behnert, I., Matthias, V., and Doerffer, R.: Aerosol optical thickness and its spectral dependence derived from sun photometer measurements over the southern North Sea coastal region, *Óptica pura y aplicada*, 37(3), 3253–3257, 2004.
- Brewer, A. W.: A replacement for the Dobson spectrophotometer, *Pure Appl. Geophys.*, 106–108, 919–927, doi:10.1007/BF00881042, 1973.
- Cazorla, A., Shields, J. E., Karr, M. E., Olmo, F. J., Burden, A., and Alados-Arboledas, L.: Technical Note: Determination of aerosol optical properties by a calibrated sky imager, *Atmos. Chem. Phys.*, 9, 6417–6427, doi:10.5194/acp-9-6417-2009, 2009.
- Che, H., Zhang, X., Chen, H., Damiri, B., Goloub, P., Li, Z., Zhang, X., Wei, Y., Zhou, H., Dong, F., Li, D., and Zhou, T.: Instrument calibration and aerosol optical depth validation of the Chinese Aerosol Remote Sensing Network, *J. Geophys. Res.*, 114, D03206, doi:10.1029/2008JD011030, 2009.
- Cheymol, A. and De Backer, H.: Retrieval of the aerosol optical depth in the UV-B from Brewer ozone measurements over a long time period 1984–2002, *J. Geophys. Res.*, 108(D24), 4800, doi:10.1029/2003JD003758, 2003.
- Cheymol, A., De Backer, H., Josefsson, W., and Stübi, R.: Comparison and validation of the aerosol optical depth obtained with the Langley plot method in the UV-B from Brewer Ozone Spectrophotometer measurements, *J. Geophys. Res.*, 111, D16202, doi:10.1029/2006JD007131, 2006.
- Cheymol, A., Gonzalez Sotelino, L., Lam, K. S., Kim, J., Fioletov, V., Siani, A. M., and De Backer, H.: Intercomparison of Aerosol Optical Depth from Brewer Ozone spectrophotometers and CIMEL sunphotometers measurements, *Atmos. Chem. Phys.*, 9, 733–741, doi:10.5194/acp-9-733-2009, 2009.
- Cordero, R. R., Seckmeyer, G., Pissulla, D., and Labbe, F.: Exploitation of spectral direct UV irradiance measurements, *Metrologia*, 46, 19–25, doi:10.1088/0026-1394/46/1/003, 2009.
- Corr, C. A., Krotkov, N., Madronich, S., Slusser, J. R., Holben, B., Gao, W., Flynn, J., Lefer, B., and Kreidenweis, S. M.: Retrieval of aerosol single scattering albedo at ultraviolet wavelengths at the T1 site during MILAGRO, *Atmos. Chem. Phys.*, 9, 5813–5827, doi:10.5194/acp-9-5813-2009, 2009.
- De Backer, H.: Time series of daily erythemal UV doses at Uccle, Belgium, *Int. J. Remote Sens.*, 30(15), 4145–4145, doi:10.1080/01431160902825032, 2009.
- Diffey, B. L.: Solar ultraviolet radiation effects on biological systems, *Phys. Med. Biol.*, 36(3), 299–328, doi:10.1088/0031-9155/36/3/001, 1991.
- Dürr, B. and Philipona, R.: Automatic cloud amount detection by

- surface longwave downward radiation measurements, *J. Geophys. Res.*, 109, D05201, doi:10.1029/2003JD004182, 2004.
- Eck, T. F., Holben, B. N., Reid, J. S., Dubovik, O., Smirnov, A., O'Neill, N. T., Slutsker, I., and Kinne, S.: Wavelength dependence of the optical depth of biomass burning, urban, and desert dust aerosols, *J. Geophys. Res.*, 104(D24), 31333–31349, doi:10.1029/1999JD900923, 1999.
- Estellés, V., Martínez-Lozano, J. A., Utrillas, M. P., and Campanelli, M.: Columnar aerosol properties in Valencia (Spain) by ground-based Sun photometry, *J. Geophys. Res.*, 112, D11201, doi:10.1029/2006JD008167, 2008.
- Gröbner, J. and Meleti, C.: Aerosol optical depth in the UVB and visible wavelength range from Brewer spectrophotometer direct irradiance measurements: 1991–2002, *J. Geophys. Res.*, 109, D09202, doi:10.1029/2003JD004409, 2004.
- Gröbner, J., Blumthaler, M., Kazadzis, S., Bais, A., Webb, A., Schreder, J., Seckmeyer, G., and Rembges, D.: Quality assurance of spectral solar UV measurements: results from 25 UV monitoring sites in Europe, 2002 to 2004, *Metrologia*, 43, S66, doi:10.1088/0026-1394/43/2/S14, 2006.
- Hatzianastassiou, N., Ghikas, A., Mihalopoulos, N., Torres, O., and Katsoulis, B. D.: Natural versus anthropogenic aerosols in the eastern Mediterranean basin derived from multiyear TOMS and MODIS satellite data, *J. Geophys. Res.*, 114, D24202, doi:10.1029/2009JD011982, 2009.
- Holben, B. N., Tanré, D., Smirnov, A., Eck, T. F., Slutsker, I., Abuhassan, N., Newcomb, W. W., Schafer, J. S., Chatenet, B., Lavenu, F., Kaufman, Y. J., Vande Castle, J., Setzer, A., Markham, B., Clark, D., Frouin, R., Halthore, R., Karneli, A., O'Neill, N. T., Pietras, C., Pinker, R. T., Voss, K., and Zibordi, G.: An emerging ground-based aerosol climatology: Aerosol optical depth from AERONET, *J. Geophys. Res.*, 106(D11), 12067–12097, doi:10.1029/2001JD900014, 2001.
- Intergovernmental Panel on Climate Change 2007: The physical science, Technical summary of the working group I report, Cambridge University Press, New York, 2007.
- Kaskaoutis, D. G., Kambezidis, H. D., Hatzianastassiou, N., Kosmopoulos, P. G., and Badarinath, K. V. S.: Aerosol climatology: on the discrimination of aerosol types over four AERONET sites, *Atmos. Chem. Phys. Discuss.*, 7, 6357–6411, doi:10.5194/acpd-7-6357-2007, 2007.
- Kaufman, Y. J., Tanré, D., and Boucher, O.: A satellite view of aerosols in the climate system, *Nature*, 419, 215–223, doi:10.1038/nature01091, 2002.
- Kazadzis, S., Bais, A., Kouremeti, N., Gerasopoulos, E., Garane, K., Blumthaler, M., Schallhart, B., and Cede, A.: Direct spectral measurements with a Brewer spectroradiometer: absolute calibration and aerosol optical depth retrieval, *Appl. Optics*, 44(9), 1681–1690, doi:10.1364/AO.44.001681, 2005.
- Kazadzis, S., Bais, A., Amiridis, V., Balis, D., Meleti, C., Kouremeti, N., Zerefos, C. S., Rapsomanikis, S., Petrakakis, M., Kelesis, A., Tzoumaka, P., and Kelektoglou, K.: Nine years of UV aerosol optical depth measurements at Thessaloniki, Greece, *Atmos. Chem. Phys.*, 7, 2091–2101, doi:10.5194/acp-7-2091-2007, 2007.
- Kazadzis, S., Kouremeti, N., Bais, A., Kazantzidis, A., and Meleti, C.: Aerosol forcing efficiency in the UVA region from spectral solar irradiance measurements at an urban environment, *Ann. Geophys.*, 27, 2515–2522, doi:10.5194/angeo-27-2515-2009, 2009.
- Kerr, J. B., Asbridge, I. A., and Evans, W. F. J.: Intercomparison of total ozone measured by the Brewer and Dobson spectrophotometer at Toronto, *J. Geophys. Res.*, 93(D9), 11129–11140, doi:10.1029/JD093iD09p11129, 1988.
- Kim, J. E., Kim, Y. J., and He, Z.: Temporal variation and measurement uncertainty of UV aerosol optical depth measured from April 2002 to July 2004 at Gwangju, Korea, *Atmos. Res.*, 81, 111–123, doi:10.1016/j.atmosres.2005.11.006, 2006.
- Kim, J. E., Ryu, S. Y., and Kim, Y. J.: Determination of radiation amplification factor of atmospheric aerosol from the surface UV irradiance measurement at Gwangju, Korea, *Theor. Appl. Climatol.*, 91, 217–228, doi:10.1007/s00704-006-0285-x, 2008.
- Kirchhoff, V. W. J. H., Silva, A. A., Costa, C. A., Paes Leme, N., Pavão, H. G., and Zaratti, F.: UV-B optical thickness observations of the atmosphere, *J. Geophys. Res.*, 106(D3), 2963–2973, doi:10.1029/2000JD900506, 2001.
- Koelemeijer, R. B. A., Homan, C. D., and Matthijsen, J.: Comparison of spatial and temporal variations of aerosol optical thickness and particulate matter over Europe, *Atmos. Environ.*, 40, 5304–5315, doi:10.1016/j.atmosenv.2006.04.044, 2006.
- Léon, J.-F., Derimian, Y., Chiapello, I., Tanré, D., Podvin, T., Chatenet, B., Diallo, A., and Deroo, C.: Aerosol vertical distribution and optical properties over M'Bour (16.96° W; 14.39° N), Senegal from 2006 to 2008, *Atmos. Chem. Phys.*, 9, 9249–9261, doi:10.5194/acp-9-9249-2009, 2009.
- Liu, S. C., McKeen, S. A., and Madronich, S.: Effect of anthropogenic aerosols on biologically active ultraviolet radiation, *Geophys. Res. Lett.*, 18(12), 2265–2268, doi:10.1029/91GL02773, 1991.
- Lohmann, U.: Possible aerosol effects on ice clouds via contact nucleation, *J. Atmos. Sci.*, 59(3), 647–656, 2002.
- Lohmann, U. and Feichter, J.: Global indirect aerosol effects: a review, *Atmos. Chem. Phys.*, 5, 715–737, doi:10.5194/acp-5-715-2005, 2005.
- Lyamani, H., Olmo, F. J., and Alados-Arboledas, L.: Physical and optical properties of aerosols over an urban location in Spain: seasonal and diurnal variability, *Atmos. Chem. Phys.*, 10, 239–254, doi:10.5194/acp-10-239-2010, 2010.
- Madronich, S.: UV radiation in the natural and perturbed atmosphere, in: Teveni, M. (Ed.), *Environmental Effects of Ultraviolet Radiation*, Lewis, Boca Raton, FL., 17–69, 1993.
- Marengo, F., di Sarra, A., and Di Luisi, J.: Methodology for determining aerosol optical depth from Brewer 300–320nm ozone measurements, *Appl. Optics*, 41(9), 1805–1814, doi:10.1364/AO.41.001805, 2002.
- Marengo, F., Santacesaria, V., Bais, A. F., Balis, D., di Sarra, A., Papayannis, A., and Zerefos, C.: Optical properties of tropospheric aerosols determined by lidar and spectrophotometric measurements (Photochemical Activity and Solar Ultraviolet Radiation campaign), *Appl. Optics*, 36(27), 6875–6886, doi:10.1364/AO.36.006875, 1997.
- Meleti, C. and Cappellani, F.: Measurements of aerosol optical depth at Ispra: Analysis of the correlation with UV-B, UV-A and total solar irradiance, *J. Geophys. Res.*, 105(D4), 4971–4978, doi:10.1029/1999JD900459, 2000.
- Mulcahy, J. P., O'Dowd, C. D. and Jennings, S. G.: Aerosol optical depth in clean marine and continental northeast Atlantic air, *J. Geophys. Res.*, 114, D20204, doi:10.1029/2009JD011992, 2009.

- Myrhe, G.: Consistency between satellite derived and modelled estimates of the direct aerosol effect, *Science*, 325(187), 187–190, doi:10.1126/science.1174461, 2009.
- Raghavendra Kumar, K., Narasimhulu, K., Balakrishnaiah, G., Suresh Kumar Reddy, B., Rama Gopal, K., Reddy, R. R., Sathesh, S. K., Krishna Moorthy, K., and Suresh Babu, S.: A study on the variations of optical and physical properties of aerosols over a tropical semi-arid station during grassland fire, *Atmos. Res.*, 95, 77–87, doi:10.1016/j.atmosres.2009.08.012, 2010.
- Ramanathan, V., Crutzen, P. J., Kiehl, J. T., and Rosenfeld, D.: Aerosols, climate and the hydrological cycle, *Science*, 294, 2119–2121, doi:10.1126/science.1064034, 2001.
- Remer, L., Kleidmann, R. G., Levy, R. C., Kaufman, Y. J., Tanré, D., Mattoo, S., Vanderlei Martins, J., Ichoku, C., Koren, I., Yu, H., and Holben, B. N.: Global aerosol climatology from the MODIS satellite sensors, *J. Geophys. Res.*, 113, D14S07, doi:10.1029/2007JD009661, 2008.
- Rieder, H. E., Holawe, F., Simic, S., Blumthaler, M., Krzyscin, J. W., Wagner, J. E., Schmalwieser, A. W., and Weihs, P.: Reconstruction of erythemal UV-doses for two stations in Austria: a comparison between alpine and urban regions, *Atmos. Chem. Phys.*, 8, 6309–6323, doi:10.5194/acp-8-6309-2008, 2008.
- Sellitto, P., di Sarra, A., and Siani, A. M.: An improved algorithm for the determination of aerosol optical depth in the ultraviolet spectral range from Brewer spectrophotometer observations, *J. Opt. A – Pure Appl. Op.*, 8, 849–855, doi:10.1088/1464-4258/8/10/005, 2006.
- Taylor, T. E., L'Ecuyer, T. S., Slusser, J. R., Stephens, G. L., and Goering, C. D.: An operational retrieval algorithm for determining aerosol optical properties in the ultraviolet, *J. Geophys. Res.*, 113, D03201, doi:10.1029/2007JD008661, 2008.
- Tevini, M. and Teramura, H. A.: UV-B effects on terrestrial plants, *Photochem. Photobiol.*, 50, 479–487, doi:10.1111/j.1751-1097.1989.tb05552.x, 1989.
- Unger, N., Menon, S., Koch, D. M., and Shindell, D. T.: Impacts of aerosol-cloud interactions on past and future changes in tropospheric composition, *Atmos. Chem. Phys.*, 9, 4115–4129, doi:10.5194/acp-9-4115-2009, 2009.
- Xia, X., Eck, T. F., Holben, B. N., Philippe, G., and Chen, H.: Analysis of the weekly cycle of aerosol optical depth using AERONET and MODIS data, *J. Geophys. Res.*, 113, D14217, doi:10.1029/2007JD009604, 2008.



Relations between erythemal UV dose, global solar radiation, total ozone column and aerosol optical depth at Uccle, Belgium

V. De Bock, H. De Backer, R. Van Malderen, A. Mangold, and A. Delcloo

Royal Meteorological Institute of Belgium, Ringlaan 3, 1180 Brussels, Belgium

Correspondence to: V. De Bock (veerle.debock@meteo.be)

Received: 25 April 2014 – Published in Atmos. Chem. Phys. Discuss.: 24 June 2014

Revised: 7 October 2014 – Accepted: 7 October 2014 – Published: 20 November 2014

Abstract. At Uccle, Belgium, a long time series (1991–2013) of simultaneous measurements of erythemal ultraviolet (UV) dose (S_{ery}), global solar radiation (S_{g}), total ozone column (Q_{O_3}) and aerosol optical depth (τ_{aer}) (at 320.1 nm) is available, which allows for an extensive study of the changes in the variables over time. Linear trends were determined for the different monthly anomalies time series. S_{ery} , S_{g} and Q_{O_3} all increase by respectively 7, 4 and 3 % per decade. τ_{aer} shows an insignificant negative trend of –8 % per decade. These trends agree with results found in the literature for sites with comparable latitudes. A change-point analysis, which determines whether there is a significant change in the mean of the time series, is applied to the monthly anomalies time series of the variables. Only for S_{ery} and Q_{O_3} , was a significant change point present in the time series around February 1998 and March 1998, respectively. The change point in Q_{O_3} corresponds with results found in the literature, where the change in ozone levels around 1997 is attributed to the recovery of ozone. A multiple linear regression (MLR) analysis is applied to the data in order to study the influence of S_{g} , Q_{O_3} and τ_{aer} on S_{ery} . Together these parameters are able to explain 94 % of the variation in S_{ery} . Most of the variation (56 %) in S_{ery} is explained by S_{g} . The regression model performs well, with a slight tendency to underestimate the measured S_{ery} values and with a mean absolute bias error (MABE) of 18 %. However, in winter, negative S_{ery} are modeled. Applying the MLR to the individual seasons solves this issue. The seasonal models have an adjusted R^2 value higher than 0.8 and the correlation between modeled and measured S_{ery} values is higher than 0.9 for each season. The summer model gives the best performance, with an absolute mean error of only 6 %. However, the seasonal regression models do

not always represent reality, where an increase in S_{ery} is accompanied with an increase in Q_{O_3} and a decrease in τ_{aer} . In all seasonal models, S_{g} is the factor that contributes the most to the variation in S_{ery} , so there is no doubt about the necessity to include this factor in the regression models. The individual contribution of τ_{aer} to S_{ery} is very low, and for this reason it seems unnecessary to include τ_{aer} in the MLR analysis. Including Q_{O_3} , however, is justified to increase the adjusted R^2 and to decrease the MABE of the model.

1 Introduction

The discovery of the Antarctic ozone hole in the mid-1980s triggered an increased scientific interest in the state of stratospheric ozone levels on a global scale (Garane et al., 2006). The ozone depletion not only occurred above the Antarctic; there is strong evidence that stratospheric ozone also diminished above midlatitudes (Bartlett and Webb, 2000; Kaurola et al., 2000; Smedley et al., 2012). While ozone depletion continued in the 2000s over the polar regions, it has leveled off at midlatitudes, although ozone amounts still remain lower compared to the amounts in the 1970s (Garane et al., 2006). Stratospheric ozone is expected to recover in response to the ban on ozone-depleting substances (ODSs) agreed upon in the Montreal Protocol in 1987 (WMO, 2006; Fitzka et al., 2012). However, it is difficult to predict future changes in ozone as the predictions suffer from uncertainties caused by the general climate change; numerical errors of simulation models; and by human behavior, which is not well controllable in several parts of the world. The decline in stratospheric ozone has shifted the focus of the scientific community and the general public towards the variability of

surface UV irradiance (Krzýscin et al., 2011). If all other factors influencing UV irradiance remain stable, reductions in stratospheric ozone would lead to an increase in UV irradiance at the ground, particularly at wavelengths below 320 nm (Garane et al., 2006). Increases of UV irradiance in response to the ozone decline have already been reported for different sites during the 1990s (Garane et al., 2006, and references therein).

The possible increase in UV irradiance raises concerns because of its adverse health and environmental effects. Overexposure can lead to the development of skin cancers, cataract, skin aging and the suppression of the immune system (Rieder et al., 2008; Cordero et al., 2009). UV irradiance also has adverse effects on terrestrial plants (Tevini and Teramura, 1989; Cordero et al., 2009) and on other elements of the biosphere (Diffey, 1991). On the other hand, UV radiation does enable the production of vitamin D in the skin, which is positively linked to health effects as it supports bone health and may decrease the risk of several internal cancers (United Nations Environment Programme, 2010). It is important to assess the changes in UV irradiance over prolonged periods of time. Not only do adverse health and environmental effects often relate to long-term exposure (from years to a lifetime); also the timescales of the atmospheric processes that are involved, such as ozone depletion and recovery, are beyond decades (Chubarova, 2008; den Outer et al., 2010).

Physically, UV trends can only be detected from direct measurements on Earth. Reconstructed data can be based on proxy data such as the abundance of ozone, solar irradiance, sunshine duration or regional reflectivity of the Earth–atmosphere system measured from space (Lindfors et al., 2003). Different sorts of reconstruction models have been used in several studies. They all use various kinds of statistical or model approaches and different meteorological or irradiance data sets (Lindfors et al., 2007; Chubarova, 2008; Rieder et al., 2010; den Outer et al., 2010; Bais et al., 2011). Techniques are either based on modeling of clear-sky UV irradiance or on empirical relationships between surface UV irradiance and the factors influencing the penetration of UV irradiance through the atmosphere (Kaurola et al., 2000; Trepte and Winkler, 2004). In addition to the reconstruction studies, changes in surface UV irradiance have also been studied using ground-based measurements at different locations (e.g., den Outer et al., 2000; Sasaki et al., 2002; Bernhard et al., 2006; Fitzka et al., 2012; Zerefos et al., 2012; Eleftheratos et al., 2014) or even in combination with satellite retrievals (Herman et al., 1996; Matthijsen et al., 2000; Kalliskota et al., 2000; Ziemke et al., 2000; Zerefos et al., 2001; Fioletov et al., 2004; Williams et al., 2004). Some studies combine both models and observations to investigate possible UV irradiance changes (e.g., Kaurola et al., 2000).

Not only stratospheric ozone influences the intensity of UV irradiance reaching the surface of the Earth. Long-term changes in solar elevation, tropospheric ozone,

clouds, Rayleigh scattering on air molecules, surface albedo, aerosols, absorption by trace gases and changes in the distance between the Sun and the Earth can lead to trends in UV irradiance (WMO, 2006). Some studies show that increased amounts of aerosols and trace gases from industrial emissions, which absorb UV irradiance in the troposphere, could even compensate for the UV effects caused by the stratospheric ozone decline (Krzýscin et al., 2011; Fitzka et al., 2012). Clouds induce more variability in surface UV irradiance than any other geophysical factor, besides the solar elevation, but their effects depend very much on local conditions (Krzýscin et al., 2011). Surface albedo is determined mostly by snow amount and snow depth (Rieder et al., 2010) and plays a significant role at high-altitude and high-latitude sites, where UV irradiance can be strongly enhanced due to multiple occurrences of scattering and reflection between snow-covered ground and the atmosphere (Fitzka et al., 2012). Several studies have been conducted to quantify the effects of the abovementioned variables on the amount of UV irradiance reaching the ground, and many of them have done so by constructing empirical models with UV irradiance (or a related quantity) as a dependent variable (Díaz et al., 2000; Fioletov et al., 2001; de La Casinière et al., 2002; Foyo-Moreno et al., 2007; Antón et al., 2009; De Backer, 2009; Huang et al., 2011; Krishna Prasad et al., 2011; El Shazly et al., 2012).

At Uccle, Belgium, simultaneous measurements of erythemal UV dose, global solar radiation, total ozone column and aerosol optical depth at 320.1 nm are available for a time period of 23 years (1991–2013). The time series is long enough to allow for reliable determination of significant changes (a minimum of 15 years is required as shown in Weatherhead et al., 1998, and Glandorf et al., 2005). The availability of the simultaneous time series allows an extensive analysis in which three analysis techniques (linear trend analysis, change-point analysis and multiple linear regression analysis) will be combined in order to increase our insights on the relations between the variables. First, a linear trend analysis will be applied to the monthly anomalies of the time series (both on a daily and seasonal timescale), and the results will be compared with results found in the literature. Monthly anomalies are used here to reduce the influence of the seasonal cycle on the analysis and are calculated by subtracting the long-term monthly mean from the individual monthly means. The monthly anomalies time series will also be the subject of change-point analysis, where the homogeneity of the time series will be investigated. Finally, the multiple linear regression (MLR) technique (with daily erythemal UV doses as the dependent variable and daily values of global solar radiation, total ozone column and aerosol optical depth at 320.1 nm as explanatory variables) will allow us to study the influence of the explanatory variables on the dependent variable on a daily and seasonal basis.

2 Data

In this study, the (all-sky) erythemal UV dose, (all-sky) global solar radiation, total ozone column and (clear-sky) aerosol optical depth at 320.1 nm are investigated over a time period of 23 years (1991–2013). These measurements are performed at Uccle, Belgium (50°48' N, 4°21' E, 100 m a.s.l.), a residential suburb of Brussels located about 100 km from the North Sea shore.

2.1 Daily erythemal UV dose

In 1989, the Brewer spectrophotometer instrument #016, a single monochromator, was equipped with a UV-B monitor (De Backer, 2009). This is an optical assembly which enables the Brewer to measure UV-B irradiance using a thin disc of Teflon as a transmitting diffuser (SCI TEC Brewer #016 manual, 1988). The Brewer measures the horizontal spectral UV irradiance with a spectral resolution of approximately 0.55 nm, full width at half maximum. The instrument performs UV scans from 290 to 325 nm with 0.5 nm wavelength steps (Fioletov et al., 2002). The erythemal irradiances are calculated using the erythemal action spectrum as determined by the Commission Internationale de l'Éclairage and are integrated to daily erythemal doses (De Backer, 2009). For wavelengths above 325 nm, for which Brewer#016 does not provide data, the intensities are extrapolated using a theoretical spectrum weighted by the intensity at 325 nm. This is justified by the fact that, at those wavelengths, the UV intensity is no longer strongly dependent on ozone and the erythemal weighting function is low. For the calculation of the daily sum, a linear interpolation between the different measurement points is performed. When there is an interruption of 2 h or more between the measurements between sunrise and sunset, the calculated daily sum is rejected. The data (in joules per square meter, J m^{-2}) are available on a regular basis from 1991. The instrument is calibrated with 50 W lamps on a monthly basis and with 1000 W lamps during intercomparisons in 1994, 2003, 2006, 2008, 2010 and 2012. The instrument was also compared with the traveling QASUME (QUality Assurance of Spectral UV Measurements in Europe) unit in 2004 (Gröbner et al., 2004).

2.2 Global solar radiation

The global solar radiation is a measure of the rate of total incoming solar energy (both direct and diffuse) on a horizontal plane at the surface of the Earth (Journée and Bertrand, 2010). The measurements at Uccle are performed by CM11 pyranometers (Kipp & Zonen; <http://www.kippzonen.com>). For this study, the daily values in J m^{-2} , derived from 10 and 30 min data, are used. The data are quality-controlled in two steps: first a preliminary fully automatic quality control is performed prior to the systematic manual check of the data (Journée and Bertrand, 2010). In May 1996 we switched to

a new system, and in 2005 half of the instruments were replaced. Corrections to the measurements were made in 2000, 2001, 2004, 2005, 2007 and 2012. For the period before 1996, no information is available concerning possible calibrations of the instrument.

2.3 Total ozone column

Total ozone column values (in Dobson Units, DU) are available from Brewer#016 direct sun (DS) measurements. The instrument records raw photon counts of the photomultiplier at five wavelengths (306.3, 310.1, 313.5, 316.8 and 320.1 nm) using a blocking slit mask, which opens successively one of the five exit slits. The five exit slits are scanned twice within 1.6 s, and this is repeated 20 times. The whole procedure is repeated five times for a total of about 3 min. The total ozone column is obtained from a combination of measurements at 310.1, 313.5, 316.8 and 320.1 nm, weighted with a predefined set of constants chosen to minimize the influence of SO_2 and linearly varying absorption features from, e.g., clouds or aerosols (Gröbner and Meleti, 2004). Brewer#016 was calibrated relative to the Dobson instrument in 1984 (De Backer and De Muer, 1991) and regularly recalibrated against the traveling standard Brewer instrument #017 in 1994, 2003, 2006, 2008, 2010 and 2012. The stability is also continuously checked against the colocated instruments Dobson#40 (from 1991 until May 2009) and Brewer#178 (since 2001). Internal lamp tests are performed on a regular basis to check whether the instrument itself is drifting. When instrumental drift is detected, it is corrected for.

2.4 Aerosol optical depth

Cheymol and De Backer (2003) developed a method that enables the retrieval of τ_{aer} values (at 306.3, 310.1, 313.5, 316.8 and 320.1 nm) using the DS measurements of the Brewer instrument. It is also possible to retrieve τ_{aer} values at 340 nm using sun scan (SS) measurements of the Brewer instrument (De Bock et al., 2010). Together with the retrieval method, De Bock et al. (2010) developed a cloud-screening procedure to select the clear-sky τ_{aer} values. However, this screening method did not perform well. Hence an improved cloud-screening method (described in Sect. 3.1) has been developed and applied to τ_{aer} values retrieved from DS and SS measurements. For this study only the cloud-screened τ_{aer} values at 320.1 nm, retrieved from the DS measurements of the single monochromator Brewer#016, will be used.

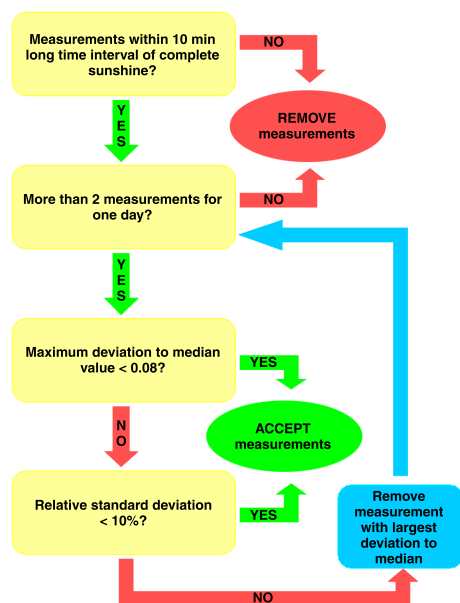
3 Method

3.1 Improved aerosol optical depth cloud-screening method

The initial cloud-screening algorithm, as described in De Bock et al. (2010), did not perform well and improvements

Table 1. Comparison of Brewer and Cimel aerosol optical depth values (2006–2013).

		Correlation	Slope	Intercept
DS 320 nm	Brewer#016	0.97	1.004 ± 0.006	-0.067 ± 0.003
DS 320 nm	Brewer#178	0.99	1.007 ± 0.005	0.017 ± 0.002
SS 340 nm	Brewer#178	0.98	0.993 ± 0.007	0.073 ± 0.002

**Figure 1.** Improved cloud-screening procedure.

were needed. The improved cloud-screening method makes use of sunshine duration data from four pyrheliometers at Uccle and is also based on the assumption that the variability of the τ_{aer} in the course of 1 day is either lower than 10 % or lower than 0.08 τ_{aer} units, which is the maximum uncertainty of the τ_{aer} retrieval algorithm. Figure 1 gives a schematic overview of the improved cloud-screening technique. First it is determined whether the individual τ_{aer} measurements were taken within a 10 min interval of continuous sunshine. The measurements for which this is not the case are removed, after which more than two individual measurements per day must remain in order to continue. For each day, we then determine the maximum deviation to the median value. If this value is less than 0.08, we accept all measurements for that day. However, if the maximum deviation exceeds 0.08, the relative standard deviation for that day is calculated. In case this value is less than 10 %, which would guarantee a given stability within the diurnal pattern of τ_{aer} , all the τ_{aer} values for that day are accepted. In the other case, the τ_{aer} measurement with the largest contribution to the standard deviation is removed, as this measurement is most likely influenced by clouds. The median value will then be recomputed and the previous steps are repeated. Days with two or less individual τ_{aer} measurements are excluded from the results, since it

does not make sense to calculate the deviation to the median and the standard deviation.

The cloud-screened τ_{aer} , both from DS and SS Brewer measurements, were compared to quasi-simultaneous and colocated Cimel level 2.0 quality-assured values (with a maximum time difference of 3 min). The Cimel sun photometer, which belongs to BISA (Belgium Institute of Space Aeronomy), is located approximately 100 m from the Brewer instrument. It is an automatic sun–sky scanning filter radiometer allowing the measurements of the direct solar irradiance at wavelengths 340, 380, 440, 500, 670, 870, 940 and 1020 nm. These solar extinction measurements are used to compute aerosol optical depth at each wavelength except for the 940 nm channel, which is used to retrieve total atmospheric column precipitable water in centimeters. The instrument is part of the AEROSOL ROBOTIC NETWORK (AERONET; <http://aeronet.gsfc.nasa.gov/>; Holben et al., 2001). The accuracy of the AERONET τ_{aer} measurements at 340 nm is 0.02 (Eck et al., 1999). For the period of comparison (2006–2013), the correlation coefficient, slope and intercept of the regression lines have been calculated, and the values are presented in Table 1. The results of the comparison show that the cloud-screened Brewer τ_{aer} values agree very well with the Cimel data.

The advantages of the improved cloud-screening method are the removal of the arbitrary maximum level of τ_{aer} values and the fact that it runs completely automatically, whereas the old one needed manual verification afterwards. This method has now been applied not only to the τ_{aer} retrieval using SS measurements at 340 nm but also to the method using DS measurements.

3.2 Data analysis methods

Since most statistical analysis tests, such as linear regression and change-point tests, rely on independent and identically distributed time series (e.g., Van Malderen and De Backer, 2010, and references therein), most data used in this study are in their anomaly form. Monthly anomalies are used to reduce the influence of the seasonal cycle on the analysis and are calculated by subtracting the long-term monthly mean from the individual monthly means. Monthly means are only calculated for months with at least 10 individual daily values. For S_{ery} , S_{g} and Q_{O_3} , accepting monthly means with only 10 daily individual values does not have an impact on the calculated trends, as respectively 85, 99 and 100 % of the

months consist of more than 20 individual daily values. For τ_{aer} , however, the number of available monthly mean values is dramatically reduced (from 92 to only 5 remaining values) when only accepting monthly means based on 20 individual values. There is a risk in accepting months with only 10 daily values, as those days could be concentrated at the beginning or end of a month, which could bias the calculated trend. However, the benefit of using 92 instead of 5 monthly mean values for τ_{aer} trend calculations outweighs this potential bias. For the multiple linear regression analysis, daily values will be used instead of anomaly values.

3.2.1 Linear trend analysis

Linear trends are calculated for the monthly anomalies of S_{ery} , S_{g} , Q_{O_3} and τ_{aer} at 320.1 nm. To determine the significance of the linear trends, the method described in Santer et al. (2000) is used. The least-squares linear regression estimate of the trend in $x(t)$, b , minimizes the squared differences between $x(t)$ and the regression line $\hat{x}(t)$:

$$\hat{x}(t) = a + b(t); t = 1, \dots, n_t. \quad (1)$$

Whether a trend in $x(t)$ is significantly different from 0 is tested by computing the ratio between the estimated trend (b) and its standard error (s_b):

$$t_b = \frac{b}{s_b}. \quad (2)$$

Under the assumption that t_b is distributed as Student's t , the calculated t ratio is then compared with a critical t value, t_{crit} , for a stipulated significance level α and $n_t - 2$ degrees of freedom (Santer et al., 2000).

However, if the regression residuals are autocorrelated, the results of the regression analysis will be too liberal and the original approach must be modified. The method proposed in Santer et al. (2000) involves the use of an effective sample size n_e in the computation of the adjusted standard error and calculated t value, but also in the indexing of the critical t value. To test for autocorrelation in the residuals of a time series, the Durbin–Watson test is used (Durbin and Watson, 1971).

The above-described linear trend analysis is also applied to the monthly anomalies of the extreme values (minima and maxima) of the variables. The extreme values are calculated by determining the lowest and highest measured value for each month. These trends will be studied together with the relative frequency distribution of the daily mean values. This distribution is determined by using the minimum and maximum values of the entire study period as boundaries and by dividing the range between the boundaries into a certain amount of bins of equal size. The daily values are distributed over the different bins, and the relative frequency in percent is calculated. This will be done for two different time periods: 1991–2002 and 2003–2013. Additionally, the medians

for these periods are calculated. In this way, it is possible to investigate whether there is a shift in the frequency distribution of the variables from the first period to the second one. The results of the analysis of the frequency distribution will only be presented in case they show a significant shift in the data.

3.2.2 Change-point analysis

Change points are times of discontinuity in a time series (Reeves et al., 2007) and can either arise naturally or as a result of errors or changes in instrumentation, recording practices, data transmission, processing, etc. (Lanzante, 1996). A change point is said to occur at some point in the sequence if all the values up to and including it share a common statistical distribution and all those after the point share another. The most common change-point problem involves a change in the mean of the time series (Lanzante, 1996). There are different tests that can be used to detect a change point in a time series. In this study we use the combination of three tests: the non-parametric Pettitt–Mann–Whitney (PMW) test (based on the ranks of the values in the sequence), the Mann–Whitney–Wilcoxon (MWW) test (a rank sum test) and the cumulative sum technique (CST). The details of these tests are described in Hoppy and Kiely (1999). The change points discussed further in this study are detected by all three tests (except when mentioned otherwise), and only the change points that exceeded the 90% confidence level were retained. The change points are determined for the monthly anomalies time series of S_{ery} , S_{g} , Q_{O_3} and τ_{aer} at 320.1 nm. When there is a clear and large-enough, statistically significant trend present in the time series, this automatically leads to the detection of a change point in the middle of the time series as, at this point, the change in the mean is large enough to be significant. In this case, it is necessary to detrend the time series, i.e., subtract the general trend from the time series.

3.2.3 Multiple linear regression analysis

The goal of a MLR analysis is to determine the values of parameters for a linear function that cause this function to best describe a set of provided observations (Krishna Prasad et al., 2011). In this study, the MLR technique is used to explore whether there is a significant relationship between S_{ery} and three explanatory variables (S_{g} , Q_{O_3} and τ_{aer}) both on a daily and seasonal scale. We use a linear model where the coefficients are determined with the least-squares method:

$$S_{\text{ery}} = a \times S_{\text{g}} + b \times Q_{\text{O}_3} + c \times \tau_{\text{aer}} + d + \epsilon \quad (3)$$

with

- S_{ery} : erythemal UV dose (in J m^{-2})
- S_{g} : global solar radiation (in J m^{-2})

- Q_{O_3} : total ozone column (in DU)
- τ_{aer} : aerosol optical depth at 320.1 nm
- a, b, c : regression coefficients
- d : constant term
- ϵ : error term.

Although the attenuation of radiation by ozone is not linear (according to the Beer–Lambert law), we consider total ozone column as a linear independent variable, based on the limited variation of this variable throughout the year and throughout the different seasons.

The model will be developed based on data from 1991 to 2008. Data from 2009 to 2013 will be used for validation of the model. For the MLR analysis to produce trustworthy results, the distribution of the errors of the model should be normal. Non-normal errors may mean that the t and F statistics of the coefficients may not actually follow t and F distributions and that the model might underestimate reality (Williams et al., 2013). However, as stated in Williams et al. (2013), even if errors are not normally distributed, the sampling distribution of the coefficients will approach a normal distribution as sample size grows larger, assuming some reasonably minimal preconditions. As we have a large data set available at Uccle for the MLR analysis, we can assume that the distribution of the coefficients of the MLR model approaches normality.

The performance of the model and its parameters will be evaluated through different statistical parameters. The adjusted R^2 value is the measure for the fraction of variation in UV explained by the regression, accounting for both the sample size and the number of explanatory variables. Compared to the R^2 value, the adjusted R^2 value will only increase if a new variable has additional explanatory power. It is possible to test the null hypothesis that a regression coefficient is equal to 0, which would mean that the variable associated with this regression coefficient does not contribute to explaining the variation in UV. This is done by looking at the p value. If we want to test whether a regression coefficient differs significantly from 0 at the 5 % level, the p value should be less than or equal to 0.05. The influence of the variation in the three parameters on the variation of S_{ery} is determined by multiplying the standard deviation of each parameter with its corresponding regression coefficient and dividing this by the average S_{ery} value.

The mean bias error (MBE) and the mean absolute bias error (MABE) are also calculated in order to evaluate the performance of the regression model. The MBE (given in %) provides the mean relative difference between modeled and measured values (Antón et al., 2009):

Table 2. Seasonal trends of erythemal UV doses (1991–2013).

Season	Trend per decade	Significance level
Spring	+9 % (± 3 %)	99 %
Summer	+6 % (± 2 %)	99 %
Autumn	+7 % (± 3 %)	95 %
Winter	–12 % (± 4 %)	99 %

$$\text{MBE} = 100 \times \frac{1}{N} \sum_{i=1}^N \frac{S_{\text{ery}_i}^{\text{modeled}} - S_{\text{ery}_i}^{\text{measured}}}{S_{\text{ery}_i}^{\text{measured}}}. \quad (4)$$

The MABE (given in %) reports on the absolute value of the individual differences between modeled and measured data (Antón et al., 2009):

$$\text{MABE} = 100 \times \frac{1}{N} \sum_{i=1}^N \frac{|S_{\text{ery}_i}^{\text{modeled}} - S_{\text{ery}_i}^{\text{measured}}|}{S_{\text{ery}_i}^{\text{measured}}}. \quad (5)$$

4 Results and discussion

4.1 Linear trend analysis

4.1.1 Erythemal UV dose

A significant positive trend (at the 99 % significance level) can be detected in the time series of monthly anomalies of S_{ery} (Fig. 2). These values increase by 7 % (± 2 %) per decade. The seasonal trends are presented in Table 2. In spring (March, April and May), summer (June, July and August) and autumn (September, October and November), S_{ery} increases significantly, whereas in winter (December, January and February) the trend is negative. The increase in S_{ery} is the largest in spring.

A significant positive trend has been found in the monthly anomalies of both the minimum and maximum values of S_{ery} . The minimum values show an increase of 10 % (± 4 %) per decade and the maximum values increased by 7 % (± 1 %) per decade (respectively at the 95 and 99 % level). The increase in the median value from 825 J m^{–2} (1991–2002) to 987 J m^{–2} (2003–2013) shows that higher S_{ery} values are more frequent in the latter period.

4.1.2 Global solar radiation

The values of S_{g} show an increase of 4 % (± 1 %) per decade at the 99 % significance level, which corresponds to an absolute change of +0.5 (± 0.2) W m^{–2} per year for the observed time period (Fig. 2). On a seasonal scale, spring and autumn exhibit a significant positive trend (Table 3). The seasonal trends of S_{g} , although not significant in summer and winter,

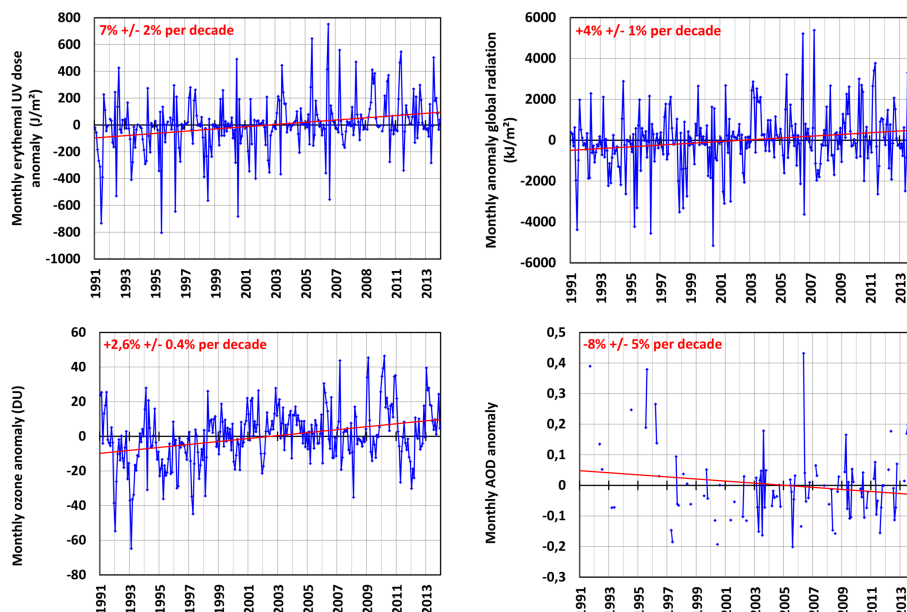


Figure 2. Trends of monthly anomalies at Uccle for erythemal UV dose (upper left panel), global solar radiation (upper right panel), total ozone column (lower left panel) and aerosol optical depth at 320.1 nm (lower right panel) for the time period 1991–2013. The blue lines represent the time series, whereas the red lines represent the trend over the time period.

Table 3. Seasonal trends of global solar radiation (1991–2013).

Season	Trend per decade	Significance level
Spring	+6 % (± 3 %)	95 %
Summer	+2 % (± 2 %)	not significant
Autumn	+6 % (± 3 %)	95 %
Winter	−4 % (± 4 %)	not significant

Table 4. Seasonal trends of total ozone column (1991–2013).

Season	Trend per decade	Significance level
Spring	+3 % (± 1 %)	95 %
Summer	+1.6 % (± 0.6 %)	95 %
Autumn	+1.8 % (± 0.9 %)	not significant
Winter	+3 % (± 2 %)	not significant

have the same sign as the seasonal S_{ery} trends. The trends of S_{g} are smaller than the S_{ery} trends, both on an annual and seasonal scale.

There is a clear difference between the trends of the monthly anomalies of minimum and maximum values of S_{g} . Both trends are positive, but the increase in the minimum values (12 % (± 5 %) per decade at 99 % significance level) is much larger than the one in the maximum values (3.2 % (± 0.7 %) per decade at 99 % significance level). Study of the median values reveals the presence of an increase from 7880 kJ m^{-2} (1991–2002) to 8902 kJ m^{-2} (2003–2013). As the global radiation data are all-sky data, it is obvious that the minimum values are the ones that are influenced by clouds. If the minimum values increase in time, the cloud properties, i.e., their amount and/or water content, must have changed over the past 23 years.

4.1.3 Total ozone column

The monthly anomalies of Q_{O_3} show a positive trend of 2.6 % (± 0.4 %) per decade (significant at 99 %) (Fig. 2). Sig-

Table 5. Seasonal trends of aerosol optical depth at 320.1 nm (1991–2013).

Season	Trend per decade	Significance level
Spring	+2 % (± 7 %)	not significant
Summer	−18 % (± 8 %)	95 %
Autumn	−36 % (± 14 %)	95 %
Winter	not enough data	

nificant positive trends occur in spring and summer (Table 4), with the trend in spring being the largest one. As opposed to the seasonal trends of S_{ery} and S_{g} , the ones for Q_{O_3} are positive for each season. We would expect an increase in Q_{O_3} over the past 23 years to be accompanied by a decrease in S_{ery} , which is not the case for the Uccle time series. This indicates that other variables might contribute to the change in S_{ery} and that the contribution of Q_{O_3} might be washed out by the influence of these other variables.

Both the minimum and maximum Q_{O_3} values increased significantly (99 % level) at the same rate: 3.0 % (± 0.6 %)

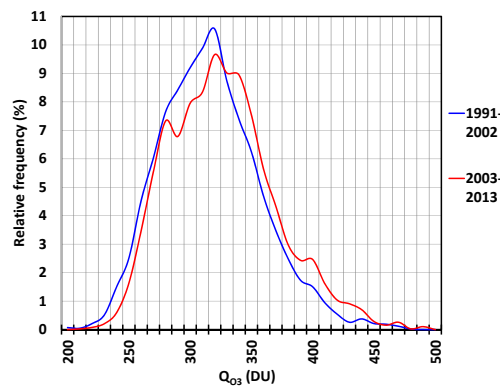


Figure 3. Relative frequency distribution of daily total ozone column values for the two time periods: 1991–2002 (in blue) and 2003–2013 (in red).

per decade for the minimum values and 3.1 % (± 0.6 %) per decade for the maximum values over the past 23 years. A clear shift can be seen in the frequency distribution (Fig. 3) of the daily Q_{O_3} values. During the second period (2003–2013), higher values are more frequent than during the previous period (1991–2002), which is supported by the increase in median values from 319.3 DU (199–2002) to 327.9 DU (2003–2013). The entire curve of the frequency distribution is shifted, which means that the minimum values of the distribution have also increased between the two decades. After a period with lower Q_{O_3} values in the 1990s, it seems that ozone has been recovering over the past 10 years. Removing the Pinatubo period (1991–1993) from our analysis does not change the trend in ozone significantly, which means that the observed recovery in ozone is not very much related to the return of the stratosphere to pre-Pinatubo time but rather that it is more likely a result of the regulations of the Montreal Protocol.

4.1.4 Aerosol optical depth at 320.1 nm

While the overall trends of S_{ery} , S_g and Q_{O_3} are all positive, the τ_{aer} values at 320.1 nm show a negative trend of -8 % (± 5 %) per decade. This trend, however, is not significant (Fig. 2). The seasonal trends (Table 5) show that the summer and autumn trends are significantly negative, with the largest trend being observed during autumn. Due to a lack of sufficient clear-sky data, it was not possible to determine the winter trend for τ_{aer} .

There are no significant changes in the minimum and maximum τ_{aer} values over the 1991–2013 period. From the relative frequency distribution of the daily τ_{aer} values (Fig. 4), it can be seen that the frequency of lower τ_{aer} values ($\tau_{\text{aer}} < 0.4$) was higher during the second period (2003–2013). The frequency of high τ_{aer} values ($\tau_{\text{aer}} > 0.7$) has also decreased towards the second decade. This is in agreement with the overall decrease in τ_{aer} over the last 23 years. However, this is

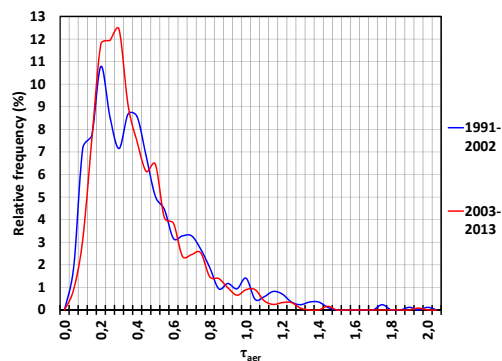


Figure 4. Relative frequency distribution of daily aerosol optical depth values for the two time periods: 1991–2002 (in blue) and 2003–2013 (in red).

not obvious from the median values as they decreased only slightly from 0.38 (1991–2002) to 0.36 (2003–2013).

4.2 Comparison of Uccle trends with other stations

4.2.1 Erythemal UV dose

Long-term UV trends for different locations around the world have been the subject of many research articles (e.g., den Outer et al., 2000; Zerefos et al., 2012; Eleftheratos et al., 2014), and it is worth checking the consistency of our results with these studies even though the time periods are never exactly the same as the one studied in this paper (1991–2013). Some trends (observed or modeled/reconstructed) found in the literature are presented in Table 6. Looking at these trends, it can be seen that for the stations with comparable latitude to Uccle (45 – 55° N), the trends in UV range from -2.1 to $+14.2$ % per decade. The increase of 7 % (± 2 %) per decade observed at Uccle falls within the range of trends reported in the literature. However, for the comparison of these trends, it has to be taken into account that not all trends in Table 6 are calculated in the same way as the one at Uccle. At Uccle, trends are based on monthly anomalies which are essentially calculated from daily doses. As such, all effects such as those from clouds are included in our analysis. Some of the studies from Table 6 report trends at a certain fixed solar zenith angle, which does not cover the same range of effects as the daily sum does, and thus the trends may not be truly comparable. The possible effect of a different concept of UV could be the subject of a later study. On a more global scale, Zerefos et al. (2012) examined UV irradiance over selected sites in Canada, Europe and Japan between 1990 and 2011. The results, based on observations and modeling for all stations, showed an increase in UV irradiances of 3.7 % (± 0.5 %) and 5.5 % (± 0.3 %) per decade at respectively 305 and 325 nm. For Europe, only the trend at 325 nm (3.4 % (± 0.4 %) per decade) was significant. The COST 726 action (Litynska et al., 2009; www.cost726.org) calculated

Table 6. Trends of UV radiation at different stations from (a) Bais et al. (2007), (b) Krzýscin et al. (2011), (c) Smedley et al. (2012), (d) Fitzka et al. (2012), (e) den Outer et al. (2010) and (f) Chubarova (2008).

Station, country	Latitude/longitude	Period	Trend/decade	Reference
Measured UV trends				
Sodankylä, Finland	67.42° N/26.59° E	1990–2004	+2.1 % (60° SZA)	(a)
Jokioinen, Finland	60.80° N/23.49° E	1996–2005	−1.9 % (60° SZA)	(a)
Norrköping, Sweden	58.36° N/16.12° E	1996–2004	+12 % (60° SZA)	(a)
Bilthoven, the Netherlands	52.13° N/5.20° E	1996–2004	+8.6 % (60° SZA)	(a)
Belsk, Poland	51.83° N/20.81° E	1976–2008	+5.6 %	(b)
Reading, United Kingdom	51.45° N/0.98° W	1993–2008	+6.6 %	(c)
Hradec Kralove, Czech Rep.	50.21° N/15.82° E	1994–2005	−2.1 % (60° SZA)	(a)
Lindenberg, Germany	47.60° N/9.89° E	1996–2003	+7.7 % (60° SZA)	(a)
Hoher Sonnblick, Austria	47.05° N/12.96° E	1997–2011	+14.2 % (65° SZA)	(d)
Thessaloniki, Greece	40.63° N/22.95° E	1990–2004	+3.4 % (60° SZA)	(a)
Reconstructed or Modeled UV trends				
Sodankylä, Finland	67.42° N/26.59° E	1980–2006	+3.6 %	(e)
Jokioinen, Finland	60.80° N/23.49° E	1980–2006	+2.8 %	(e)
Norrköping, Sweden	58.36° N/16.12° E	1980–2006	+4.1 %	(e)
Moscow, Russia	55.75° N/37.62° E	1980–2006	+6 %	(f)
Bilthoven, the Netherlands	52.13° N/5.20° E	1980–2006	+2.9 %	(e)
Hradec Kralove, Czech Rep.	50.21° N/15.82° E	1980–2006	+5.2 %	(e)
Lindenberg, Germany	47.60° N/9.89° E	1980–2006	+5.8 %	(e)
Thessaloniki, Greece	40.63° N/22.95° E	1980–2006	+4.4 %	(e)

trend values for European sites and saw a mean positive trend of 4.5 % (± 0.5 %) per decade since 1980, which was derived from reconstruction models, based on Q_{O_3} and measured total solar irradiance.

4.2.2 Global solar radiation

Concerning the global solar radiation, many publications agree on the existence of a solar dimming period between 1970 and 1985 and a subsequent solar brightening period (Norris and Wild, 2007; Solomon et al., 2007; Makowski et al., 2009; Stjern et al., 2009; Wild et al., 2009; Sanchez-Lorenzo and Wild, 2012). Different studies have calculated the trend in S_g after 1985. The trend in S_g from GEBA (Global Energy Balance Archive; http://www.iac.ethz.ch/groups/schaer/research/rad_and_hydro_cycle_global/geba) between 1987 and 2002 is equal to $+1.4 (\pm 3.4) \text{ W m}^{-2}$ per decade according to Norris and Wild (2007). Stjern et al. (2009) found a total change in the mean surface solar radiation trend over 11 stations in northern Europe of +4.4 % between 1983 and 2003. In the Fourth Assessment Report of the IPCC (Solomon et al., 2007), 421 sites were analyzed; between 1992 and 2002, the change of all-sky surface solar radiation was equal to 0.66 W m^{-2} per year. Wild et al. (2009) investigated the global solar radiation from 133 stations from GEBA/World Radiation Data Centre belonging to different regions in Europe. All series showed an increase over the entire pe-

riod, with a pronounced upward tendency since 2000. For the Benelux region, the linear change between 1985 and 2005 is equal to $+0.42 \text{ W m}^{-2}$ per year, compared to the pan-European average trend of $+0.33 \text{ W m}^{-2}$ per year (or $+0.24 \text{ W m}^{-2}$ if the anomaly of the 2003 heat wave is excluded) (Wild et al. 2009). Our trend at Uccle of $+0.5 (\pm 0.2) \text{ W m}^{-2}$ per year (or +4 % per decade) agrees within the error bars with the results from Wild et al. (2009), but seems to be somewhat at the high end range.

4.2.3 Total ozone column

Ozone and its trends have been the subject of scientific research since the discovery of ozone depletion. Many studies agree that ozone has decreased since 1980 to the mid-1990s as a consequence of anthropogenic emissions of ozone depleting substances. This period of decrease is followed by a period of significant increase (Steinbrecht et al., 2006; Harris et al., 2008; Vigouroux et al., 2008; Krzýscin and Borkowski, 2008; Herman, 2010; Bais et al., 2011). For the period before the mid-1990s, studies report on decreasing ozone values at Brussels (Bojkov et al., 1995 and Zerefos et al., 1997), Reading (Bartlett and Webb, 2000), Lerwick (Smedley et al., 2012), Arosa (Bojkov et al., 1995 and Staehelin et al., 1998), Hohenpeissenberg (Bojkov et al., 1995), Sodankylä (Glandorf et al., 2005) and Thessaloniki (Glandorf et al., 2005) (see Table 7). After the mid-1990s, most studies report on a plateau or a limited increase in ozone. For example, Smedley

Table 7. Trends of total ozone column at different stations from (a) Glandorf et al. (2005), (b) Smedley et al. (2012), (c) Bartlett and Webb (2000), (d) Bojkov et al. (1995), (e) Zerefos et al. (1997), (f) Fitzka et al. (2012), (g) Staehelin et al. (1998) and (h) Vigouroux et al. (2008).

Station, country	Latitude/longitude	Period	Trend/decade	Reference
Sodankylä, Finland	67.42° N/26.59° E	1979–1998	−5.7 %	(a)
Lerwick, United Kingdom	60.15° N/1.15° W	1979–1993	−5.8 %	(b)
Reading, United Kingdom	51.45° N/0.98° W	1993–1997	−5.9 %	(c)
Brussels, Belgium	50.84° N/4.36° E	1971–1994	−2.6 %	(d)
Brussels, Belgium	idem	1993–1996	−15.0 %	(e)
Hradec Kralove, Czech Rep.	50.21° N/15.82° E	1994–2005	−2.2 %	(d)
Hohenpeisenberg, Germany	47.80° N/11.00° E	1968–1994	−3.5 %	(d)
Hoher Sonnblick, Austria	47.05° N/12.96° E	1997–2011	+1.9 %	(f)
Arosa, Switzerland	46.77° N/9.67° E	1964–1994	−2.7 %	(d)
Arosa, Switzerland	idem	1970–1996	−2.3 %	(g)
Jungfrauoch, Switzerland	46.55° N/7.98° E	1995–2004	+4.1 %	(h)
Thessaloniki, Greece	40.63° N/22.95° E	1993–1996	−4.0 %	(e)
Thessaloniki, Greece	idem	1990–1998	−4.5 %	(a)

et al. (2012) found no clear ozone trend in the 1993–2008 period for Reading. Ozone observations from a Brewer instrument at Hoher Sonnblick (Fitzka et al., 2012) showed a small but significant increase between 1997 and 2011. Similar behavior was reported for Jungfrauoch in Vigouroux et al. (2008). Our result, a trend of +2.6 % per decade, compares well with the trend observed at Hoher Sonnblick, which is the only station with a time period comparable to the one at Uccle. From Figs. 2 and 6, it can be seen that a negative trend occurred in the Q_{O_3} values before 1998 and that this trend was followed by a positive one. However, neither trend is significant at Uccle. It is difficult to unambiguously attribute the ozone trends to changes in ODSs because other factors also contribute to ozone variability and trends. These factors are large volcanic eruptions, Arctic ozone depletion, long-term climate variability, changes in the stratospheric circulation and the 11-year solar cycle (Harris et al., 2008; Vigouroux et al., 2008). According to Rieder et al. (2013), the equivalent effective stratospheric chlorine and the 11-year solar cycle can be identified as major contributors, but the influence of dynamical features (such as the El Niño–Southern Oscillation, North Atlantic Oscillation and Quasi-Biennial Oscillation) on the ozone variability and trends can not be neglected at a regional level.

4.2.4 Aerosol optical depth at 320.1 nm

Trend analysis studies of long time series of aerosol optical depth are still very scarce at the moment. Some studies, however, do report on aerosol trends (Table 8). Mishchenko and Geogdzhayev (2007) observed a significant decrease in τ_{aer} from 1991 to 2005 over much of Europe within the GACP (Global Aerosol Climatology Project; <http://gacp.giss.nasa.gov/>) data. Alpert et al. (2012) studied τ_{aer} trends from MODIS (MODerate-resolution Imaging Spectroradiometer) and MISR (Multi-angle Imaging SpectroRadiometer) satel-

lite measurements over the 189 largest cities in the world and saw a decrease in τ_{aer} over Europe for the 2002–2010 period. The decadal trend observed by de Meij et al. (2012) over Europe between 2000 and 2009 was negative for MODIS (−30 %), MISR (−9 %) and AERONET (−25 %). Zerefos et al. (2012) – who investigated the τ_{aer} over Europe, Japan and Canada – discovered a general decline in τ_{aer} exceeding 10 % per year. For Europe specifically, the trend of τ_{aer} varied between −16.6 % (± 6 %) per decade when using the GACP data set and −42.8 % (± 5.7 %) for the MODIS data set. The insignificant trend of −8 % ± 5 % per decade observed at Uccle lies within the range of trends observed at other European stations. The long-term τ_{aer} decrease over much of Europe is quite consistent with the supposed reversal from increasing to decreasing anthropogenic sulfur and black carbon emissions owing to the enactment of clean-air legislation in many countries (Mishchenko and Geogdzhayev, 2007; Chiaccio et al., 2011; Alpert et al., 2012; de Meij et al., 2012; Hsu et al., 2012; Nabat et al., 2013). This change occurred after 1988–1989, the time period when a maximum was reached in the emissions of sulfate aerosols over Europe (Chiaccio et al., 2011). Many scientists believe that the decadal changes in aerosols have influenced the amount of solar radiation reaching the surface of the Earth and that the decrease in aerosols has played a part in the switch from global dimming to global brightening, which occurred around 1980–1990 (Augustine et al., 2008; Chiaccio et al., 2011). According to Wild et al. (2009), the reduction of aerosols may have played a role during the 1990s but not after 2000. Decreases in cloudiness or cloud albedo may have enabled the continuation of the increase in surface solar radiation over Europe beyond 2000, despite the stabilization of aerosol concentrations.

Table 8. Absolute and relative trends of aerosol optical depth at different stations from (a) Alpert et al. (2012), (b) Nyeki et al. (2012), (c) Fitzka et al. (2012) and (d) Kazadzis et al. (2007). MODIS-Terra, MODIS-Aqua and MISR measurements are represented by respectively “a”, “b” and “c” after the station name.

Station, country	Latitude/longitude	Period	Trend/decade	Reference
Berlin (a), Germany	52.50° N/13.40° E	2002–2010	−20.5 %	(a)
Berlin (b), Germany	idem	2002–2010	−17.9 %	(a)
Berlin (c), Germany	idem	2002–2010	−12.3 %	(a)
Warsaw (a), Poland	52.30° N/21.00° E	2002–2010	−2.4 %	(a)
Warsaw (b), Poland	idem	2002–2010	−0.4 %	(a)
Warsaw (c), Poland	idem	2002–2010	+12.9 %	(a)
Ruhr Area (a), Germany	51.50° N/7.50° E	2002–2010	−15.7 %	(a)
Ruhr Area (b), Germany	idem	2002–2010	−9.3 %	(a)
Ruhr Area (c), Germany	idem	2002–2010	−9.3 %	(a)
Paris (a), France	48.90° N/2.40° E	2002–2010	−8.1 %	(a)
Paris (b), France	idem	2002–2010	+5.0 %	(a)
Paris (c), France	idem	2002–2010	+9.8 %	(a)
Hohenpeisenberg, Germany	47.80° N/11.00° E	1995–2010	−10.6 %	(b)
Hoher Sonnblick, Austria	47.05° N/12.96° E	1997–2011	−5 to −6 %	(c)
Barcelona (a), Spain	41.40° N/2.20° E	2002–2010	−8.8 %	(a)
Barcelona (b), Spain	idem	2002–2010	+4.2 %	(a)
Barcelona (c), Spain	idem	2002–2010	−2.3 %	(a)
Thessaloniki, Greece	40.63° N/22.95° E	1997–2006	−29.0 %	(d)
Madrid (a), Spain	40.40° N/3.70° W	2002–2010	−18.3 %	(a)
Madrid (b), Spain	idem	2002–2010	−10.0 %	(a)
Madrid (c), Spain	idem	2002–2010	−7.4 %	(a)

4.3 Change-point analysis

4.3.1 Erythemal UV dose

According to the three tests (PMW, MWW and CST) of the change-point analysis, there is a significant shift in the mean of the monthly anomalies of S_{ery} around January 2003. The change point is located suspiciously close to the middle of the time series, however. To remove the influence of the presence of one general increasing trend, which would lead to the discovery of a change point in the middle of the time series, the time series was detrended. This is done by subtracting the general trend from the original time series. The change point in the detrended time series is located around February 1998 (Fig. 5). Since there was no change in the calibration constants of the Brewer instrument around that period, it seems that the change point is not caused by known instrumental changes but rather by natural/environmental changes.

4.3.2 Global solar radiation

A significant change point was detected (only by the PMW test) around January 2003 in the time series of S_{g} . Similar to the S_{ery} time series, there is one general positive trend present, which explains the detection of a change point near the middle of the time series. Thus, it was again decided to look at the detrended time series of S_{g} . However, the detected change point around January 2006 (only by the PMW test) was not significant at the 90 % significance level.

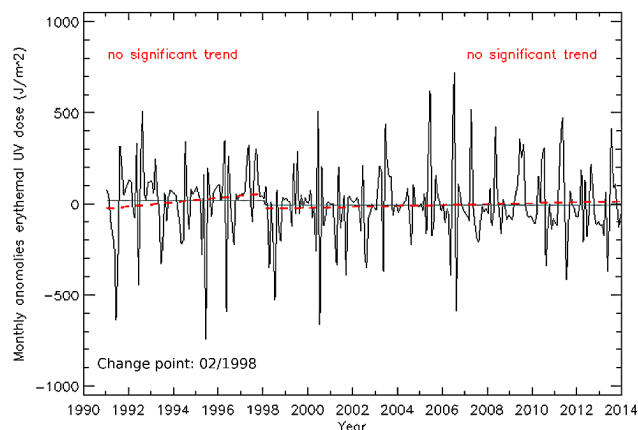


Figure 5. The black line represents the detrended time series of monthly anomalies of erythemal UV dose (1991–2013). The red (dashed) lines represent the (insignificant) positive trends before and after the detected change point. The grey lines represent the mean before and after the change point.

4.3.3 Total ozone column

All three tests confirmed the presence of a significant change point around March 1998 in the time series of monthly anomalies of Q_{O_3} , where the mean before the change point is clearly lower than the one after the change point (Fig. 6). As there is clearly more than one general trend within the

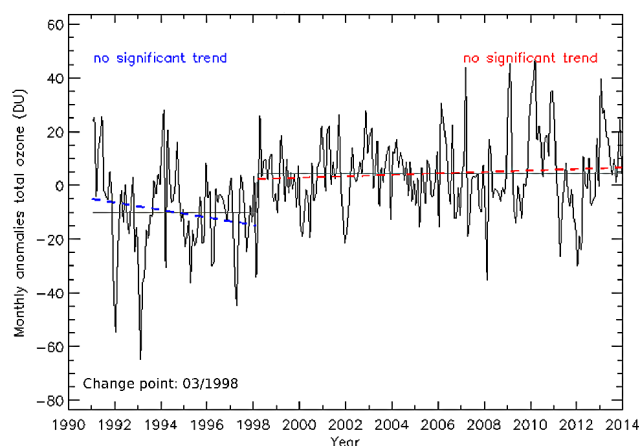


Figure 6. The black line represents the time series of monthly anomalies of total ozone column (1991–2013). The blue (dashed) line represents the (insignificant) negative trend before the detected change point, and the red (dashed) line represents the (insignificant) positive trend after the change point. The grey lines represent the mean before and after the change point.

entire time series, there is no need for detrending in this case. There was no change in the calibration constants of the Brewer instrument around 1998, so the change point has no known instrumental cause. To further exclude an instrumental cause for the step change in the mean of the Uccle ozone time series, we investigated the total ozone time series of De Bilt (the Netherlands; 52.10° N/5.18° E; data obtained from www.woudc.org). This time series is also characterized by a step change and change point in the beginning of 1998 (March 1998). At that time, there was no change in the calibration constants of the Brewer instrument at De Bilt. This confirms that the change point seen in the Uccle time series must have a natural/environmental cause.

4.3.4 Aerosol optical depth at 320.1 nm

According to the change-point analysis, no significant change was found in the mean of the monthly anomalies of τ_{aer} .

4.3.5 Overview and explanations

The change points in the time series of S_{ery} and Q_{O_3} occur around the same time period (February/March 1998). Since we were able to rule out known instrumental causes for the detected change points in both time series, we can assume that they have some natural/environmental cause and are related to each other.

The change point in the Q_{O_3} time series corresponds with results found in the literature. Recent studies have shown that, for other stations, the ozone recovery started around 1997 (Steinbrecht et al., 2006; Reinsel et al., 2005). Ozone levels seem to follow the change in chlorine concentrations

resulting from the regulations of the Montreal Protocol in 1987. When ozone starts to increase, it is expected to have some implications on the UV irradiance as ozone is a strong absorber of UV irradiance in the stratosphere (Wenny et al., 2001). An increase in ozone would normally lead to a decrease in UV irradiance, which is not what was observed at Uccle, where the UV irradiance levels continue to increase after 1998. Before 1998, the (insignificant) trends in the time series of Q_{O_3} and S_{ery} are opposite, which is what would be expected. However, after 1998, both the (insignificant) Q_{O_3} and S_{ery} trend are positive. So the behavior of Q_{O_3} can only partly explain the changes observed in the UV irradiance time series, and other parameters, such as aerosols and cloudiness, might play an important role.

4.4 Multiple linear regression analysis

Before applying the MLR technique, it has to be verified that the explanatory variables (S_{g} , Q_{O_3} and τ_{aer}) are independent variables. This is done by calculating the correlation coefficients between these parameters. The correlation coefficients between the three variables are low enough (< 0.25) to allow using these variables as independent explanatory variables for the multiple regression analysis. As opposed to the previous analysis methods, the MLR is applied to daily values, instead of monthly anomaly values. For S_{ery} and S_{g} , the daily sums are used, whereas for Q_{O_3} and τ_{aer} daily mean values are used.

4.4.1 MLR analysis of daily values using total ozone column, global solar radiation and aerosol optical depth

The MLR analysis has been applied to 1246 simultaneous daily values of erythemal UV dose (S_{ery}), global solar radiation (S_{g}), total ozone (Q_{O_3}) and aerosol optical depth (τ_{aer}) between 1991 and 2008. The amount of regression days was highly limited by the available τ_{aer} measurements. The resulting regression equation is

$$S_{\text{ery}} = 690 + 0.000169 \times S_{\text{g}} - 5.01 \times Q_{\text{O}_3} + 70.0 \times \tau_{\text{aer}} + \epsilon \quad (6)$$

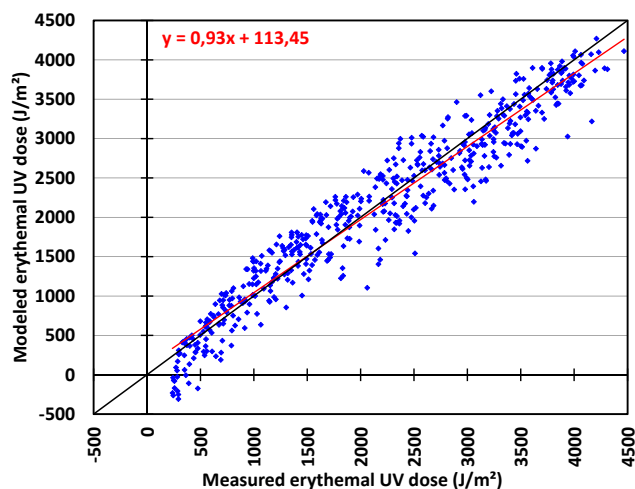
(with S_{ery} in J m^{-2} ; S_{g} in J m^{-2} ; and Q_{O_3} in DU).

The adjusted R^2 value of the multiple regression is 0.94, which means that S_{g} , Q_{O_3} and τ_{aer} together explain 94 % of the variation in daily S_{ery} . The changes in S_{ery} caused by the variation of each of the three parameters can be calculated by multiplying the standard deviation of each parameter with its corresponding regression coefficient and dividing this by the average S_{ery} value. From the results, it is clear that S_{g} , whose variation leads to a change in S_{ery} of 56 %, has the biggest influence on S_{ery} , followed by Q_{O_3} (change in S_{ery} of -9 %) and τ_{aer} (change in S_{ery} of 1 %).

The data from 2009–2013 are used to validate the model (see Fig. 7). The regression equation between the modeled and measured S_{ery} values ($f(x) = 0.93x + 113.45$ with x :

Table 9. Performance of the seasonal regression models.

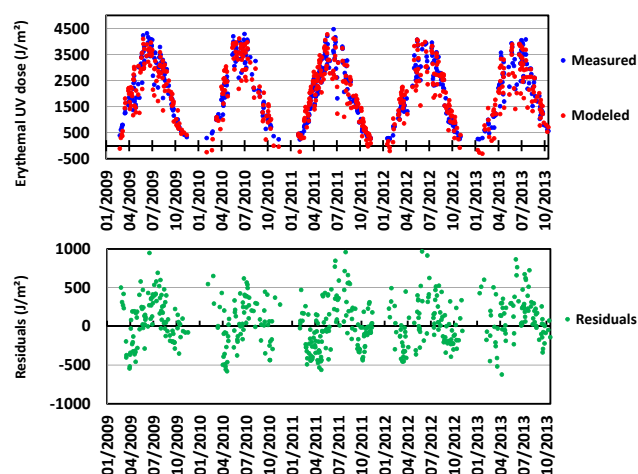
	Spring	Summer	Autumn	Winter
Correlation	0.95	0.93	0.97	0.90
Regression equation	$y = 0.89x + 145.17$	$y = 0.94x + 104.36$	$y = 0.90x + 102.48$	$y = 0.91x + 8.13$
MBE	−4 %	−2 %	0.06 %	−7 %
MABE	14 %	6 %	15 %	15 %

**Figure 7.** Scatterplot of the measured and modeled erythemal UV doses at Uccle for the 2009–2013 validation period. The red line represents the regression line of the data ($f(x) = 0.93x + 113.45$). The black line is the $f(x) = x$ line.

measured values) and the correlation coefficient (0.96) reveal the good agreement between model and reality. The MBE of the model is −3 %, meaning that the model has a slight tendency to underestimate the measurements, which can be seen in Figs. 7 and 8. The MABE, which is a useful measure to evaluate the overall performance of the model, equals 18 %. This means that the model proposed here estimates the S_{ery} with a mean error of 18 %. Figure 7 and the upper panel of Fig. 8 show that, in some cases, negative S_{ery} doses are modeled, which is a sign that the model does not always give realistic results. This is the case only during winter, when the S_{g} values are much lower than during the other seasons. When moderate to high Q_{O_3} values are combined with low S_{g} values, this leads to negative modeled S_{ery} values according to the regression equation. From Fig. 8 it is also clear that there is a seasonal cycle in the residual values. Therefore, it would be better to perform the multiple regression analysis on a seasonal scale.

4.4.2 Seasonal MLR analysis using total ozone column, global solar radiation and aerosol optical depth

The multiple regression equations for the different seasons are presented below.

**Figure 8.** Validation of the multiple linear regression equation: the upper panel shows the measured (in blue) and modeled (in red) erythemal UV values; the lower panel presents the absolute residuals.

Spring:

$$S_{\text{ery}} = 1016 + 0.0001542 \times S_{\text{g}} - 5.660 \times Q_{\text{O}_3} + 92.11 \times \tau_{\text{aer}} + \epsilon \quad (7)$$

Summer:

$$S_{\text{ery}} = 2010 + 0.0001481 \times S_{\text{g}} - 6.737 \times Q_{\text{O}_3} - 134.2 \times \tau_{\text{aer}} + \epsilon \quad (8)$$

Autumn:

$$S_{\text{ery}} = -195 + 0.000143 \times S_{\text{g}} - 1.22 \times Q_{\text{O}_3} + 120 \times \tau_{\text{aer}} + \epsilon \quad (9)$$

Winter:

$$S_{\text{ery}} = 325 + 0.0000750 \times S_{\text{g}} - 1.50 \times Q_{\text{O}_3} + 101 \times \tau_{\text{aer}} + \epsilon \quad (10)$$

For all seasons, more than 80 % of the total variation in S_{ery} is explained by the combination of S_{g} , Q_{O_3} and τ_{aer} . This could be concluded from the adjusted R^2 values for each season. What might seem strange is the negative value of the constant term in the regression equation for autumn. However, the p value for this term is higher than 0.05, which means that this coefficient does not significantly differ from 0 at the 95 % significance level.

From Fig. 9 and Table 9, it can be concluded that the seasonal models perform well in estimating the measured S_{ery} values. The correlation between the modeled and measured

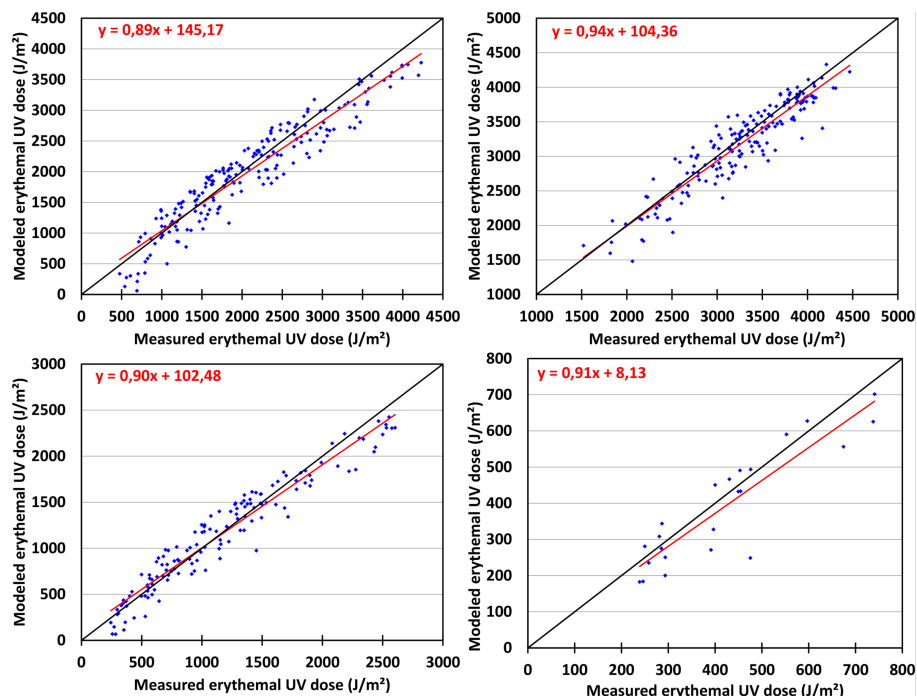


Figure 9. Scatterplots of the measured and modeled erythemal UV doses at Uccle for the 2009–2013 validation period for spring (upper left panel), summer (upper right panel), autumn (lower left panel) and winter (lower right panel). The red lines represent the regression lines of the data, and the black lines are the $f(x) = x$ lines.

Table 10. Seasonal influence of the variation of S_g , Q_{O_3} and τ_{aer} on S_{ery} .

	Spring	Summer	Autumn	Winter
τ_{aer}	1 %	−1 %	2 %	4 %
Q_{O_3}	−9 %	−4 %	−2 %	−15 %
S_g	37 %	18 %	53 %	32 %

values varies between 0.90 (in winter) and 0.97 (in autumn). The regression equations are shown in both Fig. 9 and Table 9. The negative MBE values (except for autumn, which has a value close to 0) show that each model has a tendency to underestimate the measured values. The summer model performs best, with an absolute mean model error of only 6 %. The relative residuals (shown in Fig. 10) are smallest in summer, which again points out that the performance of the summer model in estimating the measured S_{ery} is the best. The spring and autumn models have much higher relative residuals.

To determine the influence of the variation in the parameters on the variation in UV, the standard deviation of each parameter is multiplied with its corresponding regression coefficient, which is then divided by the average S_{ery} value. This will give an idea of the magnitude of the influence of each parameter on UV. The results are given in Table 10. Changes in the variation of S_g (Table 10) are the most important and

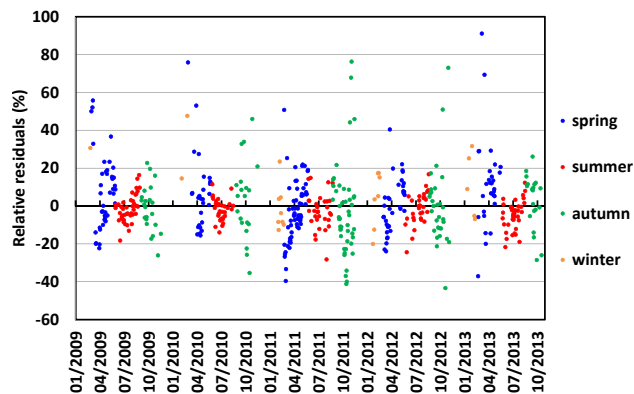


Figure 10. Relative residuals ($= (\text{measured} - \text{modeled}) / \text{measured} \times 100$) of the seasonal multiple regression models. The colors represent the different seasons: blue – spring; red – summer; green – autumn; and orange – winter.

lead to changes in S_{ery} between 18 % (in summer) and 53 % (in autumn). The influence of the variation in Q_{O_3} and τ_{aer} is much smaller. Changes in the variation of Q_{O_3} always lead to negative changes in S_{ery} (from −2 % in summer to −15 % in winter), whereas the influence of a change in variation of τ_{aer} varies from a negative value (−1 % change in S_{ery}) in summer to positive values in the other seasons, with a maximum of 4 % in winter (Table 10). τ_{aer} and S_g have their low-

est contribution in summer. Q_{O_3} on the other hand has the lowest contribution in autumn. The influence of Q_{O_3} is highest during winter and spring, and this is in accordance with the variation in Q_{O_3} itself, which is largest during winter and early spring. For τ_{aer} also, the absolute contribution to the variation in S_{ery} is the highest in winter. As the path length of UV irradiance is higher during winter, aerosols and ozone have more opportunity to influence UV irradiance on its way to the Earth's surface.

The influence of τ_{aer} on S_{ery} in the seasonal models is positive (except in summer), which is also the case when the τ_{aer} is used as the only explanatory variable in the models. This does not agree with what was observed in the trend analysis of the monthly anomalies time series, where an increase in S_{ery} is accompanied by a decrease in τ_{aer} . It has to be taken into account, however, that the negative general τ_{aer} trend is not significant. Also, this negative trend in τ_{aer} is too much driven by the high but sparse values at the beginning of the studied time period. Depending on the circumstances and the physical and optical properties of aerosols, the influence of τ_{aer} on global and UV irradiance can be either positive or negative. An increase in τ_{aer} could lead to an increase in global and UV radiation if the increase in τ_{aer} were caused by an increase in the amount of small scattering aerosol particles. If there were predominantly particles of size much smaller than the UV wavelengths (i.e., freshly formed particles, Aitken mode particles) and of high single-scattering albedo (SSA), the UV radiation could be enhanced by the multiple scattering by these aerosols. However, if the amount of all particles exceeded a certain (albeit in this study not possible to determine) threshold value, extinction would take over, and from this point an increase in τ_{aer} would lead to a decrease in UV irradiance. The aerosol composition, which determines whether a mixture is rather scattering or absorbing, the aerosol amount and the aerosol size distribution determine whether an increase in τ_{aer} will lead to either an increase or decrease in UV irradiance. At Uccle there is no information on these parameters; hence it is difficult to unambiguously characterize the influence of τ_{aer} on UV irradiance. The aerosol effects on UV in this study are solely based on τ_{aer} and not on aerosol absorption property changes. Recently, a nephelometer and an aethalometer have been installed at our site in Uccle, so in the future their measurements can be combined to derive the SSA. This will shine a new light on the influence of the aerosols on the UV radiation at Uccle. Antón et al. (2011) already reported that it is hard to determine the effect of aerosols due to their temporal and spatial variability and the difficulties associated with their characterization.

It has already been shown that S_g has the largest influence on S_{ery} , so an important issue that needs to be addressed is whether Q_{O_3} and τ_{aer} are actually necessary to capture the variation in S_{ery} . This was investigated by performing the MLR analysis using (1) only S_g , (2) S_g combined with Q_{O_3} and (3) S_g combined with τ_{aer} as explanatory variables. The

Table 11. Results of MLR analysis with only S_g , S_g combined with Q_{O_3} and S_g combined with τ_{aer} as explanatory variables.

	S_g	$S_g+Q_{O_3}$	$S_g+\tau_{aer}$
Adjusted R^2			
Spring	0.85	0.90	0.85
Summer	0.81	0.85	0.81
Autumn	0.95	0.95	0.95
Winter	0.65	0.81	0.65
MABE (in %)			
Spring	14.53	14.40	14.33
Summer	6.39	6.21	6.21
Autumn	15.45	15.25	14.89
Winter	22.20	14.25	21.47
Correlation modeled and measured UV values			
Spring	0.93	0.95	0.93
Summer	0.91	0.93	0.91
Autumn	0.96	0.96	0.96
Winter	0.75	0.89	0.76

adjusted R^2 value, the MABE and the correlation between modeled and measured S_{ery} values are given in Table 11. From these values, it becomes clear that τ_{aer} only has a minor contribution to the regression model and that, to describe the changes in S_{ery} , τ_{aer} might not be needed, except perhaps for spring. For this reason it seems unnecessary to include τ_{aer} in the MLR analysis. Q_{O_3} seems to be a more important explanatory variable, as the adjusted R^2 increases for all seasons, except summer, and the MABE of the models decreases, except in summer, when combining S_g and Q_{O_3} . The correlation between modeled and measured values does not change much, except in winter (from 0.75 when using only S_g to 0.89 when combining S_g and Q_{O_3}). The developed regression models are only valid for Uccle. For other sites, it might be necessary to include all three parameters in the regression models in order to explain the observed variation in S_{ery} .

5 Conclusions

Of the variables known to influence the UV irradiance that reaches the ground, the variability of global solar radiation, total ozone column and aerosol optical depth (at 320.1 nm) are studied by performing a trend analysis, a change-point analysis and a multiple linear regression analysis. This is done in order to determine their changes over a 23 year time period (1991–2013) and their possible relation to the observed UV changes at Uccle, Belgium. S_{ery} , Q_{O_3} and τ_{aer} are measured by the Brewer spectrophotometer instruments, and S_g measurements are performed by a CM11 pyranometer.

The trend over the past 23 years was determined for each variable using their monthly anomaly values. An overall positive trend was present in the time series of S_{ery} , S_{g} and Q_{O_3} of respectively +7 % (± 2 %), +4 % (± 1 %) and +2.6 % (± 0.4 %) per decade. In contrast, the trend of τ_{aer} , equal to -8 % (± 5 %) per decade, is insignificantly negative over the investigated time period. The sign and magnitude of the trends observed at Uccle agree with results found in the literature for stations of comparable latitude. The increase in S_{g} since 1991 could be interpreted as a sign of continuing global brightening over Belgium. The decrease in sulfur and black carbon emissions after 1989, which resulted in enhanced global solar radiation at the Earth's surface, is most probably also the driving mechanism for the decrease in τ_{aer} , which in turn could have an influence by increasing the UV irradiance.

For both S_{ery} and S_{g} , there is an increase in the frequency of higher values towards the second part of the study period (2003–2013), without the entire frequency distribution shifting. This could be explained by a decrease in cloudiness towards 2003–2013. Several studies report on a decrease in cloud cover over the past decades and a tendency for cumulus clouds to replace stratiform clouds (Norris and Slingo, 2009; Eastman and Warren, 2013). This would increase both S_{g} and S_{ery} due to enhanced scattering. However, other parameters (such as ozone and aerosols) could also influence the values of S_{ery} and S_{g} . As opposed to S_{ery} and S_{g} , a clear shift can be seen in the entire frequency distribution of daily Q_{O_3} values, with both minimum and maximum values having increased from the 1991–2002 period to the 2003–2013 period, which supports literature findings about an ozone recovery around the end of the 1990s. From the frequency distribution of daily τ_{aer} values, it can be derived that, between 1991 and 2002, higher τ_{aer} values were more frequently present than during the last period (2003–2013), which is in agreement with the overall decrease over the last 23 years.

The seasonal trends of the four variables were also studied and are similar between S_{ery} and S_{g} , with a positive trend for all seasons except winter. The Q_{O_3} trend is positive for spring and summer. Normally, we would expect a positive Q_{O_3} trend to be accompanied with a negative trend in S_{ery} . The fact that the observed trends have the same sign could indicate that the change in UV irradiance is not only influenced by a change in total ozone values. The τ_{aer} trend is negative during summer and autumn. The trend in spring is not significant, and not enough winter data were present to calculate a winter trend.

For Q_{O_3} and S_{ery} , a significant change point (i.e., a significant shift in the mean of the monthly anomalies) was detected around February/March 1998, which has no known instrumental cause. The timing of the change point in ozone corresponds to results found in the literature where studies define the change around this time period as the start of ozone recovery, following the regulations of the Montreal Protocol.

The trend in the ozone time series at Uccle does not seem very affected by the eruption of the Pinatubo, which took place in June 1991.

To investigate the influences of S_{g} , Q_{O_3} and τ_{aer} on S_{ery} , a multiple linear regression was performed using daily values between 1991 and 2008. The three variables together explain 94 % of the total variation in the observed S_{ery} values. S_{g} has the largest influence on S_{ery} , followed by Q_{O_3} and τ_{aer} . Data of 2009–2013 were used to validate the model, and the MBA and MABE were calculated to evaluate the model performance in terms of overestimation and average error. The MBE value of the model is -3 %, which means that the model has a slight tendency to underestimate the measured UV irradiance values. The average error of the model in the estimation of the measurements is equal to 18 %. Overall, the model represents reality well; however sometimes during winter, negative S_{ery} values were modeled. For this reason, seasonal regression models have been developed.

All seasonal models perform rather well in explaining the variation in UV irradiance, with adjusted R^2 values being larger than 0.8. The negative MBE values show the models' tendencies to underestimate UV irradiance. Again, S_{g} has the largest influence on S_{ery} , followed by Q_{O_3} and τ_{aer} . The summer regression model performs best, based on the very low MABE values.

What is seen in reality (i.e., an increase in S_{ery} accompanied with an increase in Q_{O_3} and a decrease in τ_{aer}) is not always what is represented by the models. According to the regression models, Q_{O_3} and τ_{aer} respectively always have a negative and positive influence on S_{ery} . However, as S_{g} is obviously the most important factor in explaining the variation in S_{ery} , the increase in Q_{O_3} (which would be expected to lead to a decrease in S_{ery}) and the change in τ_{aer} seem to be compensated for by the increase in S_{g} .

The question that remains is whether Q_{O_3} and τ_{aer} are needed as explanatory variables in the multiple linear regression models. It has been shown that the contribution of τ_{aer} to explaining the variation in S_{ery} is very small, and it can be concluded that this variable is not really needed in the multiple linear regression model. Also its influence is already partly represented by S_{g} . Q_{O_3} , however, does seem to be a more important factor in capturing the variation in S_{ery} and cannot be discarded from the regression models. It has to be kept in mind that the regression models are only valid for Uccle, which means that for other sites it might be necessary to include all three parameters in the regression models.

Acknowledgements. This research was performed under the project AGACC-II, contract SD/CS/07A, of the Belgian Science Policy. We thank Christian Hermans (Belgian Institute for Space Aeronomy, Belgium) for establishing and maintaining the AERONET site at Uccle. We would also like to thank the anonymous reviewers and the editor (S. Kazadzis) for their useful input.

Edited by: S. Kazadzis

References

- Alpert, P., Shvainshtein, O., and Kishcha, P.: AOD trends over megacities based on space monitoring using MODIS and MISR, *Am. J. Clim. Change*, 12, 117–131, doi:10.4236/ajcc.2012.13010, 2012.
- Antón, M., Serrano, A., Cancillo, M. L., and García, J. A.: An empirical model to estimate ultraviolet erythemal transmissivity, *Ann. Geophys.*, 27, 1387–1398, doi:10.5194/angeo-27-1387-2009, 2009.
- Antón, M., Gil, J. E., Fernández-Gálvez, J., Lyamani, H., Valenzuela, A., Foyo-Moreno, I., Olmo, F. J., and Alados-Arboledas, L.: Evaluation of the aerosol forcing efficiency in the UV erythemal range at Granada, Spain, *J. Geophys. Res.*, 116, D20214, doi:10.1029/2011JD016112, 2011.
- Augustine, J. A., Hodges, G. B., Dutton, E. G., Michalsky, J. J., and Cornwall, C. R.: An aerosol optical depth climatology for NOAA's national surface radiation budget network (SURFRAD), *J. Geophys. Res.*, 113, D11204, doi:10.1029/2007JD009504, 2008.
- Bais, A. F., Kazadzis, S., Meleti, C., Kouremeti, N., Kaurola, J., Lakkala, K., Slaper, H., den Outer, P. N., Josefsson, W., Feister, U., and Janouch, M.: Variability in spectral UV irradiance at seven European stations, edited by: Gröbner J., One century of UV radiation research. Proceedings of the UV conference, Davos, Switzerland, July 2007, 1, 27–28, 2007.
- Bais, A. F., Tourpali, K., Kazantzidis, A., Akiyoshi, H., Bekki, S., Braesicke, P., Chipperfield, M. P., Dameris, M., Eyring, V., Garny, H., Iachetti, D., Jöckel, P., Kubin, A., Langematz, U., Mancini, E., Michou, M., Morgenstern, O., Nakamura, T., Newman, P. A., Pitari, G., Plummer, D. A., Rozanov, E., Shepherd, T. G., Shibata, K., Tian, W., and Yamashita, Y.: Projections of UV radiation changes in the 21st century: impact of ozone recovery and cloud effects, *Atmos. Chem. Phys.*, 11, 7533–7545, doi:10.5194/acp-11-7533-2011, 2011.
- Bartlett, L. M. and Webb, A. R.: Changes in ultraviolet radiation in the 1990s: Spectral measurements from Reading, England, *J. Geophys. Res.*, 105, 4889–4893, doi:10.1029/1999JD900493, 2000.
- Bernhard, G., Booth, C. R., Ehranjian, J. C., and Nichol, S. E.: UV climatology at McMurdo Station, Antarctica, based on Version 2 data of the National Science Foundation's Ultraviolet Radiation Monitoring Network, *J. Geophys. Res.*, 111, D11201, doi:10.1029/2005JD005857, 2006.
- Bojkov, R. D., Bishop, L., and Fioletov, V. E.: Total ozone trends from quality-controlled ground-based data (1964–1994), *J. Geophys. Res.*, 100, 25867–25876, doi:10.1029/95JD02907, 1995.
- Cheymol, A. and De Backer, H.: Retrieval of the aerosol optical depth in the UV-B at Uccle from Brewer ozone measurements over a long time period 1984–2002, *J. Geophys. Res.*, 108, 4800, doi:10.1029/2003JD003758, 2003.
- Chiaccio, M., Ewen, T., Wild, M., Chin, M., and Diehl, T.: Decadal variability of aerosol optical depth in Europe and its relationship to the temporal shift of the North Atlantic Oscillation in the realm of dimming and brightening, *J. Geophys. Res.*, 116, D02108, doi:10.1029/2010JD014471, 2011.
- Chubarova, N. Y.: UV variability in Moscow according to long term UV measurements and reconstruction model, *Atmos. Chem. Phys.*, 8, 3025–3031, doi:10.5194/acp-8-3025-2008, 2008.
- Cordero, R. R., Seckmeyer, G., Pissulla, D., and Labbe, F.: Exploitation of spectral direct UV irradiance measurements, *Metrologia*, 46, 19–25, doi:10.1088/0026-1394/46/1/003, 2009.
- De Backer, H.: Time series of daily erythemal UV doses at Uccle, Belgium, *Int. J. Remote Sens.*, 30, 4145–4145, doi:10.1080/01431160902825032, 2009.
- De Backer, H. and De Muer, D.: Intercomparison of total ozone data measured with Dobson and Brewer ozone spectrophotometers at Uccle (Belgium) from January 1984 to March 1991, including zenith sky observations, *J. Geophys. Res.*, 96, 20711–20719, doi:10.1029/91JD02159, 1991.
- De Bock, V., De Backer, H., Mangold, A., and Delcloo, A.: Aerosol optical depth measurements at 340 nm with a Brewer spectrophotometer and comparison with Cimel sunphotometer observations at Uccle, Belgium, *Atmos. Meas. Tech.*, 3, 1577–1588, doi:10.5194/amt-3-1577-2010, 2010.
- de La Casinière, A., Lamine Touré, M., Masserot, D., Cabot, T., and Pinedo Vega, J. L.: Daily doses of biologically active UV radiation retrieved from commonly available parameters, *Photochem. Photobiol.*, 76, 171–175, doi:10.1562/0031-9655(2002)0760171DDOBAU2.0.002, 2002.
- de Meij, A., Pozzer, A., and Lelieveld, J.: Trend analysis in aerosol optical depths and pollutant emission estimates between 2000 and 2009, *Atmos. Environ.*, 51, 75–85, doi:10.1016/j.atmosenv.2012.01.059, 2012.
- den Outer, P. N., Slaper, H., Matthijsen, J., Reinen, H. A. J. M., and Tax, R.: Variability of ground-level ultraviolet: Model and Measurement, *Radiat. Prot. Dos.*, 91, 105–110, 2000.
- den Outer, P. N., Slaper, H., Kaurola, J., Lindfors, A., Kazantzidis, A., Bais, A. F., Feister, U., Junk, J., Janouch, M., and Josefsson, W.: Reconstructing of erythemal ultraviolet radiation levels in Europe for the past 4 decades, *J. Geophys. Res.*, 115, D10102, doi:10.1029/2009JD012827, 2010.
- Díaz, S., Deferrari, G., Martinioni, D., and Oberto, A.: Regression analysis of biologically effective integrated irradiances versus ozone, clouds and geometric factors, *J. Atmos. Sol-Terr. Phys.*, 62, 629–638, doi:10.1016/S1364-6826(00)00055-9, 2000.
- Diffey, B. L.: Solar ultraviolet radiation effects on biological systems, *Phys. Med. Biol.*, 36, 299–328, doi:10.1088/0031-9155/36/3/001, 1991.
- Durbin, J. and Watson, G. S.: Testing for serial correlation in least squares regression III, *Biometrika*, 58, 1–19, 1971.
- Eastman, R. and Warren, S. G.: A 39-yr survey of cloud changes from land stations worldwide 1971–2009: long-term trends, relation to aerosols and expansion of the tropical belt, *J. Climate*, 26, 1286–1303, doi:10.1175/JCLI-D-12-00280.1, 2013.
- Eck, T. F., Holben, B. N., Reid, J. S., Dubovik, O., Smirnov, A., O'Neill, N. T., Slutsker, I., and Kinne, S.: Wavelength dependence of the optical depth of biomass burning, urban, and desert dust aerosols, *J. Geophys. Res.*, 104, 31333–31349, doi:10.1029/1999JD900923, 1999.
- Eleftheratos, K., Kazadzis, S., Zerefos, C. S., Tourpali, K., Meleti, C., Balis, D., Zyrichidou, I., Lakkala, K., Feister, U., Koskela, T., Heikkilä, A., and Karhu, J. M.: Ozone and Spectroradiometric UV Changes in the Past 20 Years over High Latitudes, *Atmos.-Ocean*, doi:10.1080/07055900.2014.919897, 2014.
- El Shazly, S. M., Kassem, Kh. O., Hassan, A. A., and El-Nobi, E. F.: An empirical model to estimate UV index in

- some upper Egypt regions, *Resour. Environ.*, 2, 216–227, doi:10.5923/j.re.20120205.05, 2012.
- Fioletov, V. E., McArthur, L. J. B., Kerr, J. B., and Wardle, D. I.: Long-term variations of UV-B irradiance over Canada estimated from Brewer observations and derived from ozone and pyranometers measurements, *J. Geophys. Res.*, 106, 23009–23027, doi:10.1029/2001JD000367, 2001.
- Fioletov, V. E., Kerr, J. B., Wardle, D. I., Krotkov, N., and Herman, J. R.: Comparison of Brewer ultraviolet irradiance measurements with total ozone mapping spectrometer satellite retrievals, *Opt. Eng.*, 41, 3051–3061, doi:10.1117/1.1516818, 2002.
- Fioletov, V. E., Kimlin, M. G., Krotkov, N., McArthur, L. J. B., Kerr, J. B., Wardle, D. I., Herman, J. R., Meltzer, R., Mathews, T. W., and Kaurola, J.: UV index climatology over the United States and Canada from ground-based and satellite estimates, *J. Geophys. Res.*, 109, D22308, doi:10.1029/2004JD004820, 2004.
- Fitzka, M., Simic, S., and Hadzimustafic, J.: Trends in spectral UV radiation from long-term measurements at Hoher Sonnblick, Austria, *Theor. Appl. Climatol.*, 110, 585–593, doi:10.1007/s00704-012-0684-0, 2012.
- Foyo-Moreno, I., Alados, I., and Alados-Arboledas, L.: Adaptation of an empirical model for erythemal ultraviolet irradiance, *Ann. Geophys.*, 25, 1499–1508, doi:10.5194/angeo-25-1499-2007, 2007.
- Garane, K., Bais, A. F., Kazadzis, S., Kazantzidis, A., and Meleti, C.: Monitoring of UV spectral irradiance at Thessaloniki (1990–2005): data re-evaluation and quality control, *Ann. Geophys.*, 24, 3215–3228, doi:10.5194/angeo-24-3215-2006, 2006.
- Glandorf, M., Arola, A., Bais, A., and Seckmeyer, G.: Possibilities to detect trends in spectral UV irradiance, *Theor. Appl. Climatol.*, 81, 33–44, doi:10.1007/s00704-004-0109-9, 2005.
- Gröbner, J. and Meleti, C.: Aerosol optical depth in the UVB and visible wavelength range from Brewer spectrophotometer direct irradiance measurements: 1991–2002, *J. Geophys. Res.*, 109, D09202, doi:10.1029/2003JD004409, 2004.
- Gröbner, J., Kazadzis, S., Schreder, J., Bolsée, D., Brogniez, C., De Backer, H., Di Sarra, A. G., Feister, U., Görts, P., Henriques, D., Jaroslowski, J., Simic, S., Stanec, M., Steinmetz, M., Tax, R., and Villaplana Guerrero, J. M.: Report of site visits round 2004, European Commission, Joint Research Centre, EUR 21398 EN, 171–182, 2004.
- Harris, N. R. P., Kyrö, E., Staehelin, J., Brunner, D., Andersen, S.-B., Godin-Beekmann, S., Dhomse, S., Hadjinicolaou, P., Hansen, G., Isaksen, I., Jrrar, A., Karpetchko, A., Kivi, R., Knudsen, B., Krizan, P., Lastovicka, J., Maeder, J., Orsolini, Y., Pyle, J. A., Rex, M., Vanicek, K., Weber, M., Wohltmann, I., Zanis, P., and Zerefos, C.: Ozone trends at northern mid- and high latitudes – a European perspective, *Ann. Geophys.*, 26, 1207–1220, doi:10.5194/angeo-26-1207-2008, 2008.
- Herman, J. R.: Global increase in UV irradiance during the past 30 years (1979–2008) estimated from satellite data, *J. Geophys. Res.*, 115, D04203, doi:10.1029/2009JD012219, 2010.
- Herman, J. R., Bhartia, P. K., Ziemke, J., Ahmad, Z., and Larko, D.: UV-B increases (1979–1992) from decreases in total ozone, *Geophys. Res. Lett.*, 23, 2117–2120, doi:10.1029/96GL01958, 1996.
- Holben, B. N., Tanré, D., Smirnov, A., Eck, T. F., Slutsker, I., Abuhassan, N., Newcomb, W. W., Schafer, J. S., Chatenet, B., Lavenue, F., Kaufman, Y. J., Vande Castle, J., Setzer, A., Markham, B., Clark, D., Frouin, R., Halthore, R., Karneli, A., O'Neill, N. T., Pietras, C., Pinker, R. T., Voss, K., and Zibordi, G.: An emerging ground-based aerosol climatology: Aerosol optical depth from AERONET, *J. Geophys. Res.*, 106, 12067–12097, doi:10.1029/2001JD900014, 2001.
- Hoppe, H. and Kiely, G.: Precipitation over Ireland: observed change since 1940, *Phys. Chem. Earth B*, 24, 91–96, 1999.
- Hsu, N. C., Gautam, R., Sayer, A. M., Bettenhausen, C., Li, C., Jeong, M. J., Tsay, S.-C., and Holben, B. N.: Global and regional trends of aerosol optical depth over land and ocean using SeaWiFS measurements from 1997 to 2010, *Atmos. Chem. Phys.*, 12, 8037–8053, doi:10.5194/acp-12-8037-2012, 2012.
- Huang, M., Jiang, H., Ju, W., and Xiao, Z.: Ultraviolet radiation over two lakes in the middle and lower reaches of the Yangtze river, China: An innovative model for UV estimation, *Terr. Atmos. Ocean. Sci.*, 22, 491–506, doi:10.3319/TAO.2011.05.02.01(A), 2011.
- Journée, M. and Bertrand, C.: Improving the spatio-temporal distribution of surface solar radiation data by merging ground and satellite measurements, *Remote Sens. Environ.*, 114, 2692–2704, doi:10.1016/j.rse.2010.06.010, 2010.
- Kalliskota, S., Kaurola, J., Taalas, P., Herman, J., Celarier, E. A., and Krotkov, N. A.: Comparison of daily UV doses estimated from Nimbus 7/TOMS measurements and ground-based spectroradiometric data, *J. Geophys. Res.*, 105, 5059–5067, doi:10.1029/1999JD900926, 2000.
- Kaurola, J., Taalas, P., Koskela, T., Borkowski, J., and Josefsson, W.: Long-term variations of UV-B doses at three stations in northern Europe, *J. Geophys. Res.*, 105, 20813–20820, doi:10.1029/2000JD900258, 2000.
- Kazadzis, S., Bais, A., Amiridis, V., Balis, D., Meleti, C., Kouremeti, N., Zerefos, C. S., Rapsomanikis, S., Petrakakis, M., Kelesis, A., Tzoumaka, P., and Kelektisoglou, K.: Nine years of UV aerosol optical depth measurements at Thessaloniki, Greece, *Atmos. Chem. Phys.*, 7, 2091–2101, doi:10.5194/acp-7-2091-2007, 2007.
- Krishna Prasad, N. V., Niranjana, K., Sarma, M. S. S. R. K., and Madhavi, N.: Regression analysis of biologically effective UV-B irradiance versus ozone at Visakhapatnam, *Int. J. Phys. Sci.*, 6, 7838–7843, doi:10.5897/IJPS11.581, 2011.
- Krzýscin, J. W. and Borkowski, J. L.: Variability of the total ozone trend over Europe for the period 1950–2004 derived from reconstructed data, *Atmos. Chem. Phys.*, 8, 2847–2857, doi:10.5194/acp-8-2847-2008, 2008.
- Krzýscin, J. W., Sobolwieski, P. S., Jaroslowski, J., Podgórski, J., and Rajewska-Wiech, B.: Erythemal UV observations at Belsk, Poland, in the period 1976–2008: data homogenization, climatology and trends, *Acta Geophys.*, 59, 155–182, doi:10.2478/s11600-010-0036-3, 2011.
- Lanzante, J. R.: Resistant, Robust and Non-parametric techniques for the analysis of climate data: theory and examples, including applications to historical radiosonde station data, *Int. J. Climatol.*, 16, 1197–1226, doi:10.002/(SICI)1097-0088(199611)16:11<1197::AID-JOC89>3.0.CO;2-L, 1996.
- Lindfors, A. V., Arola, A., Kaurola, J., Taalas, P., and Svenøe, T.: Longterm erythemal UV doses at Sodankylä estimated using total ozone, sunshine duration, and snow depth, *J. Geophys. Res.*, 108, 4518, doi:10.1029/2002JD003325, 2003.

- Lindfors, A., Kaurola, J., Arola, A., Koskela, T., Lakkala, K., Josefsson, W., Olseth, J. A., and Johnsen, B.: A method for reconstruction of past UV radiation based on radiative transfer modeling: applied to four stations in northern Europe, *J. Geophys. Res.*, 112, D23201, doi:10.1029/2007JD008454, 2007.
- Litynska, Z., Koepke, P., De Backer, H., Gröbner, J., Schmalwieser, A., and Vuilleumier, L.: COST action 726 final report: Long term changes and climatology of UV radiation over Europe, ISBN 978-92-898-0052-5, Luxembourg: Publications office of the European Union, doi:10.2831/12065, 2012.
- Makowski, K., Jaeger, E. B., Chiacchio, M., Wild, M., Ewen, T., and Ohmura, A.: On the relationship between diurnal temperature range and surface solar radiation in Europe, *J. Geophys. Res.*, 114, D00D07, doi:10.1029/2008JD011104, 2009.
- Matthijssen, J., Slaper, H., Reinen, A. J. M. H., and Velders, G. J. M.: Reduction of solar UV by clouds: A comparison between satellite-derived cloud effects and ground-based radiation measurements, *J. Geophys. Res.*, 105, 5069–5080, doi:10.1029/1999JD900937, 2000.
- Mishchenko, M. I. and Geogdzhayev, I. V.: Satellite remote sensing reveals regional tropospheric aerosol trends, *Opt. Express*, 15, 7423–7438, doi:10.364/OE.15.007423, 2007.
- Nabat, P., Somot, S., Mallet, M., Chiapello, I., Morcrette, J. J., Solomon, F., Szopa, S., Dulac, F., Collins, W., Ghan, S., Horowitz, L. W., Lamarque, J. F., Lee, Y. H., Naik, V., Nagashima, T., Shindell, D., and Skeie, R.: A 4D climatology (1979–2010) of the monthly tropospheric aerosol optical depth distribution over the Mediterranean region from a comparative evaluation and blending of remote sensing and model products, *Atmos. Meas. Tech.*, 6, 1287–1314, doi:10.5194/amt-6-1287-2013, 2013.
- Norris, J. R. and Slingo, A.: Chapter 2: trends in observed cloudiness and earth's radiation budget, in: *Clouds in the perturbed climate system: their relationship to energy balance, atmospheric dynamics and precipitation*, edited by: Heintzenberg, J. and Charlson, R. J., 2009.
- Norris, J. R. and Wild, M.: Trends in aerosol radiative effects over Europe inferred from observed cloud cover, solar “dimming”, and solar “brightening”, *J. Geophys. Res.*, 112, D08214, doi:10.1029/2006JD007794, 2007.
- Nyeki, S., Halios, C. H., Baum, W., Eleftheriadis, K., Flentje, H., Gröbner, J., Vuilleumier, L., and Wehrli, C.: Ground-based aerosol optical depth trends at three high-altitude sites in Switzerland and southern Germany from 1995 to 2010, *J. Geophys. Res.*, 117, D18202, doi:10.1029/2012JD017493, 2012.
- Reeves, J., Chen, J., Wang, X. L., Lund, R., and Lu, Q. Q.: A review and comparison of changepoint detection techniques for climate data, *J. Appl. Meteorol. Clim.*, 46, 900–915, doi:10.1175/JAM2493.1, 2007.
- Reinsel, G. C., Miller, A. J., Weatherhead, E. C., Flynn, L. E., Nagatani, R. M., Tiao, G. C., and Wuebbles, D. J.: Trend analysis of total ozone data for turnaround and dynamical contributions, *J. Geophys. Res.*, 110, D16306, doi:10.1029/2004JD004662, 2005.
- Rieder, H. E., Holawe, F., Simic, S., Blumthaler, M., Krzyscin, J. W., Wagner, J. E., Schmalwieser, A. W., and Weihs, P.: Reconstruction of erythemal UV-doses for two stations in Austria: a comparison between alpine and urban regions, *Atmos. Chem. Phys.*, 8, 6309–6323, doi:10.5194/acp-8-6309-2008, 2008.
- Rieder, H. E., Staehelin, J., Weihs, P., Vuilleumier, L., Maeder, J. A., Holawe, F., Blumthaler, M., Lindfors, A., Peter, T., Simic, S., Spichtinger, P., Wagner, J. E., Walker, D., and Ribatet, M.: Relationship between high daily erythemal UV doses, total ozone, surface albedo and cloudiness: An analysis of 30 years of data from Switzerland and Austria, *Atmos. Res.*, 98, 9–20, doi:10.1016/j.atmosres.2010.03.006, 2010.
- Rieder, H. E., Frossard, L., Ribatet, M., Staehelin, J., Maeder, J. A., di Rocco, S., Davison, A. C., Peter, T., Weihs, P., and Holawe, F.: On the relationship between total ozone and atmospheric dynamics and chemistry at midlatitudes – Part 2: The effects of the El Niño/Southern Oscillation, volcanic eruptions and contributions of atmospheric dynamics and chemistry to long-term total ozone changes, *Atmos. Chem. Phys.*, 13, 165–179, doi:10.5194/acp-13-165-2013, 2013.
- Sanchez-Lorenzo, A. and Wild, M.: Decadal variations in estimated surface solar radiation over Switzerland since the late 19th century, *Atmos. Chem. Phys.*, 12, 8635–8644, doi:10.5194/acp-12-8635-2012, 2012.
- Santer, B. D., Wigley, T. M. L., Boyle, J. S., Gaffen, D. J., Hnilo, J. J., Nychka, D., Parker, D. E., and Taylor, K. E.: Statistical significance of trends and trend differences in layer-average atmospheric temperature time series, *J. Geophys. Res.*, 105, 7337–7356, doi:10.1029/1999JD901105, 2000.
- Sasaki, M., Takeshita, S., Oyanagi, T., Miyake, Y., and Sakata, T.: Increasing trend of biologically active solar ultraviolet-B irradiance in mid-latitude Japan in the 1990s, *Opt. Eng.*, 41, 3062–3069, doi:10.1117/1.1516823, 2002.
- SCI TEC: Brewer ozone spectrophotometer, Acceptance manual, Document number AM-BA-CO5-Rev C, SCI TEC Instruments, 1988.
- Smedley, A. R. D., Rimmer, J. S., Moore, D., Toumi, R., and Webb, A. R.: Total ozone and surface UV trends in the United Kingdom: 1979–2008, *Int. J. Climatol.*, 32, 338–346, doi:10.1002/joc.2275, 2012.
- Solomon, S., Qin, D., Manning, M., Alley, R. B., Berntsen, T., Bindoff, N. L., Chen, Z., Chidthaisong, A., Gregory, J. M., Hegerl, G. C., Heimann, M., Hewitson, B., Hoskins, B. J., Joos, F., Jouzel, J., Kattsov, V., Lohmann, U., Matsuno, T., Molina, M., Nicholls, N., Overpeck, J., Raga, G., Ramaswamy, V., Ren, J., Rusticucci, M., Somerville, R., Stocker, T. F., Whetton, P., Wood, R. A. and Wratt, D.: Technical Summary, in: *Climate Change 2007: The Physical Science Basis. Contribution of Working Group I to the Fourth Assessment Report of the Intergovernmental Panel on Climate Change*, edited by: Solomon, S., Qin, D., Manning, M., Chen, Z., Marquis, M., Averyt, K. B., Tignor, M., and Miller, H. L., Cambridge University Press, Cambridge, United Kingdom and New York, NY, USA, 19–91, 2007.
- Staehelin, J., Kegel, R., and Harris, N. R. P.: Trend analysis of the homogenized total ozone series of Arosa (Switzerland) 1926–1996, *J. Geophys. Res.*, 103, 8389–8399, doi:10.1029/97JD03650, 1998.
- Steinbrecht, W., Claude, H., Schönenborn, F., McDermid, I. S., Leblanc, T., Godin, S., Song, T., Swart, D. P. J., Meijer, Y. J., Bodeker, G. E., Connor, B. J., Kämpfer, N., Hocke, K., Calisesi, Y., Schneider, N., de la Noë, J., Parrish, A. D., Boyd, I. S., Brühl, C., Steil, B., Giorgetta, M. A., Manzini, E., Thomason, L. W., Zawodny, J. M., McCormick, M. P., Russell III, J. M., Bhartia, P. K., Stolarski, R. S., and Hollandsworth-Frith, S. M.: Long-term evolution of upper stratospheric ozone at selected stations of the

- Network for the Detection of Stratospheric Change (NDSC), *J. Geophys. Res.*, 111, D1027, doi:10.1029/2005JD006454, 2006.
- Stjern, C. W., Egill Kristjánsson, J., and Hansen, A. W.: Global dimming and global brightening: an analysis of surface radiation and cloud cover data in northern Europe, *Int. J. Climatol.*, 29, 643–653, doi:10.1002/joc.1735, 2009.
- Tevini, M. and Teramura, A. H.: UV-B effects on terrestrial plants, *Photochem. Photobiol.*, 50, 479–487, doi:10.1111/j.1751-1097.1989.tb05552.x, 1989.
- Trepte, S. and Winkler, P.: Reconstruction of erythemal UV irradiance and dose at Hohenpeissenberg (1968–2001) considering trends of total ozone, cloudiness and turbidity, *Theor. Appl. Climatol.*, 77, 159–171, doi:10.1007/s00704-004-0034-y, 2004.
- United Nations Environment Programme (UNEP): Environmental effects of ozone depletion and its interactions with climate change: 2010 assessment, 236 pp., UNEP, Nairobi, Kenya, ISBN:ISBN 92-807-2312-X, 2010.
- Van Malderen, R. and De Backer, H.: A drop in upper tropospheric humidity in autumn 2001, as derived from radiosonde measurements at Uccle, Belgium, *J. Geophys. Res.*, 115, D20114, doi:10.1029/2009JD013587, 2010.
- Vigouroux, C., De Mazière, M., Demoulin, P., Servais, C., Hase, F., Blumenstock, T., Kramer, I., Schneider, M., Mellqvist, J., Strandberg, A., Velasco, V., Notholt, J., Sussmann, R., Stremme, W., Rockmann, A., Gardiner, T., Coleman, M., and Woods, P.: Evaluation of tropospheric and stratospheric ozone trends over Western Europe from ground-based FTIR network observations, *Atmos. Chem. Phys.*, 8, 6865–6886, doi:10.5194/acp-8-6865-2008, 2008.
- Weatherhead, C. E., Reinsel, G. C., Tiao, G. C., Meng, X.-L., Choi, D., Cheang, W.-K., Keller, T., DeLuisi, J., Wuebbles, D. J., Kerr, J. B., Miller, A. J., Oltmans, S. J., and Frederick, J. E.: Factors affecting the detection of trends: Statistical considerations and applications to environmental data, *J. Geophys. Res.*, 103, 17149–17161, doi:10.1029/98JD00995, 1998.
- Wenny, B. N., Saxena, V. K., and Frederick, J. E.: Aerosol optical depth measurements and their impact on surface levels of ultraviolet-B radiation, *J. Geophys. Res.*, 106, 17311–17319, doi:10.1029/2001JD900185, 2001.
- Wild, M., Trüssel, B., Ohmura, A., Long, C. N., König-Langlo, G., Dutton, E. G., and Tsvetkov, A.: Global dimming and brightening: an update beyond 2000, *J. Geophys. Res.*, 114, D00D13, doi:10.1029/2008JD011382, 2009.
- Williams, J. E., den Outer, P. N., Slaper, H., Matthijsen, J., and Kelfkens, G.: Cloud induced reduction of solar UV-radiation: A comparison of ground-based and satellite based approaches, *Geophys. Res. Lett.*, 31, L03104, doi:10.1029/2003GL018242, 2004.
- Williams, M. N., Gómez Grajales, C. A., and Kurkiewicz, D.: Assumptions of multiple regression: correcting two misconceptions, *Pract. Ass. Res. Eval.*, 18, ISSN 1531-7714, 2013.
- WMO (World Meteorological Organization), Scientific Assessment of Ozone Depletion: 2006, Global Ozone Research and Monitoring Project-Report No. 50, 572 pp., Geneva, Switzerland, 2006.
- Zerefos, C. S., Balis, D. S., Bais, A. F., Gillotay, D., Simon, P. C., Mayer, B., and Seckmeyer, G.: Variability of UV-B at four stations in Europe, *Geophys. Res. Lett.*, 24, 1363–1366, 1997.
- Zerefos, C., Balis, D., Tzortziou, M., Bais, A., Tourpali, K., Meleti, C., Bernhard, G., and Herman, J.: A note on the interannual variations of UV-B erythemal doses and solar irradiance from ground-based and satellite observations, *Ann. Geophys.*, 19, 115–120, doi:10.5194/angeo-19-115-2001, 2001.
- Zerefos, C. S., Tourpali, K., Eleftheratos, K., Kazadzis, S., Meleti, C., Feister, U., Koskela, T., and Heikkilä, A.: Evidence of a possible turning point in solar UV-B over Canada, Europe and Japan, *Atmos. Chem. Phys.*, 12, 2469–2477, doi:10.5194/acp-12-2469-2012, 2012.
- Ziemke, J. R., Chandra, S., Herman, J., and Varotsos, C.: Erythemally weighted UV trends over northern latitudes derived from Nimbus 7 TOMS measurements, *J. Geophys. Res.*, 105, 7373–7382, 2000.